A N N U A L R E P O R T

2022

and list of publications

Bayerisches Forschungsinstitut
für Experimentelle Geochemie und Geophysik
Universität Bayreuth

Bayerisches Geoinstitut
Universität Bayreuth
95440 Bayreuth
Germany

Telephone: +49-(0)921-55-3700
Telefax: +49-(0)921-55-3769
e-mail: bayerisches.geoinstitut@uni-bayreuth.de
www: https://www.bgi.uni-bayreuth.de

Editorial compilation by: Florian Heidelbach and Petra Buchert
Section editors: Andreas Audétat, Tiziana Boffa Ballaran, Audrey Bouvier,
Leonid Dubrovinsky, Dan Frost, Florian Heidelbach, Gregor Golabek,
Tomoo Katsura, Hans Keppler, Catherine McCammon,
Nobuyoshi Miyajima, Dave Rubie, Gerd Steinle-Neumann, Tony Withers

Staff and guests of the Bayerisches Geoinstitut in **October 2022**:

Die Mitarbeiter und Gäste des Bayerischen Geoinstituts im **Oktober 2022:**

first row, from left (1. Reihe, v. links) Giacomo Criniti, Sumith Abeykoon, Narangoo Purevjav, Caterina Melai, Dorothea Wiesner, Ulrike Trenz, Alena Aslandukova, Tiziana Boffa Ballaran, Fariia Akbar

second row, from left (2. Reihe, v. links) Andrea Piccolo, Meredith Calogero, Greta Rustioni, Hu Tang, Sven Linhardt, Janina Scharnagel, Heinz Fischer, Stefan Übelhack, Dmitry Bondar

third row, from left (3. Reihe, v. links) Lin Wang, Dan Frost, Hongzhan Fei, Melanie Pöppelbaum, Gerald Bauer, Nobuyoshi Miyajima, Laura Czekay, Andreas Audétat, Jia Chang

back rows, from left (hintere Reihen, v. links) Leonid Dubrovinsky, Liang Yuan, Fei Wang, Lianjie Man, Ran Zhao, Anna Dinius, Florian Heidelbach, Alexander Rother, Tony Withers, Hans Keppler, Marc Hirschmann, Jyotirmoy Paul, Laura Cialdella, Detlef Krauße, Adrien Néri

Absent (Es fehlten) Andrii Aslandukov, Audrey Bouvier, Petra Buchert, Amrita Chakraborti, Artem Chanyshev, Jonathan Dolinschi, Gregor Golabek, Remco Hin, Tomoo Katsura, Eun Jeong Kim, Edith Kubik, Alexander Kurnosov, Dominic Langhammer, Naira Martirosyan, Rebecka Matthäus, Catherine McCammon, Raphael Njul, Edna Obengo, Sergey Ovsyannikov, Esther Posner, Anke Potzel, Dave Rubie, Hubert Schulze, Jinia Sikdar, Gerd Steinle-Neumann, Marcel Thielmann, Pedro Valdivia Munoz, Xiaoyu Wang

Contents

Foreword

In the year 2022, life and work at Bayerisches Geoinstitut slowly returned to normal. While in spring, there were still strong covid restrictions, they progressively disappeared over the course of the year and the stream of external visitors to the institute slowly resumed. Institute seminars changed back from online mode to physical presence in a lecture room and, very importantly, we were again able to have a BBQ party in summer and at least some kind of Christmas reception at the end of the year. The construction of the new laboratories for geochemistry and cosmochemistry was completed and two new mass spectrometers arrived and were installed.

In addition to our research activities, the support of young scientists always had a very high priority at our institute and we like to keep in contact with our former Ph.D. students and postdocs after they have left Bayreuth. We are therefore very happy that, in 2022, two young scientists who obtained their Ph.D. from our institute and had moved on to other places were awarded the prestigious Starting Grants of the European Research Council. A very important event for the future of Bayerisches Geoinstitut was also the search procedure for a new, tenure-track Junior Professorship in "Geomaterials". We are very pleased that Johannes Buchen from the University of Oxford accepted our offer and will move to Bayreuth in May 2023.

The current annual report illustrates the broad spectrum of research that is carried out at Bayerisches Geoinstitut. While the traditional research activities towards understanding Earth's deep interior remain very strong, there is also increasing activity in studies of extraterrestrial materials and even the structure of exoplanets. At the low-pressure end of our typical experimental research, one may note a renewed interest in volcanological studies using new methods and concepts. Among the wide diversity of subjects presented here, it is always difficult to identify some of the most notable results. I will briefly highlight here three contributions, but there are almost certainly many others that are equally important.

Textbooks usually state that Earth's lower mantle consists mostly of three minerals, bridgmanite $(Mg,Fe)SiO_3$, ferropericlase (Mg,Fe)O, and davemaoite $CaSiO_3$. In 2022, a publication in the journal *Nature* by a group of US scientists received considerable attention. They claimed that the solubility of the $CaSiO_3$ component in bridgmanite increases so much with temperature that beyond 40 GPa and 2300 K, the davemaoite phase disappears. This would imply a major change of mantle mineralogy with depth. In a contribution on page 49 of this annual report, Lin Wang and coworkers re-investigated this claim. They find that in contrast to the results of the US group, the solubility of the $CaSiO_3$ component in bridgmanite remains low and the two minerals bridgmanite and davemaoite likely coexist throughout the lower mantle. In fact, multianvil experiments at 40 GPa and 2300 K clearly show the stable coexistence of the two phases. The difference between the experimental data sets is likely due to considerable temperature gradients in the laser-heated diamond cell experiments carried out by the US group. In contrast to this, temperatures can be much better controlled in multianvil experiments and, due to the

continued efforts of the group led by Tomo Katsura, it is now possible to routinely perform multianvil experiments under conditions that extend deep into the lower mantle.

Inclusions in natural diamonds have provided invaluable insights into the mineralogy of Earth's mantle. Some of these diamonds clearly brought samples from the transition zone or even of the lower mantle back to the surface, where they can now be conveniently studied in the laboratory. However, it is not always easy to identify the depth from which diamonds and their inclusions originated. For example, inclusions of ferropericlase (Mg,Fe)O could well come from the lower mantle, but there are also possible mechanisms that could produce such inclusions at much more shallow depths. On page 54 it is reported how Caterina Melai and colleagues experimentally studied the oxidation state of iron in ferropericlase as a function of pressure. The results clearly show that many inclusions of ferropericlase in natural diamonds are so oxidized that they likely formed in the upper mantle.

About one and a half years ago, the eruption of the Cumbre Vieja volcano on La Palma made it into the headlines of news in all of Europe. In order to predict such volcanic activities, data on melt viscosity are essential. Unfortunately, viscosity may vary by many orders of magnitude depending on temperature and composition. In particular, the compositional dependence is so complicated that it cannot be captured by analytical expressions of reasonable complexity. On page 114 it is reported how Dominic Langhammer and colleagues take a fresh look at this problem. They trained an artificial neural network with a large number of viscosity data in order to predict the viscosity of various magma compositions. The results of this approach are very encouraging, yielding predictions that are considerably better than those obtained by conventional methods.

On the behalf of my colleagues, I would like to thank the *Free State of Bavaria* as represented by the *Bavarian State Ministry of Science, Research and Art*, as well as the *Advisory Board for High-Pressure Research in Geoscience of the Bavarian Academy of Sciences* for their continuing support and strong commitment to the Bayerisches Geoinstitut. I would further like to thank the *President and Leadership of the University of Bayreuth* for their high regard of our institute. We also gratefully acknowledge generous support from external funding agencies, in particular the *Alexander von Humboldt Foundation*, the *European Union*, the *German Science Foundation,* and the *Federal Ministry of Education and Research*, which continue to contribute greatly to the further development and success of the Geoinstitut.

Bayreuth, March 2022 Hans Keppler

Vorwort

Im Jahr 2022 haben sich das Leben und die Arbeitsbedingungen am Bayerischen Geoinstitut langsam normalisiert. Im Frühjahr gab es noch starke Sicherheitsvorkehrungen wegen der Corona-Pandemie, die jedoch im Laufe des Jahres mehr und mehr wegfielen, während die Besuche von externen Wissenschaftlern langsam wieder zunahmen. Die Instituts-Seminare fanden wieder in Präsenz statt an Stelle von Online-Veranstaltungen und – besonders wichtig – wir konnten wieder unsere traditionelle Grillparty im Sommer und zumindest einen kleinen Weihnachts-Empfang zum Jahresende abhalten. Die Konstruktion der neuen Labore für Geochemie und Kosmochemie wurde abgeschlossen und zwei neue Massenspektrometer wurden geliefert und in Betrieb genommen.

Neben unseren Forschungsaktivitäten hat die Förderung junger Wissenschaftler immer hohe Priorität an unserem Institut. Wir bleiben gerne in Kontakt mit unseren ehemaligen Doktoranden und Postdoktoranden, auch wenn sie bereits an andere Institutionen weitergezogen sind. Wir freuen uns daher sehr, dass im Jahr 2022 zwei unserer ehemaligen Doktoranden prestigeträchtige Starting Grants des European Research Council erhalten haben. Ein weiteres, für die Zukunft des Geoinstituts besonders wichtiges Ereignis war das Berufungsverfahren für eine Junior-Professur in "Geomaterialien". Wir freuen uns, dass Johannes Buchen von der Universität Oxford den Ruf angenommen hat und im Mai 2023 nach Bayreuth kommen wird.

Der vorliegende Jahresbericht illustriert das breite Spektrum der Forschung am Bayerischen Geoinstitut. Während die traditionellen Forschungsaktivitäten über das tiefe Erdinnere weiterhin stark bleiben, gibt es auch ein zunehmendes Interesse an der Untersuchung von extraterrestrischen Materialien bis zur Struktur von Exoplaneten. Unter den Experimenten bei relativ niedrigem Druck fallen Aktivitäten im Bereich der Vulkanologie mit neuen Methoden und Konzepten auf. Es ist immer sehr schwierig, in dem breiten Spektrum wissenschaftlicher Resultate die wichtigsten Ergebnisse herauszufinden. Ich werde hier kurz auf drei Beiträge näher eingehen, es gibt aber wahrscheinlich viele, die genauso wichtig sind.

In Lehrbüchern wird oft erklärt, dass der untere Mantel im Wesentlichen aus drei Mineralen besteht, nämlich Bridgmanit $(Mg,Fe)SiO_3$, Ferroperiklas $(Mg,Fe)O$ und Davemaoit $CaSiO_3$. Im Jahr 2022 hat eine Publikation von amerikanischen Wissenschaftlern in der Zeitschrift Nature für einiges Aufsehen gesorgt. Nach dieser Studie soll die Löslichkeit von $CaSiO_3$ im Bridgmanit mit der Temperatur so stark ansteigen, dass jenseits von 40 GPa und 2300 K die Davemaoit-Phase verschwindet und sich die Mineralogie des Erdmantels mit der Tiefe grundsätzlich ändert. In einem Beitrag auf Seite 49 dieses Jahresberichts untersuchen Lin Wang und Mitarbeiter diese Fragestellung. Im Gegensatz zur amerikanischen Gruppe finden sie eine recht niedrige Löslichkeit von $CaSiO_3$ im Bridgmanit, so dass das Mineral Davemaoit wahrscheinlich praktisch im ganzen unteren Mantel stabil ist. In der Tat zeigen Multi-Anvil-Experimente bei 40 GPa und 2300 K eindeutig die Koexistenz von Bridgmanit und Davemaoit. Der Unterschied zwischen den experimentellen Resultaten beruht wahrscheinlich auf den großen Temperaturgradienten in den Experimenten der amerikanischen Gruppe, die mit Laser-

beheizten Diamantstempel-Zellen ausgeführt wurden. Im Vergleich dazu kann die Temperatur in Multi-Anvil-Experimenten sehr viel genauer kontrolliert werden. Aufgrund der kontinuierlichen Entwicklungen in der Arbeitsgruppe von Tomo Katsura können solche Experimente jetzt routinemäßig unter Bedingungen ausgeführt werden, die tief in den unteren Mantel hineinreichen.

Einschlüsse in natürlichen Diamanten liefern grundlegende Erkenntnisse über die Zusammensetzung des Erdmantels. Manche dieser Diamanten haben eindeutig Material aus der Überganszone oder sogar aus dem unteren Mantel zur Oberfläche gebracht, wo diese Proben jetzt bequem im Labor untersucht werden können. Die Tiefe, aus der diese Diamanten stammen, lässt sich jedoch nicht immer leicht feststellen. Einschlüsse von Ferroperiklas (Mg,Fe)O können beispielsweise sehr wohl aus dem unteren Mantel stammen, es sind jedoch auch Prozesse denkbar, die solche Einschlüsse in viel geringerer Tiefe produzieren. Auf Seite 54 beschreiben Caterina Melai und Mitarbeiter Experimente, mit denen der Oxidationszustand von Eisen im Ferroperiklas als Funktion des Drucks untersucht wurde. Die Resultate zeigen eindeutig, dass viele Einschlüsse von Ferroperiklas in natürlichen Diamanten so oxidiert sind, dass sie wahrscheinlich im oberen Mantel gebildet wurden.

Vor etwa anderthalb Jahren machte die Eruption des Vulkans von Cumbre Vieja auf La Palma Schlagzeilen in ganz Europa. Für die Vorhersage solcher Eruptionen sind Daten über die Viskosität der Schmelzen unverzichtbar. Diese Viskositäten variieren jedoch über viele Größenordnungen und sie hängen von Temperatur und Zusammensetzung ab. Insbesondere der Einfluss der Zusammensetzung ist so kompliziert, dass er mit Formeln kaum beschreibbar ist. Auf Seite 114 skizzieren Dominic Langhammer und Kollegen eine mögliche Lösung für dieses Problem. Sie haben ein künstliches neuronales Netzwerk mit einer großen Zahl von Messdaten so trainiert, dass es die Viskosität von Schmelzen unterschiedlicher Zusammensetzungen vorhersagen kann. Die Resultate dieser Methode sind sehr vielversprechend und erlauben erheblich genauere Vorhersagen als konventionelle Methoden.

Meine Kollegen und ich möchten dem *Freistaat Bayern*, vertreten durch das *Bayerische Staatsministerium für Wissenschaft, Forschung und Kunst*, und dem *Beirat für Geowissenschaftliche Hochdruckforschung der Bayerischen Akademie der Wissenschaften* unseren Dank für ihre fortwährende Unterstützung des Bayerischen Geoinstituts aussprechen. Darüber hinaus möchten wir dem Präsidenten und der Hochschulleitung der Universität Bayreuth ausdrücklich für ihre zuverlässige und kontinuierliche Unterstützung unseres Instituts danken. Wir sind auch für die großzügige Förderung durch externe Geldgeber dankbar, insbesondere der *Alexander-von-Humboldt-Stiftung*, der *Europäischen Union* und der *Deutschen Forschungsgemeinschaft*, die ebenfalls wesentlich zur Entwicklung und zum Erfolg des Bayerischen Geoinstituts beigetragen haben.

Bayreuth, im März 2022 Hans Keppler

1. Advisory Board and Directorship

1.1 Advisory Board

The *Beirat für Geowissenschaftliche Hochdruckforschung der Bayerischen Akademie der Wissenschaften* advises on the organisation and scientific activities of the institute. Members of this board are:

Prof. Dr. Ulrich CHRISTENSEN	Emeritus, Max-Planck-Institut für Sonnensystem-forschung, Göttingen
Prof. Dr. Rudolf GROSS (Vice Chairman)	Walther-Meißner-Institut für Tieftemperatur-forschung (WMI), Garching
Prof. Dr. Francois HOLTZ	Institut für Mineralogie der Leibniz Universität Hannover
Prof. Dr. Klaus MEZGER	Institut für Geologie der Universität Bern
Prof. Dr. Herbert PALME	Emeritus, Institut für Mineralogie und Geochemie der Universität zu Köln – Senckenberg Forschungsinstitut und Naturmuseum Frankfurt/M.
Prof. Dr. Markus RIEDERER (Chairman)	Julius-von-Sachs-Institut für Biowissenschaften, Würzburg
Prof. Dr. Ekhard SALJE, FRS, FRSA	Emeritus, Department of Earth Sciences, University of Cambridge
Prof. Dr. Christine THOMAS	Institut für Geophysik der Westfälischen Wilhelms-Universität Münster

1.2 Leadership

Prof. Dr. Hans KEPPLER (Director)
Prof. Dr. Dan FROST (Deputy Director)
Prof. Dr. Tomoo KATSURA

2. Staff, Funding and Facilities

2.1 Staff

At the end of 2022, the following staff positions existed in the institute:

- Scientific staff: **16**
- Technical staff: **14**
- Administrative staff: **2**
- Administrative officer: **1**

During 2022, 31 scientific positions (298 months) were funded by grants raised externally by staff members of the institute. In addition, 2 long-term scientific positions (24 months) were funded by the resources of the BGI Visiting Scientists' Programme (see Sect. 8), which also supported short-term visits for discussing future projects or presenting research results (see Sect. 5). 9 student assistants (62 months) were funded by externally raised grants. 7 scientists and 3 PhD students (81 months) were supported by personal grants or stipends.

2.2 Funding

In 2022, the following financial resources were available from the Free State of Bavaria:

- Visiting Scientists' Programme: 162.000 €
- Consumables: 657.000 €
- Investment funding: 813.000 €

The total amount of national/international external funding *("Drittmittel"*) used for ongoing research projects in 2022 was 3.715.000 € (positions: 1.972.000 €; equipment, consumables and travel grants: 1.743.000 €).

	positions	**equipment, consumables, travel grants**	**total**
• AvH	85.000 €	72.000 €	157.000 €
• BMBF	35.000 €	258.000 €	293.000 €
• DFG	1.463.000 €	967.000 €	2430.000 €
• EU	378.000 €	438.000 €	816.000 €
• Others	11.000 €	8.000 €	19.000 €
	1.972.000 €	**1.743.000 €**	**3.715.000 €**

(AvH = Alexander von Humboldt Foundation; BMBF = Federal Ministry of Education and Research; DFG = German Science Foundation; EU = European Union; Others: DAAD, Chinese Science Council, Japanese Society for the Promotion of Science, Swiss National Science Foundation)

In the following list, only the BGI components of the funding are listed in cases where joint projects involved other research institutions. Principal investigators and the duration of the grants are listed in brackets. Total project funding refers to the funding over the entire duration of this project.

Funding institution	Project, Funding	Total Project Funding
BMBF	05K19WCA (H. Keppler – 7/19-6/22) "Aufbau einer Hochdruckpresse vom Multi-Anvil-Typ an der Forschungs-Neutronenquelle FRM II in Garching" Total funding:	579.116 €
DFG	AU 314/6-1 (A. Audétat – 1/21-7/23) "Bestimmung der Faktoren, die das Cu-Au Mineralisations-potenzial von Magmen in Kollisionszonen kontrollieren" Positions: E 13 (100 %), 24 months 151.000 € Consumables: 35.800 € Overhead: 41.100 €	227.900 €
DFG	BO 2550/10-1 (T. Boffa Ballaran, B. Mihailova – 7/21-6/24 "Mehrskaliges Hochdruckverhalten der bleifreien ferroelektrischen Perowskitmischkristalle $(1-x)Na_{0.5}BiTiO_{3-x}BaTiO_3$" Positions: student assistant 15.000 € Consumables: 6.900 € Overhead: 4.800 €	26.700 €
DFG	DI 2751/2-1 (D. Di Genova – 10/21-9/24) "Rheology of nanocrystal-bearing natural silicate melts" Positions: E 13 (75 %), 36 months 160.900 € student assistant 4.846 € Equipment: 18.000 € Overhead: 40.400 €	224.146 €
DFG	DU 393/13-2 (L.S. Dubrovinsky – 7/20-6/23) "Mantel-formende Materialien von Super-Erden bei statischen Drücken von über 500 GPa und hohen Temperaturen" Positions: E 13 (75 %), 36 months 158.600 € student assistant 7.000 € Equipment: 32.250 € Overhead: 43.500 €	241.350 €
DFG	FR 1555/11-1 (D.J. Frost – 3/16-2/23) Gottfried Wilhelm Leibniz-Preis 2016	2.500.000 €

DFG	INST 91/455-1 (A. Bouvier) Major Research Instrumentation Individual Proposal for a Laser Ablation – Multi-collector Inductively Coupled Plasma Mass Spectrometer with collision reaction cell. 50 % from institution (UBT and BGI) – 50% from DFG. Total from DFG:	615.000 €
DFG	INST 91/463-1 FUGG (H. Keppler – 2022-2023) Co-financing for a new electron microprobe. Total DFG funding (50 % of total costs):	611.000 €
DFG	KA3434/19-1 (T. Katsura – 02/21-08/23) "Evaluation of the aspect ratio of ferropericlase under lower-mantle conditions" Positions: E13, 24 months 152.200 € Consumables: 50.000 € Overhead: 44.400 €	246.600 €
DFG	KA 3434/20-1 (T. Katsura – 9/21-8/23) "Accurate determination of the melting relations of primitive peridotite under lower-mantle conditions up to 35 GPa using advanced multi-anvil techniques" Positions: E13, 24 months 154.100 € Consumables: 50.000 € Overhead: 44.900 €	249.000 €
DFG	KE 501/16-1 (H. Keppler – 2020-2023) "Cassiterite solubility, tin partitioning, and the origin of porphyry tin deposits" Total funding:	242.288 €
DFG	KE 501/18-1 (H. Keppler – 2022-2025) "Stability of organic molecules in subduction zone fluids" Total funding:	259.555 €
DFG	KU 3447/1-2 (A. Kurnosov – 1/22-12/24) "Einkristall-Elastizität von Mars-Mineralen und ein flexibles CO_2 Laserheizsystem" Position: E 13, 36 months 237.100 € student assistant 10.000 € Consumables and travel funding: 23.550 € Overhead: 59.500 €	330.150 €
DFG	MC 3/20-2 (C.A. McCammon – 1/18-12/22) DFG FOR 2125 (CarboPaT) "Elastic properties of carbonates at high pressure and high temperature" Position: E 13 (67 %), 36 months: 132.800 € Equipment, consumables and travel funding: 27.750 € Overhead: 35.300 €	195.850 €

DFG	ME 5206/3-1 (L.S. Dubrovinsky, (T. Meier) – 6/19-5/22) "Wasserstoffbrückenbindungen unter extremen Bedingungen: Kernquanteneffekte und Symmetrisierung der Wasserstoff-brückenbindung untersucht mit ^{1}H-NMR in Diamantstempel-zellen" Position: E 13, 36 months: 221.500 € Consumables and travel funding: 29.250 € Overhead: 55.200 €	305.950 €
DFG	MI 1721/3-1 (N. Miyajima – 9/19-2/23) "Al, Si-Interdiffusion in Bridgmanit und die Viskosität des unteren Mantels" Position: E 13 (75 %), 36 months: 149.500 € E 13 (75 %), 6 months extension 26.900 € student assistant 7.500 € Consumables and travel funding: 29.500 € Overhead: 41.000 € Overhead extension: 5.900 €	260.300 €
DFG	OV 110/3-2 (S.V. Ovsyannikov – 12/20-11/22) "High-pressure synthesis and properties of novel simple oxides with unusual stoichiometries" Position: E 13, 24 months 151.600 € Consumables and travel funding: 39.550 € Overhead: 42.100 €	233.250 €
DFG	STE 1105/13-2 (G. Steinle-Neumann – 7/20-6/23) "Thermodynamic properties of silicate solids and liquids and iron to the TPa range from *ab initio* calculations" Positions: E 13 (75%), 36 months 158.600 € student assistant 7.000 € Consumables: 8.250 € Overhead: 38.200 €	212.050 €
DFG	TH 2076/7-1 (M. Thielmann – 6/21-5/24) "Quantifizierung des Oberflächensignals durch Lithosphärenablösung in den Alpen" Positions: 244.700 € Consumables: 17.050 € Overhead: 57.600 €	319.350 €
DFG	TH 2076/8-1 (M. Thielmann – 11/21-10/24) "Identifizierung der Entstehungsprozesse tiefer Erdbeben" (Emmy-Noether-Programm) Positions: 670.913 € Consumables: 60.580 € Workshops: 5.000 € Overhead: 162.000 €	898.496 €

DFG	WI 5383/1-1 (A. Withers, A.B. Woodland – 04/20-03/23 "Gescherte Peridotite: Deformation, Metasomatose und beginnende Destabilisierung von Kratonen" Positions: student assistant 7.500 € Overhead: 1.700 €	9.200 €
DFG	YU 358/1-1 (L. Yuan, G. Steinle-Neumann – 2/22-1/25) "Partitionierung flüchtiger Elemente im tiefen Magma Ozean der Erde" Positions: E 13, 36 months 232.900 € student assistant 10.000 € Consumables: 14.250 € Overhead: 56.600 €	313.750 €
EU	European Research Council (ERC) Advanced Grant No. 787 527 (T. Katsura – 10/18-9/23) "Chemistry and transport properties of bridgmanite controlling lower-mantle dynamics" ("UltraLVP") Positions (post docs): 860.144 € Travel funding: 187.380 € Equipment: 49.250 € Consumables: 997.722 € In-kind contributions: 24.000 € Overhead: 523.624 €	2.642.120 €
EU	European Research Council (ERC) Grant No. 949 417 (R. Hin – 1/21-12/25) "The chemical consequences of vapour loss during planetary accretion (VapLoss)" ("HORIZON 2020") Positions: 756.169 € Travel funding: 44.781 € Consumables: 129.403 € Equipment: 153.802 € Internally Goods and Services: 173.235 € Overhead: 314.348 €	1.571.738 €

2.3 Laboratory and office facilities

The institute occupies an area of

ca. 1470 m^2 laboratory space

ca. 480 m^2 infrastructural areas (machine shops, computer facilities, seminar room, library)

ca. 520 m^2 office space

in a building which was completed in 1994.

2.4 Experimental and analytical equipment

The following major equipment is available at the Bayerisches Geoinstitut:

I. High-pressure apparatus
- 15 MN/1500 tonne Kawai-type multianvil high-pressure apparatus (40 GPa, 2000 K)
- 6 x 8 MN/6x800 tonne independently acting-anvil press (25 GPa, 3000 K)
- 50 MN/5000 tonne multianvil press (25 GPa, 3000 K)
- 12 MN/1200 tonne multianvil press (25 GPa, 3000 K)
- 10 MN/1000 tonne multianvil press (25 GPa, 3000 K)
- 5 MN/500 tonne multianvil press (20 GPa, 3000 K)
- 5 MN/500 tonne press with a deformation DIA apparatus
- 5 piston-cylinder presses (4 GPa, 2100 K)
- Cold-seal vessels (700 MPa, 1100 K, H2O), TZM vessels (300 MPa, 1400 K, Ar), rapid-quench cold-seal vessels (400 MPa, 1200 K, H2O)
- Internally-heated autoclave (1 GPa, 1600 K)
- High-pressure gas loading apparatus for DAC

II. Structural and chemical analysis
- 1 X-ray powder micro-diffractometer
- 1 X-ray powder diffractometer with furnace and cryostat
- 2 automated single-crystal X-ray diffractometers
- High-brilliance X-ray system
- Single crystal X-ray diffraction with super-bright source
- 1 Mössbauer spectrometer (1.5 - 1300 K)
- 3 Mössbauer microspectrometers
- 2 FTIR spectrometers with IR microscope
- FEG transmission electron microscope (TEM), 200 kV analytical, with EDS
- FEG scanning TEM, 80-200 kV analytical, with 4-SDDs EDS and post-column energy filter (EFTEM/EELS)
- FEG scanning electron microscope (SEM) with BSE detector, EDS, EBSD and CL
- Dual-beam device, focused ion beam (FIB) and FEG SEM. In situ easy-lift manipulator, STEM, EDS and EBSD detectors, and beam deceleration option
- 3 Micro-Raman spectrometers with ultraviolet and visible lasers
- Tandem-multipass Fabry-Perot interferometer for Brillouin scattering spectroscopy
- Electron microprobe; fully-automated with 14 crystals, 5 spectrometer configuration, EDX, capability for light elements
- 193 nm Excimer Laser-Ablation ICP-MS
- Water content determination by Karl-Fischer titration
- GC/MS-MS for organic analyses
- Confocal 3D surface measurement system
- 1.4 Tesla sweepable ESR magnet

Solid state 300 MHz NMR spectrometer
ESI NWRGEO 193 nm Excimer Laser Ablation system
Thermo Scientific iCAP triple quadrupole ICPMS for solution or in-situ LA- isotopic analysis
Thermo Scientific Neoma MS/MS multi-collector ICPMS for solution or in-situ LA- high-resolution isotopic ratio measurements
Isotope Cosmochemistry & Geochemistry Laboratory ISO 6 cleanrooms equipped with ISO 4 exhaust laminar flow cabinets for sample preparation

III. *In situ* determination of properties
Diamond anvil cells for powder and single crystal X-ray diffraction, Mössbauer, IR, Raman, optical spectroscopy, NMR spectroscopy, electrical resistivity measurements over 200 GPa
Facility for in situ hydrothermal studies in DAC
Externally heated DACs for in situ studies at pressures to 100 GPa and 1200 K
1-atm furnaces to 1950 K, gas mixing to 1600 K, zirconia fO2 probes
1-atm high-temperature creep apparatus
Megahertz ultrasonic interferometer
Freezing-heating stage for fluid inclusion studies
Impedance/gain-phase analyser for electrical conductivity studies
Apparatus for in situ measurements of thermal diffusivity at high P and T
Laser-heating facility for DAC
Portable pulsed laser heating system for DAC

The Geoinstitut maintains a well equipped machine shop, an electronic workshop and sample preparation laboratories. It has access to supercomputing resources at the University and Leibniz computer centres.

3. Forschungsprojekte

3.1 Struktur und Dynamik der Erde und Planeten

Die Erde ist der einzige Planet im Sonnensystem, der während nahezu seiner gesamten Geschichte flüssiges Wasser auf der Oberfläche besaß. Dies ist bedingt durch den Abstand der Erde zur Sonne, sowie durch die Masse und die innere Entwicklung unseres Planeten über 4,56 Milliarden Jahre. Aus geochemischen und geophysikalischen Randbedingungen können wir die interne Reservoir-Differenzierung von Kern, Mantel und Kruste und die langfristige Entwicklung der Erde modellieren. Die Bausteine der Erde ähneln vermutlich den chondritischen Meteoriten, die Überreste aus der Frühzeit des Sonnensystems sind, als sich die protoplanetare Scheibe um die entstehende Sonne abkühlte. Erstaunlicherweise ähneln CI-Chondrite, die in den Außenbezirken des Sonnensystems gebildet wurden, in ihrer elementaren Zusammensetzung der Photosphäre der Sonne. Da immer mehr Exoplaneten entdeckt werden, fragen wir uns, wie viele es in unserer Galaxie oder im Universum gibt, und ob wir aus der Entwicklung der Erde auch auf ihre Zusammensetzung und innere Dynamik schließen können. Aufgrund von thermischen Gradienten in den innersten Teilen des Sonnensystems, Akkretions-prozessen und der Bildung und Entwicklung von unzugänglichen tiefen Planetenreservoiren ist es jedoch nicht einfach, die Zusammensetzung der Erde und der terrestrischen Planeten zu modellieren. In diesem Abschnitt werden verschiedene Ansätze verfolgt, um die Bausteine der Erde besser zu verstehen und um die chemischen Unterschiede zwischen der Erde und verschiedenen Arten von Planetesimalen zu erklären. Nachdem sich die Erde differenziert hatte, entwickelten sich Kruste und Mantel mehr als 4,4 Milliarden Jahre lang zusammen, was die frühesten Hinweise auf die Krustenbildung verwischte. Numerische Modelle können Aufschluss darüber geben, wie die frühe kontinentale Kruste teilweise als Kratone erhalten geblieben ist, während andere tektonische Strukturen, die mit der Kontinentbildung in Verbindung stehen, verschwunden sind oder mit Reservoiren im tiefen Mantel zusammenhängen könnten.

Der zugängliche Teil des Erdmantels scheint im Vergleich zu allen bekannten Gruppen von Chondriten an Silizium verarmt zu sein, obwohl Silizium nach Sauerstoff das am häufigsten vorkommende Element im silikatischen Teil der Erde ist. Eine Möglichkeit ist, dass das fehlende Silizium im unteren Mantel und im Kern enthalten ist. Frost und Boffa Ballaran verfolgen einen geophysikalischen Ansatz, um Hinweise auf die Zusammensetzung des unteren Mantels zu erhalten und Enstatit-Chondriten als Hauptbausteine für die Erde auszuschließen.

Die Kernbildung auf Planeten entfernte vor der späten Akkretion alle siderophilen Elemente aus dem Mantel. Rubie und Kollegen kombinieren Modelle von Metall-Silikat-Gleich-gewichten mit den Ergebnissen von N-Körper-Simulationen. Sie integrieren auch die Verteilung von Metall innerhalb undifferenzierter Planetesimale wie Chondriten, um die $^{182}W/^{184}W$-Isotopenzusammensetzung des Erdmantels zu modellieren. Die Untersuchungen zeigen, dass undifferenziertes Material eine bedeutende Rolle bei der Entstehung der Erde gespielt haben muss, um die W-Häufigkeit und Isotopenzusammensetzung des Erdmantels mit Akkretions- und Kernbildungsprozessen in Einklang zu bringen.

Das radioaktive Zerfallssystem ^{146}Sm-^{142}Nd mit einer kurzen Halbwertszeit von 103 Millionen Jahren ist besonders geeignet, um die ersten 700 Millionen Jahre der Akkretions- und Differenzierungsgeschichte der Erde zu verfolgen. Unter Verwendung der Zusammensetzungen verschiedener Klassen von Chondriten und ihrer Bestandteile konnten Frossard und Kollegen eine geringere Häufigkeit von $^{142}Nd/^{144}Nd$ in primitiven Asteroiden im Vergleich zum Erdmantel sowie zu differenzierten Meteoriten ermitteln. Sie schlagen vor, dass 4 bis 20 % der Masse der früh gebildeten und angereicherten Kruste auf der Erde und auf differenzierten Planetesimalen während Planetenkollisionen weggesprengt wurden. Dieser Prozess veränderte ihre chemische Zusammensetzung insbesondere bei den inkompatiblen Elementen, einschließlich radioaktiver Elemente wie U, Th und K.

Ende 2021 wurde die Entdeckung des kurzperiodischen Super-Merkurs GJ 367b bekannt gegeben. Dieser nahe Planet in 31 Lichtjahren Entfernung wird in naher Zukunft mit dem neuen James-Webb-Weltraumteleskop untersucht werden, das in der Lage sein wird, seine Oberfläche zu charakterisieren. Golabek und Kollegen modellieren die Entwicklung des festen Planeteninneren und von Magmaozeanen auf diesem gezeitengebundenen, kurzperiodischen Planeten, was in Zukunft einen Vergleich zwischen Modellergebnissen und Beobachtungen der Oberflächenzusammensetzung ermöglicht.

Auf der Erde stellen Kratone die ältesten Teile der Lithosphäre dar, die seit mehreren Milliarden Jahren unverformt geblieben sind. Dies ist erstaunlich, da die frühe Erde eine stärkere Konvektion aufwies als heute und eine langfristige Erhaltung von Kratonen daher als schwer vorstellbar erscheint. Paul und Kollegen untersuchen die Erhaltung von Kratonen mithilfe von 3D-Modellen und stellen fest, dass mächtige und hochviskose Kratone während der Mantelkonvektion einem Spannungsfeld ausgesetzt sind, das die Erhaltung von Kratonen über lange Zeiträume unterstützen könnte.

Bei Kontinent-Kontinent-Kollisionen wie der alpinen Orogenese kann es zum Plattenabbruch kommen. Es ist zu erwarten, dass dieser Prozess an der Oberfläche eine signifikante topografische Hebung verursacht, was jedoch überraschenderweise nicht immer beobachtet wird. Piccolo und Thielmann entwickeln sowohl vereinfachte numerische 0D- als auch vollständige 2D-Modelle, in denen sie den Effekt des Mantelwiderstands einbeziehen und zeigen, dass der Mantelwiderstand für erdähnliche Parameter sowohl den Abbruchprozess als auch den Hebungsprozess erheblich verlangsamt, was den Mangel an entsprechenden geologischen Befunden erklärt.

Der untere Erdmantel besteht hauptsächlich aus den Mineralen Bridgmanit und Ferroperiklas. Paul und Kollegen wenden ein neues Korngrößen-Entwicklungsgesetz für Bridgmanit- und Ferroperiklas-Mischungen an, um die langfristige Entwicklung des Erdinneren mithilfe von 2D-Modellen zu untersuchen. Ihre erfolgreichsten numerischen Modelle zeigen sowohl eine erdähnliche mobile Oberflächentektonik als auch die selbstkonsistente Bildung und Erhaltung thermochemischer Gebilde an der Unterseite des Mantels. Letzteres ist auf große Korngrößen und damit eine hohe Viskosität dieser Bereiche zurückzuführen. Dies könnte Aufschluss über

den Ursprung der großen Low-Shear-Velocity-Provinzen (LLSVPs) im unteren Mantel der heutigen Erde geben.

3.2 Geochemie

Der Zeitpunkts, zu dem Körper im frühen Sonnensystem begannen, sich zu fraktionieren und metallische Kerne zu bilden, ist wichtig zum Verständnis der Planetenbildung. Chondritische Meteoriten enthalten eine Mischung aus Oxiden, Silikaten, Metall- und Sulfidphasen, die zu den ersten Materialien gehören, die aus dem Sonnennebel kondensiert sind. Achondritische Meteorite hingegen sind Eruptivgesteine, die durch Schmelzen und Differenzierung chondritischer Mutterkörper entstanden sind und durch die Kernbildung metallische Phasen verloren haben. Die ersten beiden Studien in diesem Abschnitt befassen sich mit einer anderen Klasse von sogenannten primitiven Achondriten, die einen Zwischenschritt in diesem Differenzierungsprozess darstellen. Sie sind zwar durch Schmelzen oder Hochtemperatur-Metamorphose entstanden, enthalten aber im Allgemeinen noch Spuren von Metallen, und ihre Untersuchung kann im Prinzip dazu dienen, den Zeitpunkt, den Mechanismus und die Folgen der frühen Kernbildung zu verstehen. In der ersten dieser Studien wird eine Reihe von primitiven achondritischen Meteoriten untersucht, die vor kurzem in der Wüste Sahara entdeckt worden sind. Auf der Grundlage von mineralogischen, geochemischen und Pb-Pb-Altersdaten wird festgestellt, dass sie die erste Gruppe primitiver Achondrite darstellen, die in der äußeren Region des Sonnensystems entstanden sind. Diese Region liegt jenseits der Umlaufbahn, in der Eis kondensierte und möglicherweise sogar jenseits von Jupiter. Außerdem scheint die Kernbildung bei den primitiven Achondriten nur eine Million Jahre nach der Entstehung des Sonnensystems schon begonnen zu haben. Die folgende Studie untersucht ebenfalls eine Gruppe primitiver Achondrite und liefert eine petrologische Grundlage, anhand derer bestimmte Mutterkörper identifiziert werden können. Dies ist eine Alternative zu Analysen von Sauerstoffisotopen, die weitaus mehr spezialisierte Analytik erfordern.

Die nächsten drei Studien verwenden stabile Isotope bestimmter siderophiler Elemente, um die Bildung der Kerne von Planeten und den Verlust flüchtiger Elemente zu untersuchen. Der Mond scheint im Vergleich zur Erde an vielen flüchtigen Elementen verarmt zu sein. Möglicherweise beruht dies auf Verdampfungsprozessen bei der Kollision von Planeten, die zur Bildung des Mondes führte, oder auf Verdunstung während der anschließenden Abkühlung des Mondes. Interessanterweise ist die Isotopensignatur von Zinn in Mondgestein im Gegensatz zu den meisten anderen flüchtigen Elementen leichter als die der silikatischen Erde. Um dies zu verstehen, wurden in einer Studie Experimente mit Stempelzylinderpressen durchgeführt, um die Verteilung der Zinnisotope zwischen Silikatschmelze und metallischer Eisen-Nickel-Schmelze zu bestimmen. Es wurde festgestellt, dass sich isotopisch leichtes Zinn in der Metallschmelze anreichert, was darauf hindeutet, dass die anomale Zinn-Isotopensignatur des Mondes eher auf Verdampfungsprozessen beruht. In der folgenden Studie wird die Entwicklung einer Multianvil-Technik für große Probenvolumina beschrieben, mit der die Drücke an der Basis des Mantels von Mars erreicht werden können. Diese Apparatur wird

benutzt, um die Verteilung der Eisen-Isotope zwischen Metall und Silikatschmelze zu untersuchen, wofür recht große Proben benötigt werden. Die Ergebnisse zeigen, dass die Metall-Silikat-Trennung unter den Bedingungen des Marsmantels keine Fraktionierung der Eisenisotope bewirkt. Dieses Ergebnis steht im Einklang mit der Tatsache, dass der Marsmantel anscheinend die chondritischen Eisenisotopenverhältnisse beibehalten hat.

Zum besseren Verständnis der Verteilung von Bor innerhalb der Erde wurden in der folgenden Studie molekulardynamische Simulationen durchgeführt, um das Verteilungsverhalten und die Isotopenfraktionierung von Bor zwischen geschmolzenem Eisen und Silikatschmelze unter Bedingungen zu berechnen, die für die Kernbildung relevant sind. Bor, und zwar vorzugsweise sein leichteres Isotop, reichert sich hier in der metallischen Phase an. Der Erdkern könnte daher bis zu 50 % des globalen Bors speichern. Die isotopisch leichte Borsignatur ozeanischer Inselbasalte, die möglicherweise aus Mantelregionen an der Grenze zum Erdkern stammen, beruht möglicherweise auf Kontamination durch Bor aus dem Kern.

In der folgenden Studie werden die Phasenbeziehungen einer kristallisierenden Schmelze mit der Zusammensetzung des unteren Mantels untersucht, was für das Verständnis der Fraktionierung innerhalb eines frühen Magmaozeans wichtig ist. Um Schmelzen unter den Bedingungen des unteren Erdmantels in der Multianvil-Presse zu erzeugen, sind einige technische Entwicklungen erforderlich, da Temperaturen von bis zu 4000 K erreicht werden müssen. Vorläufige Ergebnisse deuten darauf hin, dass das Temperaturintervall, in dem die Kristallisation bei Bedingungen im unteren Mantel stattfindet, kleiner ist als bisher angenommen. Dies unterstreicht die Notwendigkeit von Multianvil-Experimenten, bei denen die Temperaturverteilung gut kontrolliert werden kann.

In den nächsten beiden Studien wird untersucht, wie sich die Zusammensetzung der Mineralphasen mit der Tiefe im unteren Erdmantel verändert. In der ersten dieser Studien wurde die Verteilung von Kalzium und Magnesium zwischen Bridgmanit und $CaSiO_3$-Perowskit (Davemaoit) gemessen. Diese Phasen machen etwa 78 bzw. 7 Volumenprozent des unteren Mantels aus. In einer vor kurzem erschienenen Publikation wurde vorgeschlagen, dass die Löslichkeit von $CaSiO_3$ im Bridgmanit mit dem Druck und der Temperatur so weit zunimmt, dass $CaSiO_3$-Perowskit letztlich aus der Mineralparagenese des unteren Erdmantels verschwindet. Bei den hier neu durchgeführten Experimenten zwischen 27 und 40 GPa zeigte sich jedoch, dass die Löslichkeit von $CaSiO_3$ im Bridgmanit sehr begrenzt ist. $CaSiO_3$-Perowskit ist daher wahrscheinlich im gesamten Stabilitätsbereich des Bridgmanits im unteren Erdmantel vorhanden. In der folgenden Studie wird untersucht, wie sich der Fe- und Al-Gehalt von Bridgmanit mit zunehmendem Druck verändert, wenn er mit einer Al-reichen Phase koexistiert. Die Ergebnisse zeigen, dass die Konzentrationen beider Elemente im Bridgmanit mit der Tiefe zunehmen. Beim höchsten untersuchten Druck von 40 GPa wurden jedoch zwei koexistierende Bridgmanit-Phasen identifiziert, von denen eine reich an Eisen und Aluminium ist und die andere arm an beiden Elementen. Dies könnte eventuell bedeuten, dass es innerhalb der Bridgmanit-Mischkristallreihe eine chemische Mischungslücke gibt, die unter den Bedingungen des mittleren Erdmantels auftritt.

Die Verteilung von Phosphor und Seltenen Erden in den Mineralen der Übergangszone und des unteren Erdmantels wird in der folgenden Studie untersucht. Es wird festgestellt, dass Phosphor in der Mitte der Übergangszone in einer zusätzlichen akzessorischen Phase, dem $Ca_3(PO_4)_2$-Tuit, auftritt. Diese Phase ist auch ein wichtiger Träger von Seltenen Erden ist. An der Basis der Übergangszone und im unteren Erdmantel ist Tuit jedoch nicht mehr stabil, und Phosphor und Seltene Erden sind hauptsächlich in $CaSiO_3$-Perowskit eingelagert.

Ein weiteres Projekt beschäftigt sich mit dem Ursprung von Diamanten, die Einschlüsse von Ferroperiklas enthalten. Hierzu wurde der Gehalt an Eisen(III) in Ferroperiklas in Abhängigkeit von Zusammensetzung, Druck, Temperatur und Sauerstoff-Fugazität untersucht. In der Vergangenheit wurde angenommen, dass solche Einschlüsse aus dem unteren Erdmantel stammen, da Ferroperiklas dort ein verbreitetes Mineral ist. In dieser Studie wird jedoch gezeigt, dass der Eisengehalt von Ferroperiklas unter den Bedingungen der Diamantenbildung im unteren Erdmantel viel niedriger ist als die Werte, die für die meisten dieser Einschlüsse gefunden wurden. Viele dieser Einschlüsse weisen Eisengehalte auf, die nur mit einer Bildung im oberen Erdmantel vereinbar sind.

Eklogite sind Hochdruckgesteine, die durch Metamorphose von subduziertem ozeanischem Basalt entstanden sind. In einer Studie wird der Redox-Zustand von eklogitischen Einschlüssen in Diamanten aus dem sibirischen Kraton untersucht, um auf die Art des Mediums zu schließen, aus dem sich die Diamanten gebildet haben. Die Ergebnisse zeigen, dass dieses Medium wahrscheinlich eine Mischung aus Kohlendioxid und Wasser enthielt. Interessanterweise scheint das Gestein, in dem die Diamanten gefunden wurden, stärker oxidiert zu sein. Dies ist wahrscheinlich auf eine Veränderung durch eindringende Flüssigkeiten oder Schmelzen zurückzuführen, die das umgebende Gestein nach der Bildung der Diamanten beeinflusst haben. Dieser Effekt wird in der folgenden Studie näher beschrieben, in der eine solche metasomatische Aktivität für die Oxidation der Granate in einem Eklogit verantwortlich zu sein scheint.

Im folgenden Beitrag werden gescherte Peridotit-Xenolithe aus der kratonischen Lithosphäre untersucht, die durch kimberlitische Magmen an die Oberfläche gebracht wurden. Kimberlitische Magmen entgasen und kristallisieren bei niedrigem Druck, weshalb es sehr schwierig ist, ihren ursprünglichen Gehalt an flüchtigen Bestandteilen zu bestimmen. Die Mineralphasen in diesen Gesteinen können jedoch Hinweise auf die Wasserkonzentration in den kimberlitischen Schmelzen liefern, mit denen sie in Kontakt waren. Die größeren Mineralkörner in der Probe wurden mittels Infrarotspektroskopie analysiert und weisen niedrige bis mittlere Wassergehalte auf. Es sind jedoch die Bereiche mit gescherten Olivin-Gefügen, die wahrscheinlich durch Wechselwirkung mit der Kimberlit-Schmelze verändert wurden. Diese Regionen sind aber zu feinkörnig für eine Analyse mit Infrarotspektroskopie und sollen daher später mit einer Ionensonde analysiert werden.

Die nächste Studie befasst sich mit dem Beitrag subduzierter Sedimente zur Spurenelementsignatur von Magmen aus Inselbögen. Aufgrund der ähnlichen Blei-Isotopenverhältnisse dieser Magmen und subduzierten Sedimenten wurde postuliert, dass die Sedimente einen

wesentlichen Beitrag zur Spurenelementsignatur leisten, entweder durch die Bildung von wasserhaltigen Silikatschmelzen, überkritischen Fluiden oder Diapiren, die im Mantel aufsteigen. Im Gegensatz dazu deutet die Sr-Isotopensignatur der Magmen darauf hin, dass der Beitrag der Sedimente eher gering ist. Um zu prüfen, ob Wasser-reiche Fluide diese Beobachtungen erklären könnten, werden in dieser Studie Experimente mit einer Stempelzylinderpresse durchgeführt, um die Verteilung von Spurenelementen zwischen den Fluiden und metamorphen Sedimenten zu bestimmen. Die Ergebnisse zeigen, dass aus Sedimenten stammende Fluide sehr Pb-reich sind und daher sehr effizient eine sedimentäre Pb-Isotopensignatur übertragen, während dies bei Sr nicht im gleichen Umfang der Fall ist. Sehr kleine Mengen von Fluiden aus Sedimenten reichen daher aus, um die Pb-Isotopensignatur von Inselbogen-Magmen zu erklären.

Die beiden folgenden Beiträge befassen sich mit der Fraktionierung von Magmen aus Inselbögen. Um die Möglichkeiten von Kristallisationsexperimenten in Stempelzylinder-experimenten zu erweitern, wurden von *Calvo et al.* zwei wichtige Modifikationen eingeführt: Erstens wird eine Zirkonauskleidung der Probenkammer eingeführt, um eine Wechselwirkung der Probe mit der Edelmetallkapsel zu verhindern. Dies ermöglicht die Durchführung von Experimenten mit Schwefel und mit chalcophilen Elementen auch bei hoher Sauerstofffugazität. Die sonst oft verwendeten Graphitauskleidungen würden dagegen stets eine niedrige Sauerstofffugazität einstellen. Zweitens werden langsame Abkühlungsraten in der Größenordnung von 80 °C/Tag verwendet, um große Kristalle und große intergranulare Schmelzansammlungen auch bei niedrigen Temperaturen zu erzeugen. Dies ermöglicht die Bestimmung von Spurenelementen durch Laser-Ablations-Spektrometrie und die Bestimmung von flüchtigen Bestandteilen durch Infrarotspektroskopie. Die modalen Mineralhäufigkeiten, die in einer bei 700-1200 °C und 1,2 GPa durchgeführten Kristallisationsreihe ermittelt wurden, ähneln denen, die in früheren, schwefelfreien Experimenten ohne Zirkoneinlagen ermittelt wurden, so dass das Vorhandensein von Zirkon die Phasenbeziehungen offenbar nicht wesentlich beeinflusst. Mit dem gleichen experimentellen Ansatz bestimmten Chang und Audétat die chemische Entwicklung der Schmelze mit zunehmender fraktionierter Kristallisation von S-, Cl-, H_2O- und CO_2-haltigen, mafischen Kalium-reichen Magmen, die bei 850-1150 °C und 1,0 GPa kristallisieren. Intermediäre bis felsische Kalium-reiche Magmen haben wirtschaftlich wichtige porphyrische Cu(Au)-Lagerstätten in post-Subduktions-Umgebungen hervorgebracht. Die experimentellen Daten zeigen, dass diese Magmen durch fraktionierte Kristallisation aus den mafischen Magmen entstanden sein könnten und nicht durch den allgemein postulierten Mechanismus des teilweisen Schmelzens von Gesteinen der unteren Kruste. Die experimentell beobachteten Veränderungen in der Schmelzzusammen-setzung stimmen perfekt mit dem in natürlichen Gesteinen aufgezeichneten Trend überein und die erzbildenden Magmen waren wahrscheinlich sehr reich an H_2O, S und Cl.

Der nächste Beitrag befasst sich mit der Diffusion von Titan in Quarz und ihrer Anwendung auf vulkanologische Probleme. Die Titandiffusions-Chronologie in Quarz ist ein zunehmend beliebtes Instrument zur Rekonstruktion von Zeitskalen der Magmakammerbildung und der

Auslösung von Vulkanausbrüchen. Allerdings unterscheiden sich die derzeit verfügbaren experimentellen Titan-Diffusionskoeffizienten in Quarz um drei Größenordnungen. Um dieses Problem zu lösen, haben *Audétat et al.* die Titan-Diffusionskoeffizienten in Quarzkristallen aus der klimaktischen Eruption von 1991 am Pinatubo bestimmt. Hierzu wurden winzige Zirkoneinschlüsse direkt neben Titan-Diffusionsprofilen datiert. Die neu ermittelten Diffusivitäten von Titan wurden verwendet, um die Zeit abzuschätzen, die zwischen dem Eindringen von neuem Magma und der Eruption im Jahr 1991 verstrichen ist. Die Ergebnisse deuten darauf hin, dass die Magmenzufuhr 20 bis 400 Jahre vor der Eruption von 1991 stattfand, was 1-2 Größenordnungen länger ist als nach früheren Abschätzungen.

Der letzte Beitrag in diesem Abschnitt befasst sich mit Redoxreaktionen in modernen Seesedimenten. Der Spurenelementgehalt von Süßwasser hängt entscheidend vom biogeochemischen Kreislauf von Eisen, Kohlenstoff und Phosphor und insbesondere vom Elektronentransfer zwischen Fe(II)- und Fe(III)-Oxiden ab. Um die Fe(II)- und Fe(III)-enthaltenden Minerale in den Sedimenten von Süßwasserseen zu bestimmen, führten *McCammon et al.* eine Mössbauer-spektroskopische Untersuchung in den obersten 20 cm der Sedimente eines Sees in Dänemark durch. Es wurde festgestellt, dass Eisen in den oberen Teilen dieses Profils hauptsächlich in Form von nanoskaligen Fe(III)-Hydroxiden und in den unteren Teilen als Fe(II) in Form von Vivianit vorliegt. Dies deutet auf eine anorganische Ursache des Redoxgradienten und eine wichtige Rolle der abiotischen Eisenhydroxide bei der Aufnahme von Spurenelementen aus dem Wasser hin.

3.3 Mineralogie, Kristallchemie und Phasenübergänge

Unser Wissen über das tiefe Erdinnere wird durch die Kombination von Hochdruckexperimenten mit neuen analytischen Methoden ständig erweitert. Ein Schwerpunkt der Untersuchungen ist hier die Kristallchemie von Bridgmanit und Ferroperiklas unter Bedingungen des unteren Erdmantels. Substitutionen von Al^{3+} und Fe^{3+} gekoppelt mit Kationen anderer Wertigkeit sowie mit Sauerstoff beeinflussen die physikalischen und chemischen Eigenschaften der orthorhombischen Perowskitstruktur. Mit steigender Temperatur verringert sich die phasenverschobene Neigung der Oktaeder in der Struktur von Al-haltigem Bridgmanit bei hohem Druck, was neue Hinweise auf die Tiefe des Übergangs vom Perowskit zum Post-Perowskit im unteren Erdmantel liefert. Mit zunehmender Temperatur sinkt der Fe^{3+}-Gehalt von eisen- und aluminiumhaltigem Bridgmanit bei hohem Druck, was darauf hindeutet, dass die Disproportionierung von Fe^{2+} zu metallischem Eisen und Fe^{3+} in der frühen Erdgeschichte im Vergleich zu späteren Zeiten eine weniger wichtige Rolle gespielt haben könnte. Die Substitution von dreiwertigen Kationen in Bridgmanit führt zur Bildung größerer Körner, was in Verbindung mit den vorhandenen Kenntnissen über Sauerstoff-Leerstellen im Kristallgitter und die Kristallchemie darauf schließen lässt, dass die Kornwachstumsrate mit der Tiefe zunimmt und zu einer höheren Viskosität im tieferen Erdmantel führt. Die Viskosität des unteren Mantels kann auch durch die Kornmorphologie von Ferroperiklas beeinflusst werden.

Es sind neue Verformungsexperimente geplant, um verschiedene Modelle der Mikrostruktur zu testen.

Die Phasenstabilität kann mit der Löslichkeit von Elementen und flüchtigen Bestandteilen in Hochdruckphasen zusammenhängen. Die Löslichkeit von Chrom in der Post-Spinell-Phase Fe_5O_6 ist überraschend niedrig, was in Verbindung mit der geringen Mg-Löslichkeit darauf schließen lässt, dass die Struktur nur sehr begrenzt andere Kationen als Fe^{2+} und Fe^{3+} aufnehmen kann. Die erfolgreiche Synthese von Calcium(II)-Orthocarbonat, Ca_2CO_4, bei hohem Druck eröffnet neue Wege für den Kohlenstofftransport im Erdinneren. Der Wassergehalt von Hochdruck-Phasen von SiO_2 steigt mit dem Al_2O_3-Gehalt, was darauf hindeutet, dass die Post-Stishovit-Phase in subduzierter Basaltkruste Wasser im unteren Erdmantel speichern kann. Neue Experimente zeigen, wie Wasserstoff aus Eisensulfid während der Dekompression verloren gehen kann. Möglicherweise kann Wasserstoff in Eisensulfid-mineralen und -schmelzen gespeichert werden, die an der Basis der kratonischen Lithosphäre auftreten oder auch in kernbildenden Schmelzen während der Differenzierung von Planeten.

Die Mikrostruktur von Mineralien kann Aufschluss über ihre Vorgeschichte im tiefen Inneren der Erde und in anderen Planeten geben. Die Entdeckung und Charakterisierung von Zwillingen in wasserhaltigem Wadsleyit deutet darauf hin, dass sie sich während des Kristallwachstums unter quasi-hydrostatischen Bedingungen in Gegenwart einer wasserhaltigen Flüssigkeit gebildet haben und möglicherweise günstige Orte für die Keimbildung von Ringwoodit darstellen. Eine neue Methode der Analyse von Antiphasendomänen in Omphazit aus der Eklogit-Fazies liefert Einsichten in die Wachstumskinetik und damit neue Möglichkeiten zur Entschlüsselung der Temperatur-Zeit-Verläufe.

3.4 Physikalische Eigenschaften von Mineralen

Die Struktur und die Eigenschaften des Erdmantels und des Erdkerns sowie der Planeten und Exoplaneten können nur mit Hilfe von Daten über die physikalischen Eigenschaften der sie bildenden Minerale vollständig verstanden werden. In den Beiträgen dieses Kapitels werden verschiedene Kombinationen von experimentellen Hochdrucktechniken sowohl am BGI als auch an Synchrotron-Anlagen eingesetzt, um die Eigenschaften von Mineralen im Innern der Erde und in Planeten zu messen. Benutzt werden Röntgen-Beugungsexperimente, Messungen von Schallgeschwindigkeiten, Ultraschall-Interferometrie und auch theoretische Berechnungen auf der Basis von molekularer Dynamik.

Die Seismologie ermöglicht uns einen Blick in das Innere der Erde. Ohne präzise Messungen der physikalischen Eigenschaften von Mineralen kann jedoch das volle Potenzial seismischer Daten zur Untersuchung der Zusammensetzung der Erde nicht ausgeschöpft werden. In den ersten beiden Beiträgen dieses Kapitels werden Messungen der Schallwellengeschwindigkeit verwendet, um die Auswirkung der Zusammensetzung auf die elastischen Eigenschaften von

Mantelmineralen zu untersuchen. Die Fähigkeit nominell wasserfreier Minerale, Spuren von Wasserstoff einzubinden, nimmt mit dem Druck im oberen Erdmantel zu. Selbst kleine Mengen Wasserstoff können rheologische Eigenschaften und Schmelztemperaturen stark beeinflussen. Olivin, das häufigste Mineral des oberen Erdmantels, kann bei Drücken am oberen Ende seines Stabilitätsbereichs Wasser bis zu fast in den Bereich von einem Gewichts-Prozent aufnehmen. Da die Zugabe von Wasserstoff zu Mantelmineralen erhebliche Auswirkungen auf deren elastische Eigenschaften haben kann, wurde vermutet, dass Wasser im Olivin auch die seismische Signatur des Mantels verändern könnte. Im ersten Beitrag wurden die seismischen Eigenschaften von Olivin mit 0,2 Gew.-% H_2O bei Drücken untersucht, die den gesamten Stabilitätsbereich von Olivin abdecken. Die Ergebnisse von Brillouin-Spektroskopie und Röntgenbeugungs-Experimenten bei hohem Druck zeigen, dass die Schallgeschwindigkeiten in wasserstoffhaltigem Olivin bei hohem Druck nicht von wasserfreiem Olivin zu unterscheiden sind. Dies bedeutet, dass die Hydratation des Erdmantels anomale seismische Signaturen nicht erklären kann. Im zweiten Beitrag wurden die seismischen Eigenschaften von Al-reichen Phasen untersucht, von denen man annimmt, dass sie in subduzierten Platten im unteren Erdmantel vorkommen. Im Gegensatz zu früheren Studien war die in den Experimenten verwendete Phase mit Kalzium-Ferrit-Struktur (so genannte CF-Phase) Fe-haltig. Die aus Hochdruck-Brillouin-Messungen und Röntgenbeugung berechneten Elastizitätsmodule und seismischen Geschwindigkeiten waren niedriger als die in früheren numerischen und experimentellen Studien an eisenfreien Proben ermittelten Werte. Eisen kann wohl einen erheblichen Einfluss auf die elastischen Eigenschaften tief subduzierter Platten haben.

Der dritte Beitrag berichtet über die Ergebnisse von Hochdruck-Synchrotron-Röntgenbeugungsmessungen an Al-reichen wasserhaltigen Phasen. Solche Phasen können eine wichtige Rolle beim Transport von Wasser in den unteren Erdmantel in tief subduzierten Platten spielen. Um die Stabilität solcher Phasen zu berechnen, ist eine genaue Parametrisierung der Volumenänderung mit dem Druck wichtig. Die Ergebnisse für Mg-, Si- und Fe^{3+}-haltige Proben von Oxyhydroxiden des $CaCl_2$-Typs zeigen, dass die Kompression durch den Spin-Übergang von Fe^{3+} beeinflusst wird. Der Übergang findet aber über ein wesentlich größeres Druckintervall statt, wenn Silizium auf demselben kristallographischen Platz wie Fe^{3+} vorhanden ist.

Der vierte Beitrag verwendet numerische Methoden, einschließlich maschinellem Lernen, um die Diffusivität von chemischen Komponenten im Erdkern zu bestimmen. Aus diesen Ergebnissen konnten die Auswirkungen von Wasserstoff und Kohlenstoff auf die Viskosität der metallischen Flüssigkeit berechnet werden. Die Viskosität wird durch diese leichten Elemente verringert, was wichtige Konsequenzen für die Wärmeübertragung und damit für die Intensität des Geodynamos der Erde hat.

Neue Missionen zum Mars liefern Daten, aus denen man viel über das Innere des Planeten lernen kann. Um diese neuen Daten zu interpretieren, müssen die physikalischen Eigenschaften

von Mineralen mit einer für den Mars relevanten Zusammensetzung bestimmt werden. Der fünfte und der sechste Beitrag befassen sich mit solchen Messungen. Im fünften Beitrag wurden die Schallgeschwindigkeiten in Fe-reichem Olivin bei einem Druck von bis zu 5 GPa gemessen, was einer Tiefe von mehr als 400 km im Marsmantel entspricht. Im Vergleich zu irdischem Olivin führt das zusätzliche Eisen im Mars-Olivin zu einer Verringerung der seismischen Wellengeschwindigkeiten im Vergleich zur Erde. Solche Messungen sind entscheidend für die Interpretation der seismischen Daten der kürzlich abgeschlossenen InSight-Mission. Der sechste Beitrag nutzt neuartige, am BGI entwickelte Versuchsanordnungen in Kombination mit Synchrotronstrahlung. Durch *in situ*-Röntgenstreuung, Radiographie und Ultraschall-interferometrie wurden die Struktur und Dichte von flüssigem FeS bestimmt. Die Beobachtung eines großen und an leichten Elementen reichen Kerns von Mars durch InSight erfordert solche Daten, um ein thermoelastisches Modell für das Material des Marskerns zu erstellen.

Der siebte Beitrag untersucht die Zustandsgleichung von Siliziumkarbid mit Hilfe von *in situ*-Röntgenbeugung in einer Multianvil-Presse mit Synchrotronstrahlung. Siliziumkarbid könnte ein Hauptbestandteil der Exoplaneten von Sternen sein, die reicher an Kohlenstoff sind als unser Sonnensystem. Die genaue Bestimmung der Druck-Volumen-Temperatur-Beziehungen von SiC ist daher wichtig. Die Verwendung einer großvolumigen Multianvil-Apparatur bei Drücken von annähernd 30 GPa erlaubte eine beträchtliche Verbesserung der Genauigkeit bei der Temperaturbestimmung im Vergleich zu laserbeheizten Diamant-Stempelzellen.

Der letzte Beitrag untersucht die rätselhaften Texturen, die in primitiven achondritischen Meteoriten beobachtet werden. Synthetisches achondritisches Material wurde durch Mischen von Olivin, Troilit und Gold hergestellt und in Langzeit-Multianvil-Experimenten hoher Temperatur ausgesetzt, woraufhin die Texturen mittels optischer Mikroskopie dokumentiert wurden. Es wurde festgestellt, dass die Korngrenzwanderung die Konfiguration mit minimaler Oberflächenenergie in bimetallischen Zweiphasenmischungen überprägt. Dies bedeutet, dass die in den Meteoriten beobachteten Texturen nicht durch hohe Temperaturen oberhalb des Schmelzpunkts von Metalllegierungen erzeugt worden sein müssen, sondern auch bei niedrigerer Temperatur entstanden sein könnten.

3.5 Fluide, Schmelzen und ihre Wechselwirkung mit Mineralen

Fluide und Silikatschmelzen sind verantwortlich für den chemischen Transport im Erdinnern und von der tiefen Erde zur Oberfläche. Im oberen Teil des Erdmantels sind Spuren von Wasserstoff als OH-Punktdefekte in den Mineralen gelöst. Lokal findet sich auch molekulares H_2O in Wasser-reichen Fluiden oberhalb von Subduktionszonen. Im tieferen Mantel herrschen jedoch stärker reduzierende Bedingungen und H_2O ist möglicherweise zum größten Teil reduziert zu H_2. Ähnliche Bedingungen waren möglicherweise in der frühen Erdgeschichte charakteristisch für den gesamten Mantel. Frühere Arbeiten am BGI haben gezeigt, dass H_2O und H_2 sich unter den Druckbedingungen des obersten Mantels entmischen. Der erste Beitrag

in diesem Kapitel erweitert diese Daten zu einem höheren Druckbereich. Bemerkenswert ist, dass die kritische Kurve im H_2-H_2O-System mit steigendem Druck steil ansteigt. Selbst für relativ heiße Temperaturprofile im Archaikum oder späten Hadaikum würde sich daher H_2 wohl sehr leicht von H_2O abtrennen. Die schnelle Entgasung des sehr leichten H_2 ist daher ein offensichtlicher Mechanismus für die frühe Oxidation des zurückbleibenden Mantels. Erste experimentelle Daten zeigen darüber hinaus, dass Edelgase, insbesondere Xenon, sehr stark in der H_2-Phase angereichert werden. Dies könnte daher eine seit langem bekannte geochemische Beobachtung erklären, dass nämlich die durch spontane Kernspaltung von Plutonium entstandenen Isotope von Xenon offenbar bereits in der frühesten Erdgeschichte aus dem Mantel entgast sind.

Die Subduktion ozeanischer Platten transportiert flüchtige Bestandteile von der Erdoberfläche zurück ins Erdinnere. Mehrere Beiträge beschäftigen sich daher mit dem Verhalten von Wasser bei der Subduktion. In einem Projekt wurde die Diffusion von Wasser durch das Netzwerk der Korngrenzen in polykristallinem Olivin und Orthopyroxen untersucht. Die Daten zeigen, dass die Korngrenz-Diffusion relativ langsam ist und andere Mechanismen notwendig sind, um flüchtige Bestandteile über große Entfernungen von der subduzierten Platte in den darüber liegenden Mantelkeil zu transportieren. In einem weiteren Beitrag wurde studiert, in welcher Form Schwefel in den Wasser-reichen Fluiden gelöst ist, die durch die Dehydratation von Serpentin entstehen.

Die meisten wasserhaltigen Minerale in der subduzierten Platte zersetzen sich bereits bei relativ niedrigem Druck und setzen Wasser frei, das dann zum großen Teil durch Vulkanismus wieder zur Erdoberfläche zurück transportiert wird. Eine interessante Frage ist daher, wie Wasser tiefer in den unteren Mantel transportiert werden könnte. Möglich wäre dies beispielsweise in der Form von OH-Punktdefekten in Stishovit (SiO_2) und seinen Hochdruck-Modifikationen. Zwei Beiträge in diesem Kapitel zeigen, das Wasser tatsächlich im Stishovit merklich lösbar ist und noch sehr viel mehr in der Post-Stishovit-Hochdruckphase. Neben Wasser ist Stickstoff ein weiterer flüchtiger Bestandteil, der durch Subduktion in den unteren Mantel transportiert werden kann. Es ist jedoch kaum bekannt, wieviel Stickstoff der untere Mantel überhaupt speichern kann. In einem weiteren Projekt wurde daher die Löslichkeit von Stickstoff in Al-haltigem Bridgmanit, dem Hauptmineral des unteren Mantels untersucht. Die Daten zeigen, dass durch die Anwesenheit von Al die Löslichkeit von N im Bridgmanit ansteigt, was wohl auf Ladungs-gekoppelte Substitutionen zurückzuführen ist. Mehrere 100 ppm könnten im Bridgmanit gelöst werden, was durchaus konsistent ist mit direkten geochemischen Hinweisen auf ein tiefes Stickstoff-reiches Reservoir im Mantel.

Die ursprüngliche Verteilung der flüchtigen Bestandteile in unserem Planeten beruht wahrscheinlich auf dem chemischen Gleichgewicht zwischen einem Magma-Ozean und einer primitiven Atmosphäre. Um dieses Gleichgewicht zu modellieren, werden Daten über die Löslichkeit von Wasser in peridotitischen Schmelzen benötigt. Mit Hilfe einer neuen Multi-Anvil-Technik zum extrem schnellen Abschrecken von Proben konnten erstmals wasserhaltige

Peridotitschmelzen in Gläser umgewandelt werden. Die Infrarot-Spektren dieser Proben zeigen, dass der Lösungsmechanismus von Wasser in Peridotit-Schmelzen sehr verschieden ist von Basalten. Die Proben enthalten viel weniger molekular gelöstes H_2O und zusätzlich zu an Silizium gebundenem OH treten auch MgOH und CaOH-Gruppen auf. Es wurde jedoch auch darüber spekuliert, dass unter den extrem reduzierenden Bedingungen in einem Magma-Ozean nicht H_2O, sondern H_2 das wichtigste Gas ist, das sich in der Schmelze löst. Bisherige Messungen der H_2-Löslichkeit in Silikatschmelzen benutzten zur Quantifizierung meist den Infrarot-Extinktionskoeffizienten von H_2 in SiO_2-Glas. Eine Neukalibrierung deutet jetzt darauf hin, dass dieser Koeffizient in Wirklichkeit etwa um einen Faktor 10 größer ist, als bisher angenommen. Dies würde bedeuten, dass sich sehr viel weniger H_2 in der Silikatschmelze löst, als bisher vermutet wurde.

Die Viskosität von Silikatschmelzen ist von fundamentaler Bedeutung für die Vorhersage von Vulkaneruptionen. Da die Viskosität in komplexer Weise von Temperatur und Zusammensetzung abhängt, werden zur Vorhersage meist semi-empirische Modelle benutzt. Als eine Alternative wurde in einem Beitrag in diesem Kapitel ein künstliches neuronales Netzwerk mit Hilfe von über 3000 einzelnen Daten darauf trainiert, Viskositäten vorherzusagen. Die Vorhersagen dieses Netzwerks scheinen den bisherigen Modellen deutlich überlegen zu sein. In einem weiteren Beitrag werden die ersten Viskositätsmessungen an wasserhaltigen Peridotit-Schmelzen vorgestellt. Die Zähigkeit von basaltischen Schmelzen kann durch die Kristallisation von Fe-Ti-Oxiden erhöht werden, sowohl bei natürlichen Vulkaneruptionen als auch während Viskositätsmessungen im Labor. Zwei Beiträge untersuchen diesen Effekt, der möglicherweise eine Erklärung bietet für die unterschiedliche Explosivität der Vulkane Stromboli und Ätna. Die Auswirkung von dendritischen Kristallen auf das Eruptionsverhalten von Magmen wurde in einem weiteren Projekt untersucht, in dem Röntgen-Tomographie benutzt wurde, um das Wachstum von Kristallen in drei Dimensionen zu verfolgen.

3.6 Rheologie

Im Innern der Erde und vieler anderer planetarer Körper laufen dynamische Prozesse ab, die meist durch den Transport von Wärme und/oder Materie angetrieben werden. Die daraus resultierende Gesteinsverformung hängt von Materialeigenschaften wie Zusammensetzung, (Mikro-)Struktur und Gehalt an flüchtigen Bestandteilen ab, sowie von extrinsischen Faktoren wie Temperatur, Druck, Ausmaß und Dauer der deviatorischen Spannungen. Die Verformungs-mechanismen können stark variieren und zu sehr unterschiedlichen Rheologien führen. Das Verformungsverhalten wird durch Fließgesetze beschrieben, in denen Spannung und Verformungsrate zueinander in Beziehung gesetzt werden. Die Bestimmung der Rheologie von Gesteinen ist daher essentiell für das Verständnis der planetaren Dynamik. Aus diesen Gründen haben sich die Wissenschaftler des BGI intensiv mit rheologischen Untersuchungen, bei hohem Druck und hohen Temperaturen beschäftigt.

Die ersten drei Beiträge dieses Kapitels befassen sich mit der plastischen Verformung von planetaren Materialien durch duktiles Fließen. Im ersten Beitrag wird ein neuer Versuchsaufbau vorgestellt, der es erlaubt, verschiedene Phasen von Wassereis zu verformen und dabei die Spannungen und Verformungen zu messen. Mit diesen Experimenten werden Fließgesetze erstellt, die auf die Konvektion im Inneren von planetaren Körpern im äußeren Sonnensystem anwendbar sind. In der darauffolgenden experimentellen Studie wird der Einfluss von Enstatit als sekundäre Phase neben Olivin in Gesteinen des oberen Erdmantels auf die Rheologie sowie die Textur und seismische Anisotropie untersucht. Die Ergebnisse sind kompatibel mit Beobachtungen an natürlichen Proben und erlauben eine quantitative Interpretation der seismisch beobachteten Anisotropien in diesem Bereich des Erdinneren. Der dritte Beitrag stellt eine theoretische Untersuchung des Effekts der Oberflächenspannung in sich verformenden zweiphasigen Medien vor. Hiermit wird das duktile Fließen von Mineralen des unteren Erdmantels, d. h. Aggregaten von Ferroperiklas und Bridgmanit, untersucht. Die Berechnungen zeigen, dass eine hohe Oberflächenspannung zwischen Ferroperiklas und Bridgmanit die Verformung des weicheren Ferroperiklases hemmt und so eine erhebliche Verfestigung des Mineralaggregats bewirkt.

Die beiden folgenden Beiträge befassen sich mit Verformungsmechanismen bei Erdbeben im tiefen oberen Erdmantel. Hier ist ein bruchhaftes Verhalten der Gesteine, wie es bei normalen Erdbeben typisch ist, aufgrund der hohen Temperaturen und des hohen Drucks unwahrscheinlich. Im ersten Beitrag werden Ergebnisse einer experimentellen Studie vorgestellt, in der der Olivin-Spinell-Übergang als möglicher Verformungsmechanismus untersucht wird. Es zeigt sich, dass die Korngröße des Olivins bei diesem Prozess eine entscheidende Rolle spielt: Während in feinkörnigem Ausgangsmaterial die Bildung von Spinell an den Korngrenzen stattfindet und zu großen Versätzen und Verwerfungen in der Kornstruktur führt, ist sie bei grobkörnigem Olivin auf das Korninnere beschränkt und führt nur zu kleinen Versätzen. Dieser Unterschied kann das Verhältnis zwischen Häufigkeit und Stärke von Erdbeben beeinflussen, wie es im Gutenberg-Richter-Gesetz beschrieben ist. Die zweite Arbeit in diesem Teil ist eine theoretische Studie, die die Spannungserzeugung während des Olivin-Spinell-Phasenübergangs modelliert und dabei sowohl die Änderung der Viskosität als auch die Volumenverringerung berücksichtigt. Während beide Faktoren jeweils allein bereits signifikante Spannungen erzeugen können, führt ihre Kombination zu stärkeren Schwächungseffekten, die eine duktile Verwerfung erzeugen und so ein Erdbeben in großer Tiefe verursachen können.

In den letzten beiden Beiträgen werden mikrostrukturelle und chemisch-isotopische Analysen von Meteoriten verwendet, um die Einschlags- und Schock-Verformungsgeschichte ihrer Mutterkörper zu rekonstruieren. Die Studie von *Walte et al.* vergleicht die Korngrößenverteilungen in Meteoriten der Pallasit-Gruppe mit experimentellen Proben aus Verformungsexperimenten mit hoher Deformationsrate. Die beiden natürlich beobachteten Mikrostrukturtypen, die als kantig bzw. fragmentarisch bezeichnet werden, können in Experimenten mit zunehmenden Spannungen und Verformungsraten reproduziert werden. Sie hängen offenbar mit dem Grad der Einwirkung der Impakt-Schockwelle zusammen, der bei letzterem Typ

wesentlich höher ist. Im letzten Beitrag werden die mikrostrukturellen und chemischen Signaturen eines chondritischen Meteoriten vorgestellt, der aus einer Einschlagschmelzbrekzie mit großen Schmelzklasten besteht. Der starke Unterschied im Fe-Gehalt und in der Sauerstoffisotopie zwischen chondritischen Olivinen und solchen in der Schmelze zeigt, dass die Zusammensetzung der Schmelze stark vom Impaktor beeinflusst worden ist. Die mikrostrukturelle Analyse des Meteoriten ermöglicht die Rekonstruktion von drei separaten Schockereignissen. Das erste verursachte die Teilaufschmelzung des chondritischen Materials, das zweite bewirkte eine Brekziierung und Fragmentierung sowohl des Chondriten als auch der verfestigten Schmelze und das dritte erzeugte lokale Schmelzadern sowohl im Chondriten als auch an den Grenzen zu den Schmelzklasten.

3.7 Materialwissenschaften

Neben geowissenschaftlicher Forschung ist die Untersuchung von Materialien, die bei hohem Druck bemerkenswerte Strukturen oder Eigenschaften aufweisen, weiterhin eine wichtige Forschungsrichtung am Bayerischen Geoinstitut. Die meisten der in diesem Abschnitt vorgestellten Projekte beruhen auf Experimenten an Elektronen-Synchrotron-Einrichtungen, um *in situ*-Einkristall-Röntgenbeugung im Megabar-Bereich mit Diamant-Stempelzellen durchzuführen. Diese Experimente werden regelmäßig durch *ab initio*-Simulationen ergänzt, um die Plausibilität von Strukturmodellen zu testen oder deren Details zu untersuchen.

In den ersten beiden Beiträgen wird die Entwicklung von zwei molekularen Systemen (Brom und Pyren $C_{16}H_{10}$) unter Druck mit Hilfe der Einkristall-Röntgenbeugung untersucht. Brom dissoziiert aus molekularen Strukturen bei ca. 80 GPa, und kristallisiert in einer Reihe von modulierten festen Strukturen oberhalb dieses Drucks. Die Struktur des Kohlenwasserstoffs Pyren mit vier aneinander kondensierten Benzol-Ringen wird bei einem Druck von 2,5 GPa untersucht. Die Benzoleinheiten wölben sich, was zu einer ausgeprägten zwischenmolekularen Bindung in der Fischgrät-artigen Stapelung des Pyren-IV Festkörpers führt.

Kohlenstoff zeigt eine große Vielfalt an chemischem Verhalten, wobei Kohlenwasserstoffe – wie das gerade beschriebene Pyren und Carbide von Metallkationen – zwei Extreme repräsentieren. Karbide sind seit langem ein Thema der Materialforschung unter hohem Druck. Sie gehören auch zu den wenigen Materialien, die industriell unter hohem Druck hergestellt werden. Der dritte Beitrag in diesem Kapitel setzt diese Tradition fort, und zwar für das Seltenerd-Element Dysprosium als Kation. Bis zu 50 GPa werden drei verschiedene Dy-Karbide durch *in situ*-Röntgenbeugung mit unterschiedlichem Dy:C Verhältnis beschrieben. Im Gegensatz zu Kohlenstoff ging man bisher davon aus, dass Stickstoff aufgrund der extrem stabilen Dreifachbindung im N_2-Molekül eine begrenzte chemische Vielfalt aufweist. In anorganischen Verbindungen liegt Stickstoff oft als Nitrid-Anion (N^{3-}) vor. In den letzten zwei Jahrzehnten hat sich jedoch gezeigt, dass sich die Stickstoffchemie bei hohem Druck erheblich ändert. Zwei neue Yttriumnitride, die hier beschrieben werden, YN_6 und Y_2N_{11}, weisen mit

einem N_{18}-Ring bzw. einer Stickstoff-Doppelhelix neuartige Anordnungen von Stickstoff-Atomen auf.

Yttrium- und Lanthanhydride haben in der Hochdruck-Festkörperphysik große Beachtung gefunden, aufgrund von Berichten über ihre Supraleitfähigkeit in der Nähe von Raumtemperatur. Allerdings gibt es nach wie vor Unstimmigkeiten und Probleme mit den veröffentlichten Daten und Ergebnissen, einschließlich unbekannter oder schlecht charakterisierter Phasen. Dies ist auch darauf zurückzuführen, dass Strukturen bisher nur durch eine Kombination aus Pulver-Röntgenbeugung und theoretischen Vorhersagen bestimmt wurden. Einkristall-Röntgenbeugung an Phasen in den Systemen Y-H und La-H zeigen, dass diese bei hohem Druck ein viel reicheres Strukturverhalten aufweisen als bisher erwartet wurde. Diese Erkenntnisse sind wichtig für die (Neu-)Interpretation von Experimenten zur Supraleitung in Hydriden.

Die letzten beiden Beiträge des Abschnitts befassen sich mit den mechanischen Eigenschaften von Materialien, die unter hohem Druck synthetisiert wurden. Im ersten Beitrag wird Wolframborid WB_4 synthetisiert und seine Kompressibilität und Härte gemessen; dabei zeigt sich, dass es sich um ein superhartes Material handelt. Zinnselenid (SnSe) hingegen ist ein geschichtetes Chalkogenid mit ausgezeichneten thermoelektronischen Eigenschaften, die durch Kompression weiter optimiert werden können. Bei einem Druck von ca. 10 GPa ändert sich die Schicht-Morphologie vermutlich durch eine duktile Verformung im Submikronbereich. Dies ist vermutlich verknüpft mit dem Übergang von einem kovalent gebundenen spröden Material zu einem metallischen und plastischen Zustand.

3.8 Methodische Entwicklungen

Technische und methodische Entwicklungen sind ein fester Bestandteil von Experimenten bei hohen Drücken und Temperaturen. Da die physikalischen Bedingungen im Inneren der Erde und anderer Planeten die derzeit technischen Möglichkeiten teilweise noch übersteigen, bleibt es eine ständige Herausforderung, die experimentell realisierbaren Bedingungen sowie die Möglichkeiten der *in situ*-Messungen unter diesen Bedingungen zu erweitern. Aus diesem Grund bemühen sich Wissenschaftler des BGI kontinuierlich darum, neue experimentelle Ansätze zu entwickeln und die bestehenden zu verbessern und zu verfeinern.

In diesem Jahr haben wir drei Beiträge zu diesem Thema. Der erste Beitrag befasst sich mit Spannungsmessungen während Verformungsexperimenten in einer Multianvil-Presse am BGI. In Standard-Versuchsaufbauten können die Spannungen in den Proben nur durch *in situ*-Röntgenbeugung mit Synchrotronstrahlung gemessen werden. Da der Zugang zu Synchrotron-strahlung jedoch begrenzt ist, wird eine neue Methode benötigt, um Spannungen unter Laborbedingungen zu ermitteln. *Dolinschi et al.* haben es möglich gemacht, Spannungen mit Hilfe von piezoelektrischen Kristallen zu messen, die in ihren Versuchsaufbau integriert sind.

Auf diese Weise ist es ihnen gelungen, die deviatorische Spannung bei hoher Temperatur und hohem Druck in einer Multianvil-Presse zu messen. Der zweite Beitrag befasst sich mit der Messung der Probenlänge in einer Multianvil-Presse bei hohem Druck und hoher Temperatur. *Neri et al.* haben eine Methode zur Bestimmung des Probendrucks und der Probenlänge durch gleichzeitige Messung der Laufzeiten von P- und S-Wellen entwickelt, die es ermöglicht, diese beiden Parameter ohne den Einsatz von Synchrotronstrahlung zu bestimmen. Die experimentelle Messung von seismischen Wellengeschwindigkeiten ist unabdingbar für die Interpretation von seismischen Daten aus dem Erdinnern. Schließlich haben *Dominijanni et al.* die Anwendbarkeit des Ir-Fe-Sensors zur Bestimmung der Sauerstofffugazität in Hochdruckexperimenten in Multianvil-Pressen und der Diamant-Stempelzelle untersucht. Dieser Sensor eignet sich gut für die Messung des Redoxzustands bei hohen Temperaturen, war aber bisher für Hochdruckbedingungen nicht gut kalibriert. Durch die Verfeinerung des thermodynamischen Modells für diesen Sensor unter Berücksichtigung von Druckeffekten konnte eine verbesserte Messung der Sauerstofffugazität für Experimente in Multianvil-Pressen und insbesondere in laserbeheizten Diamant-Stempelzellen nachgewiesen werden. Dies macht den Fe-Ir-Sensor für Experimente bei sehr hohen Drücken besonders wertvoll.

3. Research Projects

3.1 Earth and Planetary Structure and Dynamics

The Earth is the only planet in the habitable zone of the Solar System supporting liquid water throughout its history, thanks to its position relative to its star, mass, and internal evolution over 4.56 billion years. From geochemical and geophysical constraints, we can model its internal reservoir differentiation (core, mantle, crust) and long-term evolution. Earth's building materials have long been linked to chondrite meteorites as the remnants of the first condensable matter as the solar nebula cooled around the nascent Sun. An amazing observation is that CI-chondrites formed in the outskirts of the solar system are identical in elemental composition to the solar photosphere for condensable elements. As more and more exoplanets are being detected, we question how many may be out there in our galaxy or the universe, and can we also infer their composition and interior dynamics? Owing to thermal gradients in the innermost parts of the solar system, accretion processes, and formation and evolution of inaccessible deep planetary reservoirs, it is however not a simple task to deduce the composition of the Earth and terrestrial planets. In this section, different approaches are taken to provide new constraints on the sources of materials and infer a more detailed scenario to explain the chemical variations between Earth and various types of planetesimals as potential building blocks. Once the Earth differentiated, the crust and mantle evolved together for more than 4.4 billion years, hindering the earliest evidence of crust formation. Numerical modelling can shed light on how some of the earliest continental crust is still preserved as cratons, while other tectonic structures associated with continent formation appear to be missing in the geological records or can be related to deep mantle features.

The accessible part of the Earth's mantle appears to be depleted in Si compared to all known chondrite groups, and Si is the most abundant element after oxygen in the silicate layers of the Earth. A possibility is that the missing Si is contained in the lower mantle and the core. Frost and Boffa Ballaran take a geophysical approach to provide geochemical constraints on the composition of the lower mantle and exclude enstatite chondrites as the main building blocks for the Earth.

Core formation on planetary bodies was not an instantaneous process but stripped down all siderophile elements from the mantle prior to late accretion. Rubie *et al.* combine metal-silicate equilibration models with the results of N-body simulations. They also integrate the distribution of metal within undifferentiated planetesimals, such as chondrites, to model their influence against the measured $^{182}W/^{184}W$ isotopic composition of the accessible Earth. They found that undifferentiated material must have played a significant role in the making of the Earth in order to reconcile the W abundance and isotopic composition of the Earth's mantle with accretion and core formation processes.

The ^{146}Sm-^{142}Nd radioactive decay system, with a short half-life of 103 million years, is particularly suited to track the first 700 million years of Earth's accretion and differentiation

history. Using the compositions of different classes of chondrites and their components, Frossard *et al.* recognize a lower abundance in $^{142}Nd/^{144}Nd$ in primitive asteroids compared to the Earth's mantle as well as differentiated meteorites. They propose that 4 to 20 % mass of early-formed enriched crust on Earth and differentiated planetesimals were blasted out during planetary collisions. This process depleted their overall chemical composition in the most incompatible elements, including radioactive elements such as U, Th and K.

In late 2021, the discovery of short-period super-Mercury GJ 367b was announced. This nearby planet at 31 light-years distance will be examined in the near future using the new James Webb Space Telescope, which will be able to characterize its surface. Golabek *et al.* model the solid planet and magma ocean evolution on this tidally-locked short-period planet, allowing for a future comparison between model results and surface-composition observations.

On Earth, cratons represent the oldest parts of the lithosphere and have remained undeformed for several billion years. This is puzzling since early Earth experienced more vigorous convection than at present-day, thus long-term craton preservation is difficult to envision. Paul and colleagues study craton preservation using 3D spherical geometry, finding that thick and highly viscous cratons experience a compressive stress field during mantle convection that might support craton preservation on long timescales.

Slab detachment can occur during continent-continent collisions like the Alpine orogeny. It can be expected that this process causes a significant topographic uplift on the surface. However, surprisingly, this is not always observed in the geological record. Piccolo and Thielmann develop both simplified 0D and full 2D numerical models where they incorporate the effect of mantle drag and show that for Earth-like parameters, mantle drag considerably slows down both the detachment process and the uplift process, explaining the lack of geological evidence.

The Earth's lower mantle is mostly made of minerals bridgmanite and ferropericlase. Paul and colleagues employ a new grain size evolution law for bridgmanite and ferropericlase mixtures to study the long-term evolution of Earth's interior using 2D spherical annulus models. Their most successful numerical models exhibit both Earth-like mobile lid tectonics and the self-consistent formation and preservation of thermochemical piles at the bottom of the mantle. The latter is due to large grain sizes and therefore a high viscosity of these regions. This could shed light onto the origin of the large low-shear-velocity provinces (LLSVPs) in the lower mantle of present-day Earth.

a. *Bulk compositions that are consistent with seismic velocities of the lower mantle (D.J. Frost and T. Boffa Ballaran)*

If we want to know the composition of the Earth as a whole, which is essential for understanding its formation, we need to be sure of the composition of the lower mantle, as it makes up 56 % of the entire Earth by volume. There are two opinions on lower-mantle composition; that it is

the same as the upper mantle due to homogenisation through whole mantle convection or that it is more SiO_2-rich as a result of different convection cells operating. The latter view is consistent with the fact that primitive meteorites, from which the Earth is proposed to have formed, all have more SiO_2-rich compositions compared to the Earth's upper mantle.

One-dimensional seismic velocity profiles for the lower mantle provide some of the only constraints to determine the composition of the lower mantle. To extract this information, we need to compare these velocities with mineral physics models for what these velocities should be if the mantle has a certain composition. This requires mineral elasticity measurements as a function of pressure, temperature and composition, but also a petrological model is needed to define the mineral compositions and proportions for a particular bulk composition as a function of depth. If we assume that the composition of the lower mantle is indeed the same as the upper mantle, then it should be mainly comprised of three phases, $(Mg,Fe,Al)(Al,Si)O_3$ bridgmanite, $(Mg,Fe)O$ ferropericlase and $CaSiO_3$ calcium silicate perovskite. The proportions of these phases and their compositions will depend on the exact bulk composition, and the phase compositions will change with depth mainly due to pressure and oxygen-fugacity-dependent Fe-Mg partitioning between bridgmanite and ferropericlase.

Over the last years, high-pressure experiments in Bayreuth and other laboratories have determined elastic properties of lower-mantle phases as a function of pressure, temperature and bulk composition. From these data, it is possible to calculate how different chemical components of ferropericlase and bridgmanite contribute to the combined shear-wave velocity, V_S, of these phases, as shown in Figure 3.1-1. The same analysis could be made for longitudinal velocities (Vp), but Vs appears to have a slightly larger variation with composition. The data indicate that the FeO component of ferropericlase is by far the slowest constituent. To determine how much of this component partitions into ferropericlase in different compositions, experiments have also been performed in Bayreuth over the last years to allow lower mantle Fe-Mg partitioning to be described with a thermodynamic model (*e.g.*, Jahresbericht 2019; page 49). Using these results, we can make a comparison between predicted seismic velocities for different bulk compositions and those observed.

In Figure 3.1-1, shear-wave velocities are calculated for different bulk compositions at pressure and temperature conditions compatible with 1000 km depth (~ 39 GPa), *i.e.*, 340 km into the lower mantle. The compositions are plotted as a function of the bulk SiO_2 content and compared with the velocities of two seismic reference models (PREM and AK135). A depth of 1000 km is chosen for the comparison because it is suitably distant from the 660 km discontinuity, where the reference models are not in perfect agreement, and is within a pressure range that does not require significant extrapolation of the modelled experimental data. The vertical bar is an indication of the model uncertainties.

Although there are a number of different proposed upper-mantle and bulk-silicate-Earth compositions, as shown by the blue circles in Figure 3.1-2, they all provide a good match for lower mantle Vs at this depth, except PHN 1611. This is a sheared peridotite xenolith

composition with an FeO content (~ 10 wt. %) that is probably higher than that of the mantle. Similarly, the yellow circle is calculated for a mechanical mixture of oceanic crust (OC) and harzburgite (Hz) compositions in the same ratio as produced at mid-ocean ridges and also matches the reference models very well at this depth.

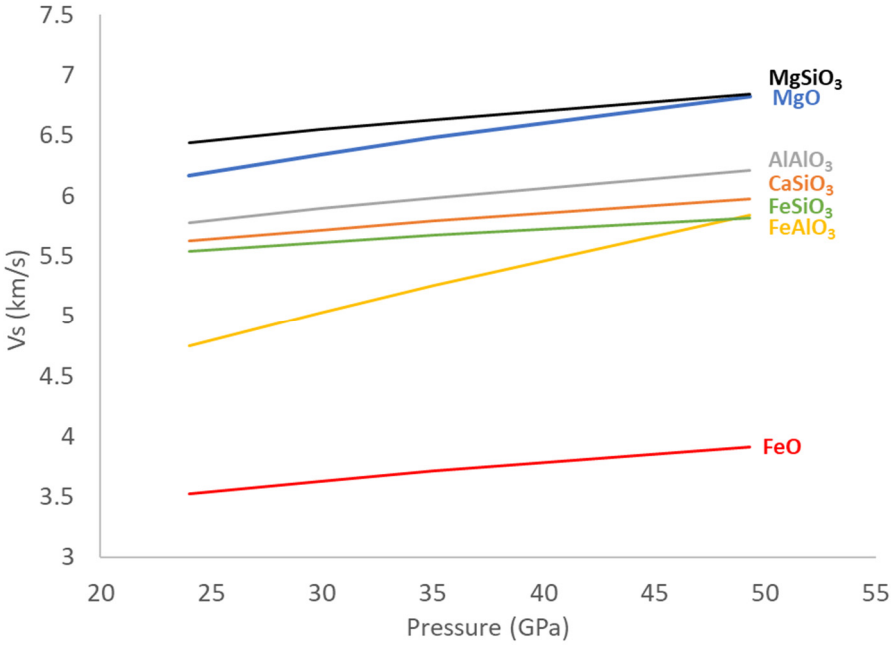

Fig. 3.1-1: Shear wave velocities calculated for individual bridgmanite and ferropericlase components at lower mantle temperatures and pressures, based on experimental measurements.

Surprisingly, the primitive carbonaceous chondrite meteorite compositions, CV and CI, also provide a good fit to the lower-mantle velocity. Both compositions are more SiO_2-rich than proposed upper-mantle compositions and might be expected to have fast Vs, because the raised SiO_2 content should mean they contain less ferropericlase and more bridgmanite. However, ferropericlase is the more FeO-rich phase. If the bulk composition contains less ferropericlase, but has a similar bulk FeO content, then bridgmanite has to contain more FeO. Even though there is a smaller amount of ferropericlase in the bulk composition, it will still contain more FeO than bridgmanite. The raised FeO content of ferropericlase in SiO_2-rich compositions lowers V_S and compensates for the increased bridgmanite content.

The same effect occurs for the lower mantle crystal pile (LMCP) composition, which is a lower-mantle composition formed from fractional crystallisation of a CI chondrite bulk composition, where the residual liquid goes on to form the upper mantle. The implication is that as long as the lower mantle has a similar FeO content as the upper mantle, it would be impossible to differentiate between lower-mantle compositions with different SiO_2 contents based on their seismic velocities, at least at this depth. A similar result is obtained when using Vp.

The lower mantle has been proposed to contain so-called bridgmanite-enriched ancient mantle structures (BEAMS), which crystallised in the lower mantle from a magma ocean. If bridgmanite crystallised at this depth, however, the resulting mantle would be faster than the observed seismic velocities. Although BEAMS could form a component of the lower mantle, their density is much lower than the other compositions, at least at this depth, and it is questionable whether they would remain in the lower mantle. If the lower mantle had an ordinary chondrite composition (L), its velocity would still be consistent with the observed seismic velocity, within the current experimental uncertainties. Future high-temperature and -pressure experimental measurements may be able to reduce these uncertainties, however. Finally, an enstatite chondrite composition (EH) at these conditions contains stishovite instead of ferropericlase and the resulting increase in *V*s means that it can be safely excluded from being the composition of the lower mantle.

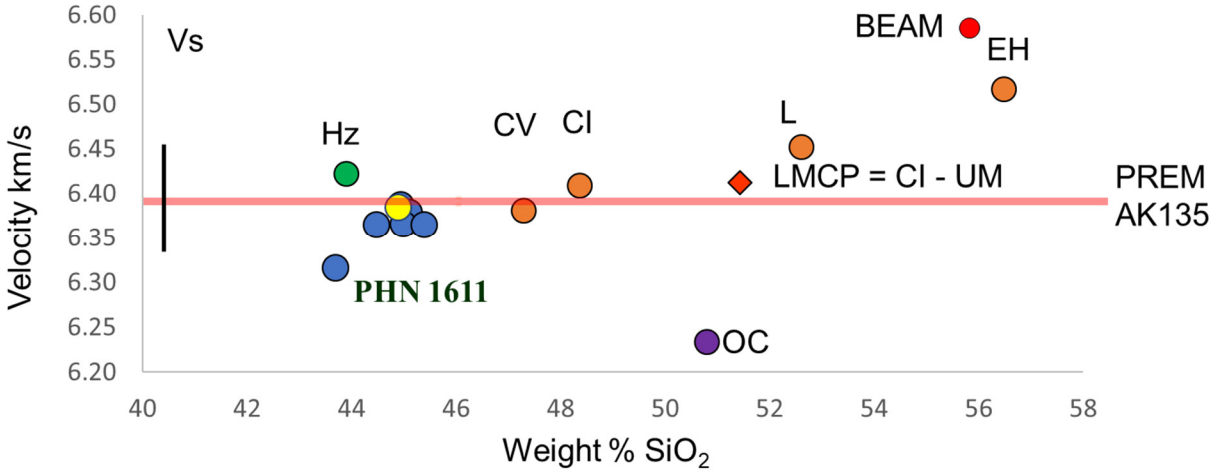

Fig. 3.1-2: Shear-wave velocities for different bulk compositions plotted as a function of their bulk SiO_2 content and calculated at conditions comparable with a depth of 1000 km in the mantle. Blue circles are proposed bulk-silicate-Earth and upper-mantle compositions, PHN 1611 is a sheared mantle peridotite xenolith. Hz is harzburgite, OC is oceanic crust and the yellow circle is a mechanical mixture of the two. Orange circles are mantle compositors based on primitive meteorites. LMCP is a lower mantle crystal pile, *i.e.*, the complementary composition to the upper mantle, if it were derived from a CI composition through fractional crystallisation into the lower mantle. BEAM is bridgmanite-enriched ancient mantle, formed through liquidus crystallisation of bridgmanite from a magma ocean. PREM and AK135 are seismic reference models, and the vertical bar shows the model uncertainty.

b. *The effects of metal-silicate fractionation mechanisms during the formation of Earth's core (D.C. Rubie and G.J. Golabek, in collaboration with A. Morbidelli/Nice)*

We have developed a now well-established model of planetary core formation by combining metal-silicate equilibration models with the results N-body simulations of planetary accretion.

The planetary core formation is modelled as a multistage process, and a core formation event occurs whenever a metal-bearing body (either a large Mars-size embryo or a small planetesimal) impacts the growing Earth. The energy of the impact causes melting and the creation of a melt pool (Fig. 3.1-3) which could extend to the core-mantle boundary in the case of a giant impact. The model is used to calculate the final compositions of Earth's mantle and core based on a combined mass balance plus element partitioning approach. Using a least-squares refinement of five free parameters, the calculated mantle composition is fit to observed mantle concentrations of a large number of elements.

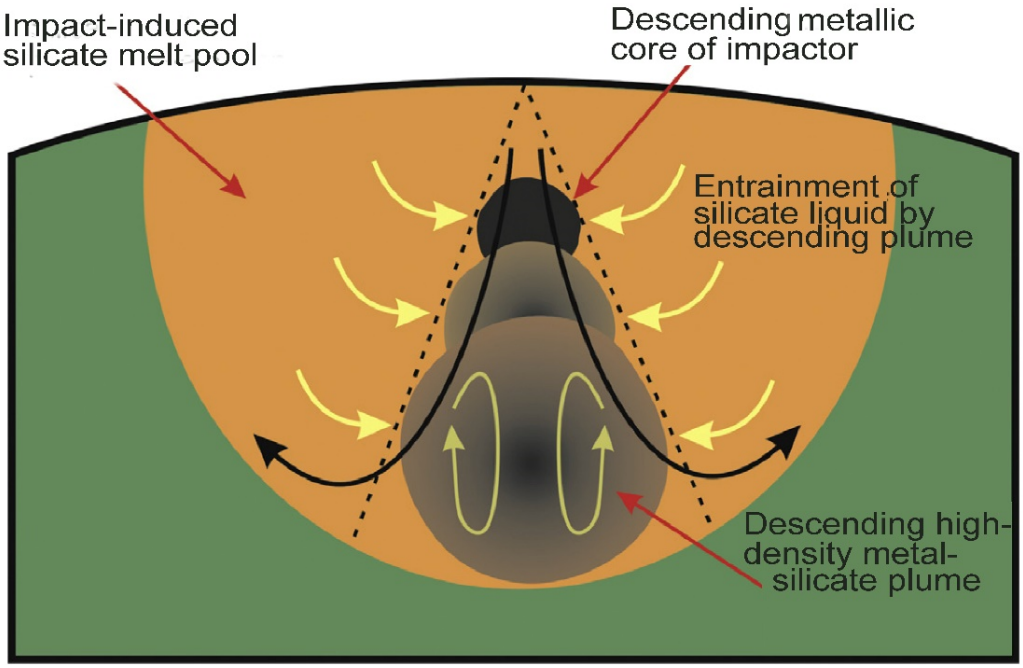

Fig. 3.1-3: Consequences of an impact of a differentiated embryo onto a growing proto-planet. When the impacting body is differentiated, as is the case here, its metallic core sinks in the impact-induced silicate-magma melt pool and thereby entrains surrounding silicate liquid. The result is a high-density plume of molten metal + molten silicate that expands as it sinks to the base of the melt pool. The final chemical equilibration of metal and silicate liquids occurs within this plume when it reaches the bottom of the melt pool.

We have previously assumed that all metal-bearing accreting bodies are differentiated and thus consist of a metallic core and silicate mantle. Following an accretion event, the metallic core of such a body sinks through the melt pool and entrains silicate liquid to form a high-density plume of mixed silicate and metal (Fig. 3.1-3). Final chemical equilibration is assumed to occur within this plume at its base, which means that the accreted metal only equilibrates with a small fraction of the planet's mantle (*e.g.*, $\leq$ 10 % of the mantle for giant impacts and much less for small planetesimal impacts). Using this hydrodynamic model, we are able to reproduce Earth's mantle concentrations of a large number of elements (Al, Mg, Ca, Fe, Si, Ni, Co, Nb, Ta, V, Cr, C and S). However, least square fits predict mantle concentrations of W and Mo that are too high by factors of 3-4 (Fig. 3.1-4a, b).

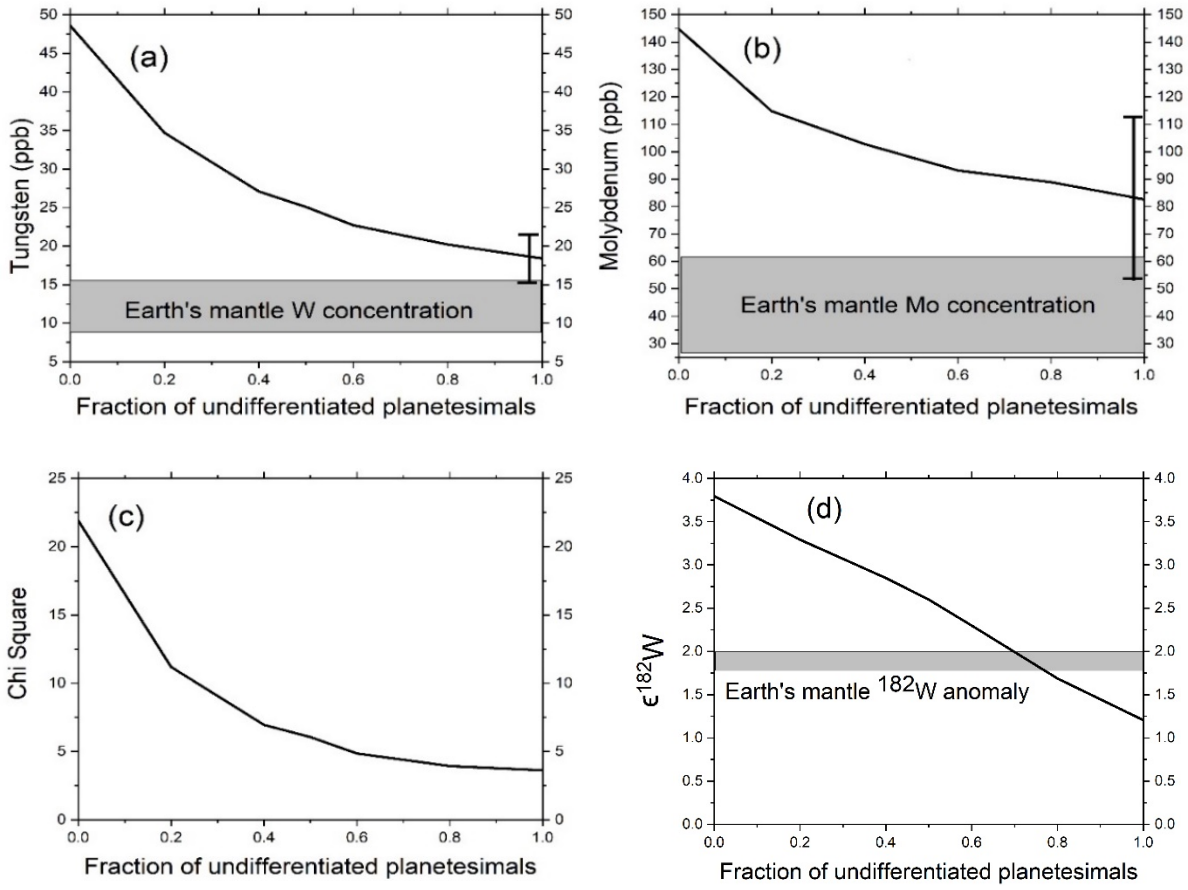

Fig. 3.1-4: The effects of increasing the fraction of accreted undifferentiated planetesimals on the calculated final mantle concentrations of W and Mo (a and b), chi square when fitting calculated concentrations of MgO, FeO, SiO_2, Ni, Co, Nb, Ta, V, Cr, W and Mo to Earth's mantle composition (c), and the mantle ^{182}W anomaly (d). These results are based on a Grand Tack N-body accretion simulation.

Meteorite samples show that many impacting planetesimals must have been undifferentiated with metal being present as small (~ 1 mm) particles. The model shown in Figure 3.1-3 is clearly not relevant for such impacts. We have therefore developed a new model of metal-silicate fractionation that is applicable when an undifferentiated planetesimal impacts an accreting planet. Because of their small grain size, particles of accreted metal are uniformly suspended and dispersed in a global magma ocean that is undergoing vigorous turbulent convection (that also keeps it well mixed). The metal particles only settle out when they enter a boundary layer at the base of the magma ocean. Metal particles finally equilibrate chemically with silicate liquid in this boundary layer before segregating to the planet's core in the form of diapirs. This process is modelled through a series of iterations until all the dispersed metal has progressively segregated to the core. Results show that calculated mantle concentrations of W and Mo decrease significantly as the fraction of undifferentiated planetesimals is increased and becomes consistent with observed mantle concentrations when this fraction is large (Fig. 3.1-

4a, b). This trend is also reflected by a strong decrease of chi square when fitting calculated mantle concentrations of elements, including W and Mo (Fig. 3.1-4c).

We have also incorporated the Hf-W isotopic system in our combined accretion/core-mantle differentiation model with the aim of investigating the origin of the tungsten isotope anomaly of Earth's mantle. ^{182}Hf decays to ^{182}W with a half-life of 8.9 Myrs. Because Hf is lithophile and W is moderately siderophile, the final mantle concentration of ^{182}W is an indicator of the timing of core formation. However, it has also been shown that it depends on a range of other factors, such as the metal-silicate partition coefficient of W, the fraction of accreted metal that equilibrates with Earth's mantle and the fraction of the mantle that equilibrates with the accreted metal. These factors are well defined in our differentiation model on the basis of element concentrations.

It is well established that there is an excess of ^{182}W in Earth's mantle, as defined by ϵ_{182W}:

$$\epsilon_{182W} = \left[\frac{(C^{182W}/C^{183W})}{(C^{182W}/C^{183W})_{CHUR}} - 1\right] \times 10^4$$

where CHUR is the undifferentiated (chondritic) ratio. For Earth's mantle, $\epsilon_{182W} = 1.9 \pm 0.1$. Using the new metal-silicate fractionation model described here, we have found that the fraction of accreting undifferentiated planetesimals strongly affects the final mantle tungsten anomaly and provides additional support for this fraction being large (Fig. 3.1-4d).

c. *Earth's composition was modified by collisional erosion (A. Bouvier, in collaboration with P. Frossard, C. Israel and M. Boyet/Clermont Ferrand)*

The short-lived samarium-146 (^{146}Sm)–neodymium-142 (^{142}Nd) decay system (half-life of 103 million years) is a powerful tracer of the early mantle-crust evolution of planetary bodies. With the advance of mass spectrometric techniques, a gap of 20 parts per million (ppm) in ^{142}Nd abundance was found between the Earth's modern mantle and chondrites. This gap suggested that an early differentiation event occurred in the early Earth, forming the depleted mantle and an elusive and unsampled complementary early enriched reservoir. In more recent works, it has been proposed that a higher ^{142}Nd/^{144}Nd ratio in modern terrestrial rocks relative to chondrite meteorites is caused by nucleosynthetic anomalies related to the *s*-process in meteorites. The similarity in ^{142}Nd abundance between Earth and chondrites removed the need for a hidden reservoir within the Earth. Earth shares the closest mass-independent isotopic affinities for most major and trace elements with the subgroup of EL3 enstatite chondrites. Nevertheless, the potential contribution of the *p*-process on ^{142}Nd was poorly constrained. Additionally, nucleosynthetic compositions identified in meteorites deviate from the astrophysical models of nucleosynthesis and may not be similar in all chondrite groups.

To better quantify the nucleosynthetic contributions, including the *p*-process, on the composition of chondrites, we here used a method of stepwise acid dissolution of primitive (unequilibrated) chondrites from both the non-carbonaceous (NC, enstatite and ordinary chondrites) and the carbonaceous (CC) groups. We obtained a comprehensive set of coupled Nd and Sm isotope compositions of bulk-rocks and of components of Orgueil (CI), NWA 8007 (L3) and Sahara 97158 (EH3). Leachates from enstatite and carbonaceous chondrites had much larger nucleosynthetic anomalies than leachates from ordinary chondrites and bulk chondrites in the range of tens to hundreds of ppm in magnitude. We used slopes defined by leachate regression lines linking a stable isotope ratio (μ^{145}Nd and μ^{148}Nd) to μ^{142}Nd to calculate the μ^{142}Nd composition of E and O chondrites without nucleosynthetic anomalies relative to the Earth. The theoretical composition of the Earth, assuming NC chondrites are its main building blocks, is calculated in this manner. We find that Earth and the silicate parts of differentiated planetesimals contain resolved excesses of ^{142}Nd relative to chondrites with an average of μ^{142}Nd = -7.9 ± 1.9 (2SD, Fig. 3.1-5A). This negative value of μ^{142}Nd for NC chondrites relative to the Earth's mantle contrasts with μ^{145}Nd and μ^{148}Nd that lie on the leachate regression line passing through the NC chondrites (Fig. 3.1-5B) and achondrites.

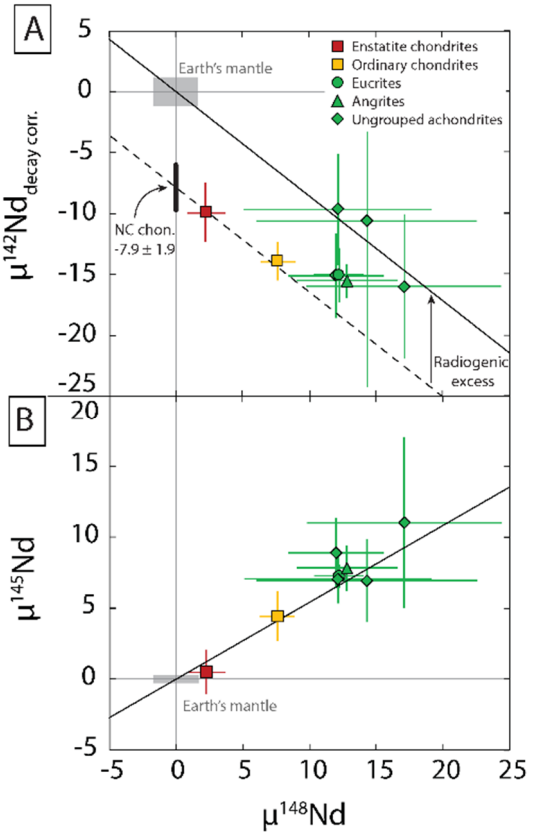

Figure 3.1-5: *s*-process nucleosynthetic contributions on Nd isotope compositions of bulk NC meteorites. A) μ^{142Nd} vs. μ^{148}Nd shows the radiogenic excess of ^{142}Nd in Earth and NC achondrites compared to NC chondrites. The two lines represent the *s*-process nucleosynthetic trend determined with leachates in this study with a terrestrial origin (μ^{142}Nd = 0; black line) and an origin corresponding to the mean of μ^{142}Nd corrected from nucleosynthetic anomalies in NC chondrites (μ^{142}Nd = 7.9 ± 1.9; dashed line). B) The Earth, NC chondrites and achondrites are all aligned on the nucleosynthetic trend with a terrestrial origin (black line). All values in ppm.

Recent studies reported high precision Nd stable isotope compositions of achondrites sampling early planetesimals (Fig. 3.1-5B). When corrected for nucleosynthetic anomalies, their μ^{142}Nd's are in between the Earth and NC chondrites, and more specifically, the average compositions for angrites and eucrites are resolved from NC chondrites (Fig. 3.1-5A).

The cause of the excess in μ^{142}Nd in Earth and achondrites may be related to several factors, (i) a *p*-process excess; (ii) accretion of material with a non-chondritic composition; (iii) early silicate differentiation and isolation of the enriched reservoir. We did not identify any *p*-process-rich carrier in leachates of chondrites, and such a carrier is unlikely to be present only in Earth and achondrites. Chondrites, despite having been formed 2-3 Ma after the first planetesimals, are representative of the early solar system composition before differentiation of planet-size objects. The most likely hypothesis is that the excess of ^{142}Nd in the Earth and achondrites reflects an early silicate differentiation of planets and planetesimals producing mantles with superchondritic Sm/Nd.

We favour collisional erosion of 4 to up to 20 % of primordial crusts to explain the ^{142}Nd excesses found in both Earth and asteroidal crusts. This process associated with planetary accretion must have produced substantial loss of incompatible elements, including long-term heat-producing elements such as uranium, thorium, and potassium (Fig. 3.1-6). Chondrites have long been considered to be the building blocks of the Earth. However, there is growing evidence that suggests that Earth accreted substantial parts of an unknown material with *s*-process excesses compared to both known meteorites and differentiated planetesimals.

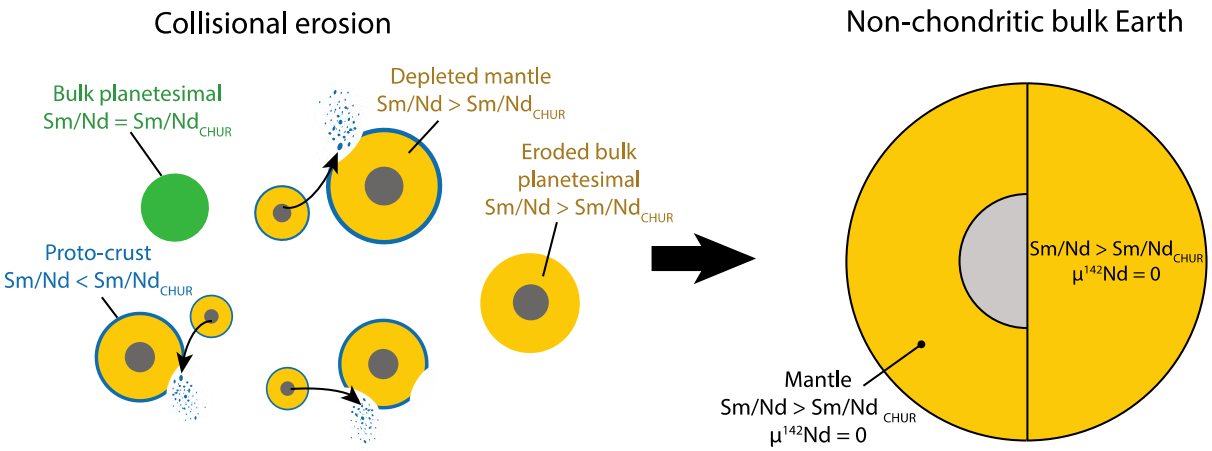

Fig. 3.1-6: Sketch of the differentiation collisional erosion scenario on planetesimals and Earth. Collisions between differentiated planetesimals strip off proto-crusts (low Sm/Nd), which leaves bodies with a mantle that is enriched in Sm over Nd compared with undifferentiated chondrites. Earth accreted from collisionally eroded planetesimals is depleted in incompatible elements and has a superchondritic Sm/Nd ratio.

d. *Magma oceanography of the dense, ultrashort-period sub-Earth GJ 367b (G.J. Golabek, T. Lichtenberg/Groningen and P.J. Tackley/Zurich)*

The dawn of high-resolution observations with the James Webb Space Telescope will enable spatially resolved observations of ultrashort-period rocky exoplanets. Some of these planets orbit so closely to their star that they lack an atmosphere, which gives direct access to their

surfaces and opens a window to infer their geodynamics. The physical parameters of the ultrashort-period sub-Earth GJ 367b have been observationally constrained to a planetary radius of about 0.72 to 0.75 Earth-radii and a mass between 0.48 and 0.55 Earth-masses, implying a density of 6200 to 8500 kg/m^3, which puts this planet in a Mercury-like interior regime with a thin mantle overlying a fractionally large core.

The dayside temperature ranges between 1500 to 1800 K, thus suggesting the presence of a permanent magma ocean or dayside magma pond on the surface, induced by stellar irradiation. The large uncertainty on the age of the stellar system, between 30 Myr and about 8 Gyr, however, introduces severe uncertainties related to the compositional and thermal evolution of the planetary mantle. We perform global 2D spherical annulus StagYY simulations of solid-state mantle convection and surface melting with the goal to constrain the geometric and compositional properties of the planet. Constraining the spatial dimensions of thermodynamic properties of partially molten, atmosphere-less planets like GJ 367b offers unique opportunities to constrain the compositional fractionation during magma ocean epochs and provides avenues to constrain the delivery and loss cycle of atmophile elements on strongly irradiated exoplanets.

e. *Convective self-compression of cratons (J. Paul, C.P. Conrad/Oslo, T.W. Becker/Austin and A. Ghosh/Bangalore)*

The oldest parts of the continental lithosphere, known as cratons, have remained tectonically stable for over a few billion years. Their long-term stability has been attributed to their low density and high strength compared to other non-cratonic lithospheres. High lithospheric strength results from thick cratonic roots equipped with large viscosity. Such highly viscous cratonic roots can slow the deformation underneath cratons, and strains accumulate close to weak plate-boundary regions. However, high-viscosity roots tend to increase the coupling with the mantle producing elevated tractions along the craton periphery. In our current study, we develop global spherical numerical models using the finite-element code CitcomS to quantify the nature of elevated tractions along the craton boundary and their role in the long-term survival of the old lithosphere.

Our models incorporate thick and viscous cratons above a convecting mantle driven by the density anomalies obtained from seismic velocity anomalies. We process $\sigma_{r\varphi}$ and $\sigma_{r\theta}$ components from the complete stress tensor to calculate traction vectors. In the absence of cratons, traction vectors are only guided by the density anomalies, and their magnitude remains limited to ~ 5 MPa (Fig 3.1-7a). In contrast, thick and viscous cratons amplify traction magnitudes 80-100 times along the craton periphery (Fig 3.1-7b). The presence of cratons also produces inwardly convergent tractions along the craton edge, giving rise to a compressive stress regime within them. We test different craton, asthenosphere, and lithosphere viscosity and find that the compressive stress regime remains universal regardless of the viscosity structure.

We hypothesize that mantle flow can be diverted (typically downward) due to thick and viscous cratonic roots, which can change the horizontal gradient of vertical velocity. The change of velocity gradient amplifies the traction magnitude, and the downward diversion of flow velocity can produce inward-directed tractions along the craton boundary. We test this hypothesis by investigating velocity cross-sections underneath all cratons. Indeed, we find such velocity diversion near the craton boundary wall. This kind of velocity diversion was earlier attributed to the edge-driven convection originating from the density anomalies. However, such diversion is a natural consequence of mantle flow in the presence of thick and viscous cratonic roots. Hence, craton can self-induce a compressive regime within them, which can support their long-term stability against the destructive forces of mantle convection.

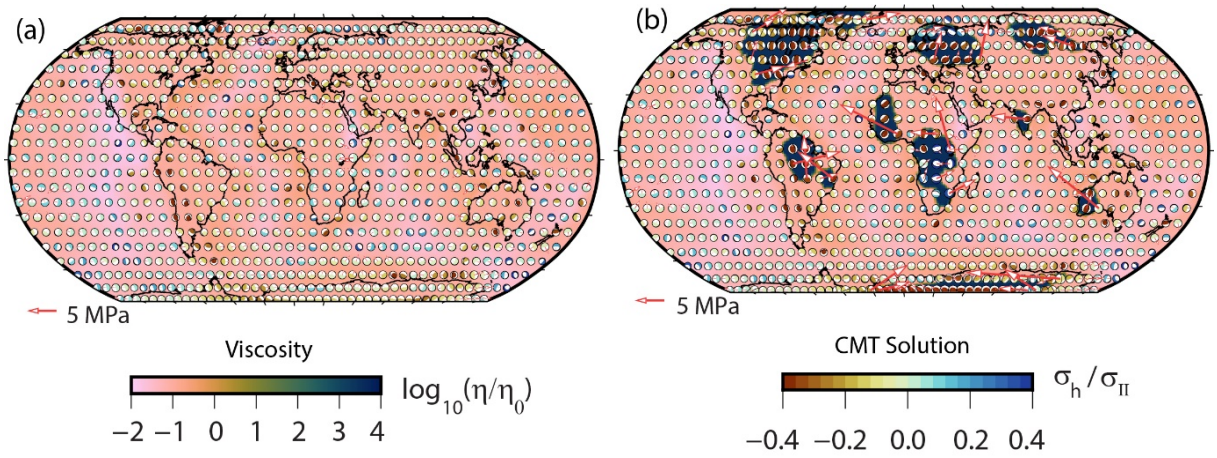

Fig. 3.1-7: Analysis of tractions and stress regimes in the absence (a) and presence of cratons (b) at 120 km depth. Viscosity is plotted as the background colour, and arrows indicate the magnitude and direction of tractions. Centroid Moment Tensors (CMT) indicate stress regime and they are coloured as the ratio of mean horizontal stress to the second invariant of deviatoric stress (σ_h/σ_{II}). Negative values represent compressive stress regimes.

f. *The role of upper mantle's drag on the evolution of the slab detachment: Insights from 0D to 2D numerical simulations (A. Piccolo and M. Thielmann)*

Slab detachment occurs when a subducting slab loses its continuity due to the internal stresses that result from the slab's negative buoyancy. This process causes a lithospheric rebound that can be associated with exhumation, seismicity and topographic uplift. The magnitude and duration of the lithosphere's response hinges on the detachment timescale, which depends on slab rheology and the effective force acting on it. Despite the potential strong impact of slab detachment on the Earth's surface, the physical processes affecting the detachment timescale are not sufficiently understood. In this study, we investigate the effects of the drag force exerted by the upper mantle on the detachment process by using 0D and 2D numerical experiments.

To better understand the essential physics of the impact of mantle drag on slab detachment, we first developed a simplified 0D model. This model then allowed us to derive a dimensionless ordinary differential equation with different dimensionless groups (*i.e.*, combinations of different material parameters). One of these dimensionless groups is given by the drag coefficient (Λ), which incorporates the effects of the viscosity contrast between upper mantle and slab and its initial length. As a function of the *drag coefficient*, the evolution detachment deviates from the ideal case: the predicted time of detachment with respect to the characteristic timescale increase as a function of Λ (see Fig. 3.1-8). To verify the predictions from the simplified 0D models, we conducted a series of 2D simulations. The results from these simulations not only allow us to improve our simplified mantle drag model, but also allow to connect the effects of slab detachment on the surface evolution. Our results show that, for Earth-like parameter ranges, mantle drag can have a significant impact on slab detachment and thus also on the related surface response. An increased mantle drag slows down detachment and, thus, delaying the surface response up to a level that it would not be visible in the geological record (see Fig. 3.1-8).

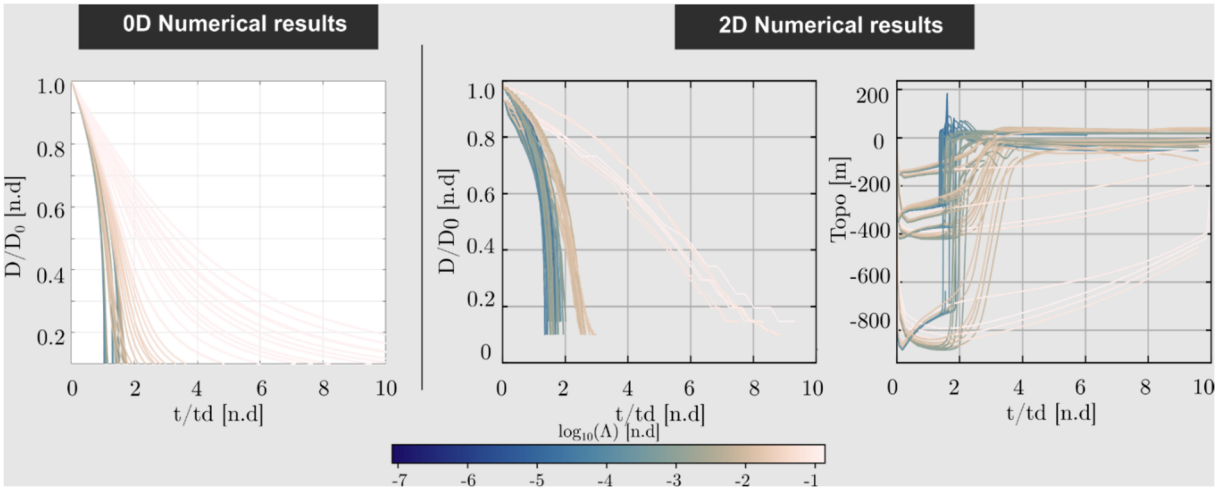

Fig. 3.1-8: **Left**: Evolution of the normalized thickness of the slab at the detachment depth with time. Time is scaled as a function of the characteristic timescales inferred by the slab rheological properties. **Middle**: normalized thickness evolution with respect to the scaled time of the 2D experiments; **Right**: Topography evolution with respect to the scaled time of the 2D numerical experiments. Colors denote the respective value of Λ.

g. *Numerical models of lower mantle dynamics using grain size evolution (J. Paul, G.J. Golabek, T. Katsura and H. Fei, in collaboration with A.B. Rozel and P.J. Tackley/Zurich)*

A crucial factor controlling the rheology and dynamics of the Earth's mantle is the grain size. An order of magnitude increase in grain size should increase the diffusion-creep viscosity, which is dominant in the lower mantle, by a factor of 100-1000. Until recently, the major limitation was the lack of experimental grain size evolution data on the lower-mantle mineral

assemblage of bridgmanite and ferropericlase. However, Fei *et al.* (2021) determined the grain-size evolution of the bridgmanite and ferropericlase mixture at 27 GPa and at 1400-2400 K. The new experimental data demonstrated that bridgmanite grain growth is significantly slower than olivine in the upper mantle.

Using the grain-size evolution data, we develop 2D annulus numerical models evolving self-consistently for 4.5 billion years using the finite volume code StagYY. The models assume a pyrolitic mantle consisting of 60 % olivine and 40 % pyroxene-garnet. The phase-transition depths, temperatures, densities, and Clapeyron slopes are calculated for olivine and pyroxene-garnet phases independently. An additional primordial layer is introduced at the base of the mantle to self-consistently produce thermochemical piles. The surface and core-mantle boundary temperatures are kept at 300 K and 4800 K, respectively. Keeping the above conditions similar, we test different models with (i) homogeneous grain growth rates based on the olivine data for the whole mantle (case I), (ii) homogeneous grain growth rates based on bridgmanite + ferropericlase data for the whole mantle (case II), (iii) heterogeneous grain growth rates based on olivine and bridgmanite + ferropericlase data in the upper lower mantle, respectively, to make the model more realistic (case III) and (iv) no grain size evolution (case IV). We also vary the yield strength in different models to understand the relations among the grain growth, yield strength, and the tectonic regime.

Case I models produce very large grain sizes in the whole mantle, making the lithosphere very strong, causing stagnant lid formation that warms up the lower mantle. As a result, the temperature-dependent viscosity dominates over the grain size-dependent viscosity in the lower mantle, making the lower mantle weaker. A weak lower mantle does not generate enough viscous stresses to break the lithospheric lid, and the model remains in the stagnant lid regime.

The case II models produce small lower-mantle grain sizes in the order of 1000 μm. In the upper mantle, the grain size becomes even smaller, a few 100 μm. Under these conditions, the stresses (~ 20 MPa) are sufficient to break the lithosphere. The models successfully evolve from the initial dripping mode into a plate-like mode.

In case III, the upper-mantle average grain size becomes slightly larger (≈ 500 μm) than in case II. The lower mantle generates enough viscous stresses to break the lithospheric lid. The initial dripping mode changes to a plate-like tectonic mode. This case as well as case II produces self-consistent thermochemical piles (Fig. 3.1-9). The piles form within ~ 2 billion years after the initiation of models. The grain size in the piles reaches 1000 μm or more, 2 to 3 times larger than the average lower-mantle grain size. This large grain size makes the piles 100 to 1000 times more viscous than in case IV, where no grain-size-dependent viscosity is implemented. We conclude that the thermochemical piles remain stable for ~ 300-400 million years due to the different grain growth rates in the upper and lower mantle, potentially explaining the long-lived LLSVPs at the core-mantle boundary.

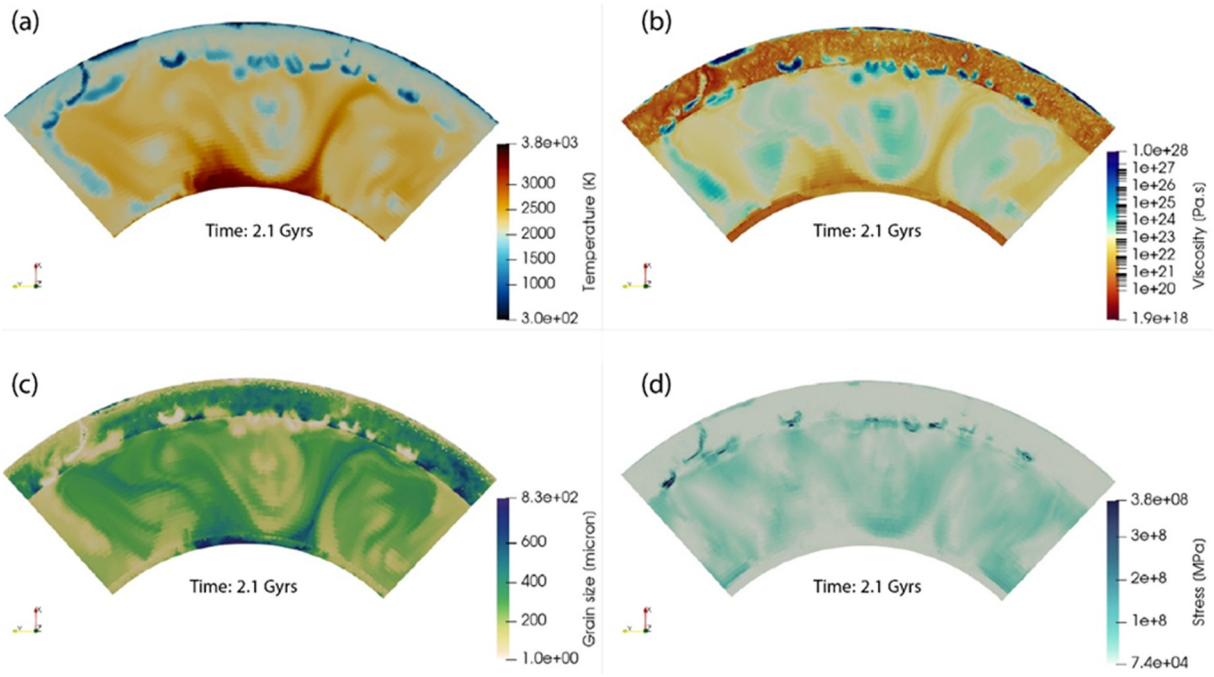

Fig. 3.1-9: Snapshots of (a) temperature, (b) viscosity, (c) grain size and (d) stress for a case III model at 2.1 Gyrs after the initiation. All the snapshots show the formation of piles at the base of the mantle identified by high temperature, low viscosity and large grain size. The snapshots show a transitional point from the initial dripping mode to the plate-like mode.

3.2 Geochemistry

Identifying when bodies in the early-formed solar system first started to fractionate to produce metallic cores is an important step in understanding planet formation. Chondritic meteorites contain a mixture of oxides, silicates, metal and sulphide phases that are some of the first materials to have condensed from the solar nebula. Achondrite meteorites, on the other hand, are igneous rocks formed through the melting and differentiation of chondritic parent bodies and have lost metallic phases as a result of core formation. The first two studies in this section concern another class of so-called primitive achondrite meteorites, which record an intermediate step in this differentiation process. While they are the products of melting or high-temperature metamorphism, they generally still contain traces of metals, and their study can, in principle, be used to understand the timing, mechanism and consequences of early core-formation. In the first of these studies, a number of primitive achondrite meteorites are examined that have been recently discovered in the Saharan desert. Based on mineralogical, geochemical, and Pb-Pb age data, it is found that they represent the first group of primitive achondrites to be identified that have formed in the outer region of the solar system, beyond the orbit where ice would have condensed and possibly even beyond Jupiter. They also appear to be caught in the process of core formation only one million years after the start of solar system formation. The following study also examines a group of primitive achondrites and provides a petrological basis through which to identify specific parent bodies, rather than employing oxygen isotope analyses, which require far more specialist equipment.

The next three studies are aimed at using stable isotopes of certain siderophile elements to study the conditions of planetary core formation and volatile loss. The Moon appears to be depleted in many volatile elements relative to the Earth, either due to vaporisation during the giant impact, or due to evaporation during the cooling of the Moon itself. Interestingly, in contrast to most other volatile elements, the isotopic signature of tin in lunar rocks is lighter than that of the bulk silicate Earth. To understand this conundrum, in the first of these studies piston-cylinder experiments were performed to determine the partitioning of tin isotopes between silicate melt and metallic iron-nickel liquid. It is found that isotopically light tin partitions into the iron-nickel liquid, implying that the anomalous tin isotopic signature of the Moon is not due to the lunar-core formation but rather due to vapour–metal partitioning during the assemblage of small, molten "moonlet" bodies. The following study describes the development of a large-volume multianvil assembly that can reach pressures compatible with the base of the Martian mantle, but can produce metal-silicate assemblages large enough for them to be separated and individually analysed for iron isotopes. The results are reported in the next study and show that metal-silicate equilibration at Martian mantle conditions does not fractionate iron isotopes. This result is actually consistent with the fact that the Martian mantle appears to have retained chondritic iron isotope ratios.

To better understand the distribution of boron within the Earth, molecular dynamics simulations were performed in the following study to constrain the partitioning behaviour and isotopic

fractionation of boron between molten iron and silicate melt at conditions relevant to core formation. It is found that boron, and preferentially its lighter isotope, starts to partition into the metallic phase at conditions compatible with a deep terrestrial magma ocean. This implies that Earth's core may store up to 50 % of global boron and provides an explanation for the isotopically light boron signature of oceanic island basalts that may originate from sources at the core-mantle boundary.

The following study seeks to determine the phase relations of a crystallising lower mantle assemblage, which is important for understanding fractionation within an early magma ocean. Many advances are required to achieve melting at lower mantle conditions in the multianvil press because temperatures of up to 4000 K must be achieved. Preliminary results indicate that the temperature interval over which crystallisation occurs at lower mantle conditions is smaller than previously determined, highlighting the need for multianvil experiments where the temperature distribution can be well controlled.

The next two studies examine how the compositions of mineral phases change with depth in the lower mantle. In the first of these, the partitioning of calcium and magnesium has been measured between bridgmanite and $CaSiO_3$-perovskite (now called davemaoite), phases which make up approximately 78 and 7 volume per cent of the lower mantle, respectively. A recent study proposed that the solubility of $CaSiO_3$ in the bridgmanite structure increases with pressure and temperature to a degree where $CaSiO_3$-perovskite would disappear from the lower mantle assemblage. In this re-examination, however, performed between 27 and 40 GPa, the solubility of $CaSiO_3$ in the bridgmanite structure is found to be very limited, such that $CaSiO_3$-perovskite is likely to be present throughout the bridgmanite stability field in the lower mantle. The following study examines how the Fe and Al contents of bridgmanite change with increasing pressure when they coexist with a more Al-rich phase. The results show that both elements increase in bridgmanite with depth due to pressure-induced changes in partitioning. However, at the highest pressure studied of 40 GPa, two coexisting bridgmanite phases are identified, one rich in iron and alumina and the other poor. Although the results are preliminary, this seems to imply that there may be regions of chemical immiscibility within the bridgmanite solid solution towards conditions of the mid mantle.

The distribution of phosphorous and rare earth elements (REE) within transition-zone and lower-mantle minerals is investigated in the following study by *Pausch et al.* It is found that at mid-transition-zone conditions, phosphorous is accommodated in an additional accessory phase, $Ca_3(PO_4)_2$ tuite, which is also a major carrier of REE. Towards the base of the transition zone and in the lower mantle, however, tuite is no longer stable and phosphorous, and REE's are mainly accommodated in $CaSiO_3$-perovskite.

The study by *Melai et al.* seeks to understand the origin of diamonds that contain inclusions of ferropericlase by examining the ferric iron and Fe(III) contents of ferropericlase as a function of composition, pressure, temperature and oxygen fugacity. Such inclusions have in the past

been considered to demonstrate a lower mantle origin due to ferropericlase being a dominant mineral there. In this study, however, it is shown that the ferric iron content of ferropericlase at conditions of diamond formation in the lower mantle would be much lower than the levels found for the majority of these inclusions. Many of them, in fact, are found to have ferric iron contents that are only consistent with formation in the upper mantle.

The next two studies examine minerals from eclogitic assemblages for their ferric iron contents, the first using eclogitic mineral inclusions in diamonds and the second from eclogitic xenolith rocks. Eclogites are high-pressure rocks formed through the metamorphism of subducted oceanic basalt. In the first of these studies, the redox state of eclogitic inclusions in diamonds from the Siberian craton is used to infer the nature of the medium from which the diamonds formed. The results indicate that this medium contained a mixture of carbon dioxide and water. Interestingly the rocks in which the diamonds were found appear to be more oxidised, likely an effect of alteration by permeating fluids or melts that affected the surrounding rocks after the diamonds had formed. This effect is further described in the following study, where such metasomatic activity appears to be responsible for the oxidation of garnet, to the extent that the garnets contain the highest levels of ferric iron ever found for such rocks.

The following contribution examines sheared peridotite xenoliths from the cratonic lithosphere, which are considered to have been deformed by the passage of the kimberlitic magmas that brought the rocks to the surface. Kimberlitic magmas degas and crystallise at the surface, and it is very difficult to determine their original volatile content. The mineral phases in these rocks, however, may record evidence for the water concentration in the kimberlitic melts with which they have interacted. The larger grains in the sample have been analysed using infrared spectroscopy and show low to moderate water contents. It is the sheared olivine assemblages that likely record interaction with the kimberlite melt, however, and these regions are too fine-grained for analysis with infrared spectroscopy and will be analysed later using an ion probe.

The next study concerns the contribution of subducted sediments to the trace element signature of arc magmas. Based on the similar lead isotopic ratios of arc magmas and subducted sediments, it has been proposed that the latter contribute significantly to the trace element signature of arc magmas, either via the generation of hydrous silicate melts, aqueous fluids, or diapirs ascending to the zone of mantle melting. In contrast, the Sr isotopic signature of arc magmas suggests that the sediment contribution is very low. To test whether aqueous fluids could explain these observations, diamond trap experiments are performed in this study using a piston-cylinder, to determine the partitioning of trace elements between saline aqueous fluids and a metapelitic starting material with the composition of average global subducting sediments. The results demonstrate that sediment-derived fluids are very Pb-rich and thus very efficient in imprinting a sedimentary Pb isotopic signature (in contrast to Sr), and that very small amounts of such fluids are sufficient to explain the sediment-like Pb isotopic signature of arc magmas.

The two following contributions deal with the fractionation of arc magmas. In order to extend the possibilities of crystallisation experiments in piston cylinder runs, two important modifications have been introduced by *Calvo et al*. Firstly, a zircon liner is introduced to prevent interaction of the sample with the noble metal capsule. This allows sulphur- and chalcophile element-bearing experiments to be conducted also at high oxygen fugacity, as the alternative is to use graphite liners which impose reducing conditions. Secondly, slow cooling rates of the order of 80 °C/day are used to generate large crystals and large interstitial melt pools also at low temperatures, allowing the determination of trace elements by laser ablation mass spectrometry and the determination of volatiles by infrared spectroscopy. The modal mineral abundances obtained in a crystallisation series conducted at 700-1200 °C and 1.2 GPa are similar to those obtained in previous, sulphur-free studies conducted without zircon liners, hence the presence of zircon does not significantly affect the phase relations. Using the same experimental approach, *Chang and Audétat* determined the liquid line of descent of S, Cl, H_2O and CO_2-bearing, mafic potassic magmas crystallising at 850-1150 °C and 1.0 GPa. In this way they are able to test whether the intermediate-to-felsic potassic magmas that produced economically important porphyry-Cu (Au) deposits in post-subduction settings, could be derived by fractional crystallisation from mafic potassic magmas, rather than via the commonly postulated mechanism of partial melting of lower crustal rocks. It was found that the experimental liquid line of descent perfectly matches the trend recorded in natural rocks, and that the ore-forming magmas were probably very rich in H_2O, S and Cl.

The next contribution focuses on titanium diffusion in quartz and its application to volcanological problems. Titanium diffusion chronology in quartz is an increasingly popular tool to reconstruct timescales of magma chamber formation and the triggering of volcanic eruptions. However, currently available experimental titanium diffusion coefficients in quartz differ by three orders of magnitude. To reconcile this problem, *Audétat et al.* constrained titanium diffusion coefficients in quartz phenocrysts from the climactic 1991 eruption at Mt. Pinatubo by dating tiny zircon inclusions next to titanium diffusion profiles measured at growth zone contacts in the quartz. The newly constrained titanium diffusivities were used to estimate the time elapsed between a conspicuous magma recharge event recorded by titanium-rich overgrowths and the eruption in 1991. The results suggest that the magma recharge event occurred 20-400 years before the 1991 eruption, which is 1-2 orders of magnitude longer than previous estimates.

The final contribution in this section deals with redox reactions in modern lake sediments. The trace element content of freshwater depends crucially on the biogeochemical cycling of iron, carbon and phosphorous, and in particular on the electron transfer between Fe(II) and Fe(III) oxides. In order to constrain the hosts of Fe(II) and Fe(III) in freshwater lake sediments, a Mössbauer spectroscopy study was undertaken by *McCammon et al*. on the uppermost 20 cm of sediments in a lake in Denmark. It was found that iron is hosted mainly in the form of nanoscale Fe(III) hydroxides in the upper parts of this profile, and as Fe(II) in the form of vivianite in the lower parts, suggesting an inorganic cause of the redox gradient and an important role of abiotic iron hydroxides in scavenging trace elements from the water.

a. *Early formation of primitive achondrites in an outer region of the protoplanetary disc. (A. Néri and A. Bouvier, in collaboration with N. Ma, W. Neumann, M. Trieloff, W. Schwarz and T. Ludwig/Heidelberg)*

Several equilibrated chondrite and achondrite meteorites (such as the ungrouped primitive achondrite Tafassasset) have been recently recovered from the Saharan desert. They have been linked to the altered CR1-3 chondrites based on their similar mass-independent anomalies in ^{17}O and ^{54}Cr isotopes. Four Tafassasset-like meteorites grouped as CR6 or CR7, and Tafassasset itself, were examined for their mineralogy and textures, and phosphate trace element compositions and SIMS Pb-Pb ages. We then carried out closure temperature and oxygen fugacity calculations and modelling of the parent body formation history. We identify in total 13 Tafassasset-related meteorites and propose that they represent the first meteorite group of carbonaceous primitive achondrites. We name this new group the Tafassites, which form a continuum from equilibrated petrological type 6 chondrites (termed T6) to partially molten type 7 primitive achondrites (T7) (Fig. 3.2-1A) and bear carbonaceous meteorite-like (C) mass-independent isotopic signatures.

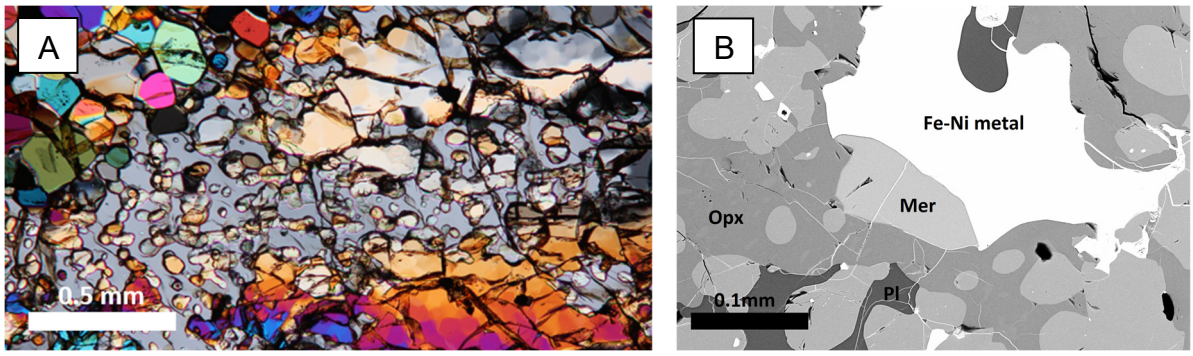

Fig. 3.2-1: A) Optical cross-polarised image (×10 magnification) of NWA 11561 T7 primitive achondrite with poikilitic texture, which variably contains olivine, low-Ca and high-Ca pyroxenes, interstitial plagioclase, Fe-Ni metal, troilite, chromite, and merrillite. B) Backscattered electron image of an area of NWA 11561 displaying Ol= olivine, Opx= orthopyroxene, Pl= plagioclase, Mer= merrillite and Fe-Ni metal.

Tafassite meteorites are characterised by: 1) a highly equilibrated texture ranging from porphyritic (T6 chondrite) to poikilitic/protogranular T7 primitive achondrite (Fig. 3.2-1A and B); 2) a mineralogy comprised of homogeneous FeO-rich olivine (Fa27-38), Ca-poor pyroxene (Fs_{22-30}), minor clinopyroxene (as exsolution lamellae when $T_{peak} > 1080$ °C), intermediate plagioclase ($An_{44-52}Ab_{46-53}Qr_{1-3}$, heterogeneous when disturbed by silicate partial melting) abundant Fe-Ni metal, troilite, Al-rich chromite ($\sim Mg_{0.2}Fe_{0.8}Al_{0.4}Cr_{1.5}Ti_{0.1}O_4$) and trace merrillite; 3) clear compositional differences in oxygen isotopic compositions between Tafassites, CR chondrites, and NWA 011 and NWA 6704 grouplets; 4) ancient retrograde metamorphic ages obtained by Pb-Pb phosphate dating between 4548 ± 16 Ma to 4560 ± 6 Ma

2σ (closure temperature 720± 50 K for grains of 25-65 µm diameter, and assuming a cooling rate of 10K/My); 5) nucleosynthetic anomalies (*i.e.*, ^{54}Cr, ^{17}O) in close similarity to carbonaceous chondrites.

Given their carbonaceous-like affinity, Tafassites therefore constitute the first early accreted chondritic meteorite group from an outer region of the protoplanetary disc, presumably close to the further CR feeding zone. They subsequently experienced extreme thermal metamorphism that spans the chondrite-(primitive achondrite) transition. Thermal numerical modelling indicates that the Tafassite parent body (TPB) accreted within 1.1(+0.3/-0.4) Myr after CAI formation into a > 50 km radius planetesimal before experiencing severe but rapid thermal annealing.

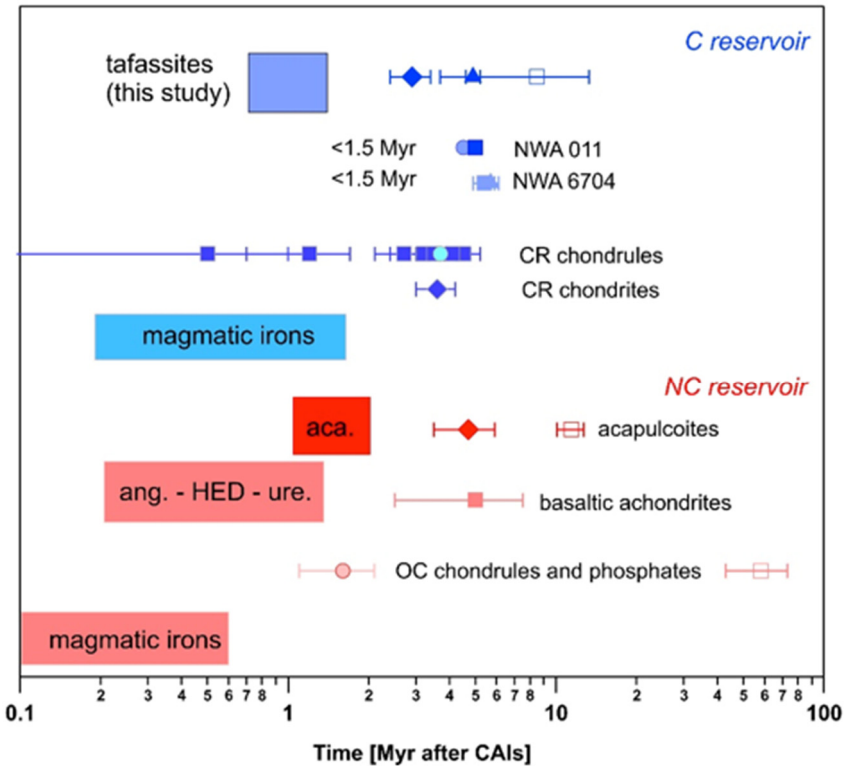

Fig. 3.2-2: Comparative chronology from CAI formation (U-corrected Pb–Pb average age of 4567.73 ± 0.81 Ma) of selected meteorite groups (data points) and modelled timing of accretion of their parent bodies (boxes) in the carbonaceous (C, blue) and non-carbonaceous (NC, red) reservoirs. Parent body accretion ages are from this study for Tafassites, and taken from literature for other relevant groups. Symbols: circle = Al–Mg; full diamond = Hf–W; triangle = Mn–Cr; square = phosphate Pb–Pb; full square = Pb–Pb.

We identified at least four parent bodies (PB) for Tafassites, NWA011 grouplet, NWA6704 grouplet, and CR chondrites. The PB accretion age of Tafassites, (1.1 +0.3/-0.4 My, likely comparable to NWA 011 and NWA 6704 grouplets) is similar to C magmatic irons and pallasites (0.9 +0.4/-0.2 My) and provides evidence for early accretion of rocky planetesimals

beyond the snow line and with coeval planetesimal formation between the inner and outer disc (Fig. 3.2-2). The divergent PB accretion ages and O, ^{54}Cr and ^{50}Ti isotopic anomalies for Tafassites and CR chondrites (1.1 +0.3/-0.4 vs. > 4.0 +0.5/-0.3 Myr) indicate a prolonged and multi-epoch duration of planetesimal formation in the Tafassite-feeding zone (related to the metal-rich carbonaceous chondrites CR, CH and CB) associated with limited radial mixing of building materials throughout the planetesimal formation period.

b. *Tissemouminites: A new group of primitive achondrites spanning the transition between acapulcoites and winonaites (A. Néri, in collaboration with A. Stephant/Rome and Milton Keynes, C. Carli/Rome, M. Anand/Milton Keynes, J. Davidson/Tempe, G. Pratesi/Rome and Firenze, T. Cuppone/Firenze, R.C. Greenwood/Milton Keynes and I.A. Franchi/Milton Keynes)*

Primitive achondrites are composed of different groups: acapulcoites-lodranites, winonaites, brachinites and ureilites. While brachinites and ureilites have very distinctive petrological characteristics, the boundary between winonaites and acapulcoites-lodranites does not seem so obvious. Hints of this are the numerous specimens that were initially classified within a given group and later reclassified into the other one, on the basis of unambiguous oxygen isotopic composition and/or cosmic ray exposure ages. Such somewhat regular misclassifications highlight several important points: 1) there is a strong need to revisit the petrological and geochemical criteria that distinguish winonaites and acapulcoites, 2) the peculiar nature of winonaites is not well understood.

To shed light on the difference between winonaites and acapulcoites, the petrological, chemical and isotopic characteristics of eight specimen were investigated: Dhofar 1222, NWA 090, NWA 725, NWA 1052, NWA 1054, NWA 1058, NWA 1463 and NWA 8614. Five of these were initially misclassified as acapulcoites or ungrouped achondrites. These meteorites were purposedly selected for their misclassification, their pristine state (chondrule bearing) and because their characteristics lie in between acapulcoites and winonaites. Interestingly, the oxygen isotope compositions of these eight samples are different and resolvable from that of acapulcoites and winonaites. Although the measurement of the oxygen isotope composition may not be accessible to all, it seems that this criterion remains unambiguous in defining groups of meteorites. However, to make classification more accessible, a combination of petrological and chemical criteria are proposed to distinguish acapulcoites, winonaites and this group of eight samples. The olivine fayalite content and FeO/MnO ratio, along with the potassium content of plagioclase, allows to separate of these three groups without the absolute necessity for oxygen isotope measurements.

Although closely related to winonaites, this new group of eight specimens seems to originate from a parent body that is distinct from both winonaites and acapulcoites. Literature isotopic data (*e.g.*, on molybdenum isotopes) support this hypothesis. This new group of primitive achondrite is proposed to be referred to as "tissemouminites", in reference to the village of Tissemoumine (Morocco), where NWA 725 was found, the first sample of this group that has been officially classified in the Meteoritical Bulletin.

c. *Experimental tin isotope fractionation: Volatile loss during Moon formation (R.C. Hin, in collaboration with C. Fitoussi and Q. Amet/Lyon and M.W. Schmidt/Zurich)*

The Moon most likely formed in the aftermath of a giant impact between a proto-Earth and a different planetary object (often referred to as Theia) that had approximately the present-day size of Mars. The Moon is depleted in volatile elements relative to Earth. This depletion is commonly thought to have resulted from the high temperatures that developed during the giant impact, which partially vaporised the Earth and its impactor. An unresolved issue is whether this volatile depletion occurred from the surface of a molten Moon as it slowly cooled, or whether it instead occurred at an earlier stage by interaction between a hot cloud consisting of vapour and condensates that are referred to as 'moonlets' (radii on the order of meters, as opposed to the modern Moon radius of ~ 1700 km) before these condensates eventually aggregated to form the Moon.

This issue has been investigated with stable isotope fractionation of moderately volatile elements, such as Zn, Ga, K. When compared to Earth, these elements are all characterised by a relative enrichment in their heavy isotopes on the Moon, which is indicative of chemical fractionation between a vapour phase and a condensate, confirming a setting in which volatiles could be lost during formation of the Moon but without discriminating between the two different settings described above. The isotopes of Sn have also been used to investigate volatile depletion on the Moon, but intriguingly the Sn isotope ratios of lunar rocks indicates enrichment in light instead of heavy isotopes relative to the bulk silicate Earth. This could be due to vapour-condensate interaction at chemical equilibrium if the vapour contains a more oxidised species of Sn compared to the condensate, where Sn would dominantly occur as Sn^0 in a metallic liquid. Core-mantle segregation could also be responsible for this signature, however, as Sn is a siderophile element and the lunar core may be very rich in Ni compared to Earth's core, which could affect the partitioning of isotopes between metal and silicate.

Augmenting previously performed analysis by Nuclear Resonance Inelastic X-ray Scattering (NRIXS), we have performed piston-cylinder experiments (1.5 GPa, 1400 °C) at the BGI to scope metal-silicate compositional systems with variable Ni content from 5 to 30 wt. %. We found systems in which we could maintain a constant oxygen fugacity (one log unit below the iron-wustite buffer), counteracting the more oxidising nature of Ni compared to Fe by the addition of increasing quantities of Si metal in starting materials with higher Ni contents. This constant oxygen fugacity was required to ascertain that the speciation of oxidised Sn did not change with increasing Ni content by an increased oxygen fugacity, because isotopic fractionation is a function of element speciation. Sample capsules were then prepared for runs in a centrifuging piston cylinder at ETH Zurich, Switzerland, again at 1.5 GPa and 1400 °C, to quantitatively segregate the liquid metal alloys from their coexisting silicate liquids (Fig. 3.2-3). Subsequently, element abundances in the quenched metal and silicate phases were determined by microprobe analysis at the BGI before the samples were dissolved for Sn isotope analysis at ENS Lyon, France.

We found that Ni-free metal is slightly enriched in heavy Sn isotopes, but the addition of Ni to the metal alloy changes this fractionation into an enrichment in light Sn isotopes in the metal. These results imply that core formation on the Moon has led to an enrichment of light Sn isotopes in the lunar core and correspondingly to an enrichment in heavy Sn isotopes in the lunar silicate rocks, which is opposite to the observed enrichment in light Sn isotopes on the Moon relative to Earth. In other words, lunar-core formation cannot explain the difference in Sn isotope composition between the Moon and Earth. Instead, we interpret our results as indicating that the Sn isotope composition of the Moon is most readily explained by fractionation between a vapour phase and liquid (Ni-bearing) metal. Such fractionation best fits in a setting in which molten 'moonlets' with metal exposed on their surface equilibrated with the vapour in which they resided in the earliest stages of the formation of the Moon, because a planetary object with the size of the present-day Moon could not support liquid metal at its surface as this metal liquid would sink too rapidly to its core.

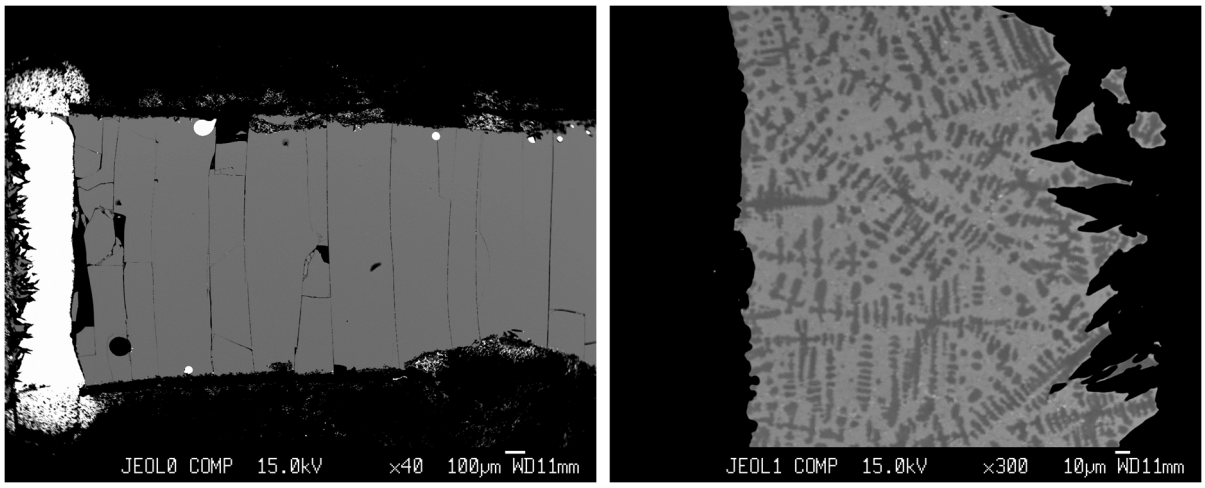

Fig. 3.2-3: Back-scattered electron images of an experiment with 30 wt. % Ni in a centrifuging piston cylinder apparatus. Left: quenched metal (white), separated from silicate glass (grey) in a graphite (black) capsule. Right: quench textures in the metal phase.

d. *The first measurements of isotopic fractionation at the conditions of Martian core–mantle differentiation (E. Kubik, A. Néri and A. Bouvier)*

Core formation occurred within deep magma oceans that formed early in the life of terrestrial planets, and importantly defined the composition of deep planetary reservoirs. Experimental isotopic fractionation of siderophile elements between metal and silicate constitutes a promising approach to (1) study the physical and chemical conditions of core formation, (2) constrain the chemistry of deep planetary reservoirs and (3) decorrelate core formation-induced isotopic fractionations from other isotopic effects occurring during planetary formation, such as post-nebular volatilisation.

The measurement of isotope compositions necessitates large sample volumes, containing around 1 μg of the studied element to characterise its isotopic composition. This requirement becomes a limiting factor above ~ 3 GPa because of the minimised experimental assembly volumes. For this reason, very few studies report metal–silicate isotopic fractionation factors above 3 GPa (only up to 7-8 GPa for Fe and Si and higher in the solid state). Therefore, our understanding of isotopic fractionation during core formation on large terrestrial planets such as Mars (and Earth), comes only from theoretical or spectroscopic means. Since the bonding environment of siderophile elements, which is the main factor driving isotopic fractionation, is very sensitive to pressure, quantifying the effect of pressure on equilibrium isotopic fractionation is critical for understanding the contribution of core formation recorded in the isotopic signatures of large terrestrial planets.

In order to measure metal–silicate isotopic fractionation of siderophile elements at conditions relevant to core formation on large terrestrial planets, two new multianvil assemblies, using 18 mm and 25 mm edge length octahedra, were designed and tested. These assemblies use a "box furnace" design, and are therefore capable of:

- hosting large-volume capsules permitting sufficient sample mass for isotope analysis (5.2 mm diameter and 7.2 mm height and 6 mm diameter and 8 mm height, respectively) – a typical run product is presented in Figure 3.2-4,
- obtaining pressures up to 20 GPa for the 18/8 configuration using the 5000-ton press
- heating at temperatures up to 3000 K with a $LaCrO_3$ box furnace, with more efficiency than standard assemblies,
- reducing considerably the thermal gradients

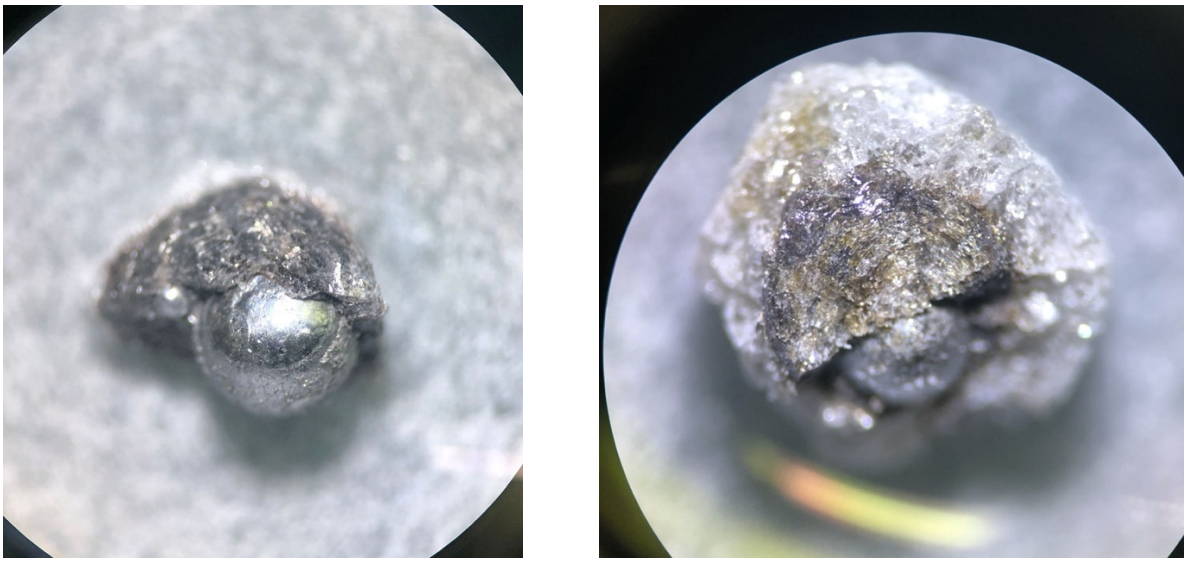

Fig. 3.2-4: Photos of typical run products of fully equilibrated experiments performed at 11 and 14 GPa, respectively. The silicate phase is visible surrounding a metal sphere (approximately 1.4 mm).

Therefore, these assemblies allow the P–T conditions at which Mars' core formed to be achieved. They will be used to assess the effect of core formation on the isotopic signatures of planetary mantles at conditions relevant to large terrestrial planets. The first isotopic results were measured in June 2022 at ETH (Zurich) (see the following contribution).

e. *Core-mantle iron isotope fractionation within large terrestrial planets (E. Kubik and A. Bouvier, in collaboration with P.A. Sossi/Zurich)*

Iron isotopes exhibit significant variability amongst inner solar system bodies as traced by the compositions of their respective mantles. In particular, the mantles of the Earth and Moon have heavy signatures compared to those of Mars and Vesta, which are chondritic. Core formation is a process that has been invoked to contribute to establishing these signatures. However, existing experiments have been performed at pressures (< 7.7 GPa) that are lower than those expected to have characterised core formation on Earth. Indeed, structural changes occurring in metallic and silicate liquids as pressure increases may cause isotopic fractionation. For instance, a Fe phase transition at 5.2 GPa is reported to have a strong effect on the partitioning behaviour of siderophile elements. These structural changes modify the bonding environment of Fe, which is the main driver of equilibrium isotopic fractionation, and therefore have the potential to influence the distribution of Fe isotopes between metal and silicate. However, these processes are very poorly understood due to a lack of experimental isotopic fractionation data at high pressure.

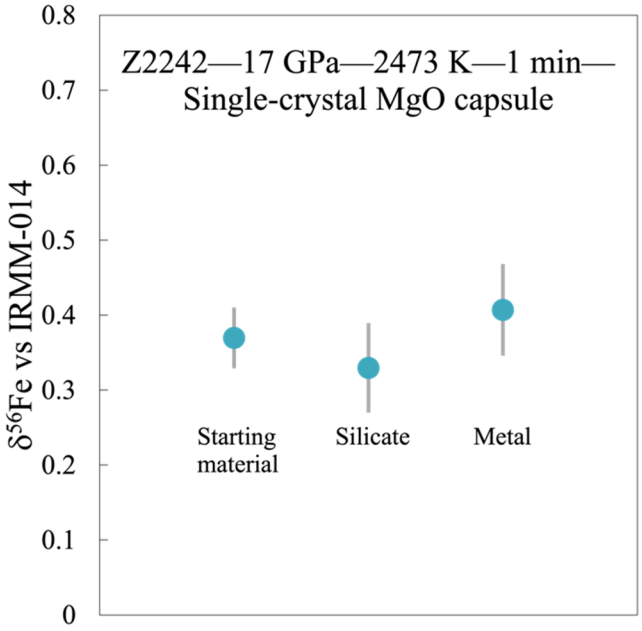

Fig. 3.2-5: Experimental δ^{56}Fe compositions from the different parts of a single experiment. Z2242 was performed at 17 GPa and 2473 K for a duration of 1 minute. The Fe isotopic compositions in the metal, silicate and initial starting material are identical within error (2 standard deviations on repeated isotopic measurements).

Stable isotopic measurements of experimental phases require a large sample volume, which becomes a challenge above 3 GPa. A new method was established to use the 5000-ton press with custom-made assemblies allowing for a large sample charge to experience pressures up to 20 GPa and temperatures up to 3000 K (see previous contribution).

In this study, we aim to measure the Fe isotopic fractionation between liquid metal and liquid silicate from 2 to 17 GPa and from 1800 to 2473 K. Preliminary measurements on a single experiment performed at 17 GPa show that isotopic fractionation between metal and silicate is very limited, as the silicate and the metal phases have Fe isotopic compositions that are within error of each other and both identical with the starting material composition (Fig. 3.2-5). This result is in good agreement with the chondritic iron isotopic signature inferred for the Martian mantle. Our measurements across a 15 GPa range covering the estimated P-T conditions for Martian core formation contribute to clarifying the controls on the variability of the Fe isotopic compositions in inner solar system planetary bodies by isolating the effect of core formation.

f. *Possible control of Earth's boron budget by metallic iron (L. Yuan and G. Steinle-Neumann)*

Boron (B) is an incompatible, lithophile element, being depleted in the upper mantle (< 0.2 µg/g), and being enriched in the oceanic crust by orders of magnitude (up to 200 µg/g). At the same time, its two isotopes, ^{11}B and ^{10}B, are highly fractionated in geological reservoirs ($\delta^{11}B = (^{11}B/^{10}B)_{sample}/(^{11}B/^{10}B)_{standard} - 1$, values given in ‰) with, for example, average compositions of $\delta^{11}B = +39.6$‰ in seawater, and $\delta^{11}B = -7.1$‰ in mantle-derived rocks. Boron is thus often used as a tracer of recycled crust in the mantle because minor additions strongly alter its B isotopic signature. Recent petrologic studies demonstrating that titanium diboride ($TiB_{2)}$ can crystallise from metallic melts at low oxygen fugacity (fO_2) suggest that metallic iron may exert an important control on Earth's boron distribution, given that low fO_2 likely governed core formation. As metallic iron is present predominantly in the core and likely at weight percent level throughout the lower mantle, its impact on Earth's boron budget merits consideration. To establish the boron content of Earth's core, its metal–silicate partitioning at high-pressure/-temperature (P–T) conditions during core formation must be known. In this study, we performed density functional theory (DFT) molecular dynamics (MD) simulations with boron in metallic and silicate melts to determine its partitioning behaviour and isotopic fractionation at 10-130 GPa and 3000-5000 K, covering the P–T conditions of core formation. We consider the partitioning of both elemental B and B_2O_3, reflecting reduced and oxidised magma ocean conditions, respectively, and integrate the results in core formation models.

We predict that the behaviour of boron changes from lithophile to siderophile with increasing P, with the calculated boron partitioning coefficients ($D^{m/s}$) between liquid metal and silicate changing from $\log_{10}D^{m/s} \leq -0.8$ at 10 GPa and 3000 K to $\log_{10}D^{m/s} \geq 3.7$ at 130 GPa and 5000 K (Fig. 3.2-6). We further predict that the silicate becomes enriched in the heavier boron isotope by > 1‰ relative to metal at these P–T conditions. Our results suggest that Earth's core may contain > 50 % of Earth's boron budget, and that high boron contents in deep diamonds and

isotopically light boron in oceanic island basalts may reflect contributions from metallic reservoirs rather than crustal subduction and recycling.

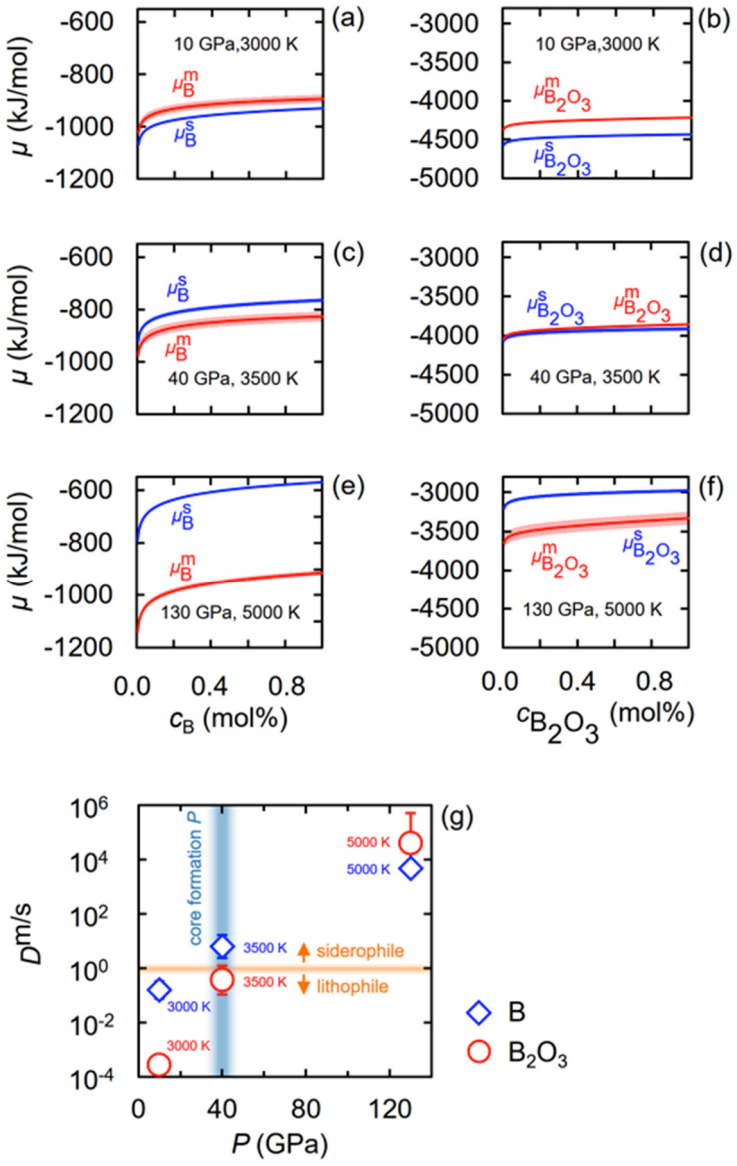

Fig. 3.2-6: Chemical potentials (μ) and partitioning coefficients of boron between metallic iron and silicate melts ($D^{m/s}$). Chemical potential of B (a, c, e) and B_2O_3 (b, d, f) in silicate (blue) and iron (red) as a function of boron content ($c_{B\ (or\ B2O3)}$ in mol. %) at three different P–T conditions. (g) Partition coefficient $D^{m/s}$ (on a log scale) as a function of P determined by equating μ in each phase. The vertical band (blue) shows the expected P during core–mantle segregation.

g. *The melting relations of primitive peridotite under lower-mantle conditions up to 35 GPa using advanced multianvil techniques (N. Martirosyan, H. Fei, A. Chanyshev and T. Katsura)*

The melting relations of peridotite under lower-mantle conditions are essential for modelling the early chemical evolution of the mantle in the primordial Earth. The Earth's mantle experienced extensive melting in its early history caused by the giant impacts that occurred during planetary accretion, radiogenic heating from short-lived radioisotopes, and core formation, leading to the formation of a deep magma ocean. Fractional crystallisation of a magma ocean and gravitational differentiation may have produced an early stratification of the mantle, which determined its initial compositional structure. The present-day composition

would then be the result of chemical evolution from this initial structure. Although the melting relations of peridotite under deep-mantle conditions have been extensively investigated using multianvil presses and diamond anvil cells (DACs), the phase relations above 22 GPa are still not well established and solidus/liquidus temperatures differ dramatically from study to study. This results from the steep temperature gradients, under which melt instantaneously segregates to the highest-temperature region of the sample chamber. Such segregation leads to a misinterpretation of the melting sequence.

In this project we conduct peridotite melting experiments in multianvil presses at lower mantle conditions and pressures above 23 GPa. Technical innovations are being developed and implemented to overcome limitations of the mult-anvil technique *i.e.*, limits in temperature and pressure generation and the steep temperature gradient within the sample. Ultra-high pressures are being generated using tapered carbide anvils with high hardness, in which the three faces around the truncation are sloped to compensate for the deformation of the anvils associated with the high-pressure generation. With a truncation size of 4.0 mm, the achievable highest pressure will be around 35 GPa. This will allow the study of peridotite melting to be extended by 11 GPa, compared to previous multianvil experiments.

The highest experimental temperatures reported for the widely used $LaCrO_3$ or Re heaters are around 2800K. This is sufficient for peridotite melting below 25 Gpa; however, a further increase in pressure will require higher temperatures due to melting temperature increasing strongly with increasing pressure. A boron-doped diamond heater is being designed and implemented to generate ultrahigh-temperatures of up to 4000 K, which will be required to perform melting experiments at 35GPa, where the liquidus temperature has been reported as 3850 K. Furthermore, a new "zero-temperature-gradient" furnace design that allows a homogeneous temperature distribution to be achieved will be used. In this design, heater rods are placed at both ends of a short cylindrical heater to eliminate the axial heat flow.

We have conducted preliminary experiments for the "KLB-1" peridotite composition at 12-25 GPa using a zero-temperature-gradient furnace technique. While the liquidus temperature is in relatively good agreement with the phase diagram determined in previous studies, the solidus is higher by 40-60 °C depending on the pressure. Furthermore, the temperature interval of the liquidus and solidus obtained by these preliminary experiments indicates a solidus temperature interval that is much smaller than the 100 K proposed in previous studies. These preliminary results demonstrate that the melting relations of primitive peridotite are still uncertain and further experimental efforts are necessary.

h. *Limited intersolubility of Ca and Mg between bridgmanite and $CaSiO_3$-perovskite in the lower mantle (L. Wang, N. Miyajima, F. Wang and T. Katsura)*

Bridgmanite and $CaSiO_3$-perovskite, respectively, are the first and third most abundant minerals in the Earth's lower mantle. The intersolubility of Ca and Mg between these two minerals is still under debate. Some studies indicated limited intersolubility, while others

suggested a complete dissolution of $CaSiO_3$-perovskite into bridgmanite at lower mantle conditions. This controversy leads to different explanations of the physical properties of the lower mantle, such as density, elasticity, and viscosity, accordingly modifying our understanding of the nature and dynamics of the Earth's interior. Therefore, it is essential to determine the intersolubility of bridgmanite and $CaSiO_3$-perovskite.

The intersolubility of Ca and Mg between bridgmanite and $CaSiO_3$-perovskite can be affected by the temperature, pressure, and bulk compositions of the system. Previous studies showed an increase in intersolubility with temperature but reported no robust pressure and composition dependence. Because $FeAlO_3$ is the second component in bridgmanite, investigating the effect of $FeAlO_3$ content and pressure dependence is essential to clarify the phase relation of the Earth's lower mantle.

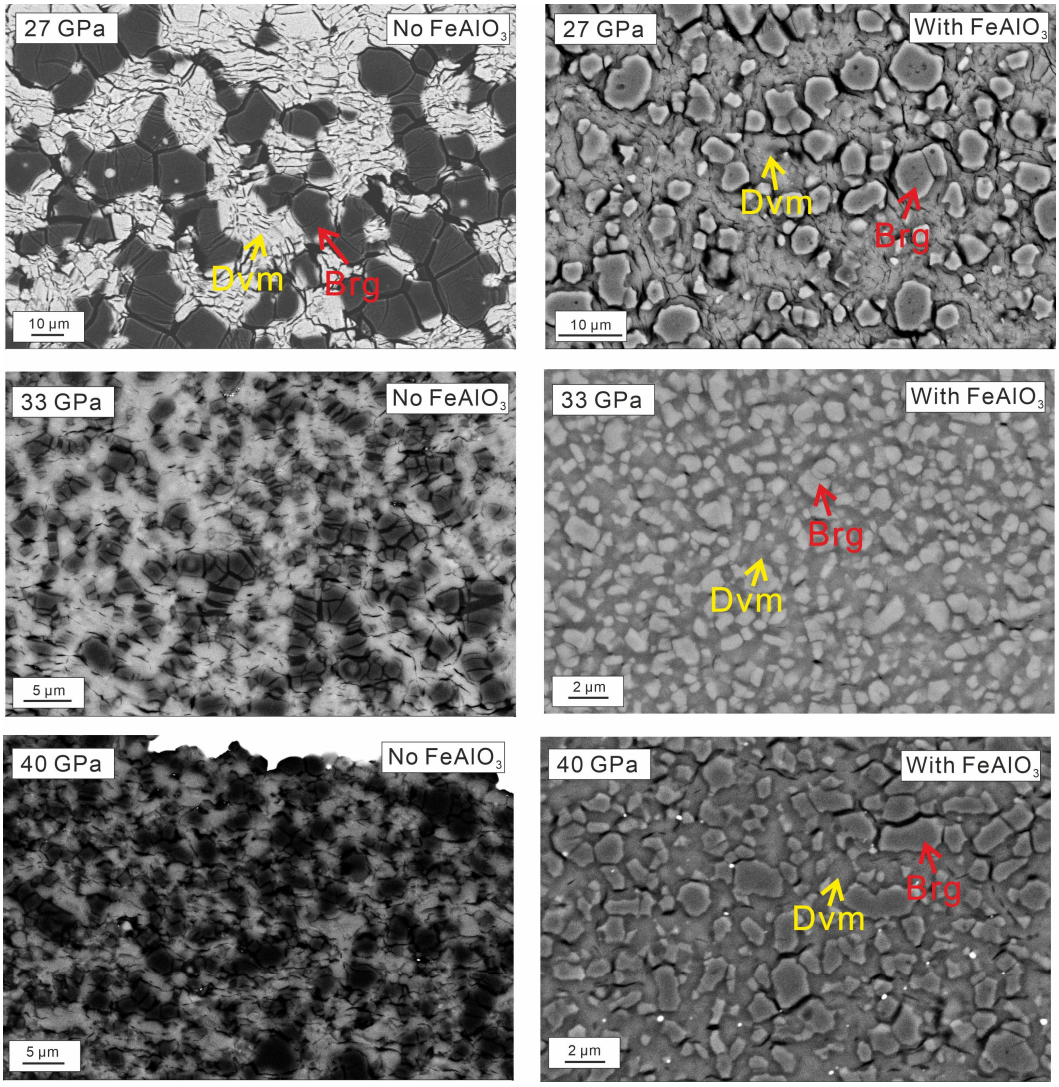

Fig. 3.2-7: Backscattered electron images of run products at different pressures. Both bridgmanite and high-pressure $CaSiO_3$-perovskite (davemaoite) can be clearly seen at different pressures and compositions.

This study determined the pressure and $FeAlO_3$ dependence on the intersolubility of bridgmanite and $CaSiO_3$-perovskite at pressures of 27 to 40 GPa at a constant temperature of 2300 K using a multianvil press. Two compositions of $MgSiO_3$:$CaSiO_3$ = 1:1 and $MgSiO_3$:$FeAlO_3$:$CaSiO_3$ = 3:2:5 were examined. SEM images clearly show the existence of two phases in all products (Fig. 3.2-7). TEM-EDS analyses indicate a decrease in the $CaSiO_3$ content of bridgmanite in both systems with increasing pressure. The $FeAlO_3$ component only slightly enhances the $CaSiO_3$ content of bridgmanite: adding the $FeAlO_3$ component increases the $CaSiO_3$ content of bridgmanite from 0.04(2) to 0.3(2) mol. % at 40 GPa (Fig. 3.2-8). The $MgSiO_3$ content of $CaSiO_3$-perovskite decreases with increasing pressure from 1.8(7) to 0.06(8) mol. % in the $FeAlO_3$-free system, and from 1.2(5) mol. % mol to an immeasurably small value in the $FeAlO_3$-bearing system. We conclude that, even with the presence of a $FeAlO_3$ component in bridgmanite, the intersolubility is limited and remains nearly constant at different pressures. Thus, bridgmanite and $CaSiO_3$-perovskite should coexist in the lower mantle, and $CaSiO_3$-perovskite is the host mineral of large ion lithophile elements such as Ca in the lower mantle.

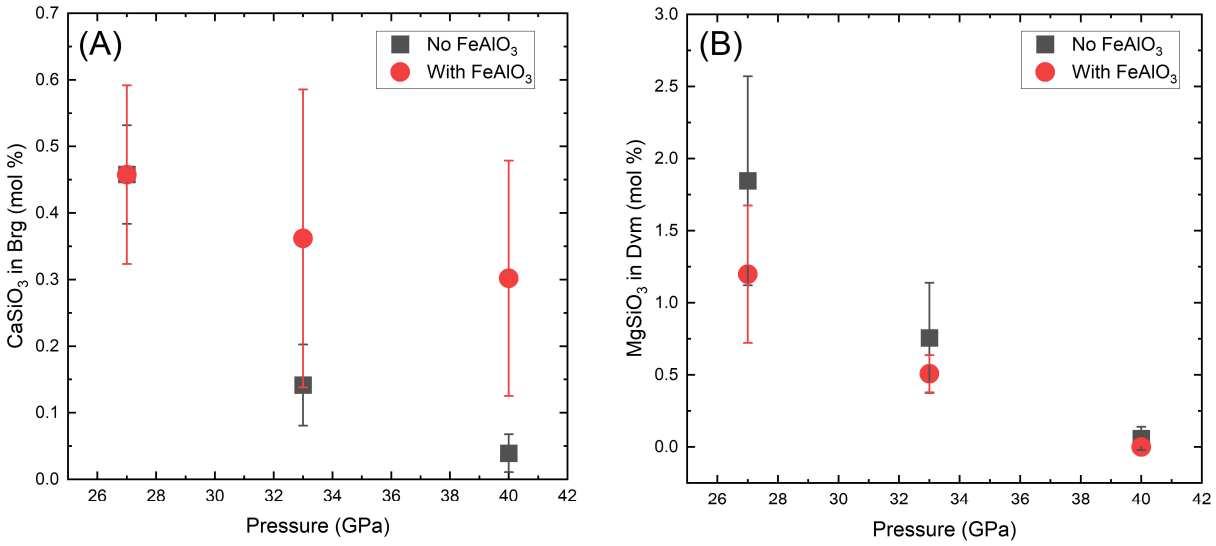

Fig. 3.2-8: Intersolubility of bridgmanite and davemaoite at 2300 K and different pressures: (A) $CaSiO_3$ solubility in bridgmanite. (B) $MgSiO_3$ solubility in davemaoite.

i. *Chemistry of bridgmanite coexisting with ferropericlase and $MgAl_2O_4$ under reducing conditions up to 40 GPa (E.J. Kim, H. Fei, K. Nishida, N. Miyajima and T. Katsura)*

Bridgmanite is the most abundant mineral in the lower mantle. While the properties of bridgmanite have long been studied to understand the lower mantle, one issue that remains unresolved is how the redox state of Fe in bridgmanite changes with increasing pressure. Previous studies on the redox state of Fe in bridgmanite reported that the fraction of Fe^{3+} is ~ 60-70 % of total Fe even under reducing conditions at 26 GPa. A recent diamond anvil cell

study showed that the Fe^{3+} content in the bridgmanite decreases drastically to ~ 10 % of total Fe with increasing pressure from 26 to 50 GPa and then increase to ~ 60 % upon further compression. The role of Al on the incorporation of Fe^{3+} in bridgmanite is also not well understood at pressures above 26 GPa. In this study, we aim to understand how the chemical composition of bridgmanite coexisting with ferropericlase and the $MgAl_2O_4$ CF-phase, changes under reducing conditions between 27 to 40 GPa by using the multianvil apparatus. The presence of the $MgAl_2O_4$ CF-phase should ensure that bridgmanite contains the highest possible Al concentration at any conditions.

MgO, Fe_2O_3, Al_2O_3 and SiO_2 oxide were mixed and ground using ball-milling machine at the Earthquake Research Institute, the University of Tokyo. Nano-powdered starting materials were dried in the gas-mixing furnace at 680 °C for 3 h to reduce all Fe into Fe^{2+}. Iron metal was added and ground together with the starting materials to produce reducing conditions during the experiments. High-pressure samples were synthesised at 27, 33, and 40 GPa using the IRIS-15 press at the BGI. TEM-EDS analysis was performed using a transmission electron microscope (FEI Titan G2 80-200 S/TEM) for samples synthesised at 40 GPa.

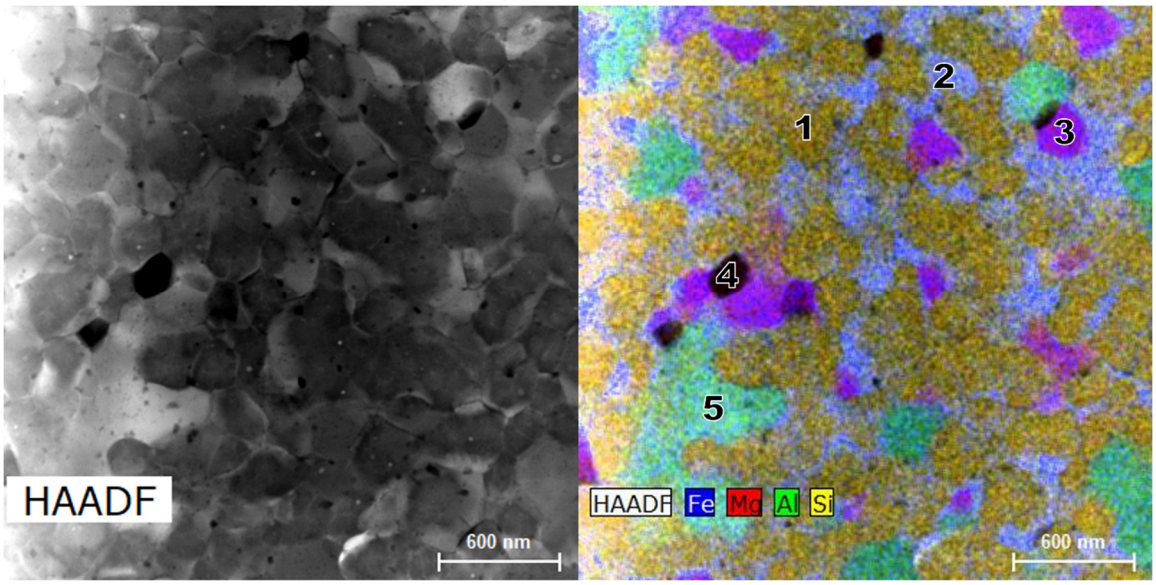

Fig. 3.2-9: Scanning transmission electron microscopy (STEM) images of an Al-rich sample synthesised at 40 GPa: (left) a high-angle annular dark-field (HAADF) image of grains. The average grain size is 300 nm. (right) a STEM-EDS mapping of Fe and Si in the corresponding HAADF image. The numbers in the figure indicate 1. Fe-poor bridgmanite, 2. Fe-rich bridgmanite, 3. ferropericlase, 4. magnesite, and 5. calcium-ferrite-like $MgAl_2O_4$, respectively.

The Al-rich composition employed produced bridgmanite and ferropericlase coexisting with the $MgAl_2O_4$ CF-phase at 27 GPa. While Fe metal droplets were observed in the products at 27 GPa, they disappeared from the assemblage formed from the same composition at 33 GPa. In

addition to the absence of Fe droplets, above 33 GPa the proportion of ferropericlase decreases significantly. Based on electron microprobe analysis totals, the sample from 33 GPa appears more reduced than that at 27 GPa, with the phases containing more Fe^{2+}. The sample synthesised at 40 GPa has a very small grain size (100-300 nm), so that only TEM analysis was possible. The TEM-EDS mapping showed four different phases at 40 GPa: Fe-poor and Fe-rich bridgmanite, CF-phase $MgAl_2O_4$, ferropericlase, and magnesite. The higher Fe bridgmanite composition was also coupled to a higher Al content. The presence of ferropericlase is observed for the sample at 40 GPa from the TEM-EDS analysis, but the proportion of ferropericlase is less than 5 %, which is much smaller than at 27 GPa (~ 20 %). The lower ferropericlase proportion at high pressure is most likely due to a reaction between the three phases that also increases the Al-content of bridgmanite at the expense of the CF phase. While further analysis is needed, it is possible that above 30 GPa, *i.e.*, towards mid-mantle conditions, as the Al content of bridgmanite increases, two coexisting compositions become stable, an Fe-Al-rich bridgmanite and an Fe-Al-poor bridgmanite. This could have important implications, particularly for the phase relations of assemblages produced by the subduction of oceanic crust.

j. *Phosphorus in the deep Earth: Volatile and trace element transport through the transition zone into the lower mantle (T. Pausch and J. Vazhakuttiyakam/Innsbruck; A.C. Withers, T. Ludwig/Heidelberg; B. Joachim-Mrosko and J. Konzett/Innsbruck)*

Phosphorus and volatiles bound in Ca-phosphates affect processes in the Earth's interior, including partial melting and melt migration, element partitioning and redistribution. Apatite, $Ca_{10}(PO_4)_6(OH)_2$, is the main phosphorous carrier into and within the upper mantle due to its frequent presence in subducting lithosphere and in subcontinental lithospheric mantle, and it is also a volatile and incompatible trace element carrier of eminent importance. Beyond the upper pressure stability limit of apatite, the anhydrous Ca-phosphate tuite, $Ca_3(PO_4)_2$, may take over the role of an important host for incompatible trace elements and phosphorus. The aim of this study is to investigate the P-T stability of tuite and its role as P, volatile and incompatible trace element carrier and storage site in the deep silicate Earth including the entire lower mantle.

We investigated the stability field, phase relations and composition of tuite in a peridotitic bulk composition at upper-to-lower mantle transition zone P-T conditions and the trace element partitioning between tuite and coexisting solids and partial melts. For this purpose, fourteen multianvil experiments were performed between 15 to 33 GPa and 1600 to 2000 °C. For the experiments a synthetic peridotite, based on the composition of a moderately fertile spinel lherzolite, was used. This peridotite was doped with 3 % synthetic β-$Ca_3(PO_4)_2$, 1 % of a trace element mix containing a range of HFSE, LILE and REEs, and approx. 2200 µg/g of Br and Cl each.

The coexisting phases that are stable within this P-T range include tuite, majoritic garnet, ringwoodite, forsterite, clinoenstatite, bridgmanite, davemaoite ($CaSiO_3$-perovskite),

ferropericlase, and melt. Tuite breaks down between 1700 and 1750 °C at 20 to 25 GPa and between 1750 and 1800 °C at 15 GPa, which yields a negative slope for the tuite-out reaction. SIMS data show that davemaoite and tuite incorporate significant amounts of REE in their lattice structures. At 20 GPa/1600 °C, REE_{tuite}/REE_{dam} ratios are 0.17 for Ce, 0.28 for Gd, and 0.09 for Lu. At 25 GPa/1600 °C, these ratios are 0.09, 0.09, and 0.04, respectively. Both tuite and davemaoite strongly fractionate LREE, resulting in steep chondrite-normalised REE-patterns (Fig. 3.2-10). At 20 GPa/1600 °C, for example, Ce_N/Lu_N ratios are 21.8 and 11.2 for tuite and davemaoite, respectively. This partitioning behaviour and the typical modal abundance indicate that davemaoite is likely to be the major host for REE in primitive mantle, whereas tuite is an additional important REE-carrier and the most important P-carrier in metasomatically altered mantle.

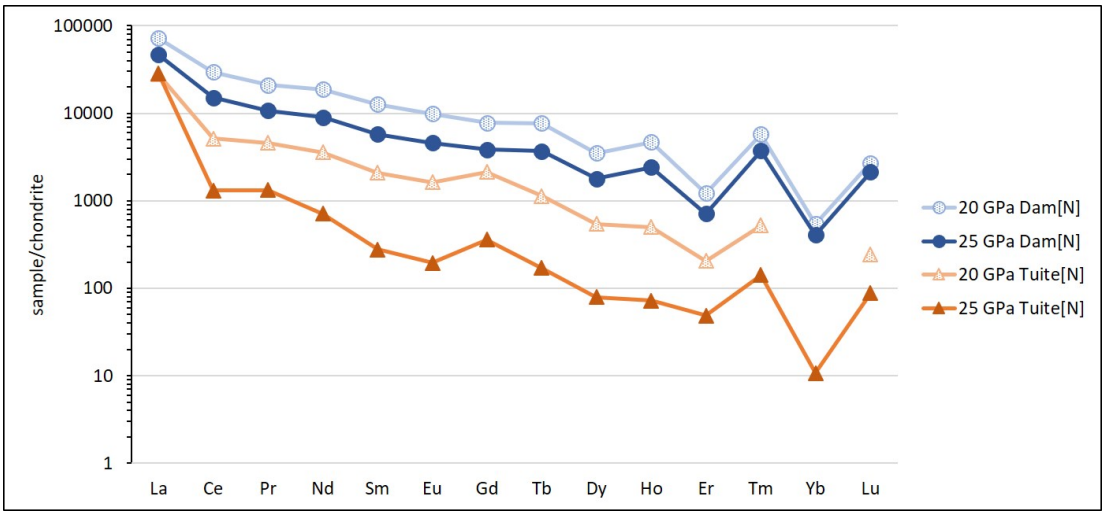

Fig. 3.2-10: Chondrite-normalised REE contents of tuite and davemaoite (Dam) at 20 and 25 GPa at 1600 °C.

k. *The oxygen fugacity and entrapment conditions of sublithospheric diamonds containing ferropericlase inclusions (C. Melai, D.J. Frost, T. Boffa Ballaran and C.A. McCammon)*

Ferropericlase is the second most abundant phase in the lower mantle and one of the more common minerals found as inclusions in sub-lithospheric diamonds. In fact, its presence has often been used to argue that the diamonds in which it is included come from the lower mantle. It would be possible, however, for such inclusions to form in shallower portions of the mantle from compositions that had lower silica contents than the typical mantle. The Mg/(Fe+Mg) ratios of such inclusions, which vary between approximately 0.35 and 0.9, seem to already indicate variations in the bulk compositions from which the inclusions formed. The Fe^{3+}/Fe_{tot} ratios of ferropericlase inclusions range up to ~0.12, which raises the possibility of being able to calculate the oxygen fugacity at which these diamonds formed. Moreover, in several transmission electron microscopy investigations of ferropericlase inclusions, coherent

nanometer-sized exsolutions of Fe^{3+}-rich oxides, belonging to the magnetite-magnesioferrite solid solution have been identified. Their presence indicates that conditions changed after entrapment such that the Fe^{3+} content of ferropericlase reached saturation, forcing the exsolution of a coexisting Fe^{3+}-rich oxide. The formation of additional Fe^{3+}-rich oxide delineates the ferropericlase stability field with respect to oxygen fugacity (fO_2). Knowledge of the fO_2 and ferropericlase Fe^{3+}/Fe_{tot} ratio at which this occurs may not only help to understand post-entrapment processes but would provide vital data to allow the fO_2 of entrapment to be determined from the Fe^{3+}/Fe_{tot} ratio. To date, there are no data on the Fe^{3+}/Fe_{tot} ratio of ferropericlase at conditions where it coexists with a more Fe^{3+}-rich oxide, such as phases along the magnetite-magnesioferrite solid solution. This is further complicated by the fact that at pressures above approximately 8 GPa magnetite-magnesioferrite phases undergo phase transformations to higher pressure oxides.

In this study, multianvil experiments were performed between 1 atm and 30 GPa and at 1200-1800 °C in order to determine the Fe^{3+}/Fe_{tot} ratio and fO_2 at which ferropericlase coexists with an Fe^{3+}-rich oxide. Ferropericlase starting compositions ranging between $(Mg_{0.86}Fe_{0.14})O$ and FeO were ground with differing proportions of Fe_2O_3. Pt powder was added to act as a redox sensor, and minor amounts of Ni, Cr, Mn and Na were also added. The recovered run products were then analysed using scanning electron microscopy, electron microprobe, Mössbauer spectroscopy, transmission electron microscopy (TEM) and X-ray diffraction. Ferropericlase was found to coexist with magnetite-magnesioferrite (O4) solid solution up to approximately 10 GPa and with $Mg_2Fe_2O_5$-Fe_4O_5 (O5) solid solution at higher pressures. For near Fe end-member compositions, Fe_5O_6 was produced. All samples that were investigated with the TEM showed that ferropericlase contains a nm-scale coherent exsolution of magnetite-magnesioferrite. At pressures above 10 GPa the grain size of the exsolution decreases to approximately 5 nm. The exsolution likely occurs on quenching as the solubility of Fe^{3+} in ferropericlase drops with temperature. The exsolution complicates Mössbauer spectroscopy determinations of the ferropericlase Fe^{3+}/Fe_{tot} ratio, as the nanocrystalline exsolution appears as a broadened O4-like sextet. Nonetheless, in most instances, it was possible to separate the contribution of the nm-phase from the signal arising from the coexisting O4 phase in the Mössbauer spectra. This allowed the combined Fe^{3+} content of the original ferropericlase, before exsolution, to be back-calculated. The recombined original Fe^{3+}/Fe_{tot} ratio of several ferropericlase samples was also determined with electron energy loss spectroscopy (EELS) using the TEM.

As shown in Figure 3.2-11, the Fe^{3+}/Fe_{tot} ratio of ferropericlase, coexisting with O4 phases below 10 GPa and O5 phases above, decreases with increasing pressure. The curves define the maximum amount of Fe^{3+} that can exist in ferropericlase at any conditions. Using equilibria involving ferropericlase and both Fe-Pt alloy and the O4 and O5 phases it is also possible to calculate the fO_2 at which these phases coexist and to calibrate a thermodynamic model to describe the ferropericlase Fe^{3+}/Fe_{tot} ratio at conditions up to 30 GPa. Ferropericlase inclusions in diamonds have Fe^{3+}/Fe_{tot} ratios within the range 0.02 to 0.12. The decrease in the solubility

limit of Fe^{3+} in ferropericlase with pressure (Fig. 3.2-11) means that it is unlikely that any of these inclusions were produced in the deep lower mantle. A further upper limit to the fO_2 at which an assemblage of ferropericlase and diamond could have been formed is defined by the additional stability of magnesium-rich carbonate. The results of the model indicate that these fO_2 conditions are met for many of the ferropericlase inclusions found in diamonds, only at upper mantle conditions, *i.e.*, ferropericlase inclusions with Fe^{3+}/Fe_{tot} ratios > 0.07 are too oxidised to have been in the diamond stability field at depths greater than the upper mantle.

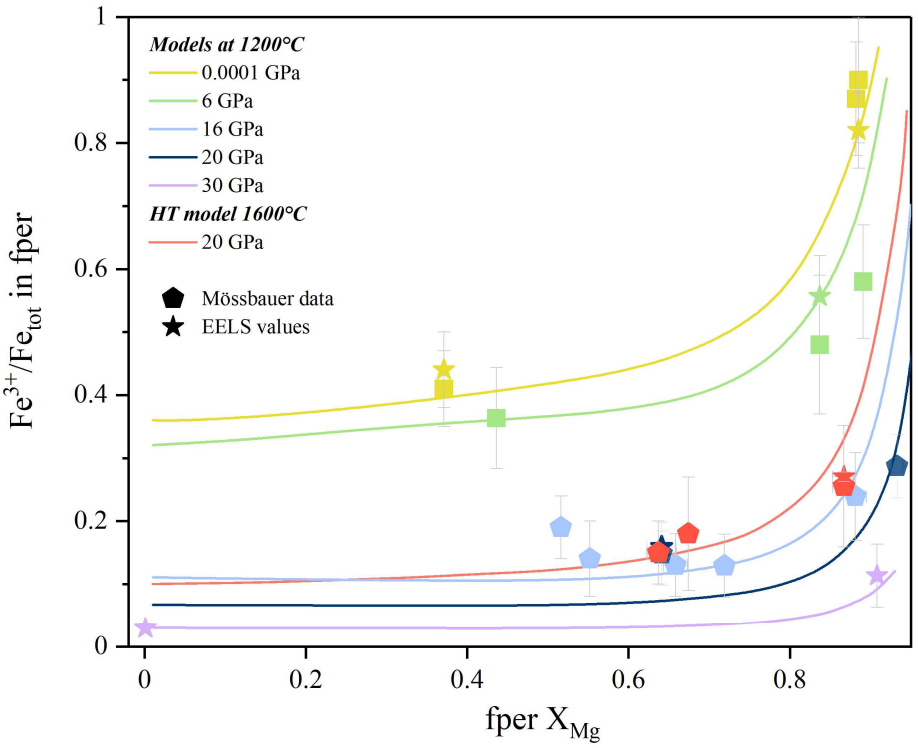

Fig. 3.2-11: Experimental results showing the Fe^{3+}/Fe_{tot} of ferropericlase as a function of the Mg/(Mg+Fe) ratio (X_{Mg}), at conditions where it coexists with magnetite-magnesioferrite phases (square symbols) and with $Mg_2Fe_2O_5$-Fe_4O_5 phases (pentagons). Solid lines show a thermodynamic model that has been calibrated from the experimental data.

l. *Iron oxidation state in mineral inclusions from Siberian E-type diamonds: Implications for the redox state of Archean oceanic crust and diamond formation (G. Marras/Rome, C.A. McCammon, S. Aulbach/Frankfurt a. M., S. Dominijanni, A. Longinova, D. Mikhailenko, V. Stagno/Rome)*

Natural mineral inclusions in diamonds, along with mantle xenoliths, provide unique information about redox processes occurring in Earth's interior, where the physical strength and chemically inert nature of diamonds preserve the trapped minerals in pristine form for

billions of years. Garnet (grt) and clinopyroxene (cpx) are common minerals found trapped in lithospheric diamonds crystallised in eclogitic rocks (E-type diamonds), which represent 33 % of the extracted diamonds. Despite suggestions from thermodynamic calculations that diamonds in eclogitic rocks are stable at more oxidised conditions compared to peridotites, information on the redox state of natural E-type inclusions is limited to only a few samples from George Creek, Colorado, USA. A study of E-type diamonds can provide information on redox conditions of subducted Archean oceanic crust at the time of diamond formation, while a study of the diamond host rock (eclogite) provides insight on redox evolution through time.

In this study, we focused on (1) a suite of nineteen E-type diamonds (Fig. 3.2-12a) from the Siberian craton with both grt and cpx inclusions (exposed after polishing and trapped) and (2) four cpx and two grt single crystals extracted from the host eclogitic rock of one of the diamonds (LGM-15). Diamonds with different mineral inclusion assemblages were observed to contain single grt (Fig. 3.2-12b), paired non-touching grt, paired non-touching/touching cpx and grt, often associated with accessory phases like sulphides (Fig. 3.2-12a). We measured i) $Fe^{3+}/\Sigma Fe$ of grt and cpx inclusions in diamonds and from the host eclogite using synchrotron Mössbauer source spectroscopy at beamline ID18 of ESRF (beam focused to ~3 x 8 μm^2); ii) the texture of exposed inclusions using SEM at BGI and iii) major element compositions (at BGI) and V concentrations (at Goethe University, Frankfurt a. M.) of exposed inclusions using EMPA.

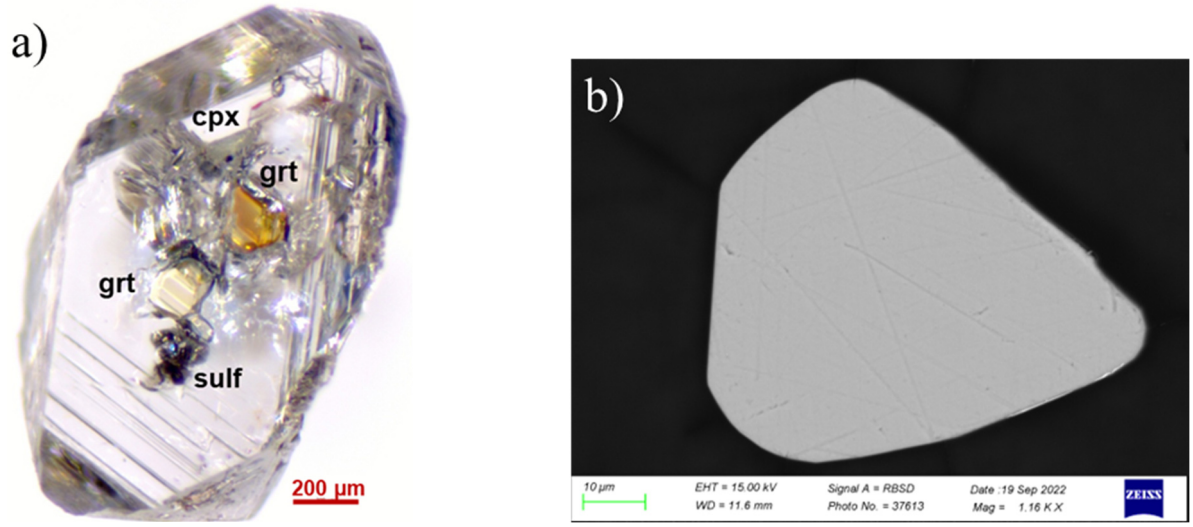

Fig. 3.2-12: **(a)** E-type diamond from the Siberian craton showing multiple inclusions of grt and cpx, both exposed and trapped. Additional mineral phases such as sulphides were also identified. **(b)** BSE image of a grt exposed inclusion.

$Fe^{3+}/\Sigma Fe$ in grt inclusions ranges from 0.02 and 0.07, while in cpx it varies between 0.11 and 0.20. $Fe^{3+}/\Sigma Fe$ values in grt from the host eclogite are comparable to those from inclusions (0.06 and 0.04, respectively), while a slight increase is observed for cpx (0.20 for the inclusion and 0.24-0.28 for the host eclogite crystals). Pressure and temperature were estimated using a grt-

cpx geobarometer (P = 4.2-6.5 ± 0.5 GPa) and geothermometer (T= 930-1283 ± 74 °C). Log fO_2 was determined using a grt-cpx oxy-thermobarometer and varies between -3.7 and -0.9 log units (relative to FMQ). These estimates suggest CO_2−H_2O-bearing fluid/melt (with a small contribution of CH_4) as a possible growth medium for the studied diamonds. Interestingly, diamond and host eclogite indicate similar redox conditions, despite the latter being exposed to secondary alteration processes over time. Evidence for metasomatic processes comes from a preliminary reconstruction of bulk rock $Fe^{3+}/\Sigma Fe$, showing variations between diamond LGM-15 (0.06) and its host eclogite (0.09), coupled with a decrease in grossular content in grt and an increase of cpx Fe^{3+} in the host eclogite. Evaluation of vanadium as an alternative redox proxy is ongoing to test a model recently reported in the literature based on V quantification in grt and cpx from both inclusions and xenoliths, arguing that eclogites are able to buffer oxygen fugacity over aeons.

m. *Coexisting garnet and clinopyroxene in eclogites from V. Griba kimberlite pipe: Ferric/ ferrous iron contents and their implications for redox conditions of the Arkhangelsk Diamondiferous Province (NW Russia) (G. Marras/Rome, C.A. McCammon, D. Mikhailenko, E. Agasheva, V. Stagno/Rome)*

Mantle-derived eclogitic xenoliths represent a direct window into the chemistry, mineralogy and redox state evolution of the subducted oceanic crust. So far, knowledge of eclogitic mantle redox state is based on oxy-thermobarometric investigations of eclogites from cratonic areas, using chemical compositions of garnet (grt) and clinopyroxene (cpx), equilibrium pressure and temperature and $Fe^{3+}/\Sigma Fe$ of grt. Most samples fall in the diamond stability field and are equilibrated with C-O-H fluids. However, the primary redox state could be altered by interaction with (metasomatic) circulating oxidised fluids. In this study, we determined $Fe^{3+}/\sum Fe$ of coexisting and unaltered grt and cpx extracted from 17 eclogites from V. Griba kimberlite to estimate the redox conditions of the Arkhangelsk Diamondiferous Province (NW Russia) that has implications for diamond origin.

$Fe^{3+}/\sum Fe$ was measured using milli-probe Mössbauer spectroscopy, at room temperature, in transmission mode on a constant acceleration spectrometer, using a nominal 370 MBq ^{57}Co point source at Bayerisches Geoinstitut. The collected spectra were fitted by a full transmission integral with a normalised pseudo-Voigt line-shape using the MossA software package. The fitting model for grt consisted of one doublet for Fe^{3+} and one doublet for Fe^{2+}, while for cpx we used one doublet for Fe^{3+} and two doublets for Fe^{2+}. Due to the effect of preferred orientation of cpx, the component area ratio of each Fe^{2+} doublet (assigned to M1 and M2 sites) was allowed to vary, but constrained to have the same value for each doublet.

$Fe^{3+}/\sum Fe$ ranges between 0.03 and 0.20 for grt and from 0.18 to 0.38 for cpx. The estimated errors, based on multiple iterations of spectra fitting, are ±0.01 for garnet and ±0.05 for cpx. Interestingly, $Fe^{3+}/\sum Fe$ of grt from five samples is well above the range reported in the literature for Fe^{3+} in eclogitic grt, which generally does not exceed 0.11, and overlaps with values for peridotitic grt. Oxygen fugacity was calculated using the grt-cpx oxy-thermobarometer and

ranges between -2.5 and 0 log units (±0.5) relative to the fayalite-magnetite-quartz (FMQ) buffer. Values overlap with fO_2 determined for Udachnaya and Yakutia eclogites (Siberian craton). These oxidised conditions imply interaction with metasomatic C-O-H fluids, which is confirmed by previous studies on xenoliths from the same area, where fluids likely acted themselves as a growth medium for diamonds.

n. *Sheared peridotites as recorders of metasomatism and destabilisation of the lithospheric mantle (C. Heckel/Frankfurt a. M., A.C. Withers, A.B. Woodland/Frankfurt a. M. and S.A. Gibson/Cambridge)*

Extensive kimberlite magmatism in the Kaapvaal craton ninety million years ago brought to the surface samples of sheared peridotites (Fig. 3.2-13). Deformation of the lithospheric mantle is probably caused by kimberlite-related, hydrous fluids or melts. Indeed, some of the observed crystallographic preferred orientations for olivine (so-called B-, C-, and E-type fabrics) are usually considered to be a product of deformation under conditions of medium to high H_2O-activities. The preservation of micrometre-sized olivines in the highly-strained shear-bands requires that the xenoliths were exhumed within or shortly after the end of the deformation (weeks to months). Together with the fast entrainment of kimberlites, there is a good chance that the sheared peridotites are recording the metasomatic signatures of the deformation process in the form of elevated OH in the nominally anhydrous minerals. It is thought that such volatile-rich rocks represent the first weak points in a cratonic root, which ultimately leads to the destabilisation of the lithospheric mantle, as is recorded for the southern margin of the Kaapvaal craton.

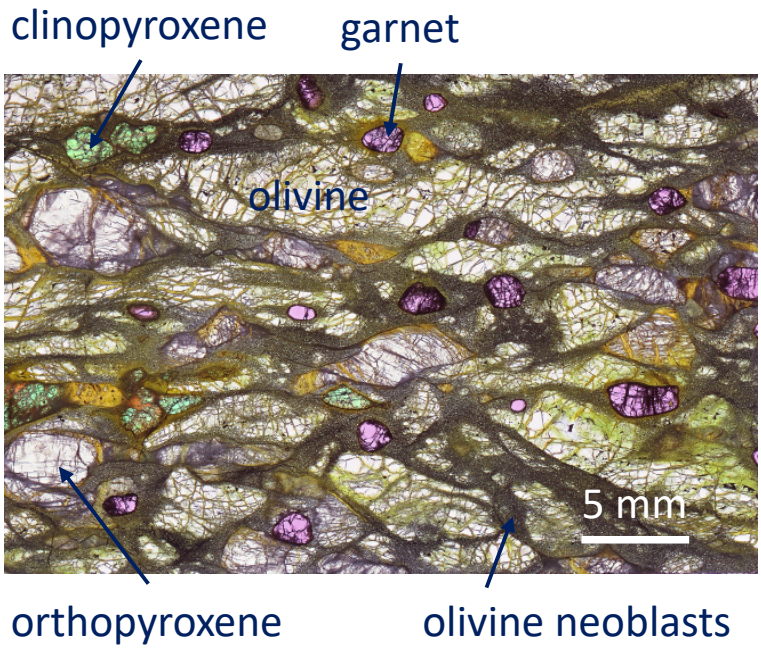

Fig. 3.2-13: Example of a sheared-peridotite xenolith from Kimberly, South Africa. A plane-polarised light image of a 50 µm thick section is shown.

The sheared peridotites have a wide range of (pre-deformation) *PT* conditions from mid-lithospheric depths (90 km) to the lithosphere-asthenosphere boundary (200 km) and temperatures from 900 to 1400 °C, close to or above a 40 mW/m² conductive geothermal gradient. Neoblastic grains, however, can record up to 200 °C higher temperatures. We have analysed the larger mineral grains from a suite of 17 sheared-peridotite xenoliths using Fourier transform infrared spectroscopy (FTIR; Fig. 3.2-14). The H contents of olivine porphyroclasts vary between 2 and 100 ppm H_2O, and those from the highest-pressure xenoliths in general show the lowest OH concentrations. Garnet porphyroclasts have negligible absorption owing to OH, while orthopyroxene and clinopyroxene typically contain ~ 100-200 ppm H_2O. In samples where only small grains are left, we will use secondary ion mass spectrometry (SIMS) to analyse H in these phases. The SIMS analyses will be made using reference materials that include a suite of synthetic olivines with elevated OH, together with natural orthopyroxenes and clinopyroxenes that have been characterised by polarised FTIR. If we find high H contents in the samples, a hydrous metasomatic agent must be invoked, while low OH contents could indicate metasomatism by a CO_2-rich melt or fluid, or rapid loss of H_2O during exhumation. Using SIMS to analyse core-to-rim profiles of H will help test these hypotheses.

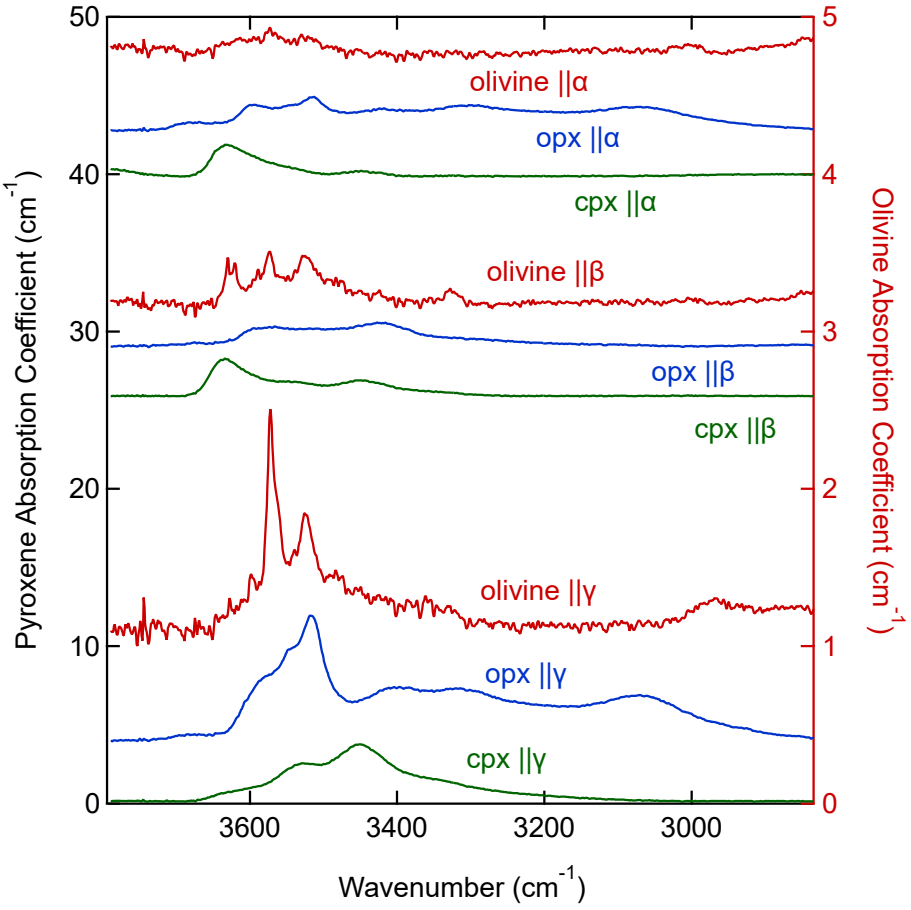

Fig. 3.2-14: Representative polarised FTIR spectra of olivine (16 ppm H_2O), orthopyroxene (234 ppm H_2O) and clinopyroxene (177 ppm H_2O) from a sheared peridotite.

o. *The influence of sediment-derived fluids on the Pb and Sr isotopic signature of arc magmas (M. Putak Juriček and H. Keppler)*

The isotopic signature of most arc magmas is distinct from that of oceanic crust and the Earth's mantle. In particular, arc melts and the subducting sediments bear strikingly similar $^{207}Pb/^{204}Pb$ and $^{206}Pb/^{204}Pb$ isotope ratios. Therefore, it has been proposed that the thin sedimentary veneer at the top of the slab contributes significantly to the total trace element flux in subduction zones. In contrast, the $^{87}Sr/^{86}Sr$ signature of most arc magmas suggests that the sediment contribution to the mantle zone of melting is very low.

The mechanism that delivers the sediment-derived component to the mantle wedge is still debated. Both slab-derived (saline) aqueous and supercritical fluids, as well as (sediment-derived) silicate melts, have been proposed as plausible metasomatic agents in subduction zones. More recently, it has also been suggested that sediments may become admixed with the oceanic crust and the overlying mantle, forming diapirs that intrude into the zone of melting. Which of these processes is responsible for the sediment geochemical signatures in arc magmas, should be dictated by the P-T conditions and the nature of the slab-mantle contact.

We investigated trace element partitioning between saline hydrous fluids and solid metapelitic residues in piston-cylinder experiments at 2.5 to 4.5 GPa and 600 to 700 °C. The starting material was a trace element doped glass with the major element composition of average GLObal Subducting Sediments (GLOSS). Aqueous solutions containing up to 15 wt. % NaCl were added to the GLOSS. Fluids were separated from the metapelitic residues using the diamond trap method. Trace element compositions of fluids and mineral phases were measured by LA-ICP-MS. The fluids were analysed in frozen state using a Peltier-cooled sample chamber. The measured fluid and mineral compositions were used to obtain bulk fluid/metapelite partition coefficients.

We then modeled a metasomatic interaction between the mantle wedge and sediment-derived fluids. The composition of sediment-derived fluids was estimated using the experimental fluid/metapelite partition coefficients, and assuming batch equilibrium conditions during fluid extraction. The published GLOSS trace element concentrations were taken as the initial composition of the metapelites, and we assumed extraction of 1 wt. % of fluid from the slab, which then was allowed to equilibrate with the GLOSS. We used the depleted MORB mantle as the composition of the pristine mantle wedge. The model tested the addition of 0.5 to 10 wt. % of sediment-derived fluid to the depleted mantle wedge (Fig. 3.2-15).

According to the model, nearly all of the Pb in the mantle wedge may originate from a sediment-derived aqueous fluid. In contrast, Sr recycling is much more dependent on the salinity of the fluid and the assumed fluid fraction in the mantle wedge. The differences in recycling efficiency of Pb and Sr may reconcile the weakly elevated $^{87}Sr/^{86}Sr$ ratios with the relatively distinct sediment Pb isotope ratios often observed in arc magmas. The isotope signatures of arc magmas may be reproduced by adding tiny amounts, just fractions of a weight percent of sediment-derived hydrous fluid to the mantle wedge.

In nature, the fluid infiltrating the mantle wedge is likely a mixture, derived from various slab lithologies. The subducting sediments have a relatively small volume, compared to the underlying oceanic crust and mantle. It is plausible that the sediment component in the slab fluid becomes diluted to ppm levels when fluids from various sources mix together. Slab dehydration may account for the Pb and Sr isotope signals reported in arc magma. Invoking additional mechanisms, such as sediment melting and diapirism, is not necessary to explain the geochemical observations.

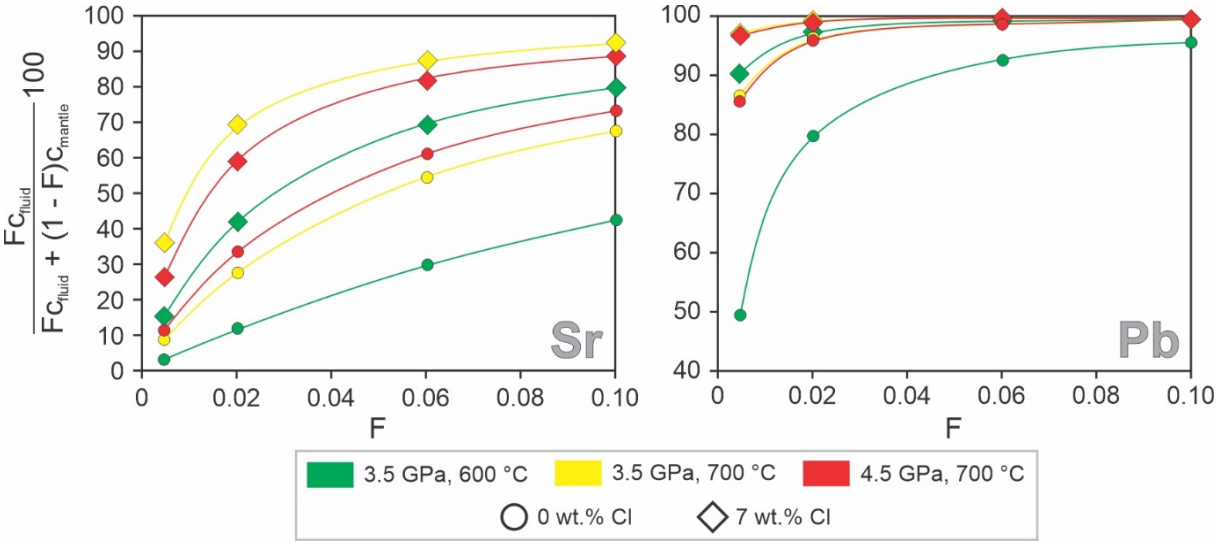

Fig. 3.2-15: The relative efficiencies of Pb and Sr recycling from the subducted sediments. The x-axis is the mass fraction of sediment-derived hydrous fluid in the mantle wedge. The y-axis shows the percentage of sediment-derived Pb and Sr in the mantle, after a theoretical metasomatic event. Nearly all Pb in the mantle wedge likely originates from the sediments. Sr recycling is highly dependent on the fluid salinity and the fluid fraction added to the mantle wedge. The fluid in this model is entirely sediment-derived, without any contributions from other slab lithologies.

p. *Slow-cooling crystallisation experiments on hydrous mafic magmas (L. Calvo, J. Chang and A. Audétat)*

Conventional fractional crystallisation and equilibrium crystallisation experiments have the problem that at temperatures below 1000 °C they typically produce crystals and interstitial melt pools that are smaller than 10-20 µm, which does not allow them to be analysed for trace elements by LA-ICP-MS, nor the melt pools to be analysed for H_2O and CO_2 by FTIR. In order to solve this problem, a slow-cooling approach has been developed, in which the starting material was first equilibrated for a few hours at 1200 °C and then slowly cooled at a rate of 80 °C/day to a specific temperature, where the sample was either quenched or held for some additional days before quenching. In addition, in order to prevent interaction of the starting material with the noble metal capsule and to allow sulphur and chalcophile elements to be

studied, a liner made of gem-quality, single-crystal zircon was used in these experiments. Most experiments were performed on a natural, primitive arc basalt that contained 4.0 wt. % H_2O, 0.5 wt. % CO_2, 0.1 wt. % S and 0.1 wt. % Cl. Two test experiments conducted at 1150 °C and 10 kbar on a slightly more evolved, potassium-rich composition in a zircon-lined capsule versus an olivine-lined capsule did not show any significant difference in the crystallising minerals (olivine + clinopyroxene + phlogopite + sulphides) and their modal abundance, suggesting that the dissolution of 1.1 wt. % ZrO_2 in the zircon-lined sample into the silicate melt did not significantly affect the phase relations. Equilibrium crystallisation experiments performed on this potassium-rich composition revealed that the fO_2 of the experiments can be buffered internally at $\log_{10}fO_2$ = FMQ+2.0 (±0.5) by the addition of 0.5 wt. % anhydrite, which partly reacts to sulphide during the run. The result of an experiment performed on the basaltic starting composition at 12 kbar and a final temperature of 800 °C is shown in Figure 3.2-16.

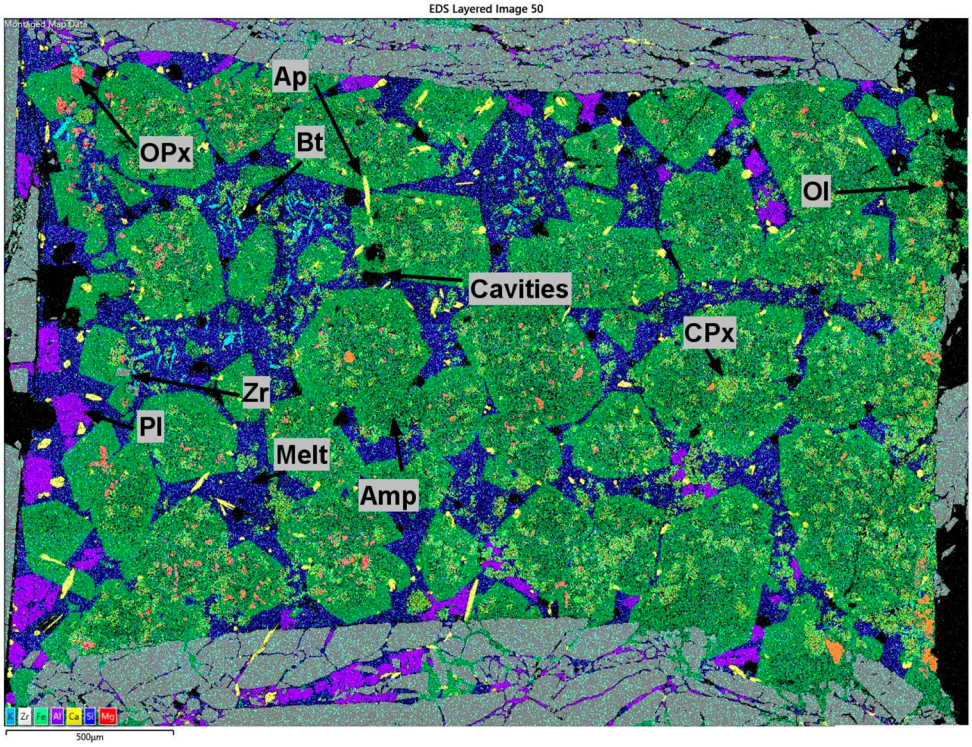

Fig. 3.2-16: Element-coded SEM map of a longitudinal cross section through run LC22, which was last equilibrated at 800 °C and 12 kbar. Width of image: 2.9 mm. The zircon liner (which is severely cracked only next to the sample charge) is shown in grey. Notice the relatively large pools of residual silicate melt (dark blue), which allows analysis of trace elements and volatiles by LA-ICP-MS and FTIR, respectively. Ol – olivine; CPx – clinopyroxene; OPx – orthopyroxene; Amp – amphibole; Ap – apatite; Pl – plagioclase; Zr – zircon.

The modal mineralogy of six experiments that last equilibrated at temperatures ranging from 1200 °C to 700 °C is shown in Figure 3.2-17. The sequence of the crystallising minerals (olivine –> clinopyroxene –> amphibole + apatite + pyrrhotite –> plagioclase –> biotite + quartz + FeTi-

oxides) is similar to that observed in previous high-pressure fractionation experiments. The near-complete disappearance of olivine and lower abundance of clinopyroxene in the experiments performed at ≤1000 °C suggests that these minerals reacted to amphibole, hence the slow-cooling experiments were closer to equilibrium crystallisation experiments than fractional crystallisation experiments.

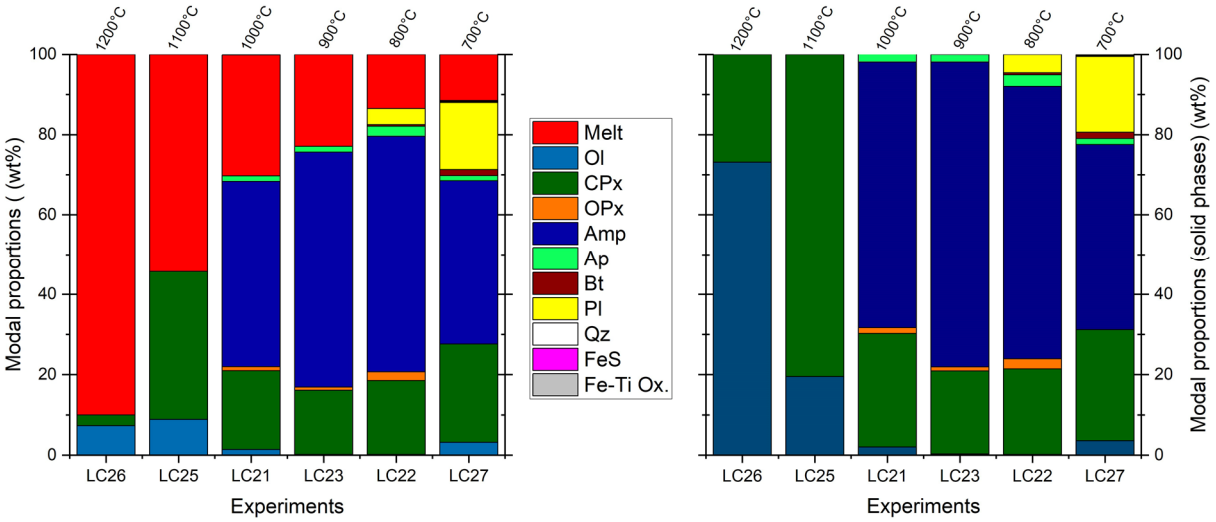

Fig. 3.2-17: Modal abundances of the crystallising minerals and residual liquids in six experiments performed on the basaltic composition at 700-1200 °C and 12 kbar.

With increasing degree of magma crystallisation, the concentrations of H_2O and Cl in the residual silicate melt increased to ca. 8 wt. % and 0.2-0.3 wt. %, respectively, whereas the concentrations of S and CO_2 first increased, and after 1100 °C decreased, in agreement with the appearance of fluid bubbles and sulphides in the runs below this temperature. Mineral/melt partition coefficients obtained from LA-ICP-MS analyses of mineral rims and the silicate melt fit with previously published values. An important observation with regard to the evolution of trace elements in the silicate melt is that the Sr/Y ratio gradually increased from a starting value of 18 at 50 wt. % SiO_2 to 201 at 67 wt. % SiO_2, after which it decreased again to 32 at 76 wt. % SiO_2. This result supports the hypothesis that high Sr/Y magmas (*i.e.*, "adakites"; which are genetically associated with porphyry Cu±Mo±Au deposits) can be produced by amphibole-dominated fractionation at high pressure in the absence of garnet.

q. *Experimental equilibrium and fractional crystallisation of a volatile-bearing potassic mafic magma at 1 GPa (J. Chang and A. Audétat)*

Potassic mafic-to-felsic magmas, though volumetrically much smaller than calc-alkaline magmas, are widespread in subduction-related magmatic arcs, continental collision zones and

intraplate tectonic settings. Some intermediate to felsic potassic magmas released S-, Cl- and CO_2-bearing aqueous fluids that led to the formation of economically important magmatic-hydrothermal Cu and/or Au deposits. However, the origin of intermediate to felsic potassic magmas is highly debated, and the behaviour of volatiles (S, Cl, H_2O and CO_2) during magma differentiation is poorly understood. To better understand the liquid line of descent of mafic potassic magmas, we performed equilibrium and fractional crystallisation experiments at 1.0 GPa and 1150-850 °C on a natural high-Mg basaltic trachyandesite from the Sanjiang region, southwestern China, using piston-cylinder presses. The starting material was doped with 3.5 wt. % H_2O, 2500 ppm S and 2700 ppm Cl, similar to the volatile content of the Sanjiang primitive magmas according to olivine-hosted melt inclusions and mantle partial melting experiments. The addition of 2500 ppm S in the form of anhydrite internally buffered the experiments at oxygen fugacities of ~ 2.0 ± 0.5 log units above the fayalite-magnetite-quartz buffer, which fits with the relatively high oxidation state of the Sanjiang potassic magmas. To avoid loss of Fe and S to the noble metal capsules, the starting material was placed inside capsule liners made of single-crystal zircon. This new technique allows to investigate the behaviour of sulphur and chalcophile elements. In addition to conventional equilibrium and fractional crystallisation experiments, we also performed slow-cooling experiments, in which the starting material was equilibrated at 1200 °C for 6 hours, then cooled 80 °C/day to a specific temperature, and finally held at this temperature for another three days. The result of one of these slow-cooling experiments is shown in Figure 3.2-18.

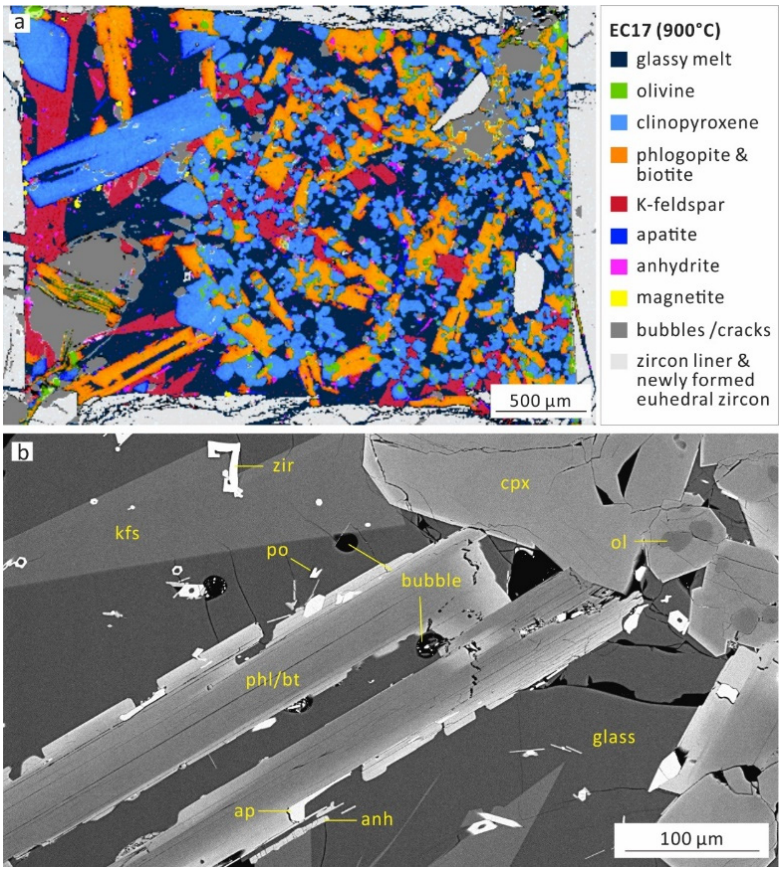

Fig. 3.2-18: Result of a slow, isobaric cooling experiment performed with a zircon liner (cooling from 1200 °C to 900 °C within four days and then holding it at 900 °C for another three days). (a) EDS phase map of the experimental charge; (b) BSE image of an area in the lower left part of the former image. kfs – potassic feldspar; zir – zircon; cpx – clinopyroxene; ol – olivine; phl/bt – phlogopite/biotite; ap – apatite; anh – anhydrite.

The sequence of crystallising minerals in the three experimental series is similar to that recorded in the Sanjiang potassic magmatic rocks. Figure 3.2-19 shows that also the compositions of the experimental melts show a good match with the Sanjiang potassic magmas. These results suggest that the origin of the Sanjiang intermediate to felsic magmas (including the felsic porphyry Cu-forming magmas) can be well explained by crystallisation-driven differentiation of mafic potassic magmas without any involvement of crustal material.

In the geologically realistic scenario studied here, the S content of the experimental intermediate to felsic melts was buffered at 800-3000 ppm S as a consequence of saturation in sulphate melt, anhydrite and/or sulphides, whereas the melt H_2O and Cl contents increased exponentially until saturation in a CO_2-bearing fluid phase was reached. These results suggest that the Sanjiang porphyry Cu-forming magmas (65-72 wt. % SiO_2), which seem to have ascended directly from the lower crust (≥1.0 GPa), probably contained up to 8-10 wt. % H_2O, 800-3000 ppm S, and 6000-8000 ppm Cl.

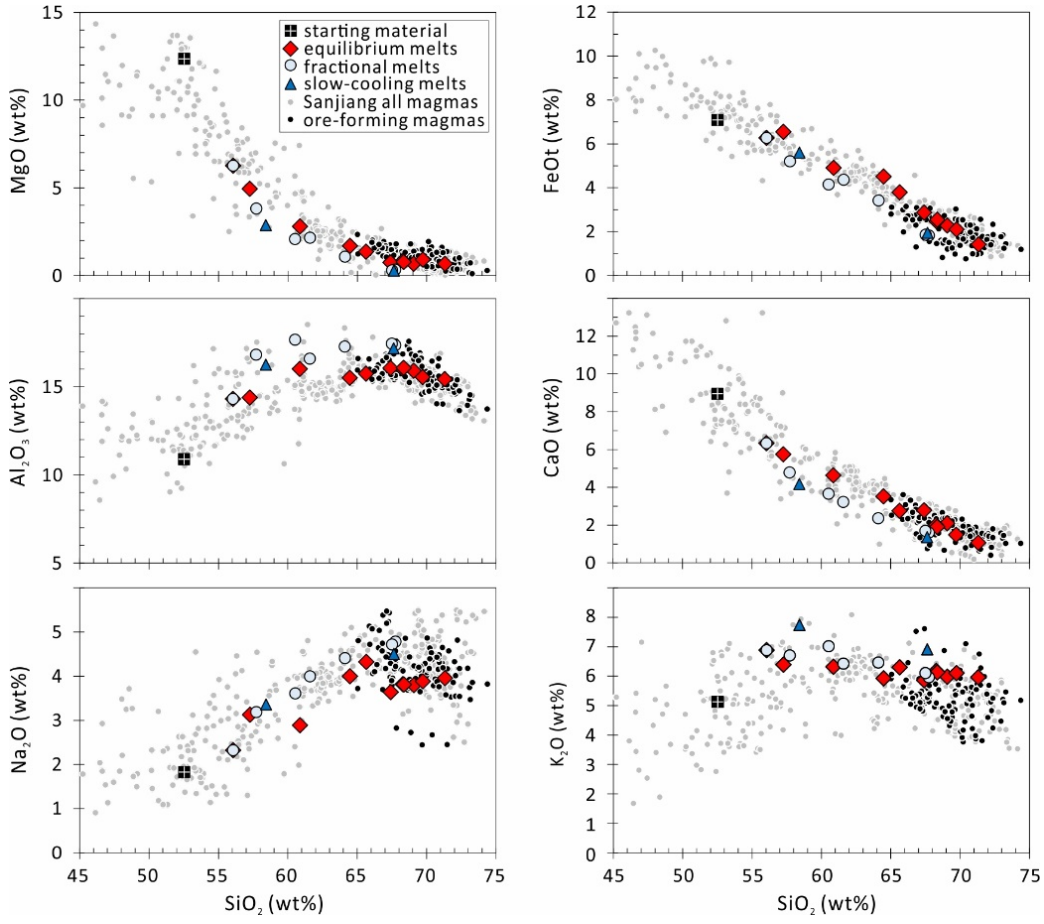

Fig. 3.2-19: Comparison of major element compositions of the experimental melts vs. the Sanjiang potassic magmas. Notice the generally good match of all experimental melts with the Sanjiang magmas, though the melts of the fractional and slow-cooling crystallisation experiments display slightly lower MgO, FeO_t and CaO contents and higher Al_2O_3 contents than those of the equilibrium crystallisation experiments.

r. *New constraints on Ti diffusion in quartz and the time spans between magma chamber recharge and eruption (A. Audétat, A. Schmitt/Heidelberg, R. Njul, A. Borisova/Toulouse, M. Harris/Bozeman and Y. Lu/Perth)*

Titanium diffusion chronometry in quartz is an increasingly popular tool to reconstruct the time scales of various magmatic, metamorphic, and hydrothermal processes. However, currently available experimental calibrations of Ti diffusion rates in quartz differ by four orders of magnitude (Fig. 3.2-20), reflecting the fact that experimental determination of such extremely slow diffusion rates is very challenging.

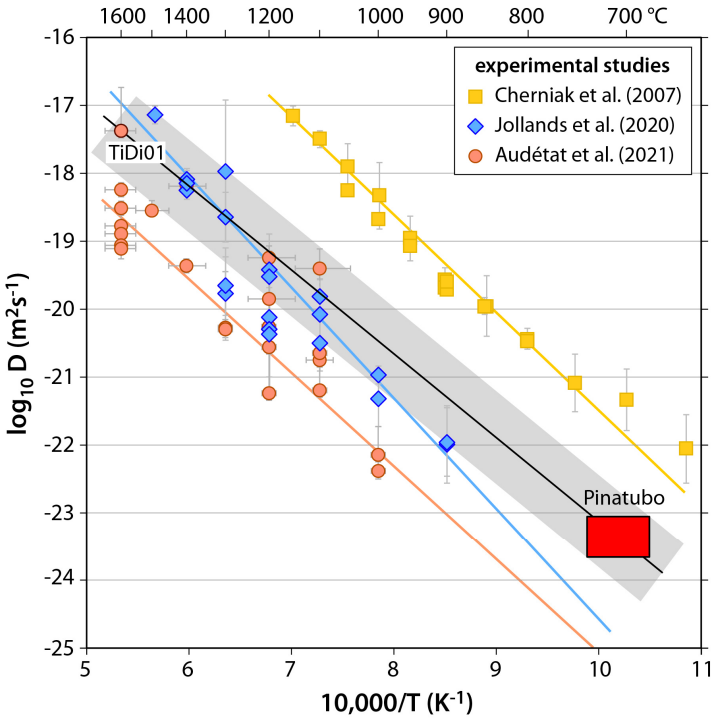

Fig. 3.2-20: Ti diffusion coefficient determined in the present study on quartz crystals from Mt. Pinatubo (red box), compared to diffusion coefficients determined in experimental studies. The solid black line shows the inferred temperature dependence, and the grey shading the associated uncertainty interval.

To obtain a reliable data point at geologically realistic temperatures, tiny (15-40 µm) zircon inclusions in quartz phenocrysts from the 1991 Mt. Pinatubo eruption were dated by the U-Th disequilibrium method, and the obtained ages of 20±5 to 197±30 ka were used in conjunction with Ti diffusion profiles measured at nearby quartz growth zone contacts (Fig. 3.2-21) to retrieve diffusion coefficients. The fact that all 18 analysed pairs of zircon inclusions + diffusion profiles return similar diffusion coefficients (Fig. 3.2-22) suggests that (1) the zircon inclusions were trapped shortly after their growth from the magma, (2) that the quartz crystals were stored at a relatively constant temperature, and (3) that the heating event associated with the formation of the CL-bright, Ti-rich rims on most quartz phenocrysts (Fig. 3.2-21) was comparatively short.

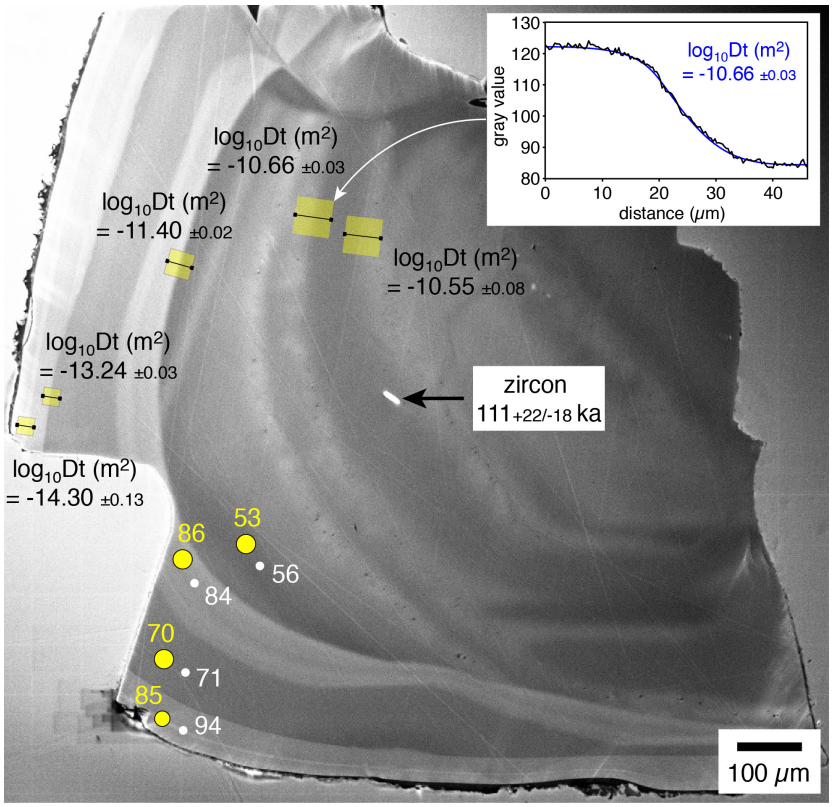

Fig. 3.2-21: Cathodoluminescence image of a quartz phenocryst that hosts a zircon inclusion with a U-Th age of 111 (±22-18) ka. Notice the increasing sharpness of growth zone contacts from core to rim. Yellow boxes show the locations of measured Ti diffusion profiles; yellow circles and white dots denote quartz analyses by LA-ICP-MS and EPMA, respectively, with the obtained Ti concentrations shown in µg/g.

The new Ti diffusivities (Fig. 3.2-20) were used together with Ti diffusion profiles measured at the contact to Ti-rich overgrowths to estimate the time elapsed between magma chamber recharge and eruption. The data suggest that rims of the quartz phenocrysts in the 1991 Mt. Pinatubo dacite started to grow between 20 and 400 years before the eruption.

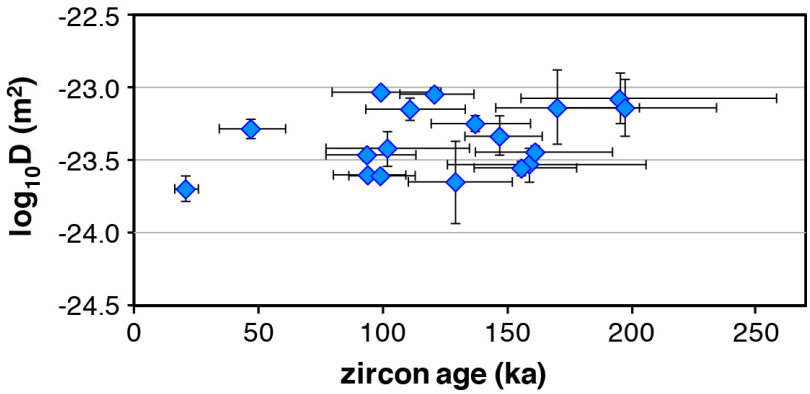

Fig. 3.2-22: Ti diffusion coefficients determined from the age of zircon inclusions and nearby Ti diffusion profiles measured in quartz.

s. *Mössbauer investigation of lake sediments at low-temperature reveals redox reaction paths (C.A. McCammon, in collaboration with D. O'Connell/Dublin and J. Byrne/Bristol)*

Electron transfer between aqueous Fe(II) and Fe(III)-oxide impacts biogeochemical cycling of iron, carbon and phosphate in surface water ecosystems and aquifers and has particular relevance to water quality since iron oxides are important scavengers of trace elements. Electron exchange can be traced using iron isotopes, and numerous studies of reactions in synthetic systems have delivered valuable insight on key parameters. While such experiments simplify reaction monitoring and sample characterisation, they lack crucial aspects of natural environments. This shortcoming was addressed by incubating natural lake sediments with an ^{55}Fe-enriched solution under different conditions, and results confirmed that extensive electron exchange took place. However, reaction paths were challenging to determine, since Fe(III) phases could not be identified in the sediments. We therefore undertook an investigation of the same lake sediments using Mössbauer spectroscopy, where measurements at low temperature were key to phase identification.

Samples were cored from the bottom of Lake Ørn, a freshwater lake in central Jutland, Denmark. The three sediments studied using Mössbauer spectroscopy came from depths of 1-2 cm, 9-10 cm and 18-19 cm below the lake bottom. Wet chemistry indicated the presence of a large pool of what would usually be called "iron oxides", but powder X-ray diffraction did not show peaks of crystalline iron oxides or even poorly crystalline material such as ferrihydrite. Instead, X-ray patterns showed strong quartz reflections, less intense vivianite reflections, and extremely weak reflections that might be clay. We collected Mössbauer spectra at 80 K, and all show an intense Fe^{3+} doublet and a weaker Fe^{2+} doublet (Fig. 3.2-23a). The latter can be unambiguously assigned to Fe^{2+} in vivianite based on its distinctive values of centre shift and quadrupole splitting. In contrast, Fe^{3+} hyperfine parameters are nearly insensitive to the local atomic environment, and the Fe^{3+} doublet centre shift and quadrupole splitting match those of many phases. Since magnetic ordering can provide better discrimination, we collected Mössbauer spectra at 4 K.

Mössbauer spectra of the two shallowest samples are similar and show a magnetic sextet with uniformly broadened lines (Fig. 3.2-23b). The combination of low observed hyperfine magnetic field (46 ± 1 T) with low quadrupole shift (-0.03 ± 0.03 mm/s) allows an unequivocal assignment to Fe(III) oxyhydroxide. Magnetic spectra of crystalline Fe(III) oxyhydroxide (*i.e.*, the mineral ferrihydrite) normally show inhomogeneous broadening due to distributions of static hyperfine interactions (next-nearest neighbour effects), but our spectra show homogeneous broadening likely caused by dynamic hyperfine interactions (*i.e.*, rapid variation on the timescale of the Mössbauer effect). The excellent fit to a model where the magnetic field flips randomly between two directions, combined with wet chemical data, suggests that Fe(III) oxyhydroxide particles are small (on the nanoscale) and are associated with other material such as organic matter or phosphate. The Mössbauer spectrum of the deepest sample shows a magnetic sextet assigned to Fe^{3+} and two magnetic octets with hyperfine parameters that match literature values for Fe^{2+} in vivianite (Fig. 3.2-23b). $Fe^{3+}/\Sigma Fe$ determined from relative areas has the same value at 80 K (0.29 ± 0.05) and 4 K (0.29 ± 0.04).

Our results confirm that electron transfer takes place between aqueous Fe(II) and Fe(III) oxyhydroxide in natural sediments. By analogy with other systems, an electron is transferred from aqueous Fe(II) to Fe(III) oxyhydroxide, followed by the migration of the electron through the solid and the reduction of a surface Fe(III) to Fe(II), which brings the electron in solution again. If a redox gradient exists in the sediment, this may provide an inorganic pathway for transmitting electrons from a more reduced to a more oxidised environment. Such reactions are likely to have a major impact on the water quality of lakes. Iron oxides are important scavengers for trace elements in natural environments and are also used for engineered entrapment of contaminants, and the stability of these iron oxides is of importance to predict the fate of such contaminants.

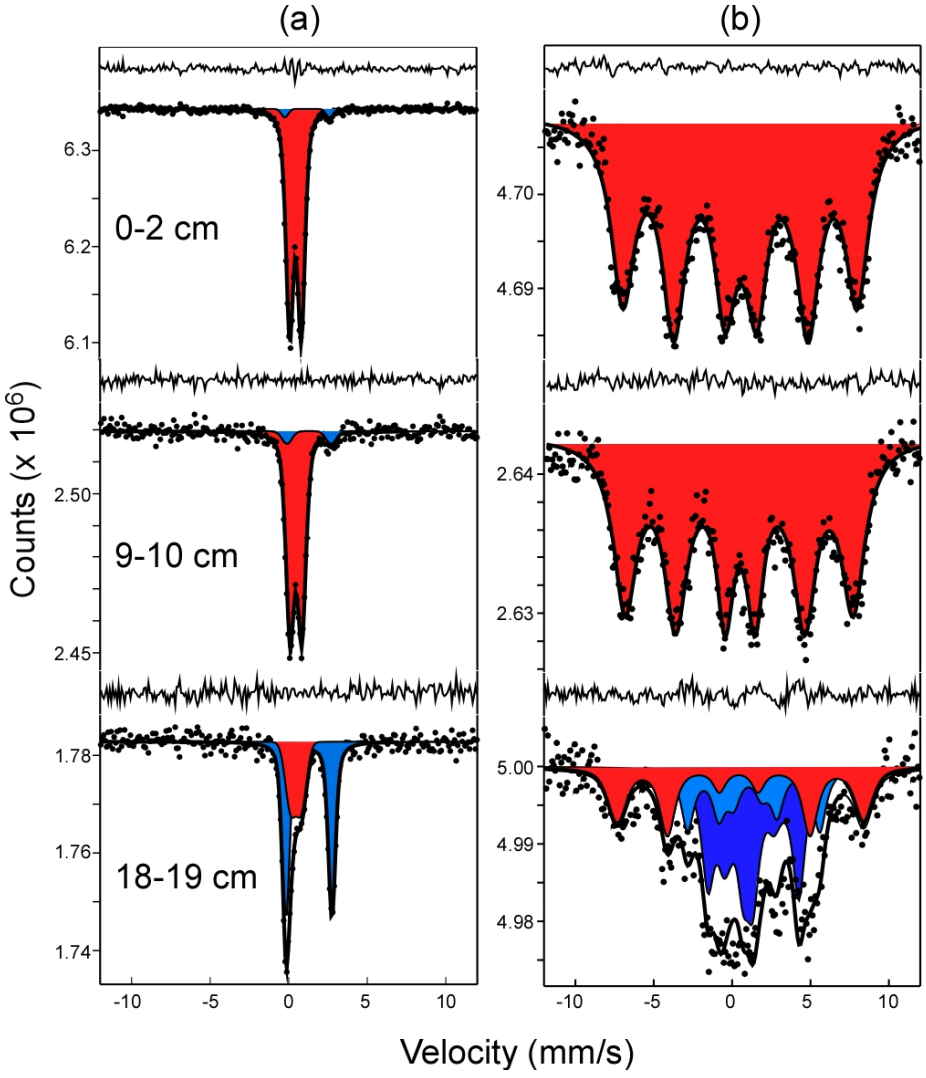

Fig. 3.2-23: Mössbauer spectra of sediments from the bottom of Lake Ørn recorded at (a) 80 K and (b) 4 K. Spectra at 80 K were fit to doublets assigned to Fe^{3+} (red) and Fe^{2+} (blue). Spectra at 4 K were fit to either (i) a single Fe^{3+} component with rapid fluctuating magnetic field (upper two spectra) or (ii) two Fe^{2+} magnetic octets (corresponding to Fe^{2+}_{I} and Fe^{2+}_{II} sites of vivianite, shaded light blue and dark blue, respectively) and one Fe^{3+} magnetic sextet (red) (bottom spectrum). The fit residual is shown above each spectrum.

3.3 Mineralogy, Crystal Chemistry and Phase Transformations

Our knowledge of Earth's deep interior continues to expand through innovative high-pressure experiments involving analysis with advanced methodologies. A major focus has been the crystal chemistry of bridgmanite and coexisting ferropericlase at lower mantle conditions, especially involving the trivalent cations aluminium and ferric iron. Substitutions coupling these cations with cations of other valences as well as oxygen play an important role in determining the physical and chemical properties of the orthorhombic perovskite structure. Increasing temperature reduces out-of-phase octahedral tilting in aluminium-substituted bridgmanite at high pressure, providing new constraints on the depth of the perovskite to post-perovskite transition in the lower mantle. Increasing temperature reduces the ferric iron content of iron- and aluminium-bearing bridgmanite at high pressure, suggesting that the disproportionation of ferrous iron to iron metal and ferric iron may have played a less dominant role in early Earth compared to later times. Trivalent cation substitution in bridgmanite promotes larger grain sizes, and combined with existing knowledge of oxygen vacancies and crystal chemistry, suggests that grain growth rate may increase with depth and lead to higher viscosity in the deeper mantle. Lower mantle viscosity may also be influenced by the grain morphology of ferropericlase, and novel deformation experiments are planned to test different models of microstructure.

Phase stabilities can be related to element solubility and volatile behaviour in high-pressure phases. The solubility of chromium in the post-spinel phase Fe_5O_6 is surprisingly limited, which combined with previous observations that Mg solubility is also low, suggests that the structure has only limited capacity to accommodate cations other than Fe^{2+} and Fe^{3+}. Successful synthesis of calcium (II) orthocarbonate, Ca_2CO_4, at high pressure provides new pathways for carbon transport within Earth's interior. The water content of high-pressure silica phases increases with alumina content, suggesting that the post-stishovite phase in subducted basaltic crust can store water in Earth's lower mantle. Innovative experiments showing how hydrogen can be lost from iron sulphide during decompression also suggest that hydrogen may be stored in iron sulphide minerals and melts that occur at the base of the cratonic lithosphere where diamonds form or in core-forming melts during planetary differentiation.

Microstructures of minerals can reveal their transformational and thermal histories in the deep interior of Earth and other planets. The discovery and characterisation of twins in hydrous wadsleyite suggests that they formed during crystal growth under quasi-hydrostatic conditions in the presence of a hydrous fluid and may provide favourable sites for the nucleation of ringwoodite. A new method of post hoc analysis of antiphase domains in eclogite-facies omphacite provides a fresh approach to evaluating growth/coarsening kinetics and hence new possibilities to unravel temperature-time histories.

a. *Structural distortion of $MgSiO_3$ and Al-bearing bridgmanite at high pressure and temperature (G. Criniti, A. Kurnosov, T. Boffa Ballaran and D.J. Frost, in collaboration with Z. Liu/Jilin, K. Glazyrin/Hamburg, M. Merlini/Milano and M. Hanfland/Grenoble)*

Structural distortions in minerals are often related to their thermodynamic stability and can be used to infer how their physical and thermal properties change in the proximity of phase transformations. Although $(Mg,Fe,Al)(Si,Al)O_3$ bridgmanite is the most abundant mineral in Earth's lower mantle, only a limited number of experimental studies have investigated how its crystal structure responds to changes in pressure and temperature. Of particular interest is to characterise and quantify the degree of distortion of the perovskite-type structure of bridgmanite, which could contribute to understanding the mechanism that leads to the formation of the post-perovskite phase at the bottom of Earth's lower mantle. To do so, we have collected and analysed single-crystal diffraction data of pure $MgSiO_3$ and Al-bearing bridgmanite samples up to 80 GPa and 1000 K using diamond anvil cells and synchrotron X-ray diffraction.

The overall distortion of each crystal structure was decomposed into displacive modes of individual oxygen atoms and cations, each complying with a specific set of symmetry operations. Out of these modes, we found that the most prominent ones are the R_4^+ and M_3^+ modes describing the displacements of the oxygens that give rise to two octahedral tilts, *i.e.*, the out-of-phase and in-phase rotations about the [110] and [001] directions, respectively, of an undistorted cubic perovskite structure. In our datasets, we observed that M_3^+ increases more steeply than R_4^+ with pressure at room temperature, although R_4^+ remains the most prominent distortion in the pressure range investigated (Fig. 3.3-1a). Additionally, we found that M_3^+ is basically temperature independent, while R_4^+ decreases at high temperature (Fig. 3.3-1b). Based on the analysis of analogous materials, it has been argued in the literature that when the out-of-phase tilting reaches a critical value, the perovskite-type structure of bridgmanite would become unstable and transform to the post-perovskite phase. Since high temperatures reduce out-of-phase octahedral tilting (Fig. 3.3-1b), the critical value of R_4^+ for which the post-perovskite transition is triggered is expected to shift to higher pressure.

Although this observation is only qualitative and does not allow prediction of the exact pressure/temperature conditions of the post-perovskite transition, it is consistent with the positive Clapeyron slope observed for this transformation in high-pressure and high-temperature experiments. Note also that distortions in Al-bearing bridgmanite tend to be higher than in the $MgSiO_3$ sample (Fig. 3.3-1a), possibly leading to lower post-perovskite transition pressures. This is in contrast with experimental and theoretical studies on the phase stability of Al-bearing bridgmanite and post-perovskite, which suggest that the transition should occur at higher pressure than in $MgSiO_3$. A likely explanation is that Si-Al interactions between neighbouring octahedral sites that develop at the local scale in Al-bearing bridgmanite might stabilise the perovskite structure to higher degrees of distortion and thus to higher pressures than in $MgSiO_3$. Single-crystal X-ray diffraction measurements at pressure and temperature conditions of the lowest part of the lower mantle will be needed to further discuss this hypothesis.

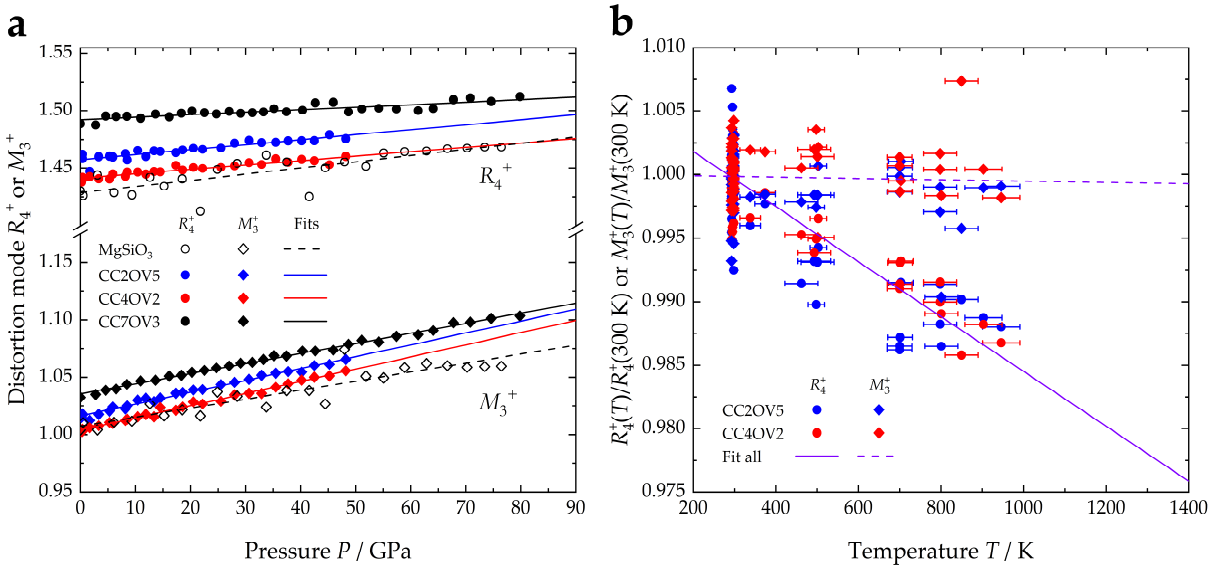

Fig. 3.3-1: (a) Pressure and (b) temperature dependence of octahedral tilting R_4^+ and M_3^+ of $MgSiO_3$ and Al-bearing bridgmanite. Labels for Al-bearing samples indicate the molar content of $AlAlO_3$ (CC) and $MgAlO_{2.5}$ (OV) components. In (b), the amplitudes of R_4^+ and M_3^+ of CC2OV5 and CC4OV2 have been normalised to their room temperature (300 K) values and plotted as a function of temperature. Additionally, due to the limited amount of data, the same linear fit (purple line) was used to model the behaviour of the two samples.

b. *Temperature dependence of the $Fe^{3+}/\Sigma Fe$ ratio in bridgmanite (F. Wang, H. Fei, L. Wang, C.A. McCammon, D.J. Frost and T. Katsura)*

Bridgmanite is considered to be the most abundant mineral in the lower mantle. It was confirmed to exist in nature by its discovery in a shocked meteorite. Bridgmanite can easily incorporate Fe^{3+} even under very reducing conditions, mainly by charge disproportionation of Fe^{2+} to Fe^{3+} and metallic iron. The amount of Fe^{3+} in bridgmanite is important for an understanding of the homogenisation of the mantle. Previous studies have shown that $Fe^{3+}/\Sigma Fe$ in bridgmanite is a function of aluminium content and oxygen fugacity, but there have been few studies on the temperature dependence of $Fe^{3+}/\Sigma Fe$. Therefore, this work was undertaken to quantify this parameter as a function of temperature.

Pyroxene with chemical formula $Mg_{0.89}Al_{0.11}Fe_{0.11}Si_{0.89}O_3$, mixed with 5 wt. % $(Mg_{0.9}Fe_{0.1})O$ ferropericlase and 5 wt. % Ir metal, was used as a starting material. The mixture was put into a Pt capsule, which was then loaded into a Bayerisches Geoinstitut (BGI) standard 7/3 cell assembly. High-pressure experiments were conducted at 27 GPa and 1800–2600 K on a 1500 tonne Kawai-type multianvil press with the Osugi-type guide block system at BGI. The oxygen fugacity (fO_2) was determined using Ir-Fe alloy to be around +2.0 ΔIW. The $Fe^{3+}/\Sigma Fe$ ratio in recovered bridgmanite was determined using Mössbauer spectroscopy and showed that $Fe^{3+}/\Sigma Fe$ decreases from 80 % at 1800 K to 50 % at 2600 K (Fig. 3.3-2). A decreasing $Fe^{3+}/\Sigma Fe$ ratio with increasing temperature indicates that charge disproportionation is less prevalent in

bridgmanite at very high temperatures, and thus it is less likely to have played a dominant role in early Earth.

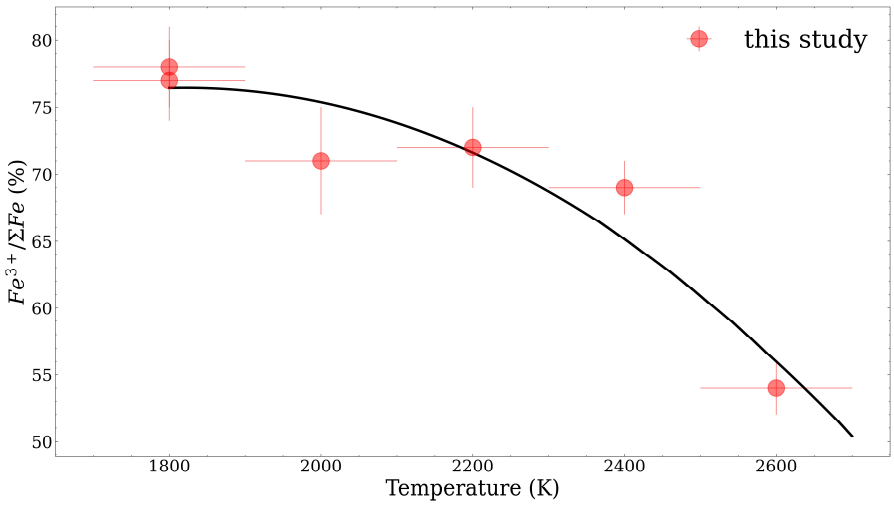

Fig. 3.3-2: $Fe^{3+}/\Sigma Fe$ in bridgmanite as a function of temperature in samples quenched from 27 GPa and $\log fO_2 \approx +2.0$ ΔIW.

c. *Effect of trivalent cation substitution on the grain growth of bridgmanite (H. Fei, F. Wang and T. Katsura)*

Bridgmanite, which comprises more than 80 % by volume of the pyrolitic lower mantle, can incorporate significant amounts of trivalent cations (primarily Al^{3+} and Fe^{3+}) in Earth's lower mantle. Incorporation takes place either through a charge-coupled substitution mechanism by the formation of $AlAlO_3$, $FeFeO_3$, and $FeAlO_3$ components, or through an oxygen vacancy substitution by the formation of $MgFeO_{2.5}$ and $MgAlO_{2.5}$ components. Because both substitution mechanisms produce external point defects on the Mg, Si, or O sites, the incorporation of trivalent cations may significantly affect the point defect-controlled physical properties of bridgmanite, such as atomic diffusion, element partitioning, elasticity, and electrical conduction.

Grain size is an important parameter for mantle dynamics since the creep rate of mineral aggregates deformed in the diffusion creep regime is inversely proportional to the second or third power of grain size. Considering that the grain growth of minerals is rate controlled by self-diffusion of elements which is dominated by the migration of point defects, it is expected that the incorporation of trivalent cations could significantly affect the grain size of bridgmanite in the lower mantle.

To understand the grain size of bridgmanite in the lower mantle, we investigated the effect of Al^{3+} and Fe^{3+} incorporation on the grain growth rate of bridgmanite. Single-phase bridgmanite aggregates were pre-synthesised from Fe^{3+}- and/or Al^{3+}-bearing $MgSiO_3$ glasses at 27 GPa and 1700 K, and annealed at 27 GPa and 2000 or 2300 K for 100 min to promote grain growth. The

grain size of samples after grain growth was determined from backscattered electron images, and Fe^{3+} and Al^{3+} contents in bridgmanite were determined by electron microprobe. The concentration of $MgSiO_3$, $FeAlO_3$, $AlAlO_3$, $FeFeO_3$, and $MgAlO_{2.5}$ components was calculated from the Fe^{3+} and Al^{3+} contents.

We observed that the grain size of bridgmanite in recovered samples increases systematically with increasing concentrations of both $AlAlO_3$ and $FeFeO_3$ components. The $FeAlO_3$ component also enhances grain growth of bridgmanite, but with smaller dependence (shallower slope of fitting curves in Figure 3.3-3) than the $AlAlO_3$ and $FeFeO_3$ components. Therefore, the grain growth of bridgmanite is enhanced significantly by the charge-coupled substitution of either Fe^{3+} or Al^{3+}. In contrast, the $MgAlO_{2.5}$ component formed by oxygen-vacancy substitution has a negligible or slightly negative effect (Fig. 3.3-3).

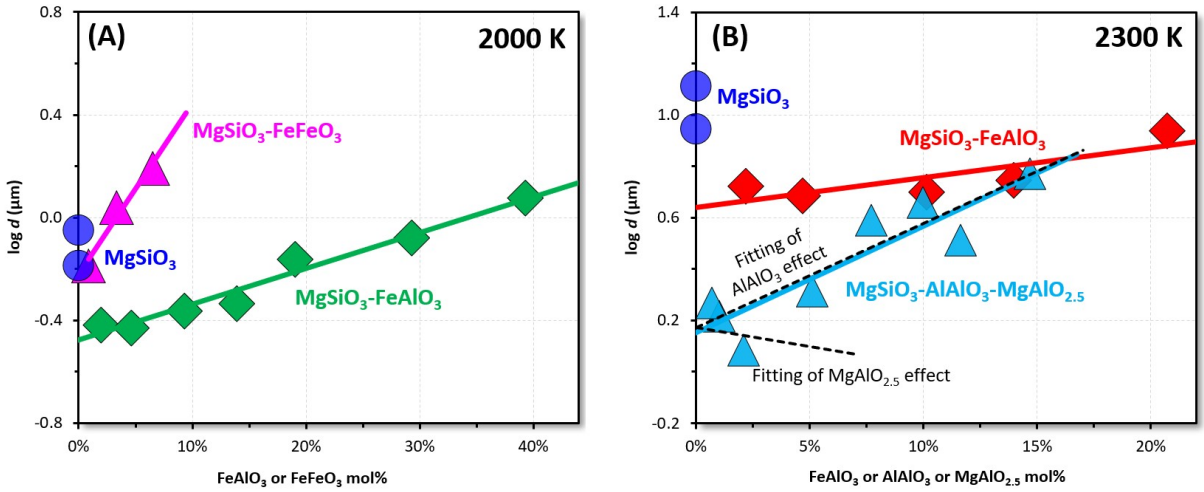

Fig. 3.3-3: Grain size of bridgmanite as a function of trivalent cation substitution. $FeAlO_3$, $FeFeO_3$, $AlAlO_3$, and $MgAlO_{2.5}$ concentrations are shown after annealing at 27 GPa for 100 min at (A) 2000 K and (B) 2300 K.

Considering the decrease of $MgFeO_{2.5}$ and $MgFeO_{2.5}$ components with increasing depth due to pressure-destabilised oxygen vacancy substitution and the increase of Fe^{3+} and Al^{3+} content in bridgmanite because of majoritic garnet decomposition at the topmost lower mantle, the grain growth rate of Fe^{3+}- and Al^{3+}-bearing bridgmanite may increase with increasing depth. Grain size-dependent diffusion creep rate may therefore decrease, which will cause an increase of viscosity with depth.

d. *Investigation of ferropericlase morphology controlled by surface energy (A. Chakraborti, H. Fei and T. Katsura)*

The lower mantle is mainly composed of bridgmanite (80 %) and ferropericlase (20 %). Bridgmanite should therefore ideally control lower mantle viscosity because of its larger

volume fraction according to the Load-Bearing Framework (LBF) model. However, geological time scales create large total strains that can interconnect ferropericlase grains in the so-called Interconnected Weak Layer (IWL) model. In this case, ferropericlase morphology would be the controlling factor. Ferropericlase morphology should also be affected by surface energy which would lead to the grain aspect ratio approaching unity over time. The aim of this project is to study the morphology of ferropericlase grains under conditions of high pressure, high temperature and large total strain to resolve whether the LBF or IWL model is more realistic for lower mantle conditions.

The planned methodology of the project is to synthesise bridgmanite and ferropericlase aggregates at high-pressure and high-temperature conditions. We will then subject ferropericlase grains to large strains to deform them adequately. Next, elongated grains will be annealed to observe the effect of surface energy on grain morphology. The observed rounding rate would establish LBF or IWL as more realistic for the lower mantle.

Currently, we are developing techniques in the multianvil apparatus to deform the aggregates in order to obtain high strain in ferropericlase grains. Figure 3.3-4 shows the assembly that is being used. We also plan to employ a D111-type apparatus in collaboration with colleagues in Japan, in order to generate additional uniaxial stress at high pressure.

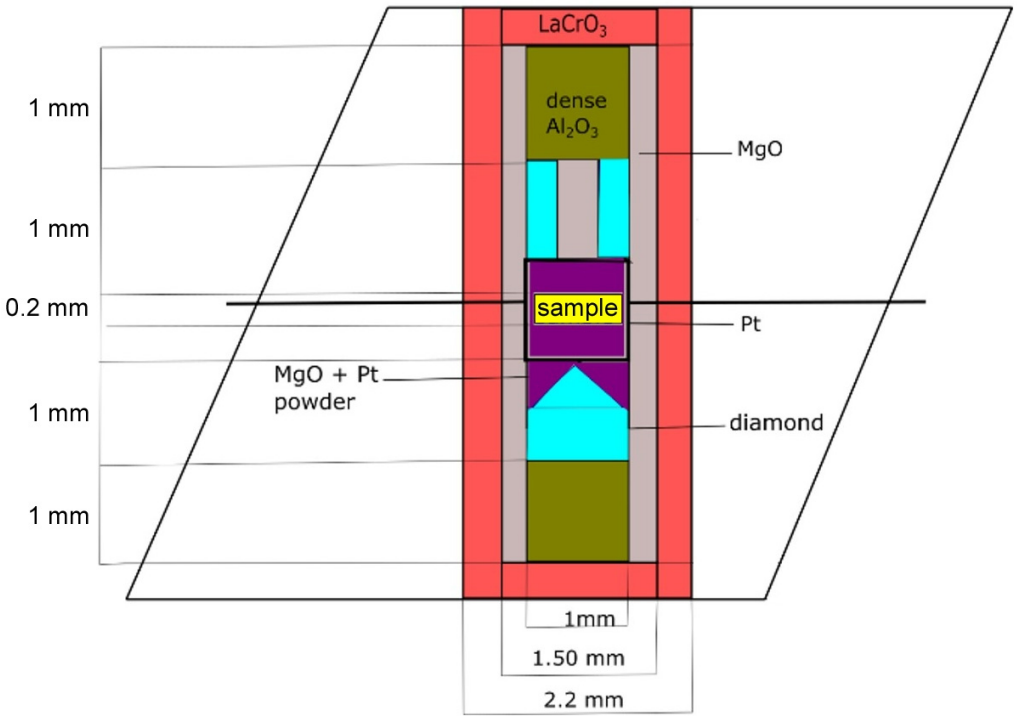

Fig. 3.3-4: Assembly design to realise the three-point bending test. The single-crystal diamond lancer pushes the sample disc supported by two diamond pieces on the opposite side. The sample is surrounded by a MgO + Pt mixture, which has low flow strength and allows the diamond lancer to approach the sample during cold compression.

e. *Chromium incorporation into the Fe_5O_6 structure (A. Woodland/Frankfurt a. M. and T. Boffa Ballaran; L. Uenver-Thiele, K. Schumann and K. Rosbach/Frankfurt a. M.)*

A complete solid solution is known to occur between the magnetite (Fe_3O_4) and chromite ($FeCr_2O_4$) endmembers of the spinel series. At high pressures corresponding to the deep upper mantle and transition zone, the spinel structure becomes unstable at the expense of oxide phases with other crystal structures and stoichiometries, such as Fe_4O_5. Recent experimental studies have demonstrated that the Cr-bearing endmembers $Fe_2Cr_2O_5$ and $Mg_2Cr_2O_5$ also become stable at high pressures above 10 GPa. We are investigating the ability of the crystallographically-related Fe_5O_6 phase to incorporate Cr.

As a first step, we set out to determine if the Cr-bearing analogues $Fe_3Cr_2O_6$ and $Mg_3Cr_2O_6$ are stable. The conditions of our multianvil experiments were guided by two considerations: i) the known stability field Fe_5O_6 as recently determined by us, and ii) literature data indicating that the breakdown of chromite and magnesiochromite to the assemblages $Fe_2Cr_2O_5$ + Cr_2O_3 and $Mg_2Cr_2O_5$ + Cr_2O_3 occurs at somewhat higher pressures than in analogous Fe^{3+}-bearing compositions. We performed experiments over the pressure range of 14 to 20 GPa at 1200-1500 °C. So far, neither $Fe_3Cr_2O_6$ nor $Mg_3Cr_2O_6$ were able to be synthesised. The resulting run products always comprised an assemblage containing $Fe_2Cr_2O_5$ or $Mg_2Cr_2O_5$ instead. Considering that we recently demonstrated that only limited amounts of Mg can be incorporated into Fe_5O_6, it appears that the structure has only limited capacity to accommodate cations other than Fe^{2+} and Fe^{3+}.

f. *Synthesis of calcium (II) orthocarbonate, Ca_2CO_4, from different precursors (L.S. Dubrovinsky; Y. Yin, W. Zhou, A. Aslandukov, D. Laniel and N.A. Dubrovinskaia/Bayreuth, M. Hanfland/Grenoble)*

Carbonates play a crucial role in the long-term global carbon cycle. Models of subduction indicate a carbon influx of about several tens of megatons per year, which is mainly controlled by the contribution of carbonate sediments and altered carbonaceous oceanic crust. Over the past decades, theoretical and a few experimental studies demonstrated that all major carbonates, such as $CaCO_3$, $MgCO_3$, $FeCO_3$, and $CaMg(CO_3)_2$, may survive at the pressure/temperature conditions of certain regions of Earth's mantle, while displaying a variety of different polymorphs. However, due to different possible redox processes, carbonates have been proposed to be altered, forming metal carbides, CO_2, or diamond depending on the degree of reduction. Nevertheless, carbonate inclusions in diamonds originating from the deep mantle are direct evidence for oxidised carbon in the form of carbonates and their presence in at least some regions of the mantle. Cold oxidised subducting slabs with low reaction kinetics are believed to provide adequate conditions for hosting carbonates even at depths of the lower mantle.

A recent remarkable experimental discovery has been confirmed that so-called tetracarbonates form, in which sp^3-hybridisation leads to CO_4^{4-} tetrahedrons instead of triangular sp^2-hybridised CO_3^{3-} groups. Up to now, experimental syntheses of tetracarbonates were carried out at

pressures > 70 GPa, which led to the conclusion that only the deep lower mantle may provide the required physical conditions for their formation. While the phase diagram of $CaCO_3$ is fairly well constrained for the pressure and temperature conditions of Earth's upper and lower mantle, experimental studies focusing on different compositions on the CaO-CO_2 join have not been reported up to now. We therefore synthesised calcium orthocarbonate, Ca_2CO_4, from different precursors and determined its crystal structure.

We employed BX90 type diamond anvil cells (DACs) equipped with Boehler-Almax type anvils and rhenium gaskets. In three different experiments, DACs were loaded with mixtures of Ca, CaO, and $CaCO_3$, or $Ca(OH)_2$ and graphite, or Ca, CaO, and nitrogen. Cells were compressed to between 20 and 90 GPa and double-side laser heated (NIR laser, 1070 nm wavelength) up to 2500 K. DACs with their samples were transferred to the Extreme Conditions Beamline (PETRA III), GSECARS (APS), or ID27 beamline (ESRF) for *in situ* X-ray diffraction structural studies of the products of chemical reactions.

Diffraction data of each sample unequivocally show the formation of a new set of diffraction spots that could be indexed with an orthorhombic unit cell of *Pnma* space group. The structures were solved and refined for data sets obtained at 20, 38 and 90 GPa. The new phase is indeed calcium (II) orthocarbonate, Ca_2CO_4. The experimentally determined structure is characterised by 4-fold carbon coordinated by oxygen forming isolated CO_4 tetrahedra, while the Ca atoms, occupying two non-equivalent crystallographic positions, form CaO_9 and CaO_{11} polyhedra (Fig. 3.3-5). The CO_4 tetrahedra share corners, edges and faces with CaO_{11} polyhedra, while they only share corners and edges with CaO_9 polyhedra. CaO_9 and CaO_{11} polyhedra are also connected via polyhedron faces. The CaO_9 polyhedra are muffin-like, while CaO_{11} polyhedra form five-fold capped trigonal prisms. On average, C-O bond lengths decrease by ~ 3 % between 20 and 90 GPa. The change in bond lengths corresponds to a volume decrease of CO_4 tetrahedra of ~ 9 %. Ca-O distances of CaO_9 and CaO_{11} polyhedra decrease much more significantly, and the pressure-induced volume reduction is ~ 20 %. The change in distortion is smaller for calcium polyhedra compared to CO_4-groups.

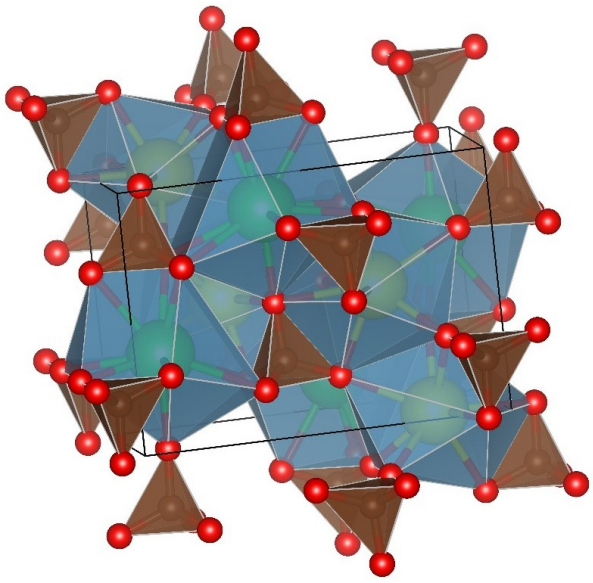

Fig. 3.3-5: Structure of calcium (II) orthocarbonate, Ca_2CO_4. Carbon atoms form isolated CO_4 tetrahedra (brown). The Ca atoms are located in two different sites and form CaO_9 (green) and CaO_{11} (yellow) polyhedrons.

g. *Phase relations in the SiO_2-Al_2O_3-H_2O system up to 28 GPa and water solubility of aluminous silicas (T. Ishii and H.-k. Mao/Beijing, E. Ohtani/Sendai, G. Criniti, N. Purevjav, H. Fei and T. Katsura)*

Water cycles between Earth's surface and interior by subducting plates and upwelling plumes, affecting the evolution of Earth's interior. It has long been known that basalts found in ocean island volcanoes, whose magmas are considered to have originated in the lower mantle, contain more water than other basalts. This observation suggests that the lower mantle is potentially a major water reservoir. However, previous high-pressure/-temperature experiments have shown that the dominant lower mantle minerals in peridotite, which comprises the lower part of subducting plates, can hold only limited water, less than 0.1 wt. %. Thus, water subducted into the lower mantle may be stored in minerals in the basaltic crust, which constitutes the upper layer of subducting plates.

We investigated phase relations in hydrous aluminous silica systems, which are abundant components of basaltic crust, at uppermost lower mantle conditions (24-28 GPa and 1000-2000 °C) using a multianvil press. We found that the alumina content in silica increases with temperature (Fig. 3.3-6a) and the water content generally increases with increasing alumina content (Fig. 3.3-6b), thus suggesting a positive temperature dependence of water solubility in aluminous silicas. This feature is opposite to other nominally anhydrous phases which show a

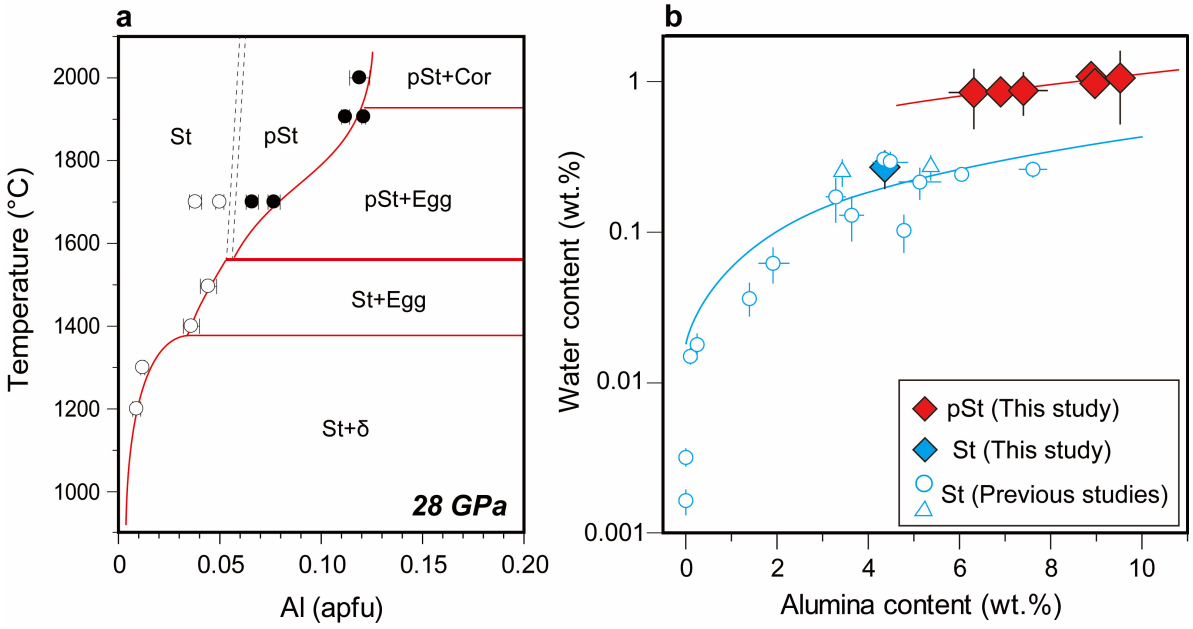

Fig. 3.3-6: (a) Phase relations in the SiO_2-Al_2O_3-H_2O system at 28 GPa. (b) Water content of silica phases with increasing alumina content.

negative temperature dependence. When the alumina content exceeds 5 wt. %, aluminous stishovite transforms to a $CaCl_2$-type phase, which can contain more than 1 wt. % water, even at upwelling plume temperatures. The water content is more than 10 times higher than that of

other nominally anhydrous minerals in the lower mantle. Water released from other minerals can be recaptured by aluminous silicas in the basaltic layer of the subducting plate, transporting water into the deeper mantle. $CaCl_2$-type hydrous aluminous silica can also transport water from the deep lower mantle to the upper mantle by upwelling plumes, suggesting that it may be the most promising candidate for transporting water in the mantle.

h. *Deuterium content and site occupancy in iron sulphide at high pressure and temperature using* in situ *neutron diffraction experiments (S. Abeykoon, C. Howard, S. Dominijanni, L. Eberhard, A. Kurnosov, D.J. Frost and T. Boffa Ballaran; H. Terasaki/Okayama; T. Sakamaki, A. Suzuki and E. Ohtani/Sendai; A. Sano-Furukawa and J. Abe/Tokai)*

Sulphides are a common accessory mineral in the upper mantle and a predominant inclusion in diamonds. They are also thought to be associated with core-forming melts during planetary differentiation processes. Previous experimental studies have indicated that iron sulphide minerals and melts may contain significant amounts of hydrogen at high pressure and temperature. Similar to many metal hydrides, however, hydrogen is likely lost from sulphide minerals and melts during quenching and can only be determined by measurements made at high pressure and temperature.

In situ time-of-flight (TOF) neutron powder diffraction measurements were performed to study the solubility of deuterium in FeS from 2.3 to 11.4 GPa in the temperature range 787-1300 K using a multi-anvil apparatus installed at the PLANET beamline of the J-PARC spallation neutron source (Tokai, Japan). Deuterium solubility is expected to be the same as that of hydrogen and was employed as a proxy to reduce background in the neutron diffraction data caused by incoherent scattering of hydrogen. Compressed powders of FeS were sandwiched between pellets of ND_3BD_3, which releases D_2 on heating. TOF neutron diffraction measurements were collected for up to 19 hours at high pressure and temperature on the NiAs-structured $Fe_{1-x}S$ pyrrhotite polytype, referred to as FeS V. The collected diffraction data were analysed by Rietveld refinement using the structural model for FeS V with Fe at the *2a* $\{0, 0, 0\}$ and S at the *2c* $\{1/3, 2/3, 1/4\}$ Wyckoff positions of the $P6_3/mmc$ space group. No extra reflections were observed, indicating that the symmetry of the deuterated phase is identical to that of FeS V. However, significant discrepancies were found between intensities of the observed high pressure and temperature patterns and those calculated with the FeS V structure. A difference Fourier map was generated showing nuclear densities at two positions that after refinement could be identified as the *6h*: $\{0.46(2), 0.54(2), 3/4\}$ and *4f*: $\{1/3, 2/3, 0.03(3)\}$ Wyckoff positions (Fig. 3.3-7). The partial deuterium occupancy in both sites could be refined with the latter position showing a greater occupancy.

Expansion of the unit cell parameter of FeS V at 6.9 GPa and 960 K due to the incorporation of deuterium was monitored in a series of diffraction measurements over five hours. The extent of the unit cell expansion was confirmed by a deuterium-free experiment at nearly the same conditions that showed no comparable expansion. The difference in unit cell volumes at these conditions is approximately 4.3 %, and the unit cell volume expansion per deuterium atom,

$\Delta V(D)$, is 1.53 ± 0.16 Å^3, which is smaller compared to that previously reported for Fe-metal hydrides at similar conditions (2.21 ± 0.04 Å^3). Our structural model shows that both deuterium positions are much closer to S atoms than to Fe atoms, which implies that S and D may form covalent bonds. If this is the case, it might explain the smaller $\Delta V(D)$ value compared to Fe-metal hydrides. Refinements of all diffraction patterns collected indicate that the D content in FeS V increases with both pressure and temperature. The total deuterium content, *x* in FeSD*x*, increases from 0.148(10) at 2.3 GPa and 787 K to 1.25(5) at 9.7 GPa and 1300 K. A comparison between FeSD*x* and FeH*x*/FeD*x* shows that there is general agreement in the magnitude of H/D occupancy with increasing pressure. The deuterium dissolved in FeS V at high temperature is mainly lost during temperature quenching at high pressure, as indicated by the decrease in unit cell volumes of the quenched experiments.

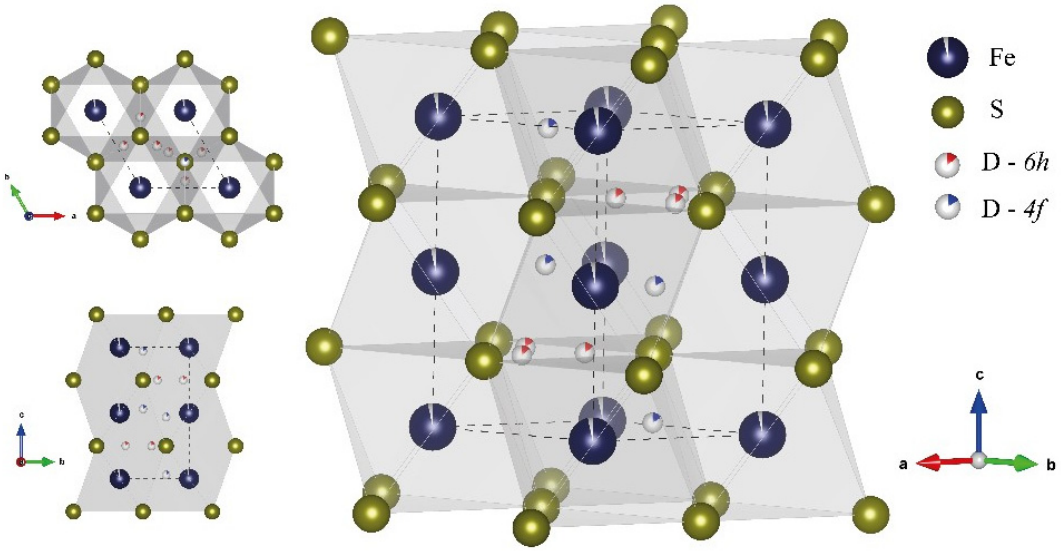

Fig. 3.3-7: Final structural model of deuterated FeS V ($P6_3/mmc$, Z=2) at 6.9 GPa and 960 K. The dashed lines mark the unit cell of FeS V, and sections viewed along the *c*- and *a*-axes of the structure are shown on the left.

The experimentally determined deuterium contents in FeS V were fitted to a thermodynamic model, which allows results to be extrapolated to different pressures, temperatures and oxygen fugacities. The model confirms that FeS V deuterium contents should drop to low levels on temperature quenching at high pressure. It can also be used to show that at oxygen fugacities compatible with the base of the cratonic lithosphere where diamond formation occurs, FeS V, which forms the main type of inclusion in diamonds, could contain significant amounts of hydrogen in the range 1700-2700 ppm. It is proposed that loss of hydrogen from diamond-hosted FeS V during decompression could play a role in the development of the rosette-like fracture systems often observed around sulphide inclusions in diamonds. Based on an average mantle sulphur content of 400 ppm, it is expected that at the base of the cratonic lithosphere a bulk mantle H_2 content of 2-3 ppm could be hosted by mantle sulphides. At greater depths, lower oxygen fugacities and melting of FeS V may lead to higher hydrogen contents in sulphides.

i. *Twinning in hydrous wadsleyite: Symmetry and relation to ringwoodite (N. Miyajima, J. Buchen/Oxford and T. Kawazoe/Hiroshima)*

Hydrous wadsleyite has the capacity to store water in the transition zone of Earth's mantle. The structure of anhydrous wadsleyite has orthorhombic symmetry (*Imma*), but samples of hydrous wadsleyite may be distorted to monoclinic symmetry (*I*2/*m*) depending on their water and iron contents. The symmetry reduction induced by hydration might give rise to twinning in the low-symmetry structure by the loss of symmetry elements, *i.e.*, mirror planes (*m*). To confirm the existence of twins and their symmetry relations, we studied twins in hydrous wadsleyite crystals.

We detected twins in hydrous wadsleyite by polarised-light microscopy (Fig. 3.3-8) and characterised the twin relations and symmetry of twin domains with transmission electron microscopy (TEM) techniques, including precession selected area electron diffraction (SAED) and large-angle convergent beam diffraction. Based on electron diffraction patterns for high-order Laue zones, we found the symmetry of the twin domains to be reduced to monoclinic, as expected for hydrous wadsleyite. Twinned domains in hydrous wadsleyite share the (244) plane as the composition plane (Fig. 3.3-9). The twin domains are related by two-fold rotation around a twin axis parallel to [212] or by reflection on (244). This twin law, however, is inconsistent with twinning by symmetry reduction as a result of hydration. Instead, the twin axis and twin plane in wadsleyite correspond to the <101> directions and the {101} planes of ringwoodite, respectively. The twin operations exchange the *c** and the [120]* directions of wadsleyite, both of which correspond to the directions of the cubic *a*-axes in ringwoodite. Based on our TEM analysis of symmetry relations and pseudo-symmetry in wadsleyite, we therefore conclude that the twins formed during crystal growth under quasi-hydrostatic conditions in the presence of a hydrous fluid. The atomic structure in the vicinity of the interface between twin domains likely resembles the crystal structure of ringwoodite. As a result, twins in hydrous wadsleyite may provide favourable sites for the nucleation of ringwoodite lamellae.

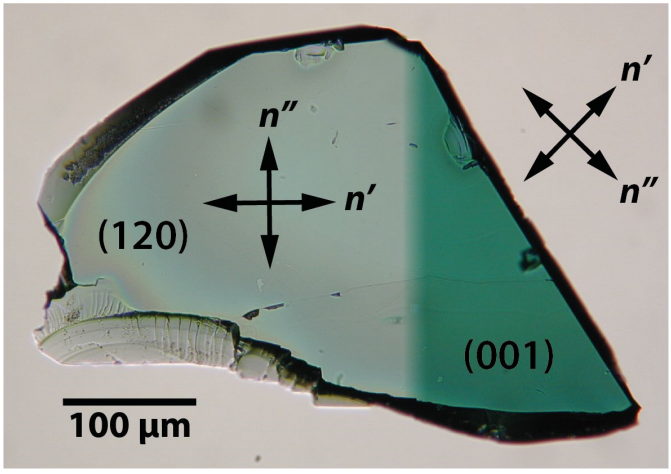

Fig. 3.3-8: Polarised light microscope image of a twinned crystal of hydrous wadsleyite.

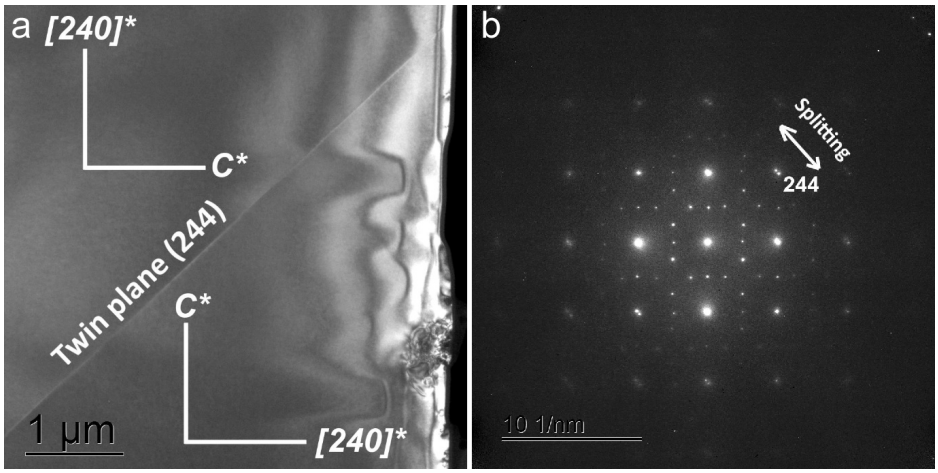

Fig. 3.3-9: (a) Dark-field TEM image (with **g** = 244) of a twinned wadsleyite grain. (b) SAED pattern of the [210] zone axis from an area including the composition plane.

j. *A new evaluation method of cation ordering history in eclogite-facies omphacite (R. Fukushima and T. Tsujimori/Sendai, N. Miyajima)*

Low-temperature eclogite, which commonly occurs in Phanerozoic subduction-related orogens, has received considerable attention because of its crucial role as a natural laboratory for subduction-zone geodynamics. Notably, omphacite (~$Ca_{0.5}Na_{0.5}[Mg,Fe^{2+}]_{0.5}Al_{0.5}Si_2O_6$), an index mineral of eclogite facies, has the potential to reveal kinetics of eclogitisation of subducted oceanic crust. For example, growth and coarsening of antiphase domains (APDs) – a disequilibrium microstructure reflecting a higher-order phase transformation from cation-disordered (*C*2/*c*) to cation-ordered (*P*2/*n*) states – occurs within blueschist- to eclogite-facies omphacites (Fig. 3.3-10a,d). Therefore, detailed analysis of APD textures, even for each omphacite grain, enables a discussion of its temperature-time (*T*-*t*) history.

Thus far, geoscientists have struggled to utilise disequilibrium textures in metamorphic minerals to unravel past geological processes. Reconnaissance of APD textures in omphacite has proved to be challenging for obtaining a specific snapshot of its time evolution. Based on the classical APD-coarsening law in alloys and size dependence on annealing time and temperature, pioneering work in the literature proposed a geospeedometer using the mean size of equiaxed APDs in omphacite. Nevertheless, a question arises whether the parameter 'mean APD size' is truly appropriate to evaluate various metamorphic *T*–*t* paths in general. This is because variations in chemical composition and density of vacancies in natural omphacites might affect individual nucleation/growth rates of initially ordered domains.

To tackle this problem, we extracted multiple characteristic values from dark-field transmission electron microscope (TEM) images of omphacite in epidote eclogites from two different localities: Syros (Greece) and Omi (Japan). With digital image processing, we obtained four parameters for each: 1) mean APD size: δ (manually measured along 200 × 200 nm^2 grids); 2) area proportion of the ordered phase: *F* (Fig. 3.3-10b,e); 3) spatial wavelength calculated from

2-dimensional autocorrelation: λ (Fig. 3.3-10b,e); and 4) spatial density of antiphase domain boundaries: L (Fig. 3.3-10c,f). Because λ and L values are respectively related to representative distances of adjacent ordered domains and their spatial density, these parameters could reveal nanotextural changes in the APD nucleation-growth regime. Despite the different magnifications and resolutions of the two images, our results clearly demonstrate that ordered domains in the Syros omphacite are smaller and more sparsely distributed in the disordered matrix. We can interpret the cause as either annealing time difference, temperature difference, or compositional difference that regulates the initial stage of APD appearance. This result suggests that natural omphacite can be incompletely ordered, which would imply that simple application of the coarsening rate law is prohibited. Our method for post hoc analysis of equiaxed APD textures provides a new way to investigate APD growth/coarsening kinetics in omphacite, which has previously not been possible using only mean APD sizes.

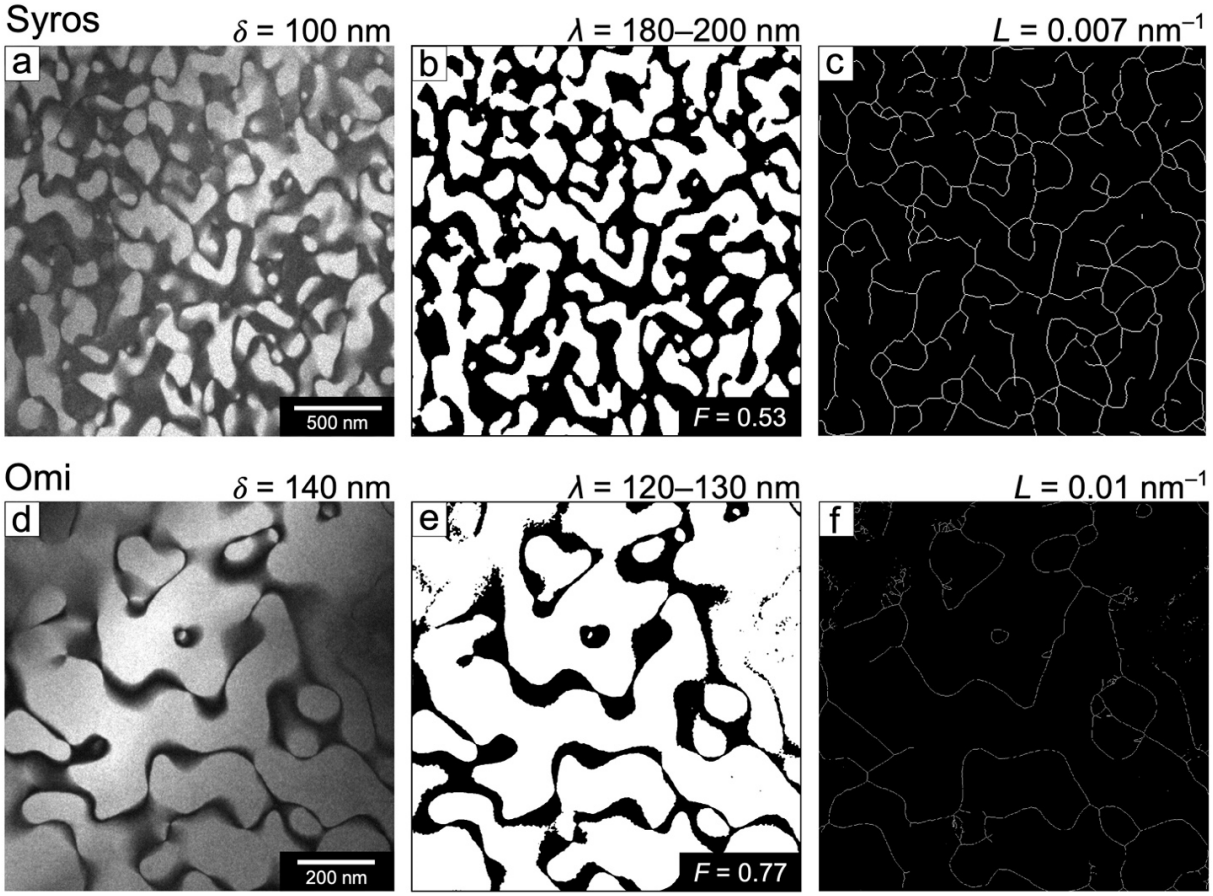

Fig. 3.3-10: Examples of acquired/processed TEM images of natural omphacites from Syros (a-c) and Omi (d-f). (a) dark-field TEM image with g = 050 showing equiaxed APDs (δ = 100 nm); (b) binarised image with black/white regions as disordered/ordered domains, respectively (F = 0.53, λ = 180-200 nm); (c) antiphase domain boundaries (1-pixel width) extracted from the binarised image (L = 0.007 nm^{-1}); (d) dark-field image with g = 050; δ = 140 nm; (e) binarised image (F = 0.77, λ = 120-130 nm); (f) antiphase domain boundaries (L = 0.01 nm^{-1}). Note that the two TEM images (a and d) are different in magnification and resolution. Image processing was performed with MATLAB scripts.

3.4 Physical Properties of Minerals

The structure and properties of Earth's mantle and core, of the meteoritic building blocks of planets, and of the interiors of exoplanets, can be fully understood only in light of our knowledge of the physical properties of the constituent minerals. Contributions in this chapter use various combinations of high-pressure experimental techniques, both at BGI and at synchrotron facilities, paired with X-ray techniques, sound velocity measurements, molecular dynamics simulations, and ultrasonic interferometry, to obtain new measurements of mineral properties that are of importance to Earth and planetary science.

Seismology gives us a view of Earth's interior. Without precise measurements of the physical properties of minerals, however, the full potential of seismic data to place tight constraints on compositional variations within the Earth cannot be realised. The first two contributions in this chapter use acoustic wave velocity measurements to investigate the effect of compositional variation on the elastic properties of mantle minerals. The ability of nominally anhydrous minerals to incorporate trace amounts of hydrogen increases with pressure in the upper mantle. Even small amounts of hydrogen can have large effects on rheological properties and melting temperatures. Olivine, the most abundant phase of the upper mantle, can dissolve hydrogen in amounts that approach the wt. % H_2O level at pressures at the high end of its stability field. Since adding hydrogen to mantle minerals can have a considerable effect on their elastic properties, it has been hypothesised that hydration of the mantle could be the cause of deviations in observed seismic signals with respect to those expected for an olivine-rich, pyrolytic composition. In the first contribution, the seismic properties of olivine containing 0.2 wt. % H_2O were investigated at pressures that cover the entire pressure range of olivine stability. Results of high-pressure Brillouin scattering and X-ray diffraction measurements showed that sound velocities for hydrogen-bearing olivine at high pressure are indistinguishable from anhydrous olivine, suggesting that hydration of the mantle cannot explain anomalous seismic signatures. In the second contribution, the seismic properties of Al-rich phases that are expected to be present in slabs subducted into the lower mantle were investigated. Notably, and in contrast to previous studies, the calcium-ferrite structured phase (so-called CF phase) used in the experiments was Fe-bearing. Elastic moduli and seismic velocities calculated from high-pressure Brillouin measurements, together with X-ray diffraction, were lower than those reported in previous computational and experimental studies on iron-free samples, indicating that the presence of Fe may have a considerable influence on the elastic properties of deeply subducted slabs.

The third contribution reports the results of high-pressure synchrotron X-ray diffraction measurements of Al-rich hydrous phases. Such phases may play an important role in transporting H_2O to the lower mantle in deeply subducted slabs. In order to calculate the stability of such phases, it is important to have an accurate parameterisation of how their volumes change with pressure. Results for Mg-, Si- and Fe^{3+}-bearing samples of $CaCl_2$-type oxyhydroxides show that compression is affected by the spin transition of Fe^{3+}, but that the transition takes places over a considerably larger pressure interval when Si is present on the same crystallographic site as Fe^{3+}.

The fourth contribution uses computational methods that include machine learning to determine the diffusivity of core components at inner core/outer core boundary pressures. From these results it was possible to calculate the effects of hydrogen and carbon on the viscosity of the metallic liquid. The decrease in viscosity associated with these light elements and the overall inviscid character of the outer core have important consequences for heat transfer and hence for the intensity of Earth's geodynamo.

Recent and ongoing missions to Mars are returning remarkable data from which we can learn much about the Martian interior. However, in order to interpret these new findings, it is critical to determine the physical properties of materials with appropriate compositions for Mars. The fifth and sixth contributions provide elastic measurements of relevant Martian materials. In the fifth contribution, acoustic velocities of Fe-rich olivine were measured at pressures of up to 5 GPa, which is equivalent to depths greater than 400 km in the Martian mantle. Relative to terrestrial olivine, the extra Fe in Martian olivine causes a reduction in seismic wave velocities relative to Earth. Such measurements are critical for interpreting seismic data from the recently completed InSight mission. The sixth contribution uses novel experimental designs developed at BGI in combination with synchrotron radiation to measure *in situ* X-ray scattering, radiography, and ultrasonic interferometry, to reveal the structure and density of FeS liquid. The observation by InSight of a large and light-element-rich core for Mars require such data to build a thermoelastic model for Martian core materials.

The seventh contribution investigates the equation of state of silicon carbide, using *in situ* X-ray diffraction in a multianvil press using synchrotron radiation. Silicon carbide may be a major component of exoplanets in star systems that have a higher carbon budget than our own. Accurate determination of pressure-volume-temperature relations is therefore important, and using the large-volume multianvil apparatus at pressures that approach 30 GPa offers a considerable improvement in precision on the temperature determination over laser-heating diamond anvil cell techniques.

The final contribution aims to explain the enigmatic textures observed in primitive achondritic meteorites. Analog achondritic material was created by mixing olivine, troilite and gold, and was annealed in long-duration multianvil experiments, after which textures were documented using optical microscopy. It was found that grain boundary migration annihilates the minimised surface energy configuration in bi-metallic two-phase mixtures. This means that, rather than requiring high temperatures above the melting point of metallic alloys, textures observed in the meteorites can be produced by annealing processes.

a. *Sound velocities and single-crystal elasticity of hydrous Fo90 olivine to 12 GPa (L. Faccincani/Ferrara, G. Criniti, A. Kurnosov, T. Boffa Ballaran, A.C. Withers, M. Mazzucchelli/Modena, F. Nestola/Padova and M. Coltorti/Ferrara)*

Although commonly referred to as nominally anhydrous minerals (NAMs), the dominant phases of Earth's upper mantle may contain significant amounts of water. The colloquial term "water" in NAMs is related to the presence of hydroxyl-bearing (OH-) point defects in their

crystal structure, where hydrogen is bonded to lattice oxygen and is charge-balanced by cation vacancies. Thus, the incorporation of even small amounts of water may substantially affect the physical properties of NAMs, such as their elasticity, rheology, and melting temperature. Olivine is considered the most abundant phase of Earth's upper mantle and constitutes about 60 vol. % of a primitive upper mantle (pyrolite) phase assemblage. Although natural olivine samples originating from the shallow upper mantle are relatively dry (maximum H_2O concentrations of about 400 ppm), a plethora of experimental data indicate that olivine may host up to 0.2-0.5 wt. % H_2O at deeper upper mantle conditions.

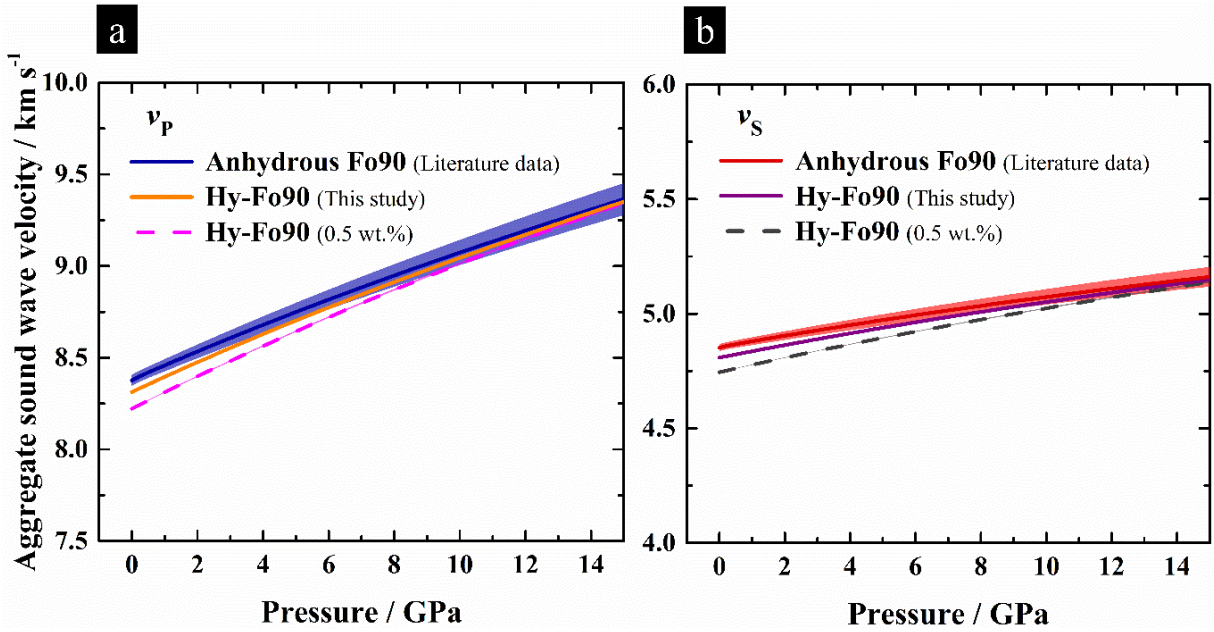

Fig. 3-4.1: Variation as a function of pressure of the aggregate sound wave velocities v_P (a) and v_S (b) of hydrous and anhydrous Fo90 olivine. The solid lines and shaded area are, respectively, the fit of the experimental data (not shown here), obtained with third-order finite strain equations of state, and the associated uncertainties, calculated by propagating the experimental errors on density and elastic moduli. The dashed lines represent a linear extrapolation of the effect of incorporation of 0.5 wt. % H_2O on the elastic properties of Fo90 olivine, which were then converted into velocities. Although at ambient conditions the sound wave velocities of hydrous olivine are slightly offset to lower values, they become indistinguishable within uncertainties with those of the corresponding anhydrous phase at deep upper mantle conditions.

We have investigated the effect of water on the elastic properties and sound wave velocities of hydrous $Mg_{1.8}Fe_{0.2}SiO_4$ (Fo90) olivine samples with realistic water contents for deep upper mantle conditions with the aim of interpreting both seismic velocity anomalies in potentially hydrous regions of Earth's upper mantle and the observed seismic velocity and density contrasts across the 410-km discontinuity between the upper mantle and the transition zone. To do so, we performed simultaneous single-crystal X-ray diffraction and Brillouin scattering

measurements at room temperature up to ~ 12 GPa on Fo90 olivine with ~ 0.20 wt. % H_2O to constrain its anisotropic elastic properties. Results are complemented with a careful re-analysis of all the available single-crystal elasticity data from the literature for anhydrous Fo90 olivine.

The variation with pressure of the aggregate sound wave velocities (v_P and v_S) of hydrous Fo90 olivine is reported in Figure 3-4.1 and compared with that obtained for anhydrous Fo90 olivine from the re-analysed literature data. Although v_P and v_S of hydrous and anhydrous Fo90 olivines are slightly different at ambient conditions, they become indistinguishable within uncertainties at pressures corresponding to the base of the upper mantle. Therefore, if amounts of water were to be incorporated into the crystal structure of Fo90 olivine, its elastic and seismic behaviour at high pressure would likely remain unchanged. This suggests that hydrous olivine is not seismically detectable, at least for water contents consistent with deep upper mantle conditions. Moreover, the incorporation of water in olivine is unlikely to be a key factor in reconciling seismological observations at the 410-km discontinuity with a pyrolitic mantle, but rather corroborates previous evidence of a deep upper mantle that is less enriched in olivine than the pyrolite model.

b. *High-pressure elasticity of (Na,Mg,Fe)(Al,Si,Fe)$_2$O$_4$ calcium-ferrite type phase (E.-M. Rogmann, X. Wang, G. Criniti, A. Kurnosov, T. Boffa Ballaran and D.J. Frost)*

The calcium-ferrite-type phase (CF) is anticipated to be the dominant Al-bearing phase in MORB compositions throughout most of Earth's lower mantle. As such, it may play a significant role in determining the seismic signature of slabs subducting into the lower mantle and therefore it needs to be properly accounted for in mineral-physics models aimed at constraining the composition of these Earth regions. To date, however, the elastic properties of CF phases have been determined only in computational studies on simple compositions along the $NaAlSiO_4$ – $MgAl_2O_4$ join. Only one experimental study has been performed so far using a polycrystalline sample for which only the shear-wave velocity could be measured. In this study, we determined the single-crystal elastic properties and acoustic wave velocities of a Fe-bearing CF-type phase with a composition that better represents that which may be encountered in MORB.

For this study, two differently oriented crystal platelets of CF were loaded into the same DAC with He as the pressure-transmitting medium. The samples were studied at room temperature over six pressure points up to 26 GPa, *i.e.*, a pressure equivalent to that at the top of the lower mantle. The acoustic velocities were determined using Brillouin scattering (Fig. 3-4.2), whereas density was measured at the same pressure points by means of single-crystal X-ray diffraction. The density and acoustic velocity measurements were used to constrain self-consistently the evolution with pressure of the full elastic tensor of the CF phase.

The variation of the unit-cell lattice parameters shows a strong anisotropy in axial compressibility. In particular, the *c*-axis was found to be the stiffest direction with a linear bulk

modulus of 757(5) GPa, whereas the *a*- and *b*-axes have similar compressibility and are significantly softer. The linear compressibility obtained by inverting the elastic stiffness coefficients at each pressure is in excellent agreement with that obtained from the X-ray diffraction data. Elastic moduli and seismic velocities were found to be lower than reported both in previous computational studies and in the experimental study, suggesting that the presence of 0.25 Fe per formula unit significantly affects the acoustic wave velocities of this phase. The anisotropy of the CF phase is significant in both v_P ($Av_{P,0}$ = 17.4 %) and v_s ($Av_{S,0}$ = 16.3 %) and decreases towards higher pressures.

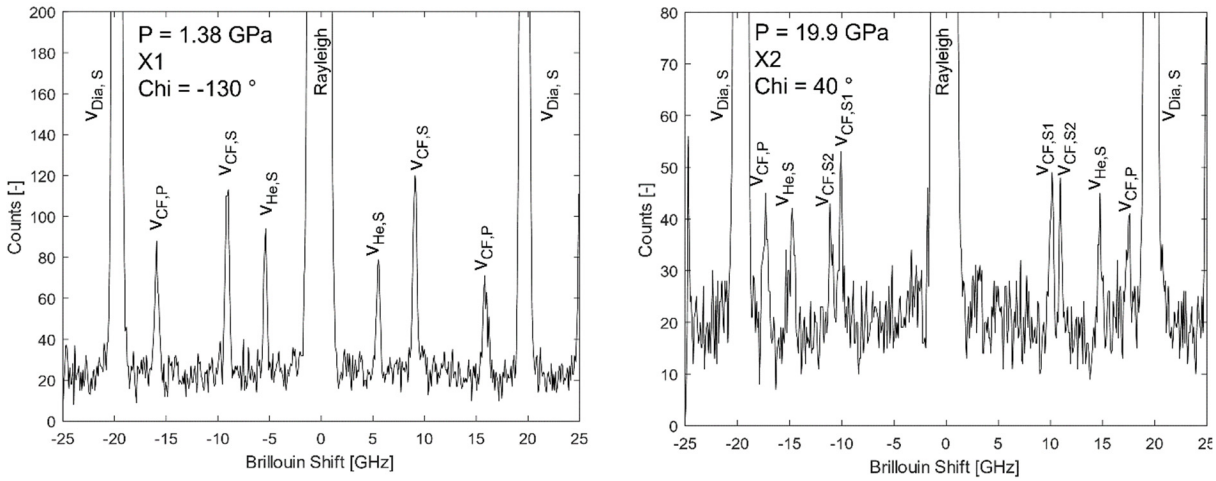

Fig. 3-4.2: Examples of Brillouin spectra collected for different orientations (Chi angle) and different pressures for the two crystal platelets of the CF phase. Two transverse modes can be observed for the (661) platelet (X2), while only one transverse mode can typically be observed for the (242) platelet (X1).

c. *Compressibility and mixing behaviour of $CaCl_2$-type oxyhydroxides (G. Criniti, A. Kurnosov, T. Boffa Ballaran and D.J. Frost, in collaboration with T. Ishii/Beijing, K. Glazyrin/Hamburg and J. Buchen/Oxford)*

Oxides and oxyhydroxides with $CaCl_2$-type structure, including δ-AlOOH, ε-FeOOH, $MgSiO_4H_2$ phase H, and SiO_2 post-stishovite, are the main carriers of water in hydrous peridotitic and basaltic rocks subducted into Earth's lower mantle. The presence of strong, symmetric H-bonds in their crystal structures makes these phases resistant to high temperatures and stiffer than other dense hydrous silicates. Additionally, the pressure-induced spin crossover of Fe^{3+} in ε-FeOOH causes the bulk modulus to soften at shallow lower mantle conditions, where it could be detected by seismic methods. Despite their importance, the solid solution behaviour and compressibility of $CaCl_2$-type phases along the AlOOH-SiO_2 and AlOOH-$MgSiO_4H_2$ joins, as well as the effect of Si incorporation on the spin crossover of Fe, have not been studied yet. To address this problem, we conducted synchrotron X-ray diffraction measurements on three Al-rich samples with $CaCl_2$-type structure at high pressure using

diamond anvil cells (DAC). The samples were synthesised in a multianvil apparatus at 27 GPa and 1573 - 1673 K from mixtures of reagent-grade oxides and hydroxides sealed in a Pt-tube capsule. Electron microprobe analyses revealed that the samples had the following compositions: $Al_{0.80}Si_{0.11}Mg_{0.09}O_2H_{0.98}$, $Al_{0.71}Si_{0.16}Mg_{0.13}O_2H_{0.97}$, and $Al_{0.72}Si_{0.19}Fe_{0.09}O_2H_{0.81}$, where the H content was inferred from charge balance calculations assuming two oxygens and one cation per formula unit. A Mössbauer spectrum was also collected on a mosaic of selected crystals from the Fe-bearing batch, revealing that 98(1) % of the total Fe is in the ferric state.

High-pressure diffraction experiments were carried out at the Extreme Conditions Beamline P02.2 of PETRA-III at DESY (Hamburg, Germany) over three separate runs. The two Fe-free samples were loaded in the same DAC and compressed up to about 50 GPa in a single run, while the Fe-bearing sample was compressed to 25 GPa in the first run and to 100 GPa in the second one. The resulting compression curves were determined using a ruby sphere as pressure standard and are shown in Figure 3.4-3. Unlike pure δ-AlOOH, all three samples exhibited the *Pnnm* space group already at room pressure. The unit-cell volume of the two Fe-free samples

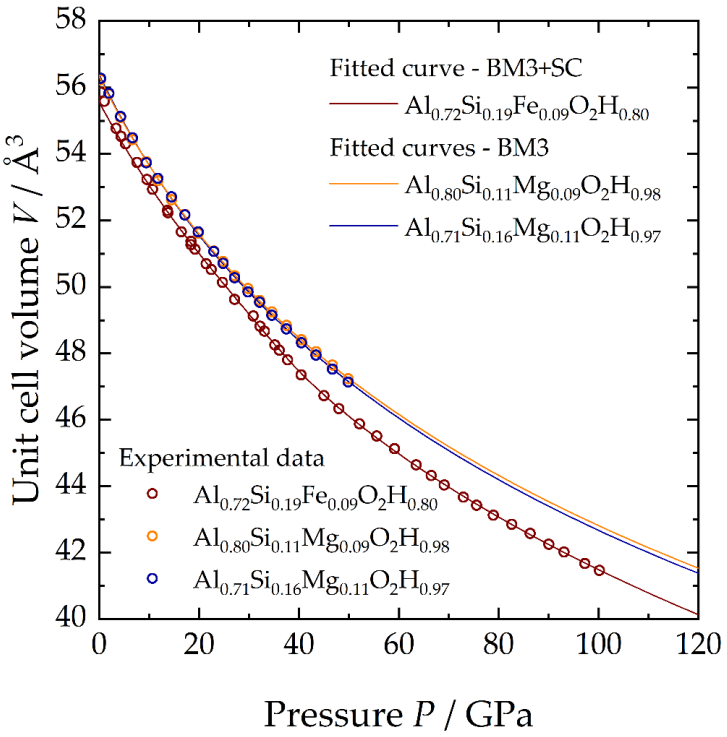

Fig. 3.4-3: Pressure-volume relations of $CaCl_2$-type phases investigated in this study (empty circles) and their respective 3rd order Birch Murnaghan (BM3) or spin-crossover (BM3+SC) equations of state (solid lines).

was found to decrease smoothly up to the maximum pressure investigated and 3rd order Birch-Murnaghan (BM3) equations of state were found to fit well the experimental pressure-volume data sets. The obtained fit parameters reveal a rather weak compositional effect on the bulk

modulus and its pressure derivative relative to δ-AlOOH. The compression behaviour of the Fe-bearing sample, on the other hand, was found to significantly change above 28 GPa, highlighting the onset of a high- to low-spin crossover of Fe^{3+}. To account for the spin transition of Fe^{3+} in our fit procedure, we used a modified BM3 equation of state that employs crystal field parameters to model the variation of the internal energy (and thus of pressure) in the sample due to changes in the electronic configuration of Fe ions. Our analysis revealed that the spin crossover of Fe^{3+} in our sample takes place between about 25 and 55 GPa and is significantly more spread out than in Si-free samples, possibly as a result of Al, Si, and Fe coexisting in the same crystallographic site. Combined with previous mineral physics and phase relations data, our results will be used to model the thermodynamic behaviour of complex solid solutions of $CaCl_2$-type oxyhydroxides and to calculate their stability in different chemical systems at the conditions of Earth's lower mantle.

d. *The viscosity of Fe and Fe-alloys at conditions of Earth's core (X. Wang, L. Yuan and G. Steinle-Neumann)*

The transport properties of Earth's outer core, including viscosity (η) and diffusion coefficient (D), directly control its fluid motions and thus the generation of a stable geodynamo. Yet these transport properties remain controversial due to the complexity of Earth's core composition and challenges in high pressure-temperature (P–T) experiments. Quantum mechanical simulations provide an alternative route to explore Earth material properties at relevant P–T conditions. These numerical simulations, however, are constrained by computational limits in space (system size < 200 atoms) and time (run duration < 50 picoseconds). Here, we overcome these limitations by performing large-scale molecular dynamics simulations with machine learning potential, and examining system size effect on the transport properties of Fe, FeH_x, and FeC_x at conditions relevant to Earth's inner core boundary.

Our computational results show that, while there is no discernible system size effect on η (Fig. 3-4.4a), the diffusion coefficient in a small system (108-Fe atoms) is underestimated by ~ 25 % compared to that in a larger (55296-Fe atoms) system (Fig. 3-4.4 b). As a computationally less demanding alternative to the Green-Kubo (G-K) method for calculating η, the Stokes-Einstein (S-E) relation has often been used to estimate η from diffusivity. Despite its popularity, we find that the S-E relation does not hold at core conditions, with η predicted by the S-E relation having values smaller by approximately one order of magnitude than the ones from the G-K method (Fig. 3-4.4c). Since Earth's core does not consist of pure iron but contains some light impurities, we further calculate transport properties for hydrogen- and carbon-bearing liquid iron and find that its η is lowered by 20 % when it contains 0.3 wt. % hydrogen and by 15 % when it contains 3.6 wt. % carbon (Fig. 3-4.4d,e). Based on our modelling results, the viscosity of the outer core is in the order of 10^{-2} Pa·s, which supports an inviscid character of Earth's outer core and scenarios in which the geodynamo would be enhanced by the turbulent flows driven by tides in the early history of Earth.

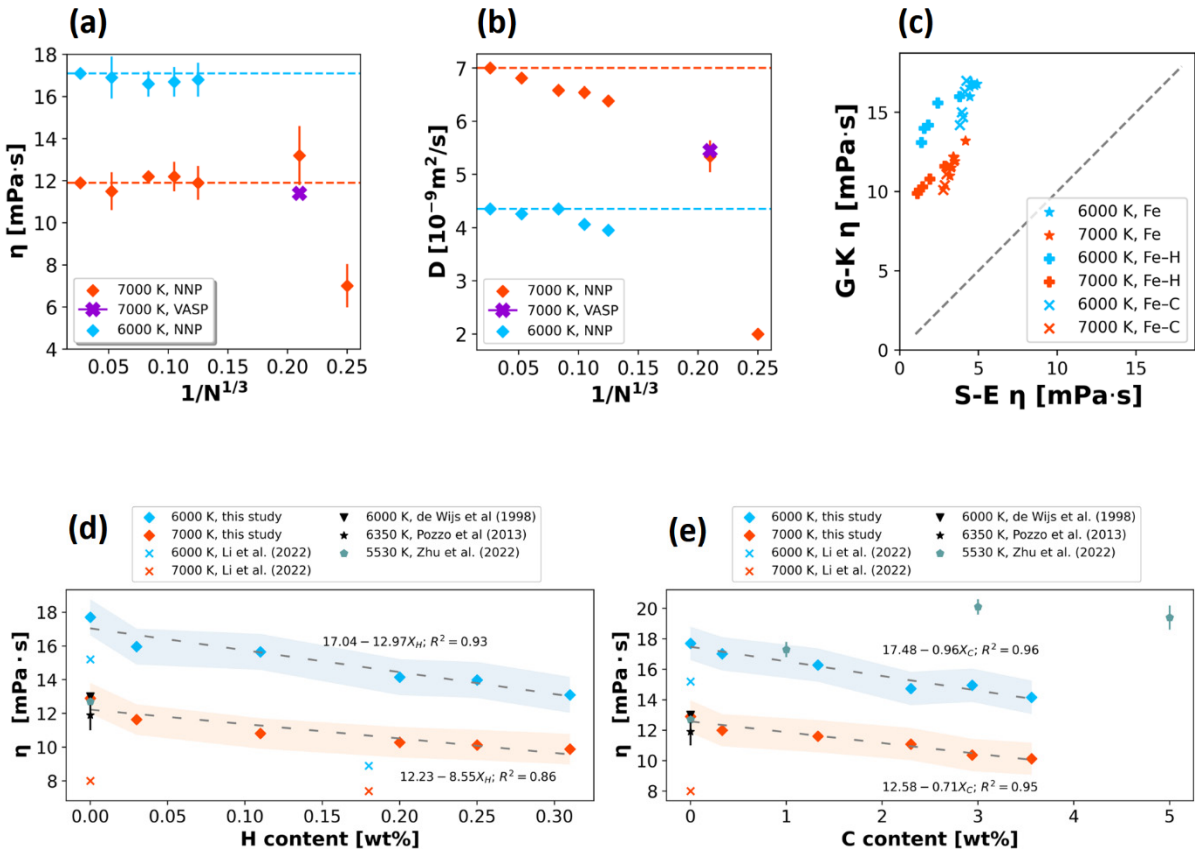

Fig. 3-4.4: Calculated viscosities (η) and self-diffusion coefficients (D) for liquid iron with respect to system size and light element concentration. (a) η computed from the Green-Kubo (G-K) method showing a limited size dependence for system sizes > 108 atoms. (b) D computed from the Einstein relation showing a noticeable finite size effect, with a difference of ~ 25 % in D between the smallest and largest system. (c) Comparison of η from the S-E relation and the G-K method for Fe (star symbols), FeH_x (plus symbols), and FeC_x (cross symbols) at 6000 K (blue colour) and 7000 K (red colour). The dashed line shows the 1:1 correspondence. (d, e) η of FeH_x and FeC_x as a function of light element concentration (x) at 6000 K (blue) and 7000 K (red).

e. *The elastic properties of martian olivine (A. Kurnosov, T. Boffa Ballaran, G. Criniti, A.C. Withers and D.J. Frost)*

As observations of the seismic wave velocity structure of the martian interior are becoming available from the SEIS seismometer incorporated into the NASA InSight lander, the comparison of these results with mineralogical and petrological models offers the opportunity to infer plausible compositions of and temperature gradients within the martian interior. The amount of iron present in martian rocks, which is significantly larger than that observed in terrestrial settings, is expected to be the major cause of the difference in the seismic signature of Mars in comparison to Earth.

The main mineral in the upper martian mantle is olivine, $(Mg,Fe)_2SiO_4$, which, from the analysis of the rock samples collected by Curiosity rover in Gale crater of Mars, appears to contain at least 0.5 atoms per formula unit (apfu) of Fe and even up to 0.8 apfu. To account for the effect of this large amount of iron in mineral physics models, the usual procedure is to use a linear extrapolation between the thermoelastic properties of the two end-member components, *i.e.*, forsterite, Mg_2SiO_4, and fayalite, Fe_2SiO_4. However, due to the fact that the end-member elastic properties values reported in the literature are quite scattered (for example, the bulk modulus value of fayalite ranges between 125 and 135 GPa depending on the study) it is difficult to assess which linear extrapolation between the elastic moduli of the two end-members need to be used or even whether any linear extrapolation is actually correct. Moreover, there are only a few constraints on the high-pressure/high-temperature behaviour of these end-member minerals, resulting in large uncertainties when the thermoelastic properties are calculated at temperatures consistent with the martian mantle. The aim of our study is therefore to accurately determine the high-pressure and high-temperature elastic properties of a single-crystal of olivine having the composition $Mg_{1.44}Fe_{0.56}SiO_4$ in order to provide the correct thermoelastic properties for modelling the upper martian mantle. Here we report the results obtained so far at room temperature and high pressure.

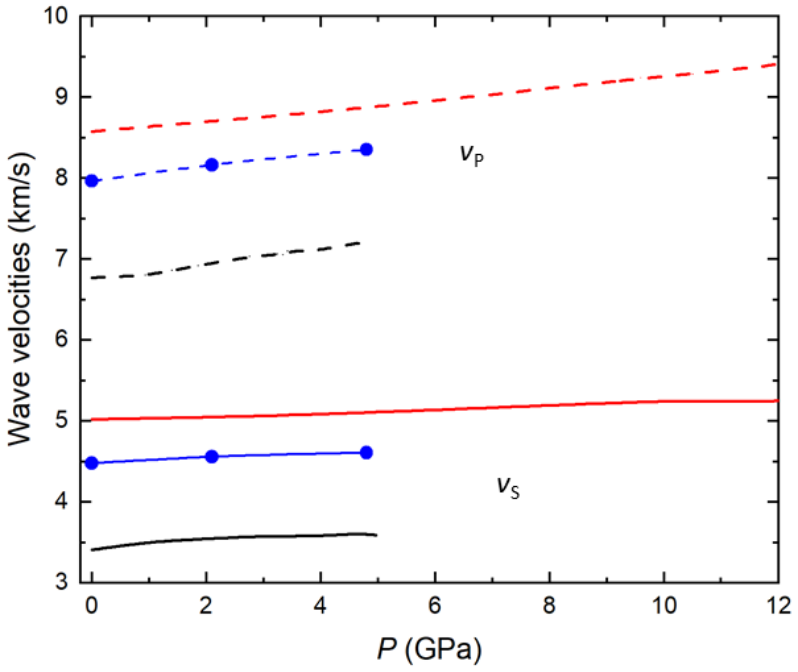

Fig. 3.4-5: Variations with pressure of the aggregate wave velocities of olivine with martian composition (blue) obtained up to 5 GPa. Data for Mg_2SiO_4 forsterite end-member (red, Zha *et al.*, JGR, *101*, 17535, 1996) and for Fe_2SiO_4 fayalite (black, Béjina *et al.*, Eur. J. Mineral., *33*, 519, 2021) are shown for comparison.

High-quality single-crystals of $Mg_{1.44}Fe_{0.56}SiO_4$ olivine synthesised and characterised in a previous work have been selected and oriented along the [404] and [161] directions using a

Huber single-crystal diffractometer. The oriented crystals have been then double-side polished down to a thickness of 17 μm and cut first into disks of 120 μm in diameter using a Focused Ion Beam (FIB) instrument. The disk was then FIB cut to 4 equivalent pieces. Two of the resulting 60 μm quarter-circular crystals (one for each orientation) were loaded together in a diamond anvil cell, with He as a pressure-transmitting medium to ensure quasi-hydrostatic conditions at all pressures. Simultaneous Brillouin scattering measurements and single-crystal X-ray diffraction have been performed at the same conditions in order to determine the elastic tensor of the martian composition olivine in a self-consistent manner, without having to rely on the use of secondary pressure standards or previously determined pressure-volume equations of state. Data have been collected so far up to 5 GPa at room temperature. Olivine is elastically anisotropic at room pressure and, in contrast to the Fe-rich ringwoodite polymorph (see annual report 2021), anisotropy decreases only slightly with increasing pressure.

The variations with pressure of the aggregate velocities (v_P and v_S) of the sample investigated in this study are reported up to 5 GPa in Figure 3.4-5 and compared with those obtained for forsterite and fayalite reported in the literature. Iron substitution majorly decreases both wave velocities and gives rise to a larger bulk modulus and lower shear modulus with respect to the Mg_2SiO_4 forsterite end-member. Experiments are now undertaken to reach pressures up to 10 GPa before starting Brillouin scattering experiment with the *in situ* laser heating system newly installed at the BGI.

f. *Structure and acoustic velocities of Fe-FeS liquids up to conditions of the martian core (L. Man, A. Néri, J. Chantel/Lille, L. Yuan, T. Boffa Ballaran, L. Henry/Paris, N. Guignot/Paris and D.J. Frost)*

The success of seismic data acquisitions from the InSight mission provides robust constraints on the interior structure of Mars. The new observations reveal a large (~ 1830 km), liquid, and light-element-rich martian core. The incorporation of light elements into planetary cores not only accounts for the observed density deficits, but also influences the redox, thermal evolution of planets, and the generation of a magnetic field. Combined with geochemical constraints from martian meteorites, the most likely light elements in the martian core are believed to be sulfur, oxygen, and hydrogen. However, due to experimental difficulties in determining the elastic properties of liquids under high-pressure conditions, the light element budget in the martian core is still controversial. To provide more experimental constraints on the composition of the martian core, in this study, we conducted *in situ* ultrasonic interferometry and X-ray scattering measurements on Fe-FeS melts up to 17.6 GPa and 2100 K.

The experiments were conducted in a multianvil press at the beamline PSICHE, in Soleil, France. An X-ray transparent 10 mm multianvil assembly was used to reach the target pressure and temperature. A boron-doped diamond (BDD) tube was used as a heating element. The rigid

BDD furnace minimises deformation in the hot portion of the assembly, which aids in accurate sound velocity measurements. The Fe-FeS starting materials (pure Fe, Fe with 6 wt. % S, and Fe with 15 wt. % S) were pre-sintered and machined into a cylinder with parallel opposite faces, which is also essential in order to obtain good quality ultrasonic data, and to maintain the regular shape of the sample at high-pressure and high-temperature conditions. Temperatures are determined using a thermocouple and pressures are obtained from *in situ* X-ray diffraction data collected from a pressure standard. After reaching the liquidus conditions, the P-wave velocities of the metallic melts were determined by combining the two-way travel time measured by the ultrasonic interferometry with the sample lengths measured by X-ray imaging. An example of the measurements conducted at 17 GPa is shown in Figure 3-4.6. Simultaneously, X-ray scattering measurements were conducted on the molten samples to determine the structure of the liquids. The combined angular- and energy-dispersive structural analysis and refinement (CAESAR) technique was used for liquid structure measurements. This technique allows us to cover a large Q range despite the limited opening angle of the multianvil press, and eliminates background problems using redundant datasets. Structure and density information can be extracted from the X-ray scattering spectrum (Fig. 3-4.7). Using the collected data, a multi-approach thermoelastic model of Fe-FeS liquids will be established to better constrain the light element budgets in the martian core.

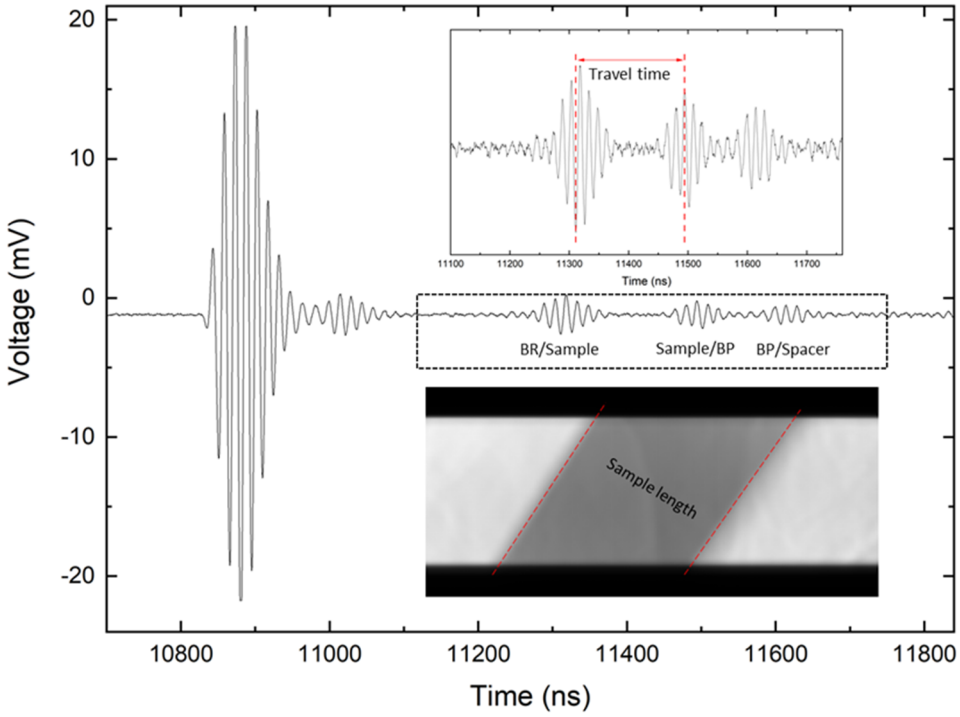

Fig. 3-4.6: An example of an ultrasonic interferometry experiment conducted at 17 GPa and 1573 K. The sample is a Fe-rich liquid with 15 wt. % S. BR and BP refer to buffer rod and backing plate, respectively. We used a 36° Y-cut $LiNbO_3$ transducer to generate P-waves from 50 to 80 MHz. The image of the sample was obtained by X-ray radiography.

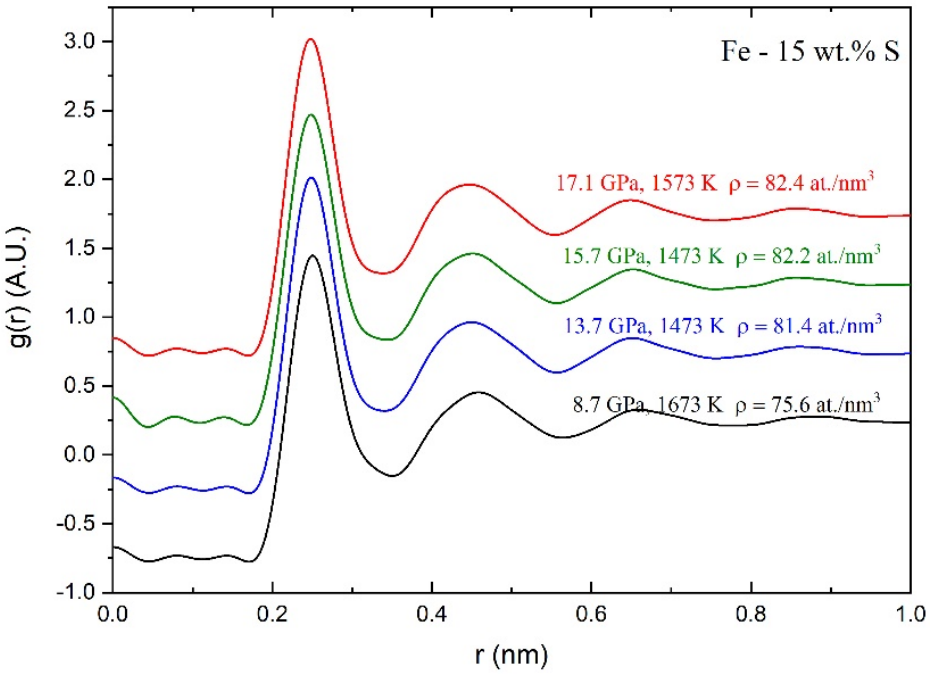

Fig. 3-4.7: Radial distribution function of Fe-rich liquids (Fe – 15 wt. % S) up to 17 GPa.

g. *Thermal equation of state of cubic silicon carbide at high pressures (A. Chanyshev, N. Martirosyan, L. Wang, A. Chakraborti, N. Purevjav, F. Wang, E.J. Kim, H. Tang; S. Bhat and R. Farla/Hamburg; T. Katsura)*

Silicon carbide SiC is a solid, hard compound stable at ambient conditions. Its natural form is named moissanite. Moissanite has been found in various rocks such as eclogites, serpentinites, and chromitites. Moreover, it was found as inclusions in diamonds from kimberlites. SiC minerals also could be dominant in the deep interiors of carbon-rich extrasolar terrestrial planets. For this reason, knowledge of the high-pressure behaviour of SiC is important to constrain its stability in planetary interiors.

SiC has a large number of polytypes. The most studied one is beta silicon carbide (β-SiC), with a zinc-blende crystal structure (B3). This SiC transforms to its high-pressure modification with a rock-salt structure (B1) between 60 and 80 GPa at room temperature. The pressure-volume equation of state (EOS) of the B3 SiC has been investigated by Raman and Brillouin spectroscopies, as well as by *in situ* X-ray diffraction (XRD). Previous XRD studies also determined the thermal EOS of the B3 SiC. These results were used to model the mass-radius relations and to determine rheological parameters for ideal C-rich exoplanets using numerical simulations. However, since all these studies were conducted using laser-heated diamond anvil cells, the pressures and temperatures had significant uncertainties, likely leading to poorly constrained EOS and thus highly imprecise exoplanet models. In this study, the thermal EOS of the B3 SiC has been investigated using experimental techniques with more precise pressure and temperature determination.

We determined an EOS of B3 SiC using *in situ* X-ray diffraction (XRD) with a 3 × 5-MN six-axis multianvil apparatus, Aster-15, installed at beamline P61B at the German synchrotron radiation facility, DESY. We conducted 3 runs in the pressure and temperature ranges of 3.6-29.7 GPa and 300-2200 K, respectively. Using 3rd-order Birch-Murnaghan and Mie-Grüneisen-Debye (MGD) models (Fig. 3.4-8), we determined the bulk modulus and thermal pressure parameters of B3 SiC as K_0 = 236(8) GPa, K_0' = 4.3(6), γ_0 = 1.18(3) and q = 2.33(61), where K_0, K_0', γ_0 and q are the isothermal bulk modulus, its first pressure derivative, the Grüneisen parameter, and its logarithmic volume dependence, respectively. Using instead a 3rd-order Birch-Murnaghan EOS with thermal expansion, the thermoelastic parameters were found as K_0 = 222(6) GPa, K_0' = 5.1(6), α_0 = 0.89(2) 10-5 K-1, where α_0 is the thermal expansion coefficient at room pressure and temperature. The obtained elastic parameters are comparable with those determined in previous studies, whereas the thermal pressure parameters, especially the logarithmic volume dependence of the Grüneisen parameter q, are quite different, resulting in different models of mass-radius relations of ideal C-rich exoplanets.

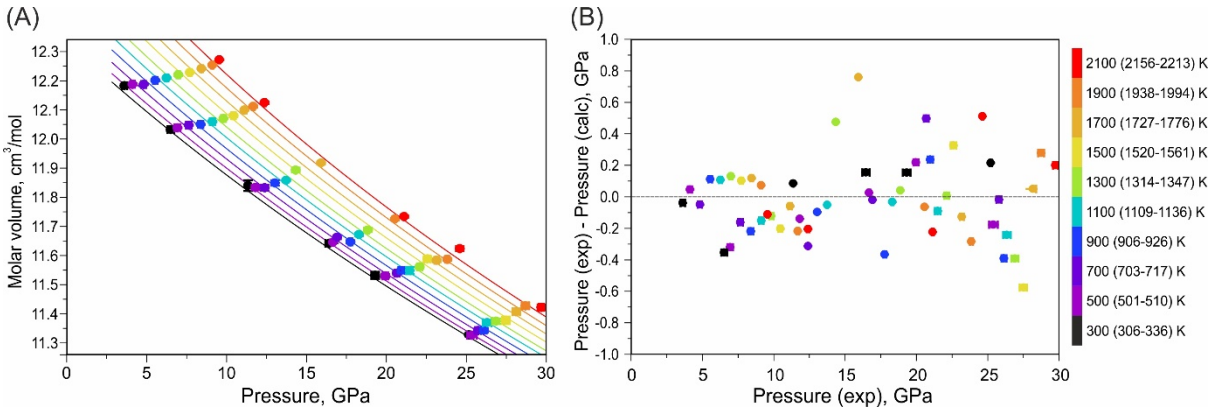

Fig. 3.4-8: Results obtained fitting our experimental data collected for the B3 phase of SiC using the MGD thermal model: (A) Pressure-volume relations at 300-2100 K. The circles are experimental data points. The curves are fitting to isotherms whose temperature are represented by the color scheme on the right of the figure. (B) The pressure residuals of the fitting procedure. The different colors indicate different temperatures. On the right is the temperature scale. The number in parentheses are temperatures after the pressure correction of the thermocouple electromotive force (EMF).

h. *Reproducing iron-rich phase textures in primitive achondrites: Overcoming surface tension in solids (A. Néri, E. Kubik, G.J. Golabek and A. Bouvier, in collaboration with N.P. Walte/Garching)*

Primitive achondrites like acapulcoites and lodranites are partially differentiated meteorites and originate from parent bodies that accreted at around 1.3 Myr after CAIs, with limiting heating potential (up to 25 vol. % of melting for the lodranites). However, these samples show a high

degree of equilibration, as proved using both compositional and textural arguments. In particular: (i) Phase compositions in between sections of the same specimen are extremely homogeneous; (ii) Grain boundaries between silicate phases are smoothly curved and triple junctions often meet at 120°; (iii) Silicate – Fe-Ni / troilite phase boundaries are also smoothly curved. In contrast, the textures of iron-rich phases (*i.e.*, troilite and kamacite-taenite) in acapulcoites and lodranites do not seem to represent a high degree of equilibration. These samples most likely reached a peak temperature of ≈ 1200 °C, meaning that the metallic subsystem was composed of a Fe-Ni residue and a sulfur-rich metallic melt. Previous experimental work showed that sulphide melts have lower surface energies in contact with silicate phases than Fe-Ni melts, a feature reflected in the lower dihedral angles of sulphides. Hence, at the peak temperature the minimisation of interfacial energies dictates that the Fe-Ni residues should be surrounded by the sulphide melt. This configuration is, however, not observed in sections of acapulcoites and lodranites (Fig. 3-4.9A), where kamacite-taenite and troilite are both in contact with the silicate phases and both of these phases are spatially separated.

In order to understand these textures and their formation, a series of high-pressure experiments have been conducted. A simplified system with San Carlos olivine representing the silicate matrix, and troilite and gold mimicking the low- and high-surface-energy melt and residue was used as an analogue of acapulcoites. The samples were enclosed in graphite capsules and compressed to 2.5 GPa using a 25/17 (octahedron edge length to truncation edge length) BGI multianvil assembly.

When equilibrated at 1300 °C, the recovered textures consist of gold pools fully surrounded by troilite melt (Fig. 3-4.9B), regardless of the duration of the experiment (ranging from 3 h to 1 week). Such texture is indeed the local minimum surface energy configuration. Therefore, the textural features observed in acapulcoites and lodranites do not originate from high-temperature equilibration. Additional experiments were conducted initially at 1300 °C for 3 h, then the temperature was rapidly (within ≈ 2 min) decreased to 1000 °C and held constant for durations ranging from one week to one month, in an attempt to simulate the long and slow cooling that meteorites might experience. Even though both troilite and gold are solid at 1000 °C, the temperature is high enough for silicate grain growth to occur, allowing for solid-state geometrical rearrangements of FeS and gold grains. After one week at 1000 °C, the textures of the recovered samples show a slight spatial sorting of troilite and gold that is further enhanced after one month of static annealing (Fig. 3-4.9C). In addition to the FeS and gold phase separation, pockets where both these phases are in contact are asymmetric, *i.e.*, the gold is directly in contact with the surrounding silicates. Both textures are very similar to those observed in acapulcoites and lodranites.

The mechanism driving the separation of gold and troilite appears to be related to small-scale reorganisation driven by grain growth, rather than by local minimisation of interfacial energies. It is known that grain growth can temporarily induce local disequilibrium features during

topological rearrangements, such as neighbor switches. In the solid state, metallic phases have high viscosities and diffusion is sluggish, meaning that the timescale required to maintain the local low surface energy configuration is much greater than that for geometrical changes induced by silicate grain boundaries migrations. In summary, the textures of iron-rich phases in primitive achondrites do not reflect local high-temperature equilibration, but instead record annealing processes during the slow cooling history of the parent body.

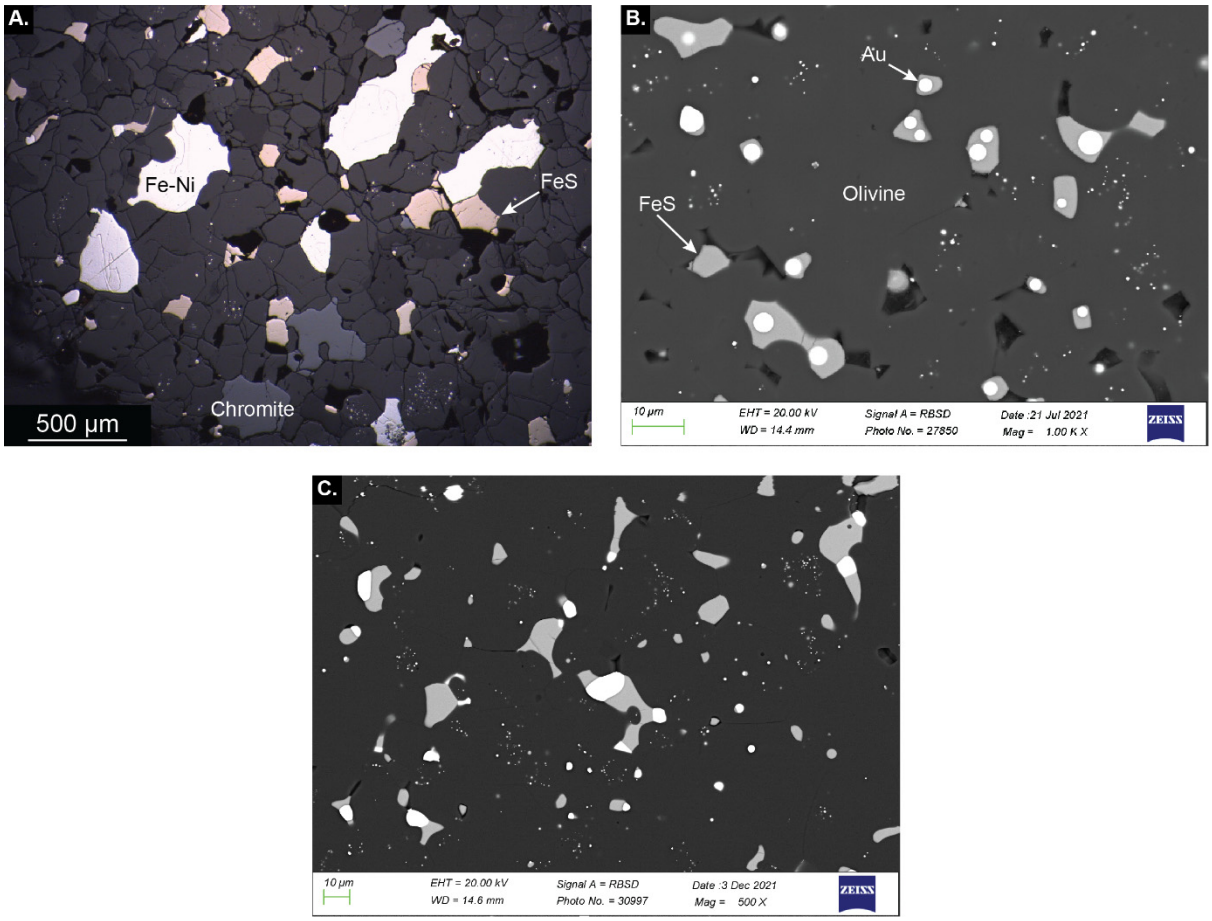

Fig. 3-4.9: (A) Optical image of a section of meteorite Acapulco. (B) and (C) Scanning Electron Microscopy (SEM) images of recovered samples (B) after equilibration at 1300 °C and 2.5 GPa for 3 h and (C) after equilibration at 1300 °C and 2.5 GPa for 3 h and then subsequent re-equilibration at 1000 °C lasting for one month.

3.5 Fluids, melts and their interaction with minerals

Fluids and silicate melts are the main agents of chemical transport in Earth's interior and from the deep Earth to the surface. In the upper part of the mantle, traces of hydrogen occur mostly as OH point defects in silicate minerals or locally, mostly above subduction zones, as molecular H_2O in aqueous fluids. However, in the deeper part of the present mantle, more reducing conditions prevail, where H_2O may be largely reduced to H_2. Such conditions may have been representative for the entire mantle in the very early stages of Earth's history. Previous work at BGI had shown that H_2O and H_2 become immiscible at shallow upper mantle conditions. The first contribution below extends these data to greater pressures. Notably, the critical curve in the H_2-H_2O system steepens with pressure. This means that even for rather hot geotherms in the Archean or late Hadean, H_2 would readily separate from H_2O. The rapid degassing of highly buoyant H_2 fluid would be an obvious mechanism to oxidise the remaining mantle. Moreover, some first experimental data show that noble gases, in particular xenon, strongly partition into the H_2 phase. This could therefore explain the rapid loss of xenon isotopes produced by the fission of plutonium in the earliest times of Earth's history, as indicated by the isotopic composition of current mantle xenon.

Subduction of oceanic plates back into the mantle is the main mechanism for recycling volatiles from Earth's surface into Earth's deep interior. Several contributions therefore investigate the fate of water in subduction zones. In one study, the diffusivity of water through the grain boundary network of polycrystalline olivine or orthopyroxene was investigated. The data suggest that grain boundary diffusion would be rather slow and other mechanisms, such as channelised flow along fractures in the rock, are likely required to achieve large-scale volatile transfer from the subducted plate to the overlying mantle. In another contribution, the speciation of sulfur in aqueous fluids produced by serpentinite dehydration was investigated.

Most of the hydrous minerals in the subducted slab decompose at a rather shallow pressure and release water that may be largely recycled to the surface by arc magmatism. An interesting question is therefore how water may be transported deeper into the lower mantle. One possibility could be the dissolution of OH point defects into SiO_2 stishovite and its high-pressure polymorphs. Indeed, two contributions in this chapter show that water is appreciably soluble in pure (Al-free) stishovite and even more so in aluminous post-stishovite. Aside from water, nitrogen is another volatile that may be recycled into the lower mantle by subduction. However, for nitrogen, the storage capacity of the lower mantle is only poorly constrained. Therefore, in another project, nitrogen solubility in aluminous bridgmanite, the main phase of the lower mantle, was systematically studied. The data show that Al enhanced nitrogen solubility, probably through some charge-coupled substitutions. Several 100 ppm of N may be dissolved in aluminous bridgmanite, which is consistent with geochemical evidence for a deep, nitrogen-rich reservoir in the mantle.

The initial distribution of volatiles in our planet was likely achieved by the equilibration of a magma ocean with a dense primordial atmosphere. In order to model this process, the dissolution mechanism of water in peridotitic melts needs to be understood. With a new rapid-

quench multianvil assembly, it was possible for the first time to quench hydrous peridotitic melts into glasses. The infrared spectra of these samples suggest that the dissolution mechanism of water in peridotitic melts is quite different from basalts. There is much less molecular H_2O dissolved in these samples and in addition to OH groups attached to Si, there also seem to be CaOH and MgOH species. However, it has been speculated that at the very reducing conditions that likely prevailed in a magma ocean, not H_2O, but H_2 may actually the most important gas species dissolving in the melt. Previous experimental measurements of H_2 solubility in silicate melts largely relied on an infrared extinction coefficient of H_2 in silica glass. New re-calibration experiments suggest that this extinction coefficient may be in error by about one order of magnitude, with the implication that the actual H_2 solubility in silicate melts is much smaller than previously thought.

The viscosity of silicate melts is of fundamental importance for understanding and forecasting volcanic eruptions. As viscosity depends in a complex way on temperature and melt composition, usually semi-empirical models are used for predictions. As an alternative, a contribution in the section of the annual report trains an artificial neural network on a data set containing more than 3000 viscosity measurements. The resulting model appears to be more precise than the existing semi-empirical calibrations. In another contribution, the first data on the viscosity of hydrous peridotitic melts are presented. Viscosities of basaltic melts may increase by the crystallisation of Fe-Ti-oxides, a phenomenon that may occur both in nature during eruptions and in the laboratory during viscosity measurements. Two contributions look into this effect, which may perhaps be related to the different explosivities of Mt. Etna and Stromboli. The effect of dendritic crystals on the eruption behaviour of Mt. Etna magmas is studied in another project, which used *in situ* X-ray tomography to record crystal growth in three dimensions.

a. *Immiscibility between H_2 and H_2O in Earth's upper mantle (K. Vlasov and H. Keppler)*

Hydrogen speciation in deep planetary environments depends on oxidation state. Earth's lithospheric upper mantle is relatively oxidised. Here, $f(O_2)$ ranges from +2 to -3 log units relative to the QFM buffer, with the primary hydrogen species being molecular H_2O or hydroxyl groups (OH^-). At greater depths and pressures, exceeding 200 km and 5-7 GPa, respectively, oxygen fugacity evolves towards more reducing values, approaching the iron-wustite (IW) buffer, such that molecular hydrogen H_2 as well as methane CH_4 become important H-species. As discovered by previous research at BGI, water and molecular hydrogen can be immiscible in the mantle, which may lead to the formation of super-reducing domains and may cause the selective re-distribution of some elements.

To extend the pressure range of the critical curve in the H_2-H_2O system covered by previous experiments, we synthesised fluid inclusions in the piston-cylinder apparatus utilising a ½ inch talc-Pyrex assembly at pressures ranging from 1 to 4 GPa. Two series of inclusion-capturing experiments were performed: One series to investigate the location of the critical curve itself

and a second one to quantify possible element partitioning effects during H_2-H_2O unmixing. In both cases, thermally shocked samples of olivine or quartz were loaded into a Pt-Rh capsule, filled with water, and sealed by arc welding. To control the oxygen fugacity at the IW buffer level, this capsule was placed in an outer iron capsule, containing a mixture of FeO and water. At the end of the run, experiments were quenched, and crystals were cut and polished. Fluid inclusions were investigated by Raman spectroscopy. For element partitioning experiments, the layout of the inner capsule was more complicated, containing layers of $Ca(OH)_2$, XeF_2, and trace element-doped MORB glass. Moreover, instead of pure water, an internal standard solution containing 1000 ppm of Rb and Cs was used. To determine the distribution of element between the phases, resulting inclusions were analysed with LA ICP-MS.

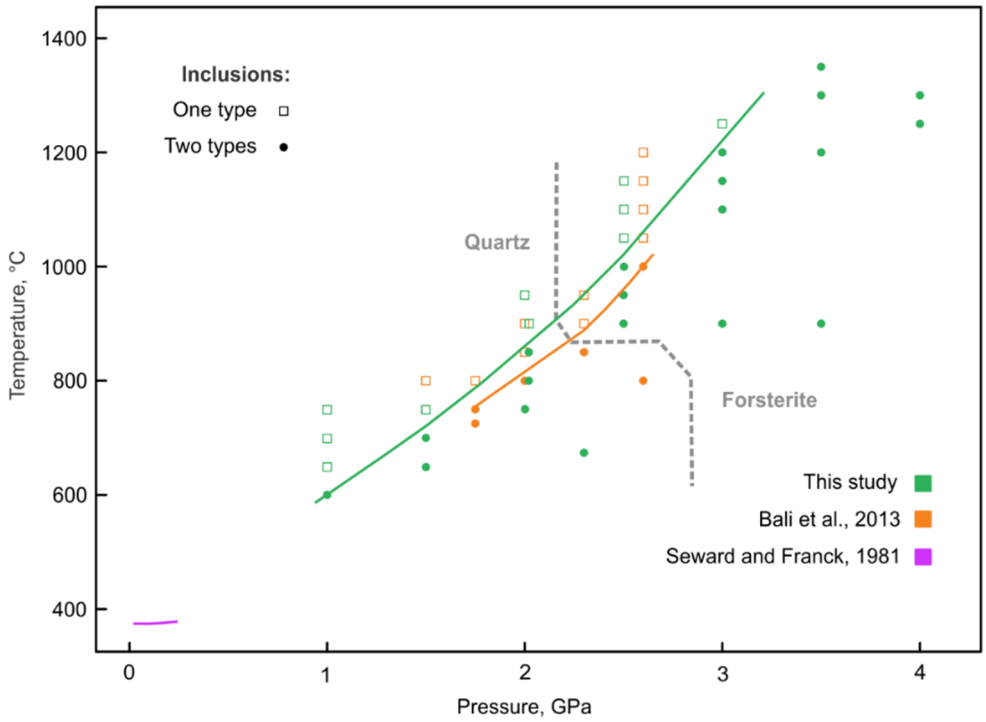

Fig. 3.5-1: Location of the critical curve in the H_2-H_2O system (green line) according to our experimental data (green symbols). Open squares indicate mixed water-hydrogen inclusions, filled circles refer to the coexistence of water and hydrogen-dominated inclusions. The critical curve from Bali *et al.* (2013, Nature 495: 220-222) is plotted as an orange line with experimental data being symbols of the same colour. The lavender line is a critical curve established by Seward and Franck (1981, Ber. Bunsenges. Phys. Chem. 85, 1: 2-7). The thick, dashed dark grey line separates experiments performed with quartz or olivine both in this work and in the work of Bali *et al.*

Two main types of inclusion populations were observed in retrieved samples. Some samples contained inclusions with a mixture of H_2O and H_2, which are interpreted as evidence for full miscibility. Other samples contained coexisting water or hydrogen-dominated inclusions, indicating the entrapment of two coexisting immiscible fluids. Our results (Fig. 3.5-1) suggest

that below ~ 2.5 GPa the critical curve has a mostly linear slope of 200 °C/GPa, while at more elevated pressure, it becomes significantly steeper, approaching 400 °C/GPa. This implies that in most of the reduced upper mantle settings, water and hydrogen are immiscible, even for rather hot geotherms in the Archean or late Hadean. We also observed that most trace elements, such as Rb and Cs, partition preferentially into the water-rich phase, while C and Xe prefer the hydrogen-rich with $D^{Xe}_{H2/H2O} \approx 23$ (Fig. 3.5-2). Such partitioning pattern may, for example, explain the observed underabundance of xenon isotopes produced by the fission of plutonium in the mantle. Xenon could have been selectively removed by a primordial H_2-H_2O unmixing event during the early stages of planetary formation and cooling.

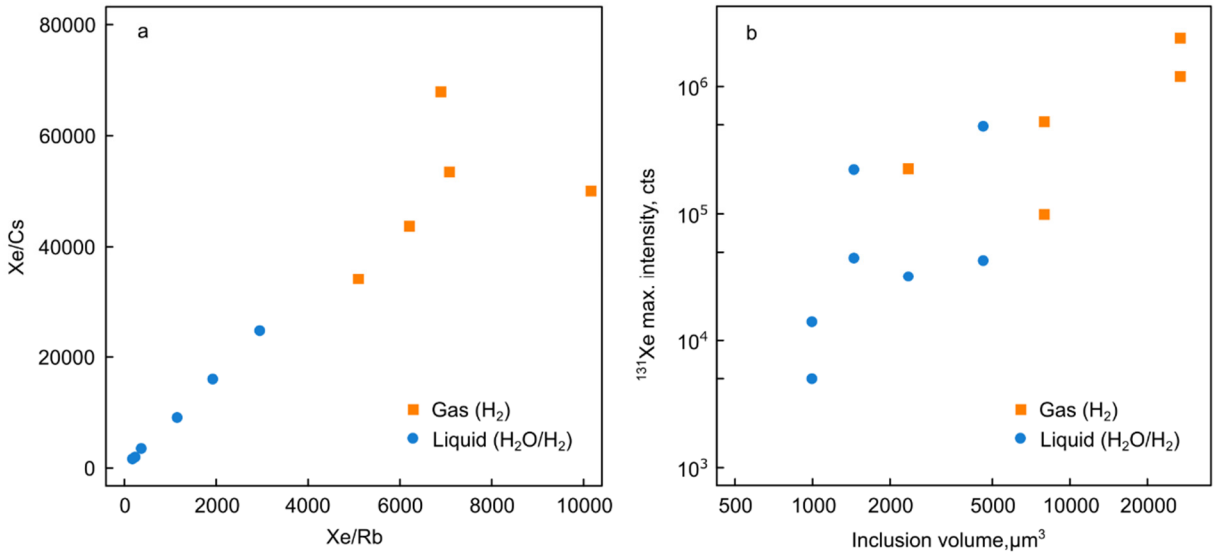

Fig. 3.5-2: Partitioning of trace elements between the coexisting H_2 and H_2O phases. (a) LA ICP-MS established Xe/Cs count ratio plotted versus Xe/Rb count ratio for individual inclusions; (b) the intensity of ^{131}Xe signal plotted versus the inclusion volume. Data for hydrogen-rich inclusions are given in green, for inclusions with liquid water and possible co-trapped hydrogen in blue.

b. *The diffusivity of water through mantle assemblages under subduction zone conditions (M. Pöppelbaum, A. Néri and D.J. Frost)*

Subduction-related fluids are known to be involved in arc melting and source metasomatism, but the nature of fluid flow processes that allow transport from the subducting slab to the mantle wedge is poorly understood. The nature of these processes has implications for the geochemistry of the fluids, as the pervasive flow can leach elements from much larger volumes of the slab as compared to channelised flow. The transport timescales are also important because if these are too slow, fluids will tend to be subducted with the slab rather than being released into the overlying mantle. To evaluate the mechanisms and time scales of fluid transport in subducting slabs, experiments are being performed at subduction zone conditions to examine the rate of fluid flow through hot-pressed mantle minerals.

In this phase of the project, multianvil experiments were carried out at 2.5 GPa and 500 °C on sintered polycrystalline olivine or orthopyroxene cores with a mean grain size of 5-10 µm. The core was sandwiched between a fluid source of aluminium hydroxide $Al(OH)_3$ and a fluid sink of MgO. The run durations were 6-144 hours. At the experimental conditions, the $Al(OH)_3$ dehydrates, inducing an overpressure and resulting in a fluid flow through the dense sintered core. The fluid can then be captured in the MgO fluid sink on the other side of the core through the formation of brucite ($Mg(OH)_2$). This method (see Fig. 3.5-3) allows the rate of water transport through the bulk sample, including along the grain boundaries, to be determined and does not require spectroscopic methods or an ion probe to determine the amount of water, which is challenging for samples with small grain sizes.

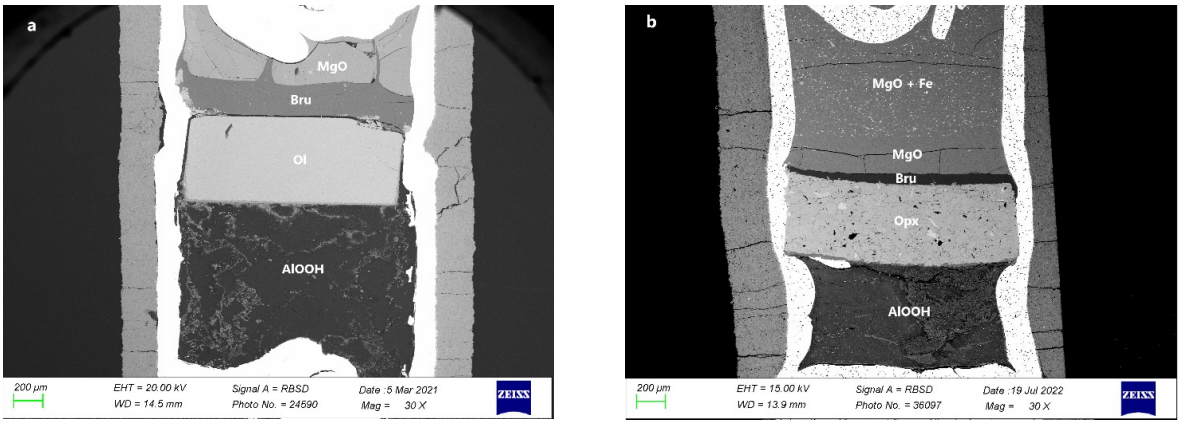

Fig. 3.5-3: BSE images of the run products for olivine (Ol; a) and orthopyroxene (Opx; b). Pressure and temperature conditions for both runs are 2.5 GPa and 500 °C with experimental run times of 18 h and 48 h for Ol and Opx, respectively. The difference in diffusivity between Ol and Opx can be seen from the thickness of the brucite (Bru) layer.

The first experimental observation was that it is possible for water to move through the mineral cores using an $Al(OH)_3$ water source, whereas this is not possible on similar experimental timescales when serpentine is used as the source. We interpreted this to imply that the fluid overpressure, which is much higher in the case of $Al(OH)_3$, plays a role in the rate of transport. The observed rate of fluid flow is slow, with diffusivities of 1.7×10^{-11} m²/s and 1.3×10^{-12} m²/s for olivine and orthopyroxene, respectively. Therefore, even though large overpressures were produced, only processes with rates similar to those expected for grain boundary diffusion of water seem to be in operation at these conditions. When these diffusivities are extrapolated to grain sizes of the upper mantle (~ 1 mm), they allow for a water transport of only 2.4 m and 0.6 m in a million years, which is far too slow to allow the transport of water into the overlying mantle wedge. Of course, these rates will increase at higher temperatures, but based on other estimates, it is likely that grain boundary diffusion remains too slow to account for the transport of water to the mantle wedge and a different mechanism is likely required. Experiments are continuing at higher temperatures to test this.

c. *The speciation of sulphur in fluids released from sulphide-bearing serpentinite (M. Pöppelbaum and D.J. Frost)*

Arc magmas are more oxidised than mid-ocean ridge basalts or ocean island basalts, which has been attributed to oxidation of the mantle wedge caused by water-rich fluids leaving the subducting slab. Serpentinites dehydrate at sub-arc depths and can release significant amounts of water. They are also oxidised, as they contain a portion of their iron as magnetite. Of the three most abundant redox-sensitive elements, iron, carbon, and sulphur, sulphur has perhaps the largest potential to transport oxidised species from dehydrating serpentine to the mantle wedge. Ferric iron, on the other hand, is barely soluble in fluids and CO_2 or dissolved carbonate would not be able to oxidise the mantle wedge above the level of graphite stability. Although serpentinites are likely to contain sulphides, the oxidation state of sulphur in fluids released from serpentinites is controversial.

We performed two types of multianvil experiments to evaluate the oxidation state of sulphur in serpentinite-derived fluids. In the first type of experiment, FeS-enriched natural antigorite-bearing serpentinite was dehydrated at 2.5 GPa and 700 °C for 4-6 days, such that the released hydrous fluid would pass through a ~ 0.4 mm thick, hot-pressed layer of orthopyroxene (Opx) and react with MgO on the other side to form brucite. A final layer was comprised of MgO and 5 wt. % of Fe metal. On the relatively short time scale of the experiment, water did not pass through the Opx layer, although some passed between the capsule and the Opx. However, Fe-metal in the lowest layer completely oxidised to produce magnetite, pyrrhotite and magnesite (Fig. 3.5-4). It is possible, therefore, that both sulphur and carbon were transported by a very mobile oxidised, fluid phase that was water-poor because no brucite was formed. To test whether the serpentine might be the source of such an oxidised fluid component, we performed a control experiment with the same experimental setup, but replacing the serpentinite with $Al(OH)_3$, containing FeS and graphite. In these experiments, even though the fluid produced did diffuse through the Opx layer and reacted to form brucite, the iron metal in the lower layer was not oxidised.

In order to isolate the fluids released from serpentinite, a second type of experiment was performed, with a setup similar to the first one, but with the MgO layers replaced by a pre-fractured quartz core. Synthetic fluid inclusions were formed in the quartz at the same experimental conditions as those in the first type of experiments. Raman spectra of the fluid inclusions appear to contradict the results of the first type of experiment, however, as they contained, in addition to water, the reduced species H_2S and CH_4 and no sign of oxidised sulphur species. Longer (6-9 days) experiments produced inclusions with more CH_4, so it is possible that reduction is occurring in these experiments through the ingress of H_2 from outside of the capsule. Thermodynamic calculations were performed with the PERPLEX software package that indicates that the switch in dominance between reduced and oxidised sulphur species in water-rich fluids occurs over only a few log units in oxygen fugacity. Experiments are continuing to resolve the discrepancies between the two types of experiments.

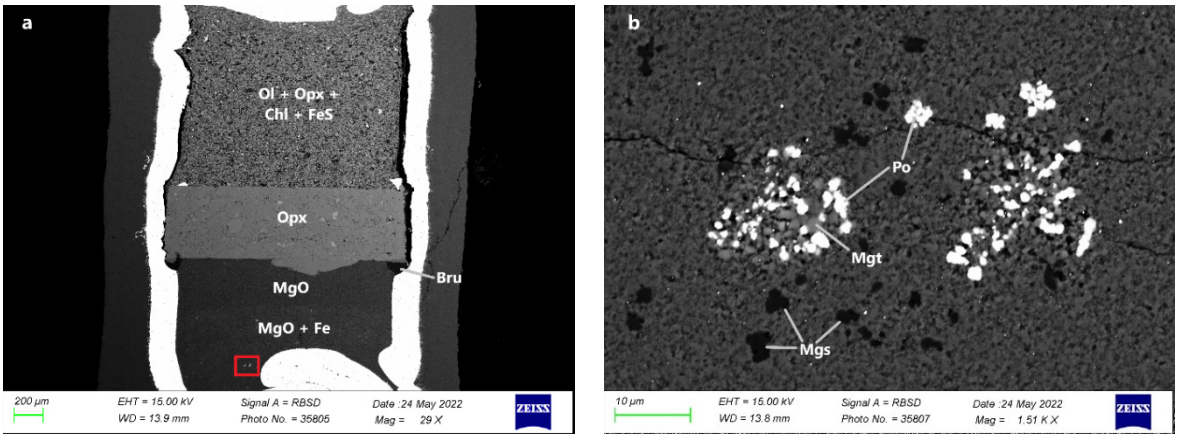

Fig. 3.5-4: a: Backscattered electron (BSE) image of the capsule with a layered setup. A layer of decomposed serpentinite, consisting of olivine (Ol), orthopyroxene (Opx), chlorite (Chl), and FeS is at the top, followed by a hot-pressed Opx core, an MgO layer, and a bottom layer comprised of MgO and Fe metal. Brucite (Bru) formed from MgO and water at the edges of the Opx core. The red rectangle marks the area of the magnified BSE image in b. b: Fe metal reacted with, likely, oxidised sulphur to form magnetite (Mgt) and pyrrhotite (Po). The increased CO_2 activity of the fluid allowed then for the precipitation of magnesite (Mgs).

In order to isolate the fluids released from serpentinite, a second type of experiment was performed, with a setup similar to the first one, but with the MgO layers replaced by a pre-fractured quartz core. Synthetic fluid inclusions were formed in the quartz at the same experimental conditions as those in the first type of experiments. Raman spectra of the fluid inclusions appear to contradict the results of the first type of experiment, however, as they contained, in addition to water, the reduced species H_2S and CH_4 and no sign of oxidised sulphur species. Longer (6-9 days) experiments produced inclusions with more CH_4, so it is possible that reduction is occurring in these experiments through the ingress of H_2 from outside of the capsule. Thermodynamic calculations were performed with the PERPLEX software package that indicate that the switch in dominance between reduced and oxidised sulphur species in water-rich fluids occurs over only a few log units in oxygen fugacity. Experiments are continuing to resolve the discrepancies between the two types of experiments.

d. *The temperature dependence of H_2O solubility in Al-free stishovite (N. Purevjav, H. Fei, and T. Katsura)*

Subducted slabs may transport water into the deep mantle through hydrous minerals such as lawsonite and phengite in the sedimentary and basaltic layer, and by dense hydrous magnesium silicates in peridotite. However, these hydrous minerals are thermodynamically unstable at relatively high temperatures, *i.e.*, above 1300-1400 °C. Therefore, they likely transport water only to the mantle transition zone. In contrast, the dominant nominally anhydrous minerals in peridotite, such as olivine, wadsleyite, and ringwoodite, can incorporate up to 3 wt. % water.

However, the major minerals in the lower mantle, bridgmanite, and ferropericlase, may only dissolve less than 100-1000 wt. ppm water. Therefore, the mechanism of water transport to the lower mantle requires further study. Stishovite in the subducted oceanic crust may perhaps be a suitable carrier for water.

Stishovite is the high-pressure polymorph of quartz stable above 10 GPa and constitutes 20 ~ 25 vol. % of the subducted basaltic layer. However, previous measurements of water solubility in stishovite yielded widely diverging results. To constrain the water solubility in Al-free stishovite and the role of stishovite in deep water transport, we investigated the water solubility of Al-free stishovite as a function of temperature from 1300-2100 °C at 22 GPa. High-quality stishovite single crystals were synthesised under water-saturated conditions using a multianvil press. Each crystal was doubly polished to a thickness of 80-100 μm and studied by unpolarised Fourier transform infrared spectroscopy. Two to three crystals from each run were analysed, and five infrared spectra were taken from each crystal using a Bruker IFS 120 high-resolution spectrometer coupled with a Bruker IR microscope. The water contents were calculated from the infrared absorbance between 2600 and 3400 cm^{-1} using the Paterson calibration (Fig. 3.5-5).

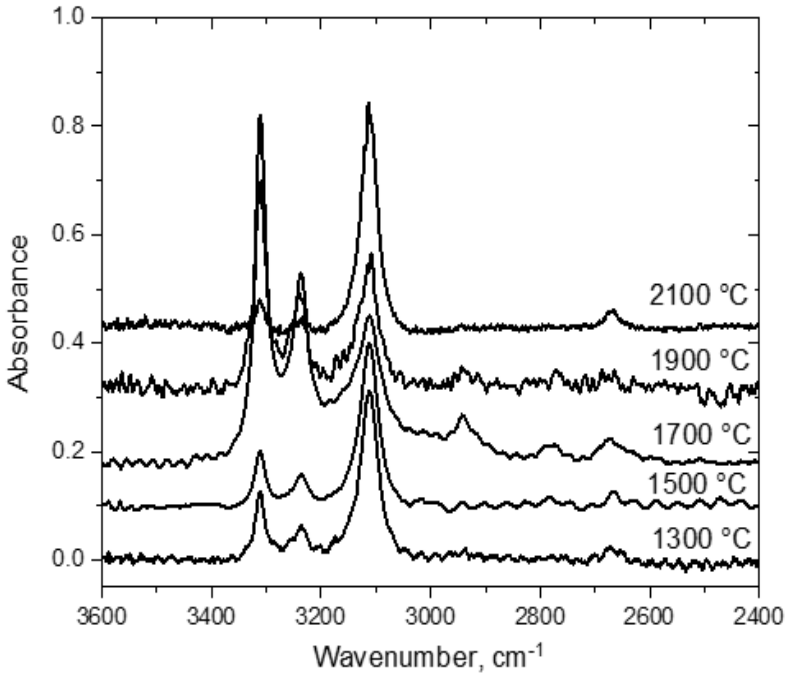

Fig. 3.5-5: Representative unpolarised infrared spectra of stishovite synthesised at various temperatures at 22 GPa. All the spectra are baseline subtracted. The sample thickness is 80-100 μm. The spectra were vertically shifted for visibility.

Water solubility in stishovite was found to increase from 128 (20) to 521 (47) ppm with temperature increasing from 1300 to 1700 °C, while it decreases at higher temperatures to 145 (26) ppm at 2100 °C. We conclude that Al-free stishovite has only a limited capacity to transport water to the lower mantle.

e. *The pressure dependence of Al and water solubility in post-stishovite (D. Liu, N. Purevjav, H. Fei, F. Wang, A.C. Withers, and T. Katsura)*

Water transported to the Earth's mantle by subduction of oceanic plates affects the physical properties of minerals and rocks at high pressures and temperatures and thus influences the dynamics of Earth's interior. Stishovite and post-stishovite, which are the main phases in the subducting oceanic crust, are considered as potential water carriers to the lower mantle. Previous studies showed that the incorporation of Al and H might decrease the transition pressure between stishovite and post-stishovite. Therefore, the solubility of Al and water in post-stishovite needs to be studied as a function of pressure.

We performed multianvil experiments to investigate the pressure dependence of Al and water solubility in post-stishovite in the SiO_2-Al_2O_3-H_2O system. We synthesised hydrous Al-bearing post-stishovite at pressures from 18 to 27 GPa at a temperature of 1900 °C. The phases present in the sample capsules were identified using a Bruker AXS D8 Discover micro-focus X-ray diffractometer. All run products contained single crystals of post-stishovite coexisting with quenched hydrous fluid or melt. The crystals were polished on both sides and analysed by unpolarised Fourier transform infrared spectroscopy (Fig. 3.5-6) and by electron microprobe. After baseline subtraction, the water contents in post-stishovite were calculated from the infrared absorbance in the 2400-to-3400-cm^{-1} range using the Paterson calibration. Our results suggest that the solubilities of Al and H_2O in post-stishovite are 8.6-11.6 wt. % and 0.7-1.3 wt. %, respectively, at 18-27 GPa and 1900 °C. These values are much higher than for the lower-pressure polymorph stishovite. Our results also indicate that pressure has only a minor effect on the Al and water solubility in post-stishovite.

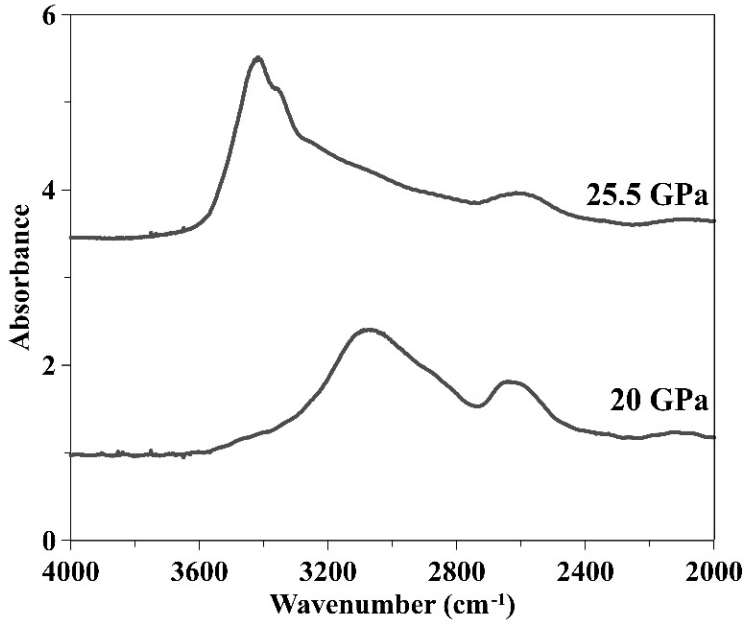

Fig. 3.5-6: Typical infrared spectra of Al-bearing hydrous post-stishovite synthesised at 20 GPa and 25.5 GPa at a temperature of 1900 °C. Sample thickness is 37 and 102 μm, respectively.

f. *The solubility of nitrogen in aluminous bridgmanite (G. Rustioni, M. Wiedenbeck/Potsdam, A. Chanyshev, C. Howard, and H. Keppler)*

Traditionally, it was believed that most of the nitrogen in our planet resides in the atmosphere. However, recent experimental studies at BGI have shown that under reducing conditions near the iron-wustite (Fe-FeO) buffer, nitrogen is actually quite soluble in some mantle minerals, notably those that are stable in the transition zone. This implies that early in Earth's history, during the crystallisation of the magma ocean, a significant amount of N must have been trapped in the deep mantle, and this nitrogen reservoir may actually be larger than the atmosphere.

While nitrogen solubility in upper mantle and transition zone minerals is rather well understood, there are almost no data on lower mantle phases. Previous experiments at BGI suggested that N solubility in bridgmanite, the dominant phase of the lower mantle, is rather low, in the order of 20 ppm. However, these data were derived from one single experiment with an Al-free composition. The introduction of Al into bridgmanite may facilitate the dissolution of nitrogen by allowing charge-coupled substitutions. We therefore carried out a systematic study of nitrogen solubility in aluminous bridgmanite as a function of pressure, temperature, and bulk composition.

Multianvil experiments were carried out to crystallise bridgmanite from oxide starting mixtures in the presence of an excess, N-rich fluid phase. All experiments were buffered by adding metallic Fe to the platinum capsules, such that an oxygen fugacity close to the iron wustite (Fe-FeO) buffer was attained, which is realistic for the lower mantle. The source of nitrogen was ^{15}N-enriched ammonium nitrate $^{15}NH_4{}^{15}NO_3$. Under run conditions and the oxygen fugacity imposed by Fe-FeO, ammonium nitrate will decompose to NH_3 and H_2O. After polishing, samples were studied by Raman spectroscopy for phase identification and by electron microprobe for major element chemical composition. Nitrogen concentrations were measured by SIMS (secondary ion mass spectrometry; Cameca 1280-HR) at GFZ Potsdam. The use of nitrogen starting materials enriched in the rare ^{15}N isotope allowed a reliable distinction of the sample signal from atmospheric or environmental contamination.

Figure 3.5-7 shows a typical sample texture and analytical data on nitrogen in bridgmanite are compiled in Figure 3.5-8. The data clearly show that the presence of Al enhances nitrogen solubility by more than one order of magnitude. Interestingly, the data suggest a maximum of N solubility near 4 wt. % of Al_2O_3, with a decrease at higher Al contents. This may be due to the presence of two competing Al dissolution mechanisms in brigmanite, which has been extensively discussed in the literature: (i) In the "oxygen vacancy mechanism", the substitution of Al^{3+} for Si^{4+} is compensated by the formation of oxygen vacancies. This would be a natural place, where N^{3-}, maybe in protonated form as NH_2^- may substitute. However, at higher Al concentrations, the (ii) charge-coupled substitution mechanism becomes dominant, where 2 Al^{3+} substitute for $Mg^{2+} + Si^{4+}$. This type of substitution should not enhance N solubility, and the maximum in the nitrogen contents shown in Figure 3.5-8 may be consistent with the

expected change from the "oxygen vacancy" to the "charge coupled" substitution mechanism of Al. The charge-coupled mechanism is favoured at higher Al concentrations, as it requires two Al^{3+} ions to be close to each other.

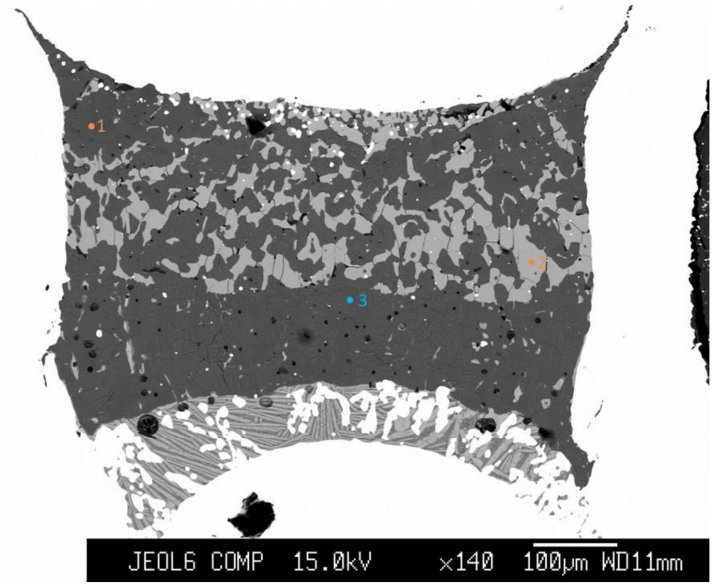

Fig. 3.5-7: BSE image (COMPO mode) of a sample with nitrogen-saturated bridgmanite, synthesised at 24 GPa and 1700 °C. Dark grey (measurement spots 1 and 3) is bridgmanite, light gray (spot 2) magnesiowustite. At the bottom of the capsule is some feather-like material produced by quench crystallisation of a volatile-rich melt. The nearly white grains are metallic Fe, containing some Pt.

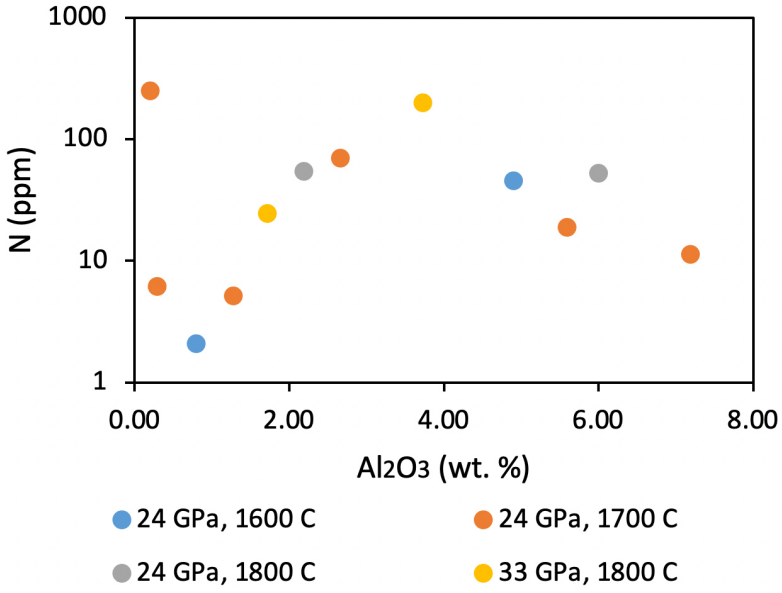

Fig. 3.5-8: Nitrogen (^{15}N) solubility in bridgmanite as a function of Al_2O_3 content. Every data point represents one single SIMS measurement and therefore, no error bars are shown.

The data shown here suggest that the nitrogen storage capacity of the lower mantle is much larger than previously thought. During magma ocean crystallisation, the lower mantle may retain most of the nitrogen on the planet. This may imply that the "subchondritic N/C ratio of the Earth" that has been the subject of extensive discussion in recent years does not really exist. The N/C ratio of the bulk Earth may very well be similar to the chondritic value. Only the under-sampling of material from the deep mantle (that may be entrained in the source of some OIB basalts with high N/Ar ratio) perhaps creates the impression of a subchondritic N/C.

g. *The dissolution mechanisms of water in peridotitic glasses (D. Bondar, A.C. Withers, A.G. Whittington, D. Di Genova, H. Fei, and T. Katsura)*

The dissolution of water changes the chemical and physical properties of silicate melts. Previous research mainly focused on relatively polymerised melts, while the dissolution mechanisms of water in highly depolymerised melts have not been well studied. The reason for this is the poor glass-forming ability of highly depolymerised hydrous melts that makes it very difficult to quench them into glasses. The novel rapid-quench multianvil technique developed at BGI enabled us for the first time to produce peridotitic (KLB-1) glasses with H_2O contents from 0 to 5 wt. % at pressures up to 4 GPa. The synthesised glasses are transparent, optically isotropic, and chemically homogeneous. Raman spectroscopy revealed no long-range atomic ordering.

Infrared spectra of these glasses provided the following four essential observations: First, the intensity of the band of molecular H_2O at ~ 5200 cm^{-1} dramatically decreases relative to the OH^- bands with increasing depolymerisation (Fig. 3.5-9a). The low proportions of molecular H_2O in the peridotitic glasses may primarily result from their high fictive temperatures caused by their ultramafic compositions. Second, a band at 4320-4180 cm^{-1} appears next to the (Si,Al)OH peak (network hydroxyl) at high CaO or MgO contents (Fig. 3.5-9b). We assigned this peak to the (Mg,Ca)OH group; this is the first identification of this group in hydrous silicate glasses by infrared spectroscopy. This assignment is also supported by the IR data on crystalline $Mg(OH)_2$ and $Ca(OH)_2$ phases in the literature. Third, the ratio of (Si,Al)OH and (Mg,Ca)OH band absorbances remains nearly constant as a function of water content. This suggests that there is no effect of water on the polymerisation of extremely depolymerised melts. Fourth, the (Si,Al)OH peak shifts to lower wavenumbers with increasing depolymerisation. As a result, the (Si,Al)OH peak position could potentially be used to evaluate the degree of melt polymerisation in general, and the effect of water on melt polymerisation in particular.

The dissolution of water as CaOH and MgOH species is significant in various settings, from magma oceans in the early history of the Earth and other terrestrial planets, to present-day melting over a wide range of depths in the mantle. Since changes in water dissolution mechanisms significantly affect phase relations and physical properties of the melts, the dissolution mechanisms of water must be taken into account when producing quantitative models involving depolymerised hydrous silicate melts.

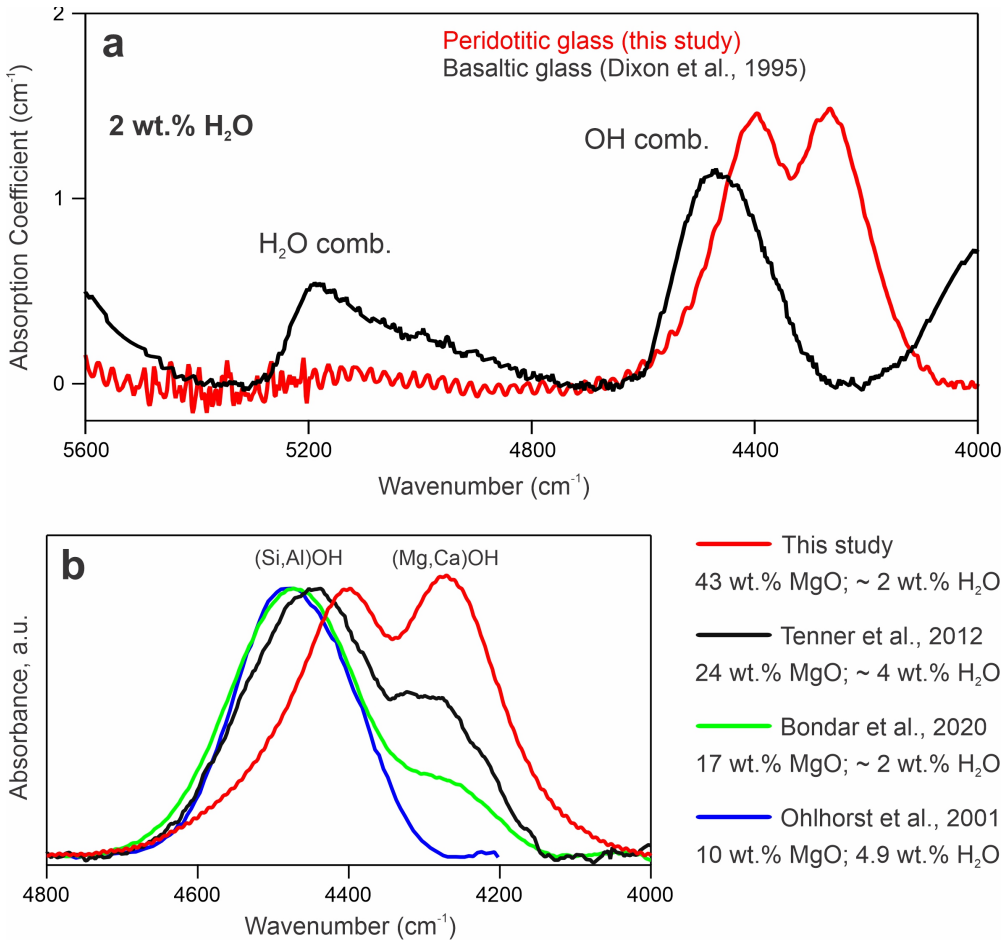

Fig. 3.5-9: Infrared spectra of hydrous peridotitic to basaltic glasses. (a) comparison of spectra of basaltic and peridotitic glasses; (b) occurrence and growth of a combination band related to OH- with increasing MgO concentration. Data sources: Tenner *et al.* (2012, G-cubed 13: Q03016); Ohlhorst *et al.* (2001, Chem Geol 174: 5), Dixon *et al.* (1995, J Petrol 36: 1607), Bondar *et al.* (2020, Rev Sci Instr 91: 065105).

h. *Re-calibration of the infrared extinction coefficient of H_2 in silicate glasses (H. Keppler)*

The primordial volatile inventory of our planet was likely determined by the equilibrium between a magma ocean and a primitive atmosphere. Under the reducing conditions of a terrestrial magma ocean, H_2O may have been largely reduced to H_2. Therefore, the solubility of H_2 in silicate melts needs to be known in order to constrain the fate of hydrogen in the early evolution of our planet. Moreover, very reducing conditions still prevail today in the lower mantle of the Earth, and H_2 may therefore also be a major hydrogen species in Earth's deep interior.

Previous studies of H_2 solubility in silicate melts often used infrared spectroscopy to determine the concentration of H_2 in quenched glasses. While H_2 itself does not possess a dipole moment and therefore should not absorb infrared radiation, it becomes infrared active in silicate glasses due to dipoles induced by the interaction with the glass matrix. H_2 contents in glasses are

therefore usually quantified using an infrared extinction coefficient for H_2 in silica glass. However, this extinction coefficient (Shelby 1994, J Non-Cryst Solids 179: 138) was calibrated in a way – by estimating the amount of H_2 dissolved in the glass simply from the weight loss upon heating – that may introduce very severe errors. Therefore, a series of experiments was carried out to re-determine the extinction coefficient of H_2 in silicate glass.

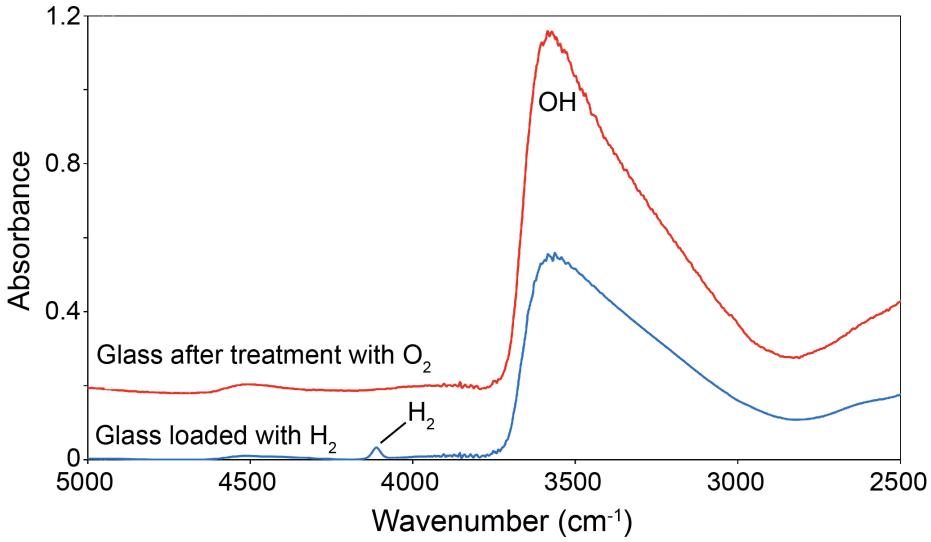

Fig. 3.5-10: Infrared spectra of a H_2-saturated haplogranitic glass before and after treatment with O_2 at 2kbar and 1100 °C. Upon O_2 treatment, the weak H_2 band at 4100 cm^{-1} disappears, while the OH band at 3500 cm^{-1} increases due to the conversion of H_2 to H_2O. The thickness of the samples is about 2 mm.

Hydrogen-saturated haplogranitic glasses were produced in rapid-quench TZM cold seal vessels at 1-2 kbar and 1000-1100 °C as well as in piston-cylinder experiments at 10-30 kbar and 1200-1500 °C. As a source of hydrogen, CaH_2 was used, which decomposes upon heating into metallic Ca and H_2. In this way, glasses containing abundant H_2, but little H_2O or OH were produced. In order to quantify the amount of dissolved H_2, two different analytical methods were used: (1) Karl-Fischer titration. Glasses were heated to 1300 °C, the released gas passed over Cu_2O in order to soxidise H_2 to H_2O and the amount of H_2O was then determined by a coulometric titration using the reaction $I_2 + SO_2 + 2\ H_2O = H_2SO_4 + 2\ HI$. (2) Glasses were loaded together with pure O_2 gas into gold capsules and re-heated to 1100 °C under 2 kbar pressure. This converts all H_2 into H_2O or OH, which can then be determined by infrared spectroscopy (Fig. 3.5-10).

Both analytical methods yielded generally consistent results. A preliminary evaluation of the data suggests that the infrared extinction coefficient of H_2 in glasses is about one order of magnitude larger than previously thought. This implies that measured H_2 solubilities in silicate melts are much lower than suggested by previous measurements and the dissolution of H_2 in a magma ocean probably had only a very limited effect on the volatile inventory of the early Earth.

i. *Modelling volcanic melt viscosities using artificial neural networks (D. Langhammer, D. Di Genova, and G. Steinle-Neumann)*

The shear viscosity η of volcanic melts is a primary factor in determining the eruptive dynamics of volcanos and is mainly influenced by temperature T, melt composition x and melt water content. The water content largely determines whether a volcano erupts explosively or effusively. During magma ascent, the degassing process leads to gas bubbles forming, which build up potential energy as pressure drops. The release of this energy can lead to violent explosions. Highly viscous melts couple to the bubbles and transport them up a conduit, increasing the chances of explosive eruptions. Low-η magmas, on the other hand, decouple and allow the gas to escape from the magma before it reaches the exit. At the same time, η itself is reduced with increasing H_2O content, creating an interesting feedback loop.

Due to the complexity of chemical interactions in natural silicate melts, no physical model that would allow predicting the compositional dependence of η has been found to date. Current descriptions are extensions of empirical equations. They have turned out to be problematic when predicting η of compositions that were not used in fitting. Due to the empirical nature of the equations used, they also have been shown to miss important chemical effects which influence melt viscosity.

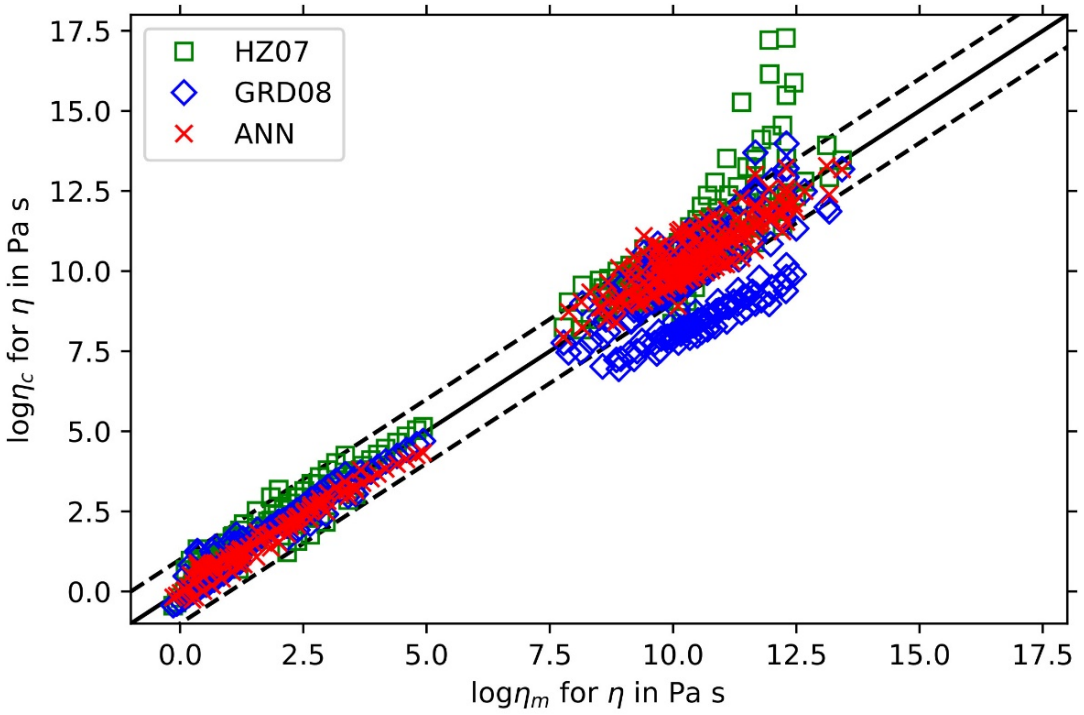

Fig. 3.5-11: Comparison of calculated (log η_c) and measured (log η_m) viscosities for the artifical neural network (ANN, red crosses, RMSE = 0.45), the model by Giordano *et al.* (2008, *Earth Planet Sci Lett 271:*123) (GRD08, blue diamonds, RMSE = 1.23) and Hui and Zhang (2007, *Geochim Cosmochim Acta 71:* 403) (HZ07, green squares, RMSE = 0.89) for melts in the test sets. The one-to-one correspondence is shown by the solid black line; dashed lines indicate a ±1 log-unit deviation from identity.

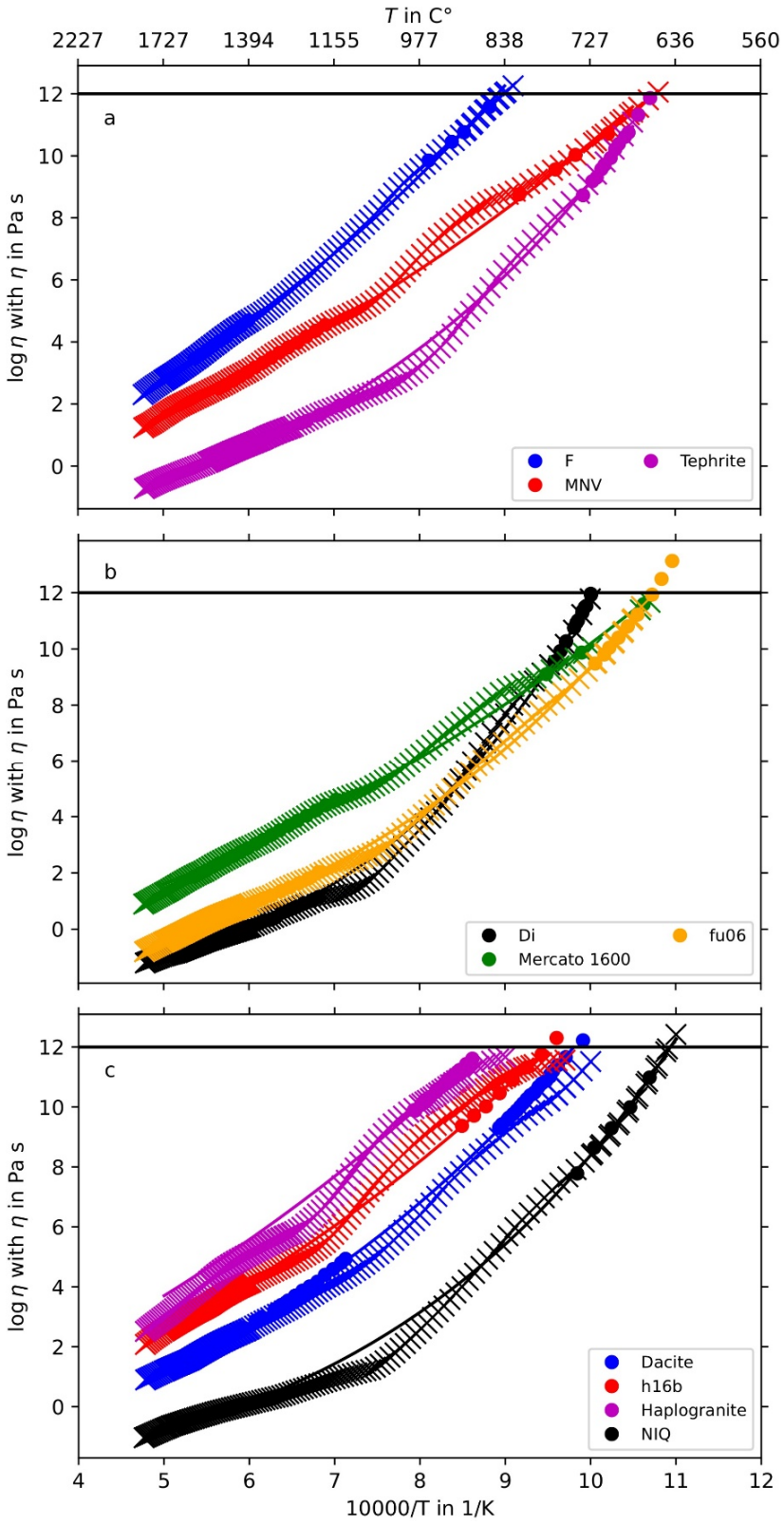

Fig. 3.5-12: Viscosity (log η) as a function of inverse temperature (10000/T) for some anhydrous compositions in the training/validation database (panels a and b) and the test set (panel c). Measurements are shown by filled circles, viscosity values predicted from the ANN by crosses. Solid lines show MYEGA fits to the experimental data. The horizontal lines indicate 10^{12} Pa s.

We train an artificial neural network (ANN) on a data set containing 3482 η measurements, using oxide composition, H_2O content and T as parameters. The data set contains compositions spanning virtually all terrestrial volcanic melts and some more exotic compositions. Due to the lack of an empirical equation, even unknown effects can be included in the ANN model, as long as they are present and detectable for the neural network within the data used. As ANN, we use a feed-forward multilayer perceptron with two layers. Our data is split into three disjointed sets for training, validation and testing. The training set is used for the regression steps of the ANN, the validation set is used as a diagnostic to check for overfitting and the generalisation capabilities of the ANN during the training procedure. The test set is used to assess the prediction accuracy of the ANN. Choosing the network architecture is performed in two steps: First, a stochastic Bayesian optimisation searches the parameters space for combinations of parameters (*e.g.*, neurons per layer, learning rate) that result in high accuracy. The resulting ANN is then retrained using a 20-fold cross validation to improve generalisation capabilities. The network yielding the highest accuracy when predicting the test set is chosen as the final model.

We compare our final ANN with two literature models by Giordano *et al.* (2008, *Earth Planet Sci Lett 271:* 123) and Hui and Zhang (2007, *Geochim Cosmochim Acta 71:* 403). Both of these models are based on empirical *T*-dependent viscosity equations, which include compositional dependence, and our model outperforms both significantly (Fig. 3.5- 11). Since measurements between the low and high η regimes, *i.e.*, in the transition zone between glass and liquid, are currently not possible for natural silicate melts, no data for training exists in this gap. An investigation of the ANN in this interval reveals unphysical behaviour, *i.e.*, a non-exponential decrease of viscosity with temperature (Fig. 3.5-12). Due to the lack of data, this is not surprising, but must be addressed in the future.

j. *Viscosity of anhydrous and hydrous peridotite melts (D. Di Genova, D. Bondar, A. Zandonà/Rome, P. Valdivia Munoz, R. Al-Mukadam/Orleans, H. Fei, A.C. Withers, T. Boffa Ballaran, A. Kurnosov, C.A. McCammon, J. Deubener/Clausthal, and T. Katsura)*

The viscosity of peridotite melts was investigated only to a limited extent so far, without considering the effect of dissolved water. This is due to the very low glass-forming ability of these melts, which prevents conventional viscosity measurements. However, ultramafic liquids play a key role in our understanding of deep mantle dynamics and of planetary formation. The Earth is thought to have experienced a large degree of melting in its early history. The resulting peridotite magma ocean facilitated core formation through silicate-metal segregation and generated the primordial atmosphere and hydrosphere through degassing. Moreover, highly ultramafic and Mg-rich melts (such as picrites and kimberlites) may be formed in the modern Earth by partial melting of peridotite in the upper and lower mantle, with far-reaching implications for the transport of incompatible elements such as hydrogen.

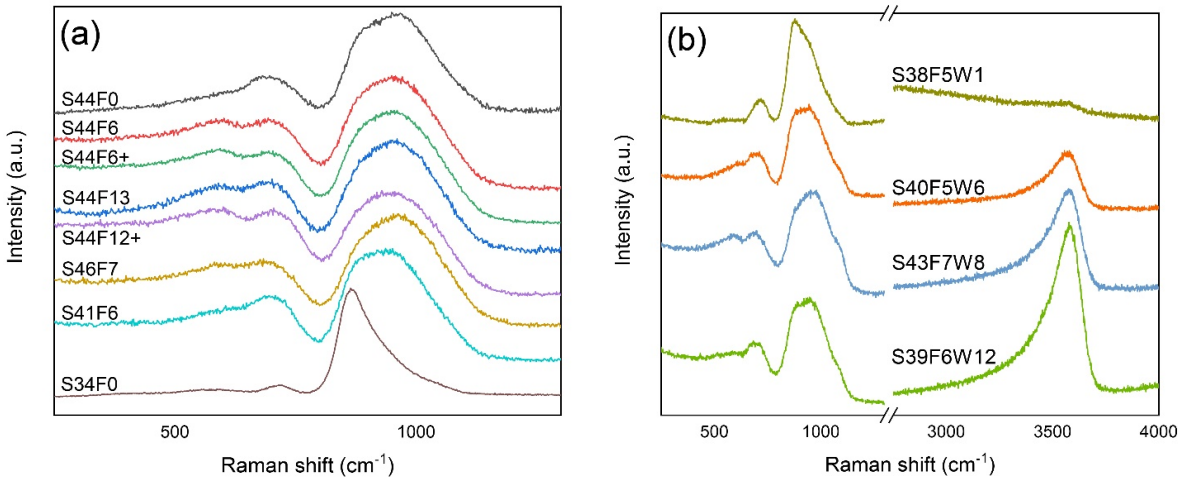

Fig. 3.5-13: Raman spectra of peridotite glasses synthesised within this work. (a) Anhydrous peridotite glasses synthesised by aerodynamic levitation coupled to laser heating at CNRS CEMHTI; (b) Hydrous peridotite glasses synthesised using a novel rapid-quench multianvil technique developed at BGI.

The melt viscosity (η) of anhydrous and hydrous peridotite was therefore studied using a multipronged approach combining micropenetration viscometry, conventional DSC (differential scanning calorimetry), flash DSC and Brillouin spectroscopy. The peridotite glasses used for the investigations were synthesised by: (i) aerodynamic levitation coupled to laser heating at CNRS CEMHTI in Orléans (France) in the case of anhydrous samples; (ii) a novel rapid-quench multianvil technique developed at BGI for hydrous samples. Raman spectroscopy measurements confirmed first the glassy state of the samples (Fig. 3.5-13) and were then used to verify the absence of crystallisation and/or degassing during viscosity and calorimetric measurements.

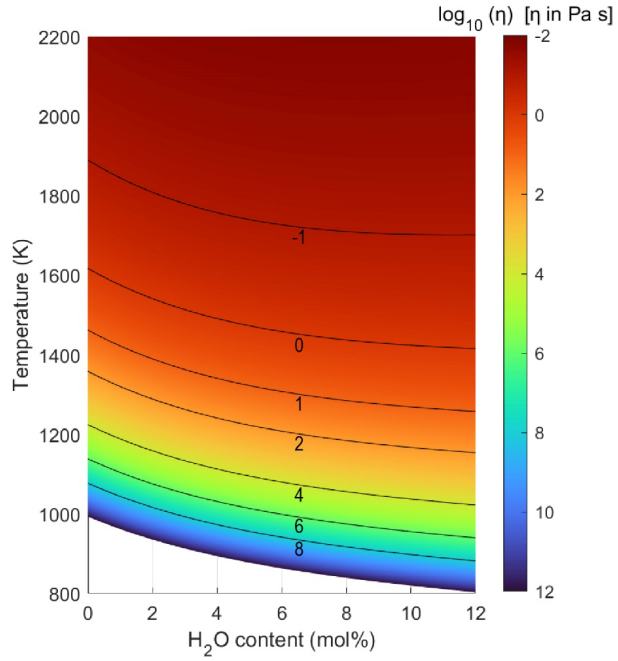

Fig. 3.5-14: Viscosity of hydrous peridotite melts as a function of temperature and H_2O content.

Using the approach described and by fitting the measured data with the MYEGA equation, it was possible to obtain an accurate description of the pure liquid viscosity of peridotite melts over thirteen orders of magnitude (from T_g to $\eta \cong 10^{-1} Pas$), covering a broad range of compositions and oxidation states. Comparing our experimental data with the predictions of the most widespread empirical viscosity models, significant variations were noticed, demonstrating that peridotite melts fall well outside the domain of reliability of such models due to their exotic composition. Consequently, a new optimised model was developed for the temperature- and H_2O-dependent viscosity of peridotite melts with H_2O contents up to 12 mol. % (Fig. 3.5-14).

k. *Are volcanic melts less viscous than we thought? The case of Stromboli basalt (P. Valdivia Munoz, A. Zandonà/Orleans, A. Kurnosov, T. Boffa Ballaran, J. Deubener/Clausthal, and D. Di Genova)*

Recent investigations have demonstrated that volcanic melts can be prone to nano-crystallisation and dehydration during viscosity measurements. Previous studies of melt viscosity did not account for such effects. This may have hindered the accurate measurement of melt viscosity, negatively affecting the reliability of the current viscosity models of magmas and hampering the forecasting of volcanic eruptions from a probabilistic standpoint. In this work, we constrain the viscosity of Stromboli basaltic melt as a function of temperature and dissolved water content. Stromboli volcano is known for its persistent strombolian activity and its sporadic paroxysmal events. Paroxysms are responsible for the most hazardous behaviour of Stromboli volcano, being associated with the rapid ascent of basaltic magma.

Our experimental results show that hydrous Stromboli basaltic melts are prone to crystallise nano-sized Fe-Ti-oxides during experimental measurements, causing an overestimation of viscosity at temperatures above the glass transition temperature (T_g). To overcome this problem, we propose a new viscosity model based on the Mauro–Yue–Ellison–Gupta–Allan parametrisation, incorporating T_g conservatively measured via differential scanning calorimetry and m derived by Brillouin spectroscopy. Figure 3.5-15 shows the comparison of our viscosity model with previous models between 0 and 5 H_2O wt. %. For the anhydrous endmember (left border in Fig. 3.5-15a), and close to T_g (*i.e.*, around 10^{12} Pa s), our model shows similar behaviour with respect to the GCA and GRD models. Nevertheless, at water contents higher than 1 wt. %, our model predicts lower viscosities (Fig. 3.5-15b). For example, at pre-eruptive conditions (T = 1150 °C and ~ 3 wt. % H_2O), our model predicts viscosities of $10^{0.35}$ Pa s, in contrast to the $10^{0.55}$, $10^{1.01}$, and $10^{0.66}$ Pa s predicted by the GCA, GRD, and HZ models, respectively, 2-4 times lower than previous predictions. We attribute these differences to the overestimation of the hydrous viscosity data in the literature, which particularly invalidates the determination of m as a function of H_2O. The literature sources assume that m decreases with water content, while we found that m is not affected by water. This agrees with our configurational heat capacity results and the theoretical analysis of melt dynamics. The differences observed between our model and those in the literature can strongly affect the ability to predict magma emplacement and volcanic processes. For example, if we consider a simple

ascent rate model neglecting the shear-rate dependence of viscosity, halving the pure melt viscosity doubles the emplacement velocity. In conclusion, the accurate and reliable parametrisation of melt viscosity is crucial for the numerical modelling of magma dynamics, which is ultimately the basis for assessing eruptive scenarios and facilitating decision-making during a volcanic crisis.

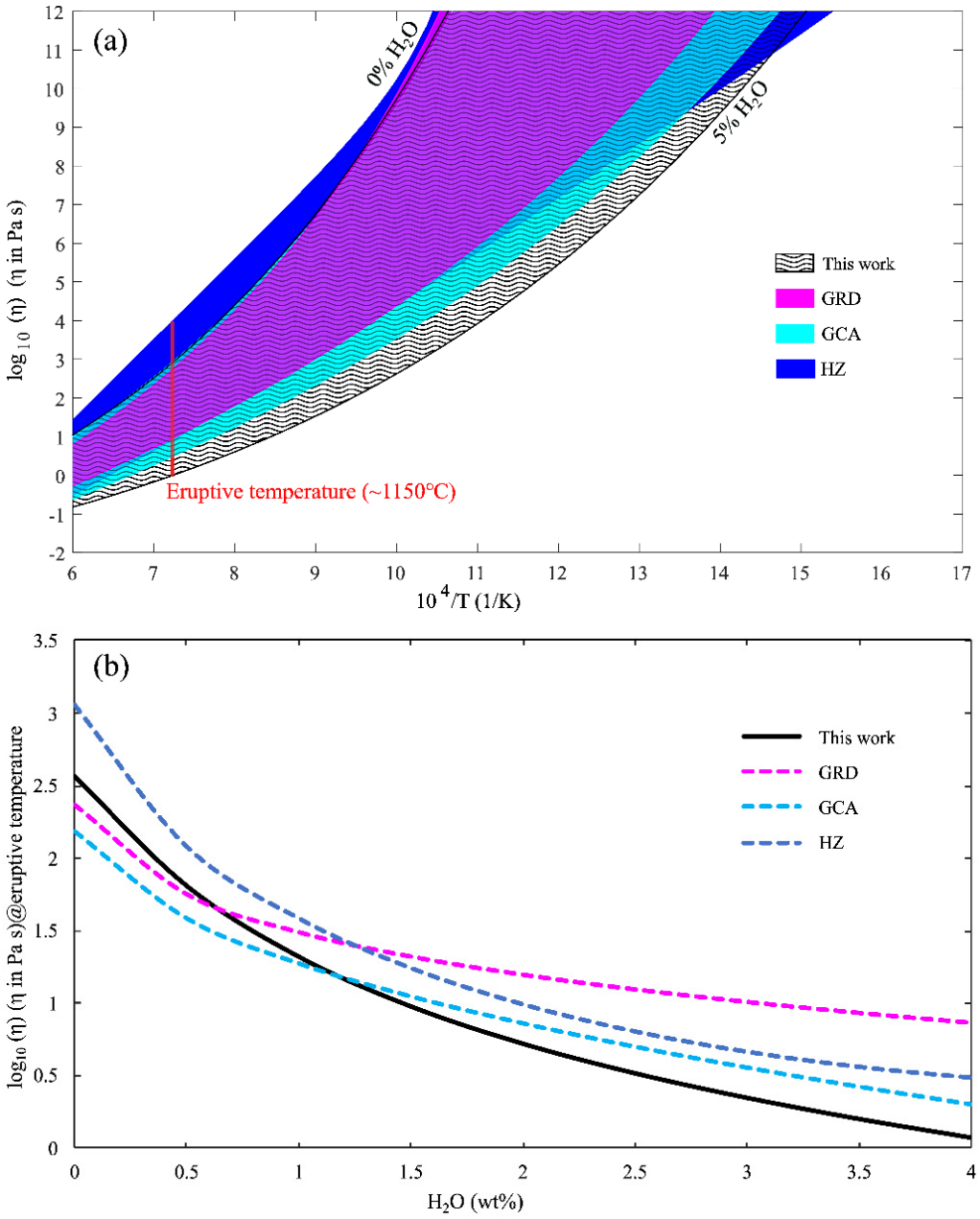

Fig. 3.5-15: (a) Comparison of four viscosity models for Stromboli basalt from 0 wt. % (left border) to 5 wt. % H_2O content (right border). Giordano *et al.* (2008; Earth Planet Sci Lett 271: 123), GRD; Giordano *et al.* (2009; Geochim Cosmochim Acta 73: 6613), GCA; Hui & Zhang (2007; Nature 402: 648), HZ. The vertical red line corresponds to the most common pre-eruptive temperature of Stromboli basalt (T = 1150 °C). (b) Predicted viscosity as a function of water content at pre-eruptive temperature, comparing this work, GRD, GCA and HZ.

l. *A chemical threshold controls nano-crystallisation and degassing behaviour in basaltic magmas (A. Scarani, F. Di Fiore, A. Vona, and C. Romano/Rome, A. Zandonà/Orleans, H. Bornhöft and J. Deubener/Clausthal in collaboration with P. Valdivia Munoz, R. Putra, N. Miyajima, and D. Di Genova)*

Volcanic eruptions represent a serious threat to humans, infrastructure, and economy. As such, the probabilistic prediction and mitigation of volcanic risks are of paramount importance in modern Earth science. Such predictions rely on the numerical modelling of magma ascent, which is strongly affected by the melt phase viscosity of the magma. For this reason, the temperature and composition dependence of melt viscosity is one of the most studied topics in experimental volcanology in the last decades. However, as already noted in the previous contribution, nano-crystallisation during viscosity measurements may cause the viscosity of the liquid to be overestimated by up to two orders of magnitude and thus brings into question on the accuracy of our present knowledge of the magma viscosity.

Here, we combine Raman spectroscopic and scanning transmission electron microscopic (Fig. 3.5-16) studies of glasses with viscosity measurements (Fig. 3.5-17) to demonstrate the experimental challenges related to the correct determination of the viscosity of magmatic liquids. We show that the nano-crystallisation of iron titanium oxides substantially increases the viscosity of a Mt. Etna trachybasalt, while this phenomenon is far less pronounced in a Stromboli high-K basalt. We attribute this difference to small, but significant differences in total iron and titanium contents. Our results thereby emphasise the need for a critical review and validation of the published viscosity data.

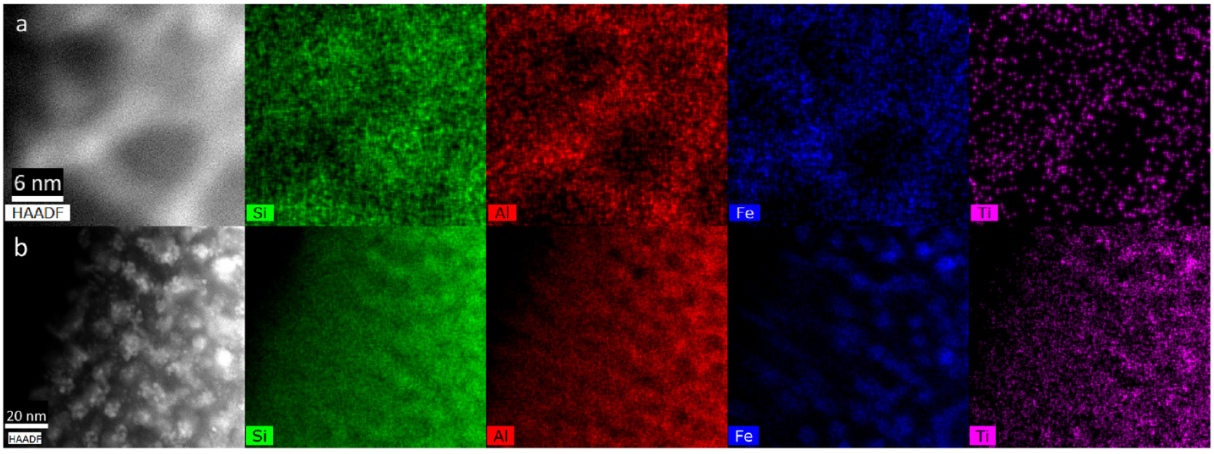

Fig. 3.5-16: Scanning transmission electron microscope high-angle annular dark-field (HAADF) micrographs and energy-dispersive X-ray spectroscopic elemental maps of basaltic glasses, demonstrating nanoscale clustering of Fe, Ti, and Al. (a) Mt. Etna sample that experienced lower temperature than the sample in (b). Note the heterogeneous distribution of Si, Al, Fe and Ti at the nanoscale and mind the different magnification levels, scale bars are provided. From Scarani *et al.* (2022, Nature Comm Earth Environm 3: 284).

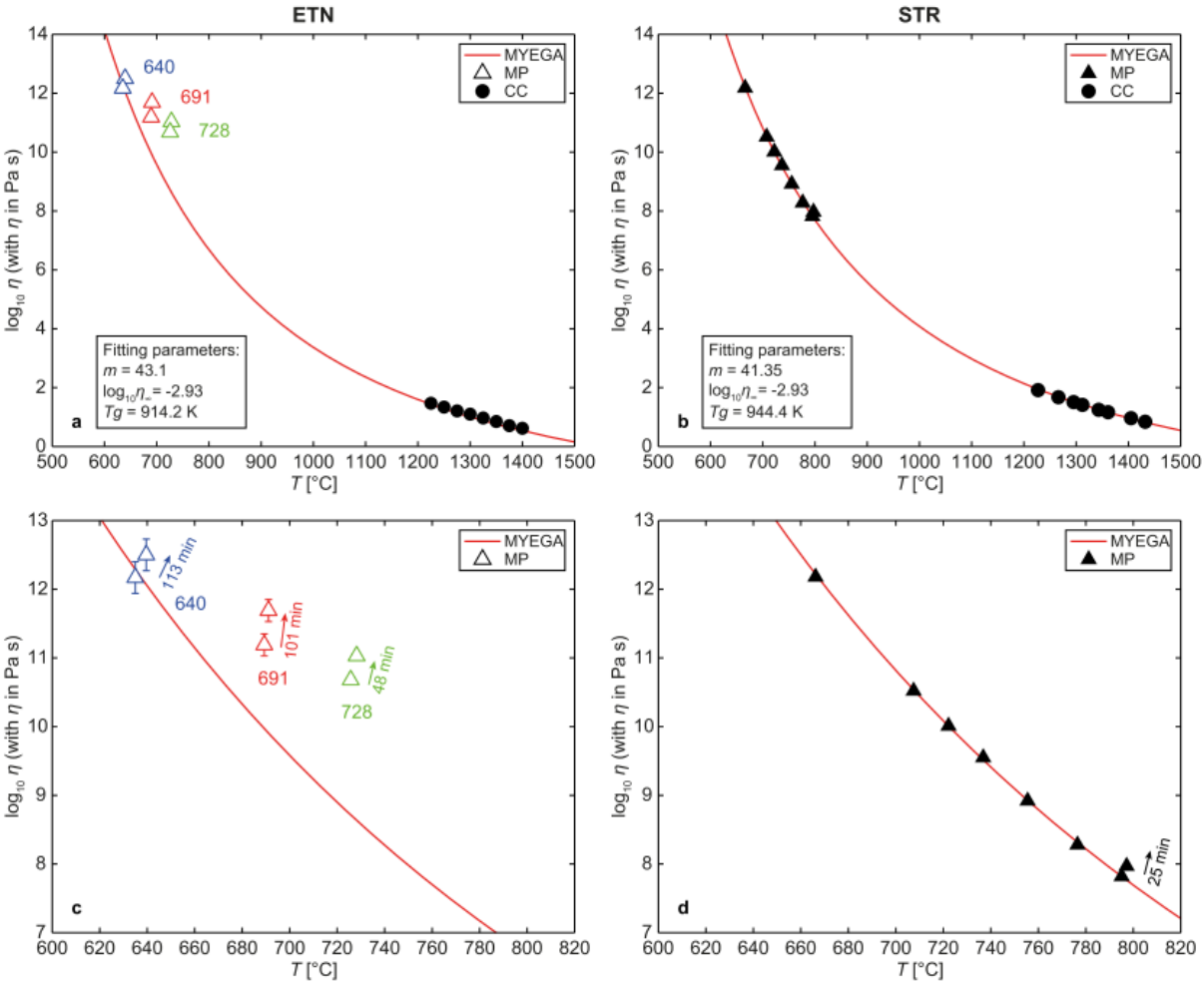

Fig. 3.5-17: (a) Viscosity measurements of Mt. Etna and Stromboli basaltic glasses. Viscosity measurements performed by micropenetration viscometry (MP; low-temperature range) and rotational viscometry (CC; high-temperature range) on (a) ETN and (b) STR melts, compared to the complete viscosity curves of the pure melts. The low-temperature range is shown in greater detail in panels (c) and (d), manifesting the much wider temperature interval in which STR was reliably measurable, whereas ETN invariably exhibited a time-dependent increase in viscosity and a strong deviation from the expected values. Red lines correspond to the MYEGA fit using. Error bars correspond to the standard deviations of MP measurements. Where not reported, error bars are smaller than symbols. From Scarani *et al.* (2022, Nature Comm Earth Environm 3: 284).

Our results have important implications, since nanocrystals have been identified in various rocks formed during explosive eruptions. The formation of nanocrystals not only increases magma viscosity but also triggers vigorous nucleation of bubbles upon magma decompression. We therefore performed high-pressure and high-temperature experiments using hydrous melts from Mt. Etna and Stromboli. We found that at eruptive conditions, nano-crystallisation occurs more pervasively in Mt. Etna basalt as compared to Stromboli samples, fostering bubble nucleation. The peculiarly dissimilar eruptive activities of Mt. Etna (generally more explosive) and Stromboli may therefore also originate from a different degree of decompression-driven

oversaturation in Fe- and Ti-oxides, controlling the tendency of their magmas to nano-crystallise.

m. *Dendritic crystallisation in hydrous basaltic magmas controls magma mobility within the Earth's crust (F. Arzilli/Camerino, M. Polacci, D.A. Neave, M.E. Hartley and M.R. Burton/Manchester, G. La Spina/Catania, N. Le Gall/London, E.W. Llewellin/Durham, R.A. Brooker and H.M. Mader/Bristol, R. Torres-Orozco/Xalapa, D. Di Genova, D. Giordano/Torino, R. Atwood/Didcot, P.D. Lee/Harwell and F. Heidelbach)*

Magma ascent towards the surface occurs mainly through dikes, which commonly develop as near-vertical features within the crust. Dikes have the potential to either reach the surface and to trigger an eruption, or to be frozen within the crust. Whether or not a dike reaches the surface and produces an eruption depends on the flux of magma supplied from the magma reservoir, as well as on the evolution of the physico-chemical properties of the magma and the mechanical properties of its host rock. Crystallisation kinetics can have a major effect in controlling the rheological behaviour of magma, promoting sudden and drastic transitions in magma rheology during dike propagation.

Dendritic crystallisation can occur rapidly, resulting in a rapid evolution of crystal shapes and the development of complex textures. These can be resolved directly in real time in three dimensions (3D) using *in situ* 4D (3D + time) X-ray computed microtomography (μCT) experiments. Until now, these experiments have been restricted to anhydrous samples at atmospheric pressure, allowing investigation of crystallisation and its influence on magma rheology only at high temperatures and surface pressure.

Here, we use a novel high-pressure experimental apparatus to perform *in situ* 4D μCT experiments at high temperatures and water-saturated conditions at crustal pressures, to investigate crystallisation kinetics and the 3D evolution of clinopyroxene shape in real time (Fig. 3.5-18) using a trachybasaltic melt from Mt Etna. The experiments were carried out at the DIAMOND light source (UK) with a high-temperature cell onto which pressure was applied through a piston from a mechanical rig. These are the first experiments in which it was possible to quantify the crystal growth rate directly in 3D through time under water-saturated conditions at moderate pressure. Consequently, crystallisation kinetics and the morphological evolution of clinopyroxene as a function of ΔT can be studied, allowing to quantify how crystallisation and the evolution of crystal aspect ratio can affect magma rheology under conditions relevant to crustal transport. We used a simple numerical dike propagation model to simulate magma ascent and test the effects of the observed systematics of dendritic crystallisation on magma rheology and mobility. This model showed that dendritic crystallisation might drastically reduce magma mobility and eruption potential. This improved understanding of a basaltic volcanic systems will play an important role in hazard assessment and risk mitigation strategies in areas of active basaltic volcanism.

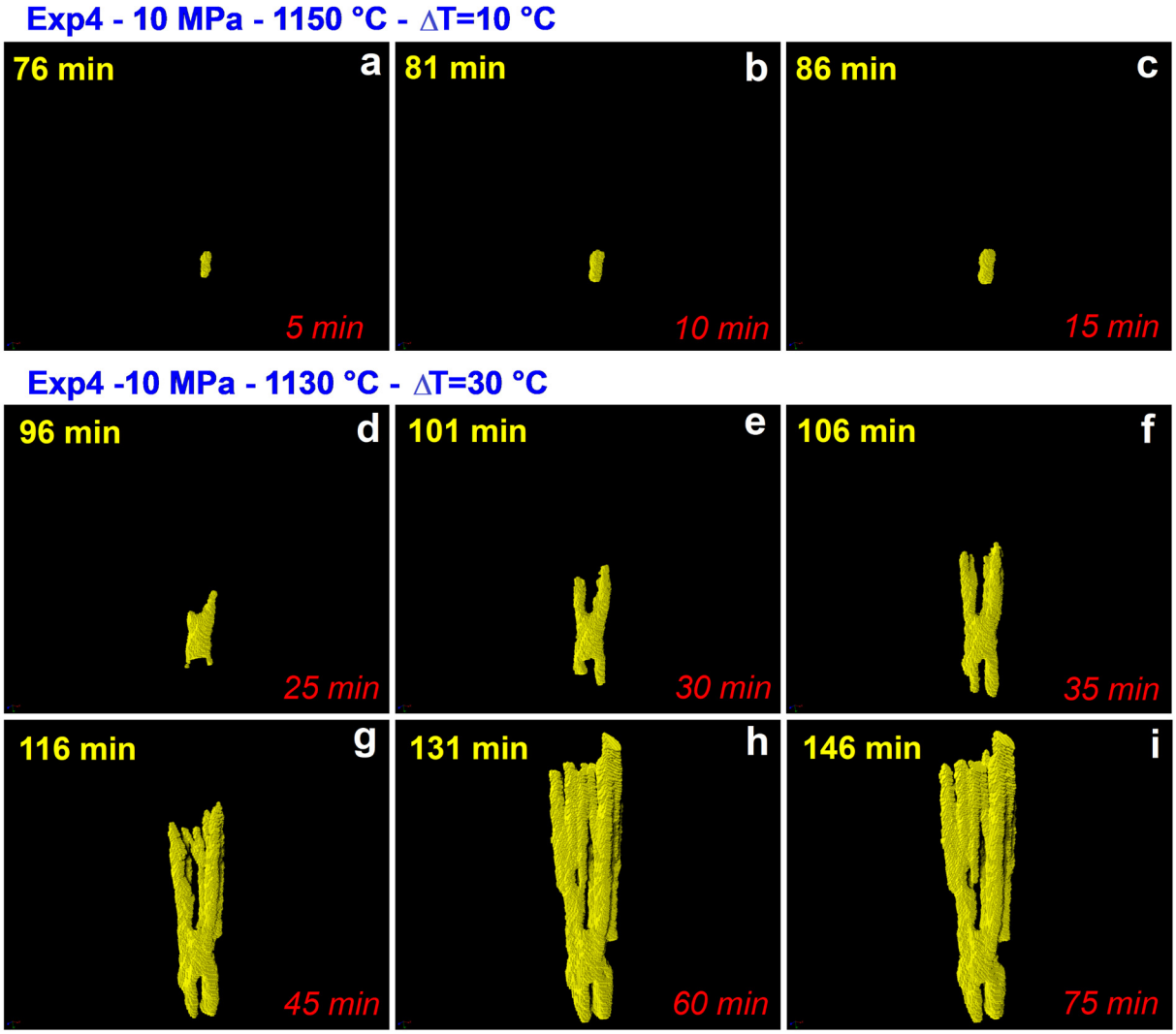

Fig. 3.5-18: Crystallisation and crystal shape evolution of a clinopyroxene crystal through time during experiments. (a, b, c) Volume renderings show the growth of a euhedral clinopyroxene crystal through time at 1150 °C and ΔT = 10 °C. (d, e, f, g, h, i) Volume renderings show the transition between euhedral to dendritic shapes and the growth of a dendritic clinopyroxene crystal through time at 1130 °C and ΔT = 30 °C. The time in yellow reported in each panel indicates the time passed from the beginning of the experiment. The time in red reported in each panel indicates the time passed from the formation of the pyroxene crystal. The width of each image is about 0.5 mm. From Arzilli *et al.* (2022, Nature Comm 13: 3354).

3.6 Rheology

The interior of the Earth and many other planetary or cosmic bodies is characterized by dynamic processes which are mostly driven by the transport of heat and/or matter. The resulting rock deformation is dependent on a combination of intrinsic factors such as composition, (micro)structure, and volatile content, as well as extrinsic factors such as temperature, pressure and magnitude and duration of deviatoric stress. Depending on these factors, the deformation mechanisms may vary and lead to very different rheologies, which are then described by stress-strain rate relationships or flow laws. Determining the rheology of rocks is, therefore, one of the most important fields of mineralogy for understanding planetary dynamics and evolution. For these reasons, BGI scientists have put effort into rheological studies, particularly at high pressures and high temperatures.

The first three contributions of this chapter are concerned with the plastic deformation of planetary materials by ductile flow. In the first article, a new experimental setup is presented that allows to deform various phases of water ice and measure the stresses and strains for constructing flow laws that are applicable to the convecting interiors of planetary bodies in the outer solar system. The following experimental study evaluates the influence of enstatite as a secondary phase next to olivine in upper mantle rocks on the rheology as well as the texture and seismic anisotropy. Results are very compatible with observations from natural samples and allow for a quantitative interpretation of seismically observed anisotropies. The third contribution presents a theoretical investigation of the effect of surface tension in deforming two-phase media and applies them to the ductile flow of lower mantle materials, *i.e.*, ferropericlase-bridgmanite mixtures. The calculations show that high surface tension inhibits the elongation of the weaker ferropericlase and causes a significant strengthening of the bulk material.

The following two contributions focus on deformation mechanisms during earthquakes in the deep upper mantle, where the brittle behaviour of rocks is considered unlikely due to the high temperatures and confining pressures. The first one presents results from an experimental study where the olivine-spinel transition is investigated as a possible faulting mechanism. The grain size of the olivine is shown to play a critical role in this process: whereas in fine-grained starting materials, the formation of spinel is on to grain boundaries producing large offsets and faults, it is restricted to grain interior in coarse-grained olivine with only small offsets. This difference may influence the relationship between the frequency and magnitude of earthquakes (Gutenberg-Richter law). The second in this part is a theoretical study that models the stress generation during the olivine-spinel phase transition taking into account both the change in viscosity as well as the reduction in volume. Whereas both factors alone may already produce high stresses, a combined activation would result in stronger weakening effects causing ductile faulting.

The last two contributions use microstructural and chemical/isotopic analysis to reconstruct the impact and shock deformation history of meteorites as parts of their parent body. The study of

Walte *et al.* compares grain size distributions in pallasite meteorites as indicators of the impact process with those produced in experimental samples during high strain rate deformation experiments. The two natural types of microstructure, referred to as angular and fragmental, can be reproduced by experiments with increasing stresses and strain rates, and are associated with the degree of exposure to the shock wave, which is much higher in the latter type. The last contribution presents the microstructural and chemical signatures of a chondritic meteorite consisting of an impact melt breccia with large melt clasts. Chemical and isotopic comparison of chondritic and melt clast olivines shows that the composition of the melt is strongly influenced by the impactor. The microstructural analysis allows to reconstruct three separate shock events, with the first one producing the melting of the chondrite host, the second causing a brecciation and fragmentation of both host and melt, and the third generating local melt veins both in the chondrite host and at the boundaries to the impact melt rock clasts.

a. *Utilizing the direct piezoelectric effect to measure the stress-strain relationship of cryogenic water ice at high pressures (J. Dolinschi and D.J. Frost, in collaboration with C. Howard and N.P. Walte/Garching)*

Water can arguably be considered to be the most important substance for life on Earth. Every form of life depends on water for its existence, and it is present in every environment on Earth. However, below the surface, water is present within the Earth's interior, where it also plays an important role. Many minerals can contain water, and from experimental and computational studies, we know that it changes the properties of minerals in the Earth's interior depending on the amount of water that is contained within the mineral's structure. Beyond Earth, water is present within all cosmic bodies in the Solar System. The further out into the Solar System a cosmic body is, the more important water becomes. In regions beyond the asteroid belt, water exists mainly as ice and can even make up the majority of the mass of planetary and asteroidal bodies. In the larger bodies, the pressure in the interior is high enough that water-ice transforms into different polymorphs. Even though it is a relatively simple molecule, water has a surprisingly diverse and complex phase diagram. While there have been many studies on glacial ice and some on high-pressure ices, there have been relatively few measuring the strength of deforming ices, and some high-pressure ice phases have not been studied at all. This is a critical missing piece of knowledge because in the interior of these bodies, ice can be considered to be the equivalent of rock in the Earth, and their interiors are likely to undergo convection as occurs in the Earth's mantle. Convection involves deformation of materials in response to applied stresses, so to develop accurate and realistic models for the interiors of these icy bodies, knowledge of the flow laws and the strength of ice is required.

A new method for performing deformation experiments, involving a portable sample assembly, has been developed using the SAPHiR press of BGI at the FRM II neutron source in Garching to subject water-ice to high pressure in a large-volume press. The sample is cryogenically cooled to low temperature using liquid nitrogen, and then deformed using the 6-anvil cubic

press. The sample strain is measured using precise laser measurements of the anvil positions. Stress is measured using a novel *in situ* stress sensor developed at BGI utilizing a piezoelectric crystal within the assembly and inside the deformation column. Using this technique, we can explore the strength of ice undergoing deformation up to 5 GPa, and at temperatures down to -150 °C (Fig. 3.6-1). Strains up to 30 % and strain rates as low as 10^{-4} s^{-1} are possible using 6-axis cubic press at BGI that is capable of individual anvil movements for deformation experiments. The stress is measured with a piezoelectric CTGS ($Ca_3TaGa_3Si_2O_{14}$) crystal. By pumping to specific pressures and controlling the sample temperature with the flow rate of liquid N_2 (LN_2) through the sample assembly, we can produce a specific phase of water-ice. We can then deform the ice and measure strain and stress *in situ* and thus create a stress-strain curve. Preliminary experiments have been performed, and we have confirmed that the assembly successfully contains the water in a Teflon capsule throughout the entire experiment. The sample temperature is tightly controlled by adjusting the LN_2 flow rate, and the stress can be measured in real-time and *in situ* with the piezoelectric crystal stress sensor in the assembly. Some challenges remain, such as anomalously low electrical resistance across the piezoelectric crystal that causes a large measurement error and an improved control of the LN_2 flow rate and thus temperature is required to increase the accuracy of the stress measurement. Some preliminary deformation experiments have been performed, showing that ice VI is weaker than ice VIII in both compression and tension (Fig. 3.6-2), a world-first measurement that previously was only calculated theoretically.

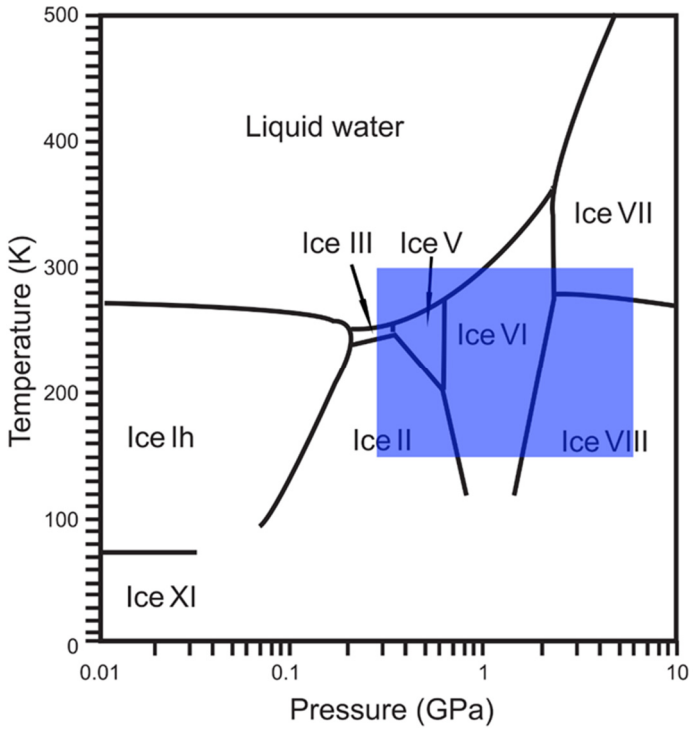

Fig. 3.6-1: The pressure-temperature phase diagram of water, with the region achievable with the system developed at BGI and at the Technical University Munich shown by the blue shaded rectangle.

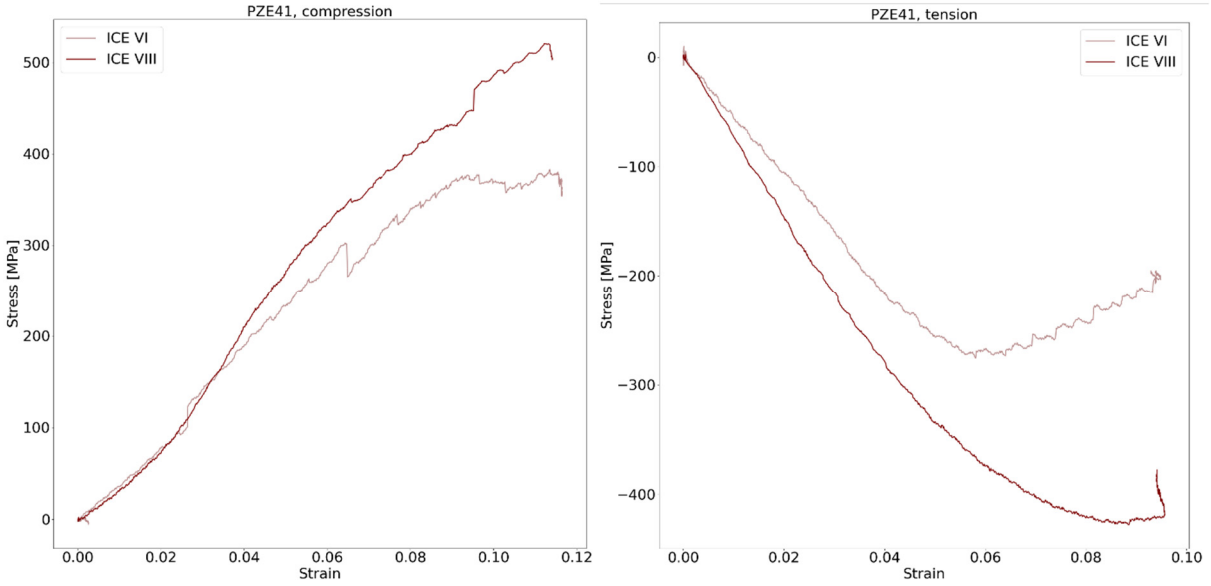

Fig. 3.6-2: Results of high-pressure deformation experiments of ice VI and ice VIII under both compression and tension. Ice VI was deformed at 1.3 GPa and 166 K and ice VIII was deformed at 3.2 GPa and 184 K.

b. *High-temperature deformation of enstatite-olivine aggregates (F. Heidelbach, M. Bystricky/ Toulouse, J. Lawlis/University Park and S. Mackwell/Minneapolis)*

The rheology of the upper mantle is of particular importance for the understanding of the mechanisms of plate tectonics as well as heat transport and convection in the whole mantle. Geophysical anisotropies observed for this region of the Earth's interior have been interpreted through the microstructures and textures (crystallographic preferred orientations, CPO) that develop as a result of large-scale plastic deformation and as such give an indication of the convective motion in the upper mantle. The rheological behaviour of upper mantle rocks is complicated by their polyphase mineralogy and has often been approximated by the properties of the dominant, and likely weakest, phase, olivine. In this study, we investigated the influence of the second most abundant phase, orthopyroxene, on the deformation of olivine aggregates in order to reproduce a more realistic mantle mineralogy.

Samples were prepared as mixtures of San Carlos olivine $(Mg_{0.9}Fe_{0.1})_2SiO_4$ and enstatite, which had been produced through the reaction of San Carlos olivine with quartz in a one-atmosphere furnace under controlled oxygen fugacity conditions near Ni/NiO ($10^{-5.5}$ atm). The two phases were then mixed thoroughly in different proportions and finally hot-pressed together in an internally heated gas-medium pressure vessel for up to 12 h at 1300 °C and 300 MPa confining pressure producing an equigrained microstructure with a grain size of about 10 µm for both phases and less than 2 % porosity. Axial-compression creep experiments were performed at constant load using a Paterson gas-medium deformation apparatus at 1100-1300 °C, 300 MPa confining pressure and strain rates ranging from 4×10^{-7} s^{-1} to 10^{-4} s^{-1}. Deformed samples were sectioned and polished in the plane containing the compression and extension directions for

microstructural analysis with SEM-EBSD, which enabled the grain structure and fabrics of the two phases to be determined.

The mechanical data are best approximated by a combined diffusion/dislocation creep flow law with the dislocation component being dominant at high stresses and strain rates. Microstructural analysis shows that the olivine-enstatite aggregates deform rather homogeneously with no obvious strength contrast between the two phases as shown here for sample PI399 with 25 % enstatite and 75 % olivine (Fig. 3.6-3). Both phases also show weak but distinct CPOs (Fig. 3.6-4): for olivine, the b-plane (010) is aligned in the compression plane, and both (100) and (001) display girdle distributions in the compression plane consistent with a- and c-slip on the b-plane. For enstatite, (001) forms a girdle in the compression plane, whereas (100) and (010) are aligned with the compression direction. This is consistent with the c-slip on the a- and b-planes of enstatite, but could however also be caused by pronounced dissolution/precipitation creep in the c-direction.

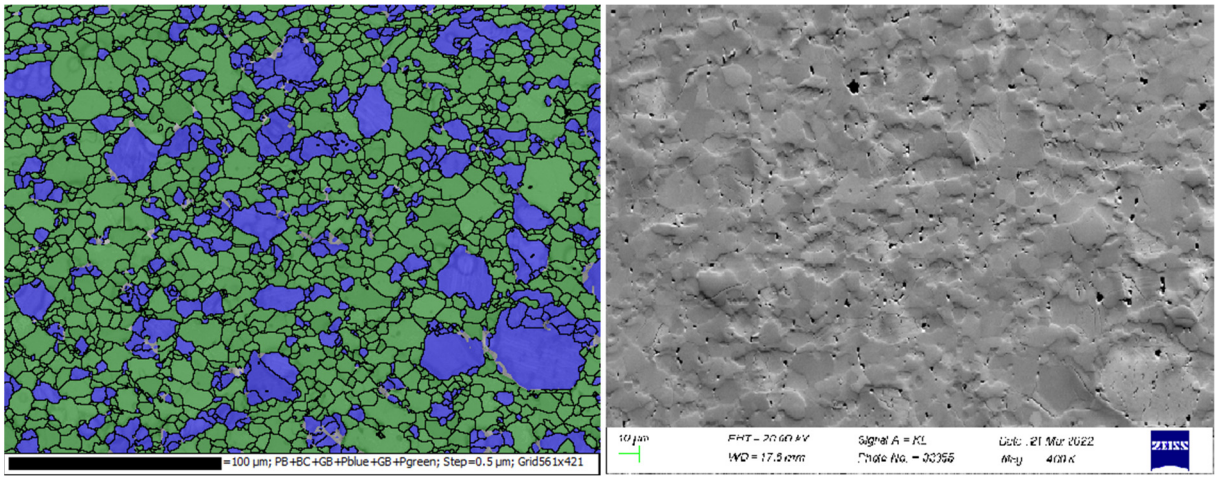

Fig. 3.6-3: Microstructure of sample PI399 (18 % strain, 25 % opx, 75 % olivine); left: EBSD map with color-coded phases (olivine-green, enstatite-blue) and grain boundaries (misorientation > 10°) in black; right: SEM orientation contrast image of the same area.

The texture information was then used in combination with the single crystal elastic tensors of olivine and enstatite to calculate the resulting elastic anisotropy of the sample (Fig. 3.6-5). The p-wave anisotropy is about 3 %, with the lowest and highest velocities perpendicular and parallel to the compression plane, respectively. Shear wave splitting is strongest (2 %) in the compression plane with the polarization of the fast shear wave in the compression plane. In the compression direction, the shear wave splitting reduces practically to zero. The anisotropies are relatively low relative to naturally observed values which are partly due to the low strain and weak texturing in the investigated sample. However, the alignment of the anisotropy in the experimental samples is nevertheless qualitatively quite compatible with the seismologically determined anisotropy patterns assuming that the compression plane is horizontal in the upper mantle indicating that the experimental conditions may be applicable to the upper mantle deformation.

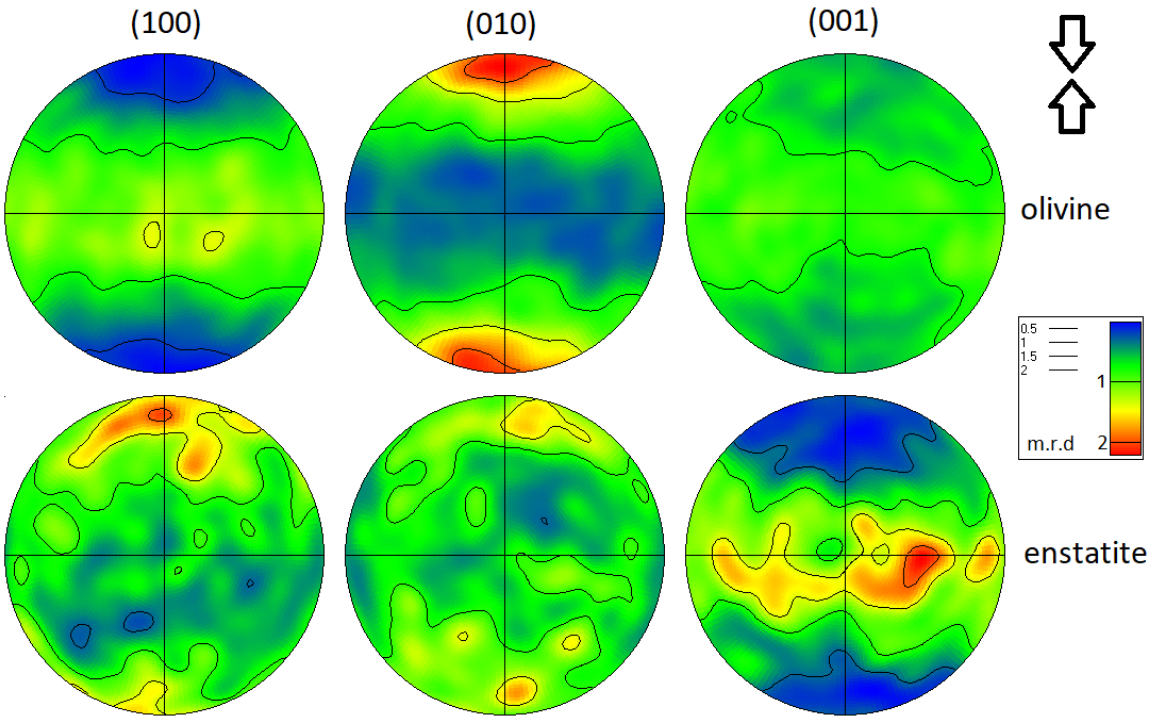

Fig. 3.6-4: Pole figures for sample PI399; top: olivine; bottom: orthopyroxene. Compression direction is vertical; equal-area projections, lower hemisphere.

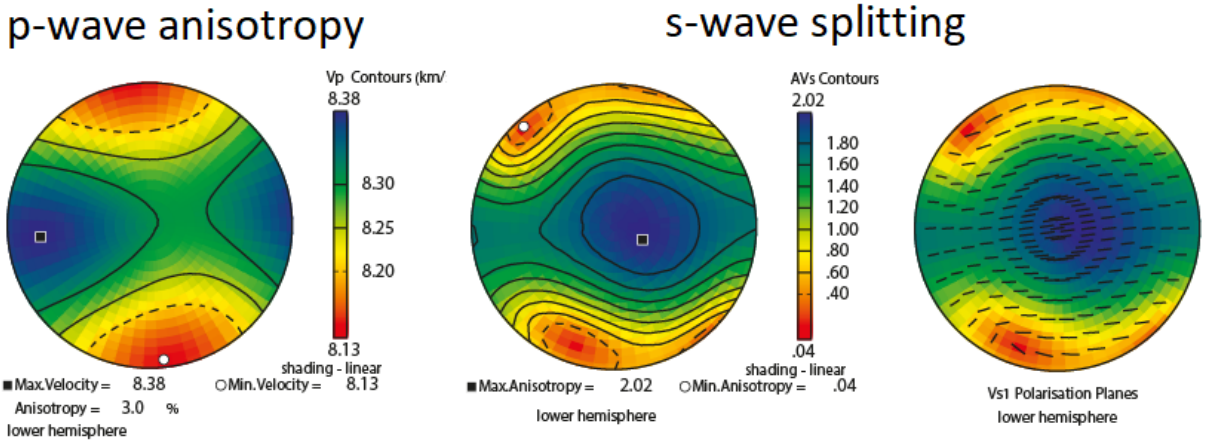

Fig. 3.6-5: Calculated seismic anisotropies for sample PI399 combining single crystal elastic tensors of olivine and enstatite and the CPOs of both phases. Orientation is the same as in Fig. 3.6-4.

c. *Strengthening of two-phase media due to surface tension effects (M. Thielmann, D. Andreieva, M. Dabrowski/Warsaw and G.J. Golabek)*

In the past, the rheology of the Earth's lower mantle was thought to be governed by diffusion creep. However, recently it has been argued that this may not be the case because deformation

of a lower mantle consisting of weak ferropericlase and strong bridgmanite may cause elongation of weak ferropericlase inclusions that in turn may result in significant rheological weakening. Due to this process, the viscosity of Earth's mantle may be significantly decreased in regions of high-strain deformation. As a result, certain regions in the Earth may have been shielded by such low viscosity regions from mixing due to mantle convection, thus representing chemical reservoirs that may reconcile geochemical and geodynamical observations. However, these considerations have so far not taken into account the potential role of interfacial tension on the elongation process. If surface tension effects are non-negligible, elongation of ferropericlase inclusions should be impeded.

In this study, we use two-dimensional numerical models of a circular weak inclusion subjected to simple shear to quantify the effect of surface tension on ferropericlase elongation and the effective viscosity of ferropericlase-bridgmanite mixtures. To reduce the number of independent parameters, we nondimensionalize the governing equations, which results in the number of free parameters being reduced to only two parameters, namely the viscosity contrast between ferropericlase and bridgmanite $\Delta\eta$ and the capillary number Ca, which represents the ratio between viscous and surface tension stresses.

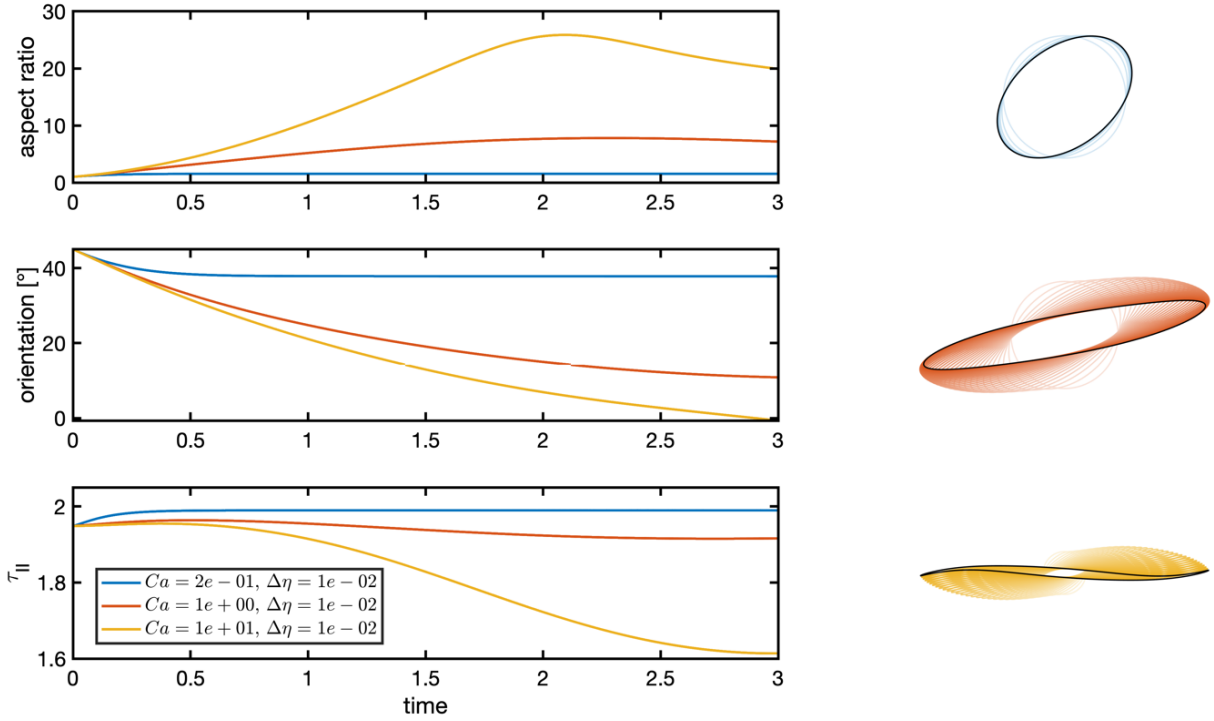

Fig. 3.6-6: Inclusion shape evolution and average stress evolution for a model with an initially circular weak inclusion. **Left:** Evolution of inclusion aspect ratio, orientation and average stress vs. time. for inclusions with different capillary numbers. **Right:** Shape evolution of the different inclusions, with the black line representing the inclusion shape at the end of the simulation. Colors correspond to the legend in the left column.

Results show that ferropericlase elongation is indeed strongly inhibited at low capillary numbers (Fig. 3.6-6), which results in almost isotropic inclusion shapes. In addition, surface tension results in an effective strengthening of the two-phase mixture, thus counteracting the effect of weak ferropericlase. This effect could potentially contribute to the observed slab stagnation at 1000 km depth in the Earth's lower mantle.

d. *Effect of grain size on the mechanism responsible for deep-focus earthquakes (S. Sawa, J. Muto and H. Nagahama/Sendai; N. Miyajima)*

Deep-focus earthquakes occur at depths from 410 km to 660 km in subducting slabs. Geophysical observations and deformation experiments show that the olivine-spinel phase transformational faulting mechanism may be the precursor of deep-focus earthquakes. This mechanism involves metastable olivine undergoing the phase transformation to fine-grained spinel with a shear instability developing as a consequence of the grain size reduction. Although the initial grain size of metastable olivine may affect the faulting mechanism, there have been no deformation experiments with different olivine grain sizes that might reveal the effect of olivine grain size on phase transformational faulting. Therefore, we conducted deformation experiments on germanate olivine aggregates with various grain sizes that range from a few microns to more than a few hundreds of microns.

Germanate olivine (Mg_2SiO_4) is an analogue material of silicate olivine and undergoes a phase transformation to spinel at much lower pressures than silicate olivine. We prepared three sets of germanate olivine aggregates with different grain sizes: sample A: < 10 μm, B: < 100 μm, and C: > 100 μm. We conducted deformation experiments on samples A, B, and C with a Griggs-type solid-confining medium deformation apparatus. Confining pressure, temperature, and strain rate were 1.2 GPa, 900 °C, and 2.0×10^{-4} s^{-1}, respectively. The recovered samples were examined with a scanning electron microscope (SEM), micro-Raman spectroscopy, and scanning transmission electron microscope (STEM).

All samples deformed at high temperatures showed strain weakening. STEM observations combined with electron diffraction showed the differences in phase transformation mechanism as a function of the olivine grain size. In fine-grained olivine (sample A, Figs. 3.6-7a-c), the nucleation and grain growth of spinel occurred along olivine grain boundaries accompanied by the development of faults having offsets of tens of microns. In contrast, in the coarse-grained olivine, (sample C, Figs. 3.6-7d-f), the nucleation and growth of spinel grains occurred in the interior of the olivine grains and was also accompanied by the development of faults having offsets of a few microns. Slip bands composed of fine-grained spinel form along (100), (011), and (010) planes of olivine. Although both fine-grained and coarse-grained aggregates formed small faults, the difference in the phase transformation mechanism has the potential to affect the seismic parameters of deep-focus earthquakes, such as *b*-values in the Gutenberg-Richter law.

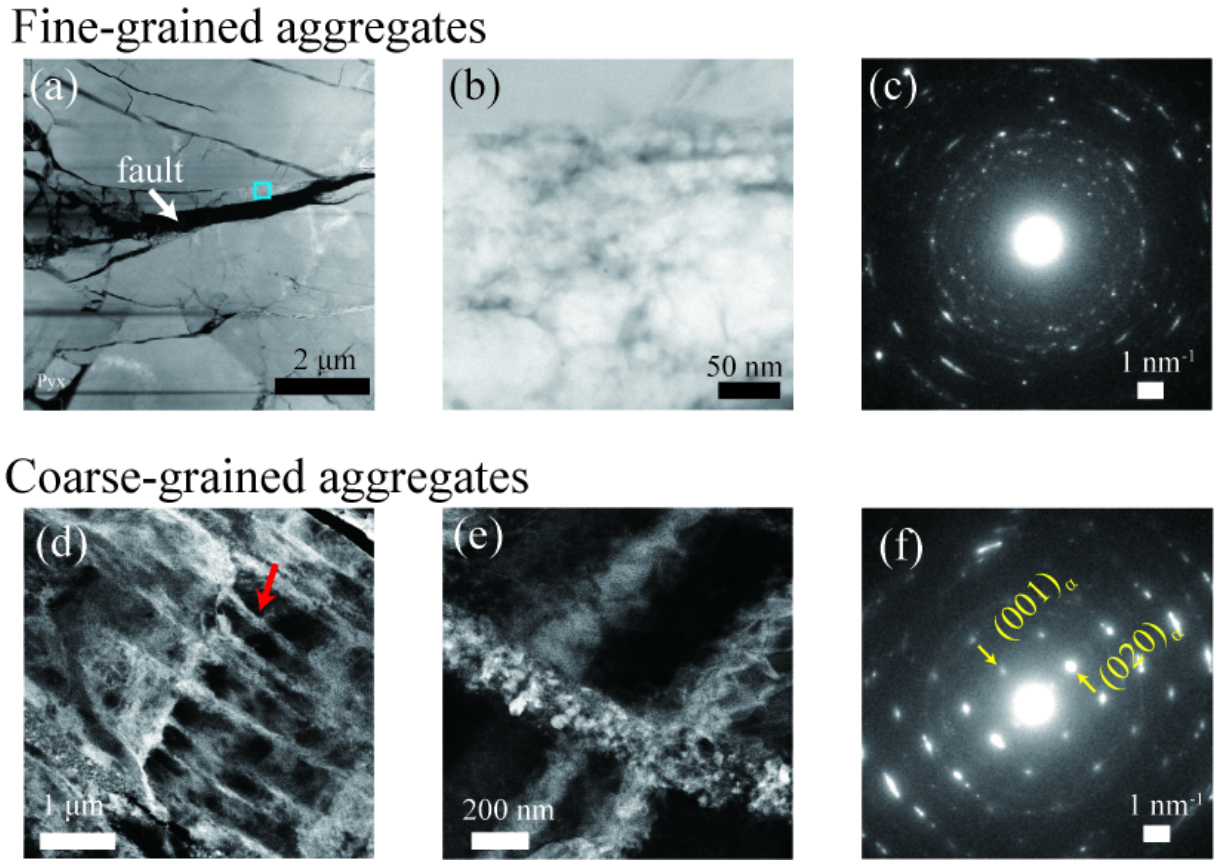

Fig. 3.6-7: STEM images and electron diffraction patterns. (a) High angle annular dark-field (HAADF) image of a fine-grained sample. Gray and light gray minerals are germanate olivine and germanate pyroxene (Pyx), respectively. (b) This HAADF image corresponds to the blue box in (a). White grains are germanate spinel, which indicates a higher density than that of olivine. (c) Selected area electron diffraction (SAED) pattern corresponding to white grains in (b). The spotty Debye ring pattern indicates the identification of polycrystalline spinel with random crystal orientations. (d) Dark-field (DF) image of a coarse-grained sample. The red arrow shows one of the slip bands. (e) DF image of slip bands in (d). (f) SAED pattern corresponding to a host olivine grain in (e) and taken along the [100] zone axis. The splitting of spots corresponds to ~ 3° angular misorientation, indicating a grain rotation along the [100] axis.

e. *Phase transformation – induced stresses and their implications for deep earthquakes (M. Thielmann, E. Aharonov/Jerusalem, P. Yamato/Rennes and T. Duretz/Frankfurt a. M.)*

The nucleation and rupture processes of deep-focus earthquakes have remained enigmatic ever since their discovery. These earthquakes occur mostly within the mantle transition zone where brittle failure is extremely unlikely due to the highly elevated pressures and temperatures at these depths. Hence, other mechanisms have to be invoked to explain the occurrence of these events. To date, two main hypotheses have been proposed to explain deep focus earthquakes: (1) transformational faulting (due to the polymorphic phase change of metastable olivine to either wadsleyite or ringwoodite) and (2) thermal runaway (due to the conversion of

deformational work to heat). More recently, it has been proposed that the feedback between those two mechanisms may explain the observed two-stage ruptures of several deep-focus earthquakes.

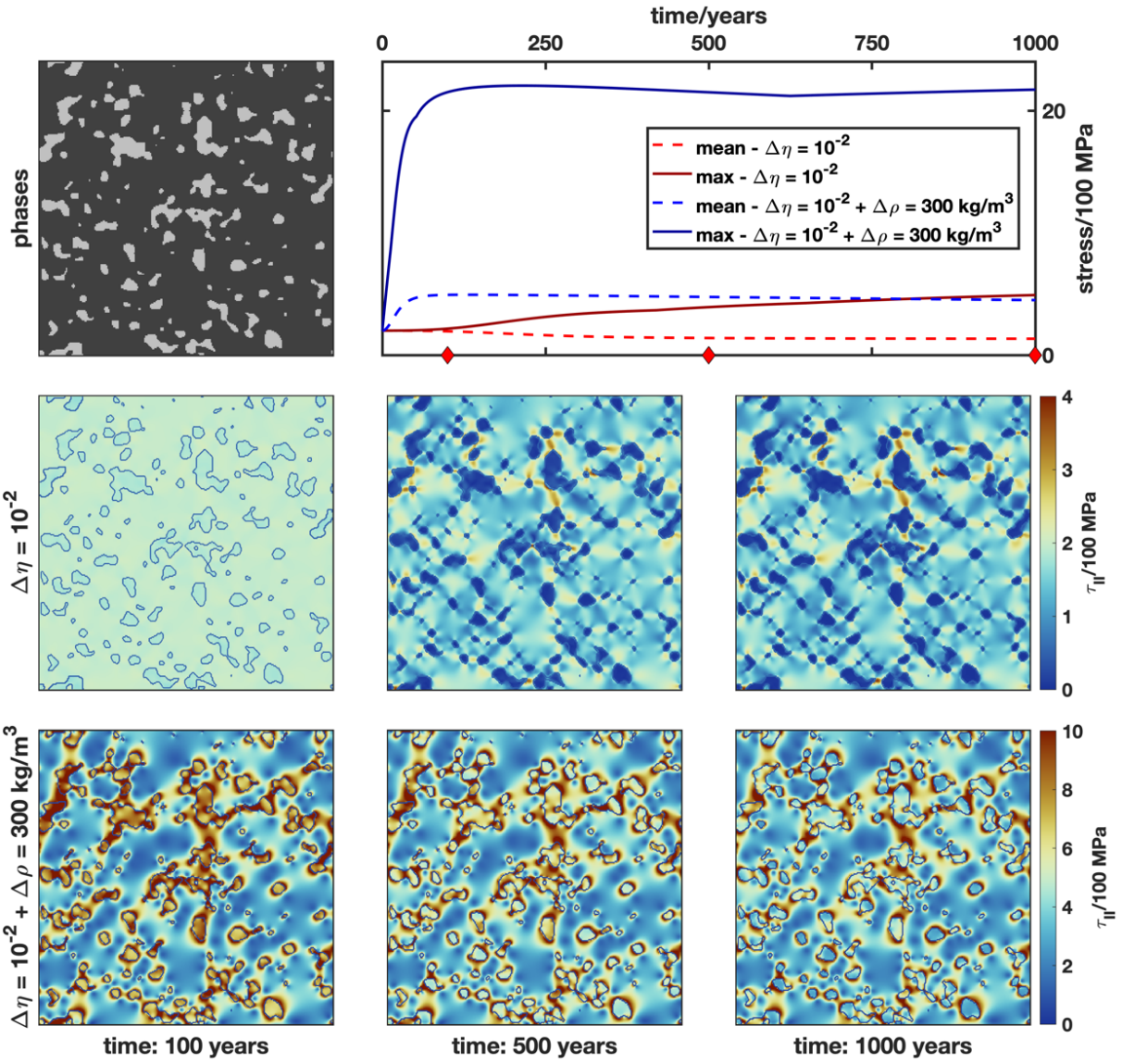

Fig. 3.6-8: Example of the stress evolution of two simulations where a phase transformation results in (1) a viscosity reduction $\Delta\eta = \frac{\eta_i}{\eta_m} = 10^{-2}$ and (2) the same viscosity reduction combined with a density increase $\Delta\rho = 300$ kg/m^3. Both models are deformed in simple shear at a strain rate of 10^{-14} s^{-1}. **Upper left:** Distribution of transforming material (in light grey). **Upper right:** Temporal evolution of mean and maximum stresses in both models. Red diamonds denote the times at which snapshots are taken. **Middle row:** Stress field in the model after 100, 500 and 1000 years for the model where the phase transformation only results in a viscosity change. The color scale is limited to values between 0 and 400 MPa. **Bottom row:** Same as shown in the middle row, but for the model where the phase transformation affects both viscosity and density. The color scale is limited to values between 0 and 1 GPa.

To understand this potential feedback, it is first necessary to determine the stresses induced by the phase change due to i) the grain size reduction and corresponding viscosity reduction of the transformed material and ii) the volume reduction of the transformed phase. The former process will trigger a stress transfer from the transformed material to the untransformed material, whereas the latter will result in elevated stresses around the transformed phase. We employ numerical models with viscoelastic compressible rheology to quantify the stresses resulting from both processes. The modeled phase transformation is described using a simplified model where the kinetics of the phase transformation is governed by a prescribed transformation time scale t_t.

We model the stress evolution of both simplified models where transforming regions have elliptical shapes, but also more realistic geometries (Fig. 3.6-8). Results show that both processes result in significantly different stress evolution upon a phase transformation (Fig. 3.6-8). Whereas a phase transformation affecting only the viscosity of the transformed material results in moderate stress increases, which occur on relatively long timescales, a phase transformation affecting both viscosity and density results in significantly larger stresses, which also exhibit a significantly faster build-up (see top right time series plot in Fig. 3.6-8). In both cases, the attained stress levels may potentially activate additional ductile weakening mechanisms that could trigger ductile ruptures. The higher stress levels resulting from the combined effect of a viscosity and density change would, however, very likely result in stronger weakening effects and the faster occurrence of ductile failure.

f. *Particle size distributions of pallasites and experiments that help to understand impact fragmentation mechanisms in the main-group pallasite parent body (N.P. Walte and C. Howard/ Garching and G.J. Golabek)*

Recent studies have confirmed the two-body collision model for the formation of main-group pallasites. The collision caused fragmentation of the dunitic mantle of the pallasites parent body and intrusion of the core melt from the impactor, which was likely the IIIAB iron meteorite parent body. In order to better constrain these processes, we investigated the particle size distribution (PSD) of different pallasites and compared the results to high strain-rate deformation experiments. The experiments were performed using the SAPHiR multianvil press of BGI that is situated at the FRM II neutron source in Garching. The samples were composed of olivine + FeS melt ± gold melt in a central cavity of the sample that collapsed during deformation, thereby simulating the intrusion of metal melt into the olivine matrix (see previous annual reports). PSD plots have been widely used for characterizing brittle rocks from terrestrial fault zones and impact fragmented rocks in nature and experiments. It is suggested that the particle size distribution follows a power law equation

$$N(d) \sim d^{-D} \qquad (1)$$

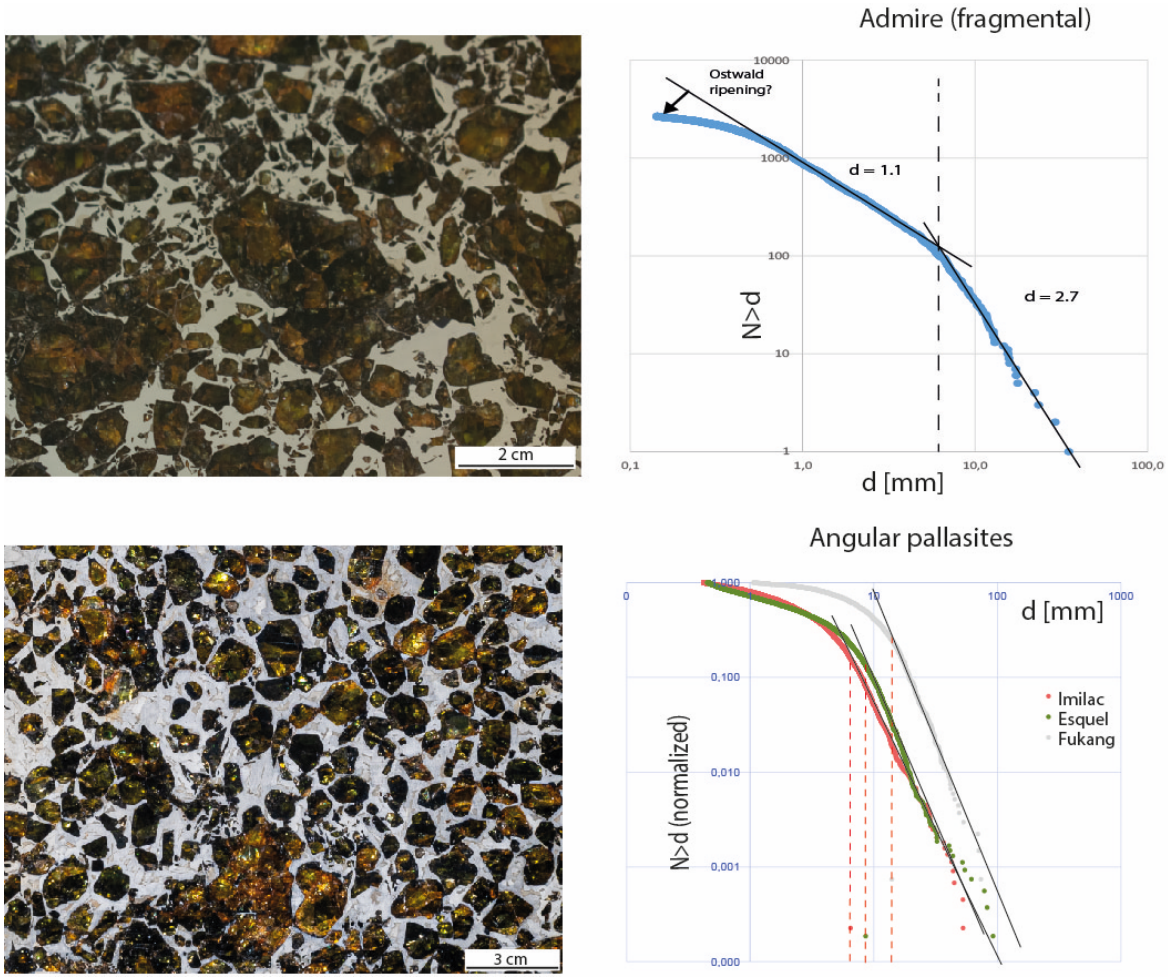

Fig. 3.6-9: Overview and particle size distribution (PSD) plots of fragmental pallasites (top) and angular pallasites (bottom). Red dashed lines in the bottom PSD indicate the average grain sizes of the respective host rocks before the fragmentation, which coincides with the transition between the respective linear segments.

with d being the grain diameter, $N(d)$ the number of particles larger than d, and D the slope of a linear size distribution in a double-logarithmic plot. The D-value is a measure of the efficiency of the fragmentation mechanism, with a higher value indicating a higher fraction of smaller fragments. High-resolution images of sample sections were first converted to binary images before determining the size (diameter of area equivalent circles) of olivine particles (olivine fragments, single crystals, or coherent olivine aggregates) with the freeware ImageJ. The 2-D raw data were plotted as log $N(d)$ vs. log d to derive the PSD diagrams for the different samples. The PSD plots of fragmental pallasites show two linear segments with different D-values and a threshold at ca. 8 mm (Fig. 3.6-9). At sub-mm particle size, the values diverge from linearity, which can be attributed to post-deformational Ostwald ripening. The PSD of pallasites dominated by equiaxed angular olivines (angular pallasites) are characterized by a linear trend at larger particle sizes with a high D-value and a curved non-power-law distribution at lower particle sizes (Fig. 3.6-9). The transition occurs at 7-14 mm, which corresponds to the average

grain size of the respective pallasites (see previous annual reports). Experimental samples that are dominated by olivine fragments show PSDs that roughly resemble the PSD of fragmental pallasites, while regions in samples that are dominated by local extension and metal intrusion resemble the PSD of angular pallasites (Fig. 3.6-10), albeit at a much smaller scale reflecting the smaller grain size in the micron range.

The thresholds in the PSD diagrams indicate that the fragmentation mechanism is determined by the original grain sizes of the dunitic host rocks. Fragmental pallasites were likely closest to the impact site, where the impact shock wave created a high number of olivine fragments, while angular pallasites were partly shielded from the shock wave. The secondary rarefaction shock wave likely aided intrusion of the core melt from the impactor that migrated further into the mantle driven by its higher density. This led to extensional strain and produced efficient further fragmentation of both fragmental and angular pallasites. The threshold close to the respective grain sizes indicates that the fragmentation predominantly occurred by tensile fracturing along grain boundaries, which was aided by a small fraction of metal melt that was already present before the impact (primary metal pockets, see previous annual report) that weakened the grain boundaries. This mechanism may have led to widespread mantle impregnation with metal melt and thereby opposed efficient core-merging during collisions in the early solar system.

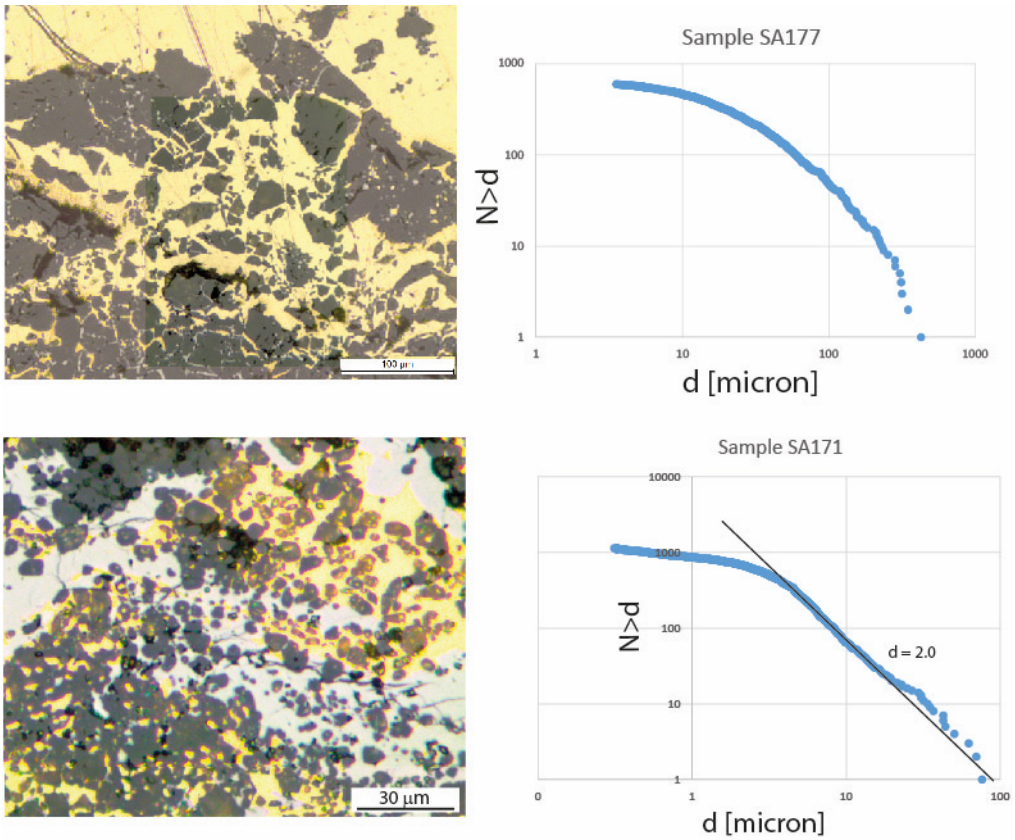

Fig. 3.6-10: Overview and particle size distribution (PSD) plots of two experiments that produced fragmental particles (top) and angular particles (bottom) that show some similarities to pallasites.

g. *The origin and impact history of ordinary chondrite melt breccia Northwest Africa 12520 (R. Zhao and A. Bouvier, in collaboration with M. Trieloff, W. Schwarz and T. Ludwig/Heidelberg)*

Northwest Africa (NWA) 12520 is an LL6 ordinary chondrite melt breccia. The meteorite consists of unmelted chondritic material and centimeter-size impact melt rock (IMR) clasts (Fig. 3.6-11), the origin of which is unknown. Shock-induced melt veins were identified within a chondritic clast and in between the chondrite and impact melt lithologies. These veins contain relict olivine and low Ca-pyroxene. High-pressure polymorphs (*e.g.*, ringwoodite, majorite) were not identified in the shock-veins in the matrix of the chondritic clast. The strong mosaicism and planar deformation fractures in olivine and the partially isotropic plagioclase in the chondritic clast matrix suggest that the shock stage of the chondritic clast should be shock level S4 (on a scale of S1 to S6).

The composition of olivine in the chondrite host is homogeneous with Fa30.2±0.3. The olivine in the impact melt clast is chemically zoned from core to rim (Fig. 3.6-11B) with corresponding compositional variations from Fa15.0±1.5 to Fa33.6±2.8, respectively. The triple oxygen isotopic compositions of olivine were measured by SIMS Cameca 1280-HR at Heidelberg University. The olivine analyses in the impact melt clast (n=23) have on average $\delta^{18}O$=+4.45 (2SE=±0.13‰), $\delta^{17}O$=+3.52 (2SE=±0.10‰), $\Delta^{17}O$=+1.17 (2SE=±0.05‰). The chondrite clast olivines (n=11) have on average $\delta^{18}O$=+5.90 (2SE=±0.10‰), $\delta^{17}O$=+4.44 (2SE=±0.08‰), $\Delta^{17}O$=+1.33 (2SE=±0.06‰). These oxygen isotopic compositions combined with elemental geochemistry indicate that the impactor has modified the oxygen isotopic composition of the protolith (if similar to the host rock).

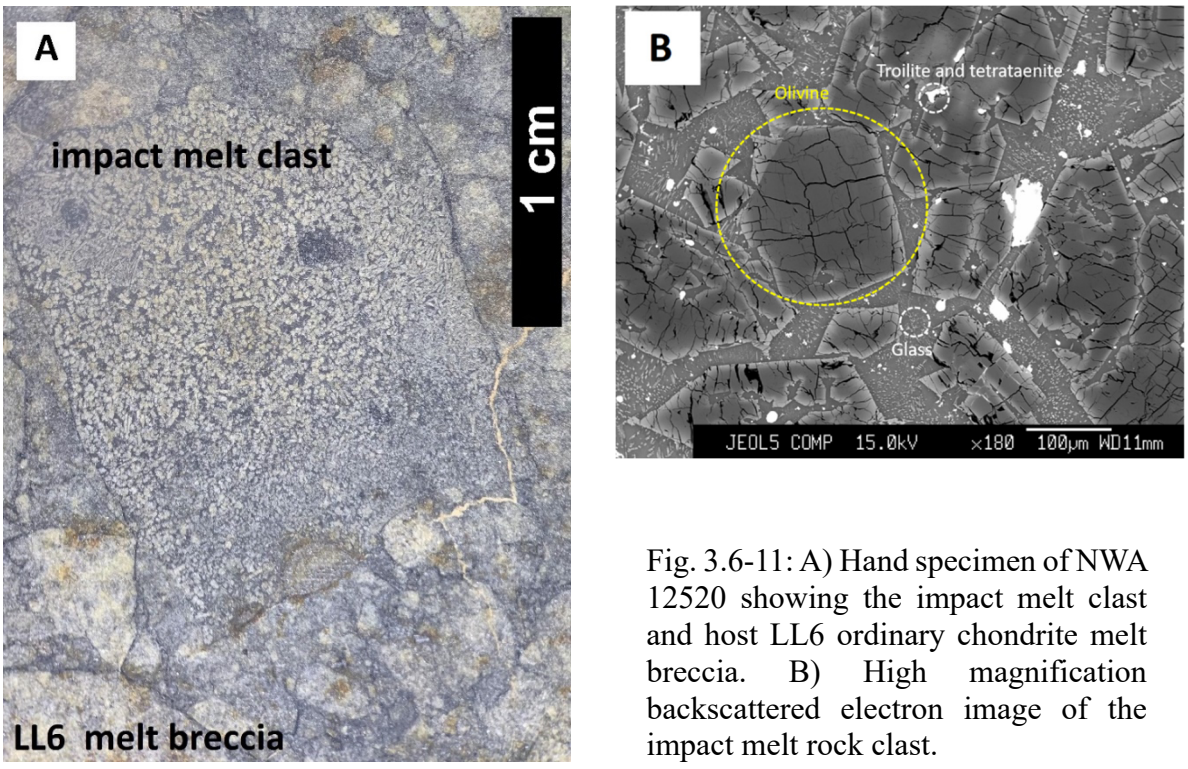

Fig. 3.6-11: A) Hand specimen of NWA 12520 showing the impact melt clast and host LL6 ordinary chondrite melt breccia. B) High magnification backscattered electron image of the impact melt rock clast.

Three main shock events were identified in NWA 12520. During the first shock event, parts of the parent body were completely melted and then cooled rapidly to form the olivine- and glass-bearing impact melt rock. In a subsequent shock event, chondritic rock and impact melt rock clasts were shocked, fragmented, and brecciated together. A third shock event formed the melt veins found locally in both the chondrite host and between the chondrite host and impact melt rock clast. Additional mass-independent isotopic analyses and chronological data may shed light on both the source reservoir of the impactor and the timing of the shock events.

3.7 Material Sciences

In addition to Earth and planetary materials, the investigation of materials that exhibit remarkable structure or properties at high pressure continues to be an important direction of research at Bayerisches Geoinstitut. Most of the projects presented in this section rely on the access of researchers from Bayerisches Geoinstitut to synchrotron radiation facilities in order to perform *in situ* single crystal X-ray diffraction in the megabar range, using the diamond anvil cell. These experiments are now regularly complemented by *ab initio* simulations to test the plausibility of structural models or explore their details.

The first two contributions explore the pressure evolution of two molecular systems by means of single-crystal X-ray diffraction: bromine and $C_{16}H_{10}$ pyrene. For bromine, the dissociation of the molecular state is observed at ~ 80 GPa, and a series of modulated solid structures are described above this pressure. The structural evolution of the hydrocarbon pyrene C16H10 with the underlying unit of four benzene rings, by contrast, is explored at a pressure of 2.5 GPa. The initially flat benzene units buckle, which leads to distinct bonding in the fish-bone-like stacking of the pyrene-IV solid.

Carbon shows a rich variety of chemical behaviour, with hydrocarbons – like pyrene just described – and carbides – formed with metal cations – being extreme examples. Carbides have long been a topic of materials research at high pressure and are one of the few materials synthesised industrially at high pressure. The third contribution in the section continues this tradition, for the lanthanum-group element dysprosium as the cation. Up to 50 GPa, three different Dy carbides are described by *in situ* X-ray diffraction with varying Dy:C ratios. In contrast to carbon, nitrogen has been thought to show limited chemical variety through the extremely stable triple bond in the N_2 dimer, and in inorganic compounds, nitrogen is typically present as a nitride N^{3-} anion. However, for the past two decades, it has been shown that at high-pressure nitrogen chemistry significantly changes, and two novel yttrium nitrides described in a contribution here, YN_6 and Y_2N_{11}, feature novel arrangements of nitrogen, an N_{18} macrocycle and a polynitrogen double helix, respectively.

Yttrium and lanthanum hydrides have received considerable attention in high-pressure solid-state physics due to reports on their high-temperature superconductivity, approaching room temperature. However, inconsistencies and problems in published data and results remain, including unknown or poorly characterised phases. This is also due to the fact that they have previously been characterised by a combination of powder X-ray diffraction and theoretical structure search. Single-crystal diffraction results on the Y-H and La-H systems demonstrate that these systems exhibit much richer structural behaviour at high pressure than previously expected and described. These findings are important for the (re-)interpretation of experiments on superconductivity in hydrides.

The final two contributions to the section explore mechanical properties of materials synthesised at high pressure. In the first one, tungsten boride WB_4 is synthesised and its

compressibility and hardness is measured, showing that it is a superhard material. Tin selenide, SnSe, by contrast, is a layered chalcogenide, exhibiting excellent thermoelectronic properties that can be further tuned by compression. When compressed to ~ 10 GPa, the morphology of the structure changes, with deformation in the layers on the sub-micron level, suggesting ductile deformation as the material is in transition from a brittle covalent to a plastic metallic state.

a. *Studies of the high-pressure behaviour of solid bromine in the pressure range of 72 to 96 GPa using synchrotron single-crystal X-ray diffraction (Y. Yin/Bayreuth, A. Aslandukova, A. Aslandukov, W. Zhou/Bayreuth, F.Ia. Akbar, L.S. Dubrovinsky, N.A. Dubrovinskaia/Bayreuth, D. Laniel/Edinburgh; A. Pakhomova, C. Giacobbe, E.L. Bright and M. Hanfland/Grenoble)*

The behaviur of halogens under pressure (*P*) provides insight into how simple molecular systems respond to extreme conditions. Fundamental problems to be addressed are the structure evolution, band gap closure and metallisation, and phase transformations. Extensive theoretical studies based on density functional theory (DFT) calculations and experimental investigations using powder X-ray diffraction (XRD), X-ray absorption spectroscopy, and Raman spectroscopy measurements have been carried out to determine the behaviour of halogens under *P*; experimental studies are especially important, as DFT calculations appear to face problems for halogens. So far, experiments found that Cl_2, Br_2, and I_2 undergo similar phase transitions, first forming solids with a molecular (*oC*8) structure and – at higher *P* – none-molecular (*oI*2) allotropes. Here, we have studied the behaviour of solid bromine in the *P* range of 72 to 96 GPa using synchrotron single-crystal (SC) XRD in a diamond anvil cell (DAC). We found five new bromine allotropes (*oF*28 and *oC*44 at 81 GPa; *oC*20, *oF*36, and *oF*44 at 96 GPa). Their structures were solved and refined.

High purity CBr_4 was used as a starting material because carbon tetrabromide decomposes at *P* above 40 GPa under heating and releases bromine. The samples were compressed in the BX90-type screw-driven DAC to 72, 81, and 96 GPa and laser heated up to ~ 2600 K at each *P*. Synchrotron SCXRD measurements were conducted at the European Synchrotron Radiation Facility (ESRF). The data were analysed using our methodology for processing XRD from multi-grain multi-phase samples, implementated in the DAFi program.

We found that bromine preserves its molecular structure up to 72 GPa, as only single-crystal domains of the *oC*8 molecular allotrope were detected at this *P*. According to theoretical predictions, an incommensurate phase of Br, intermediate between molecular and non-molecular bromine, should appear at 80 GPa, which we did not observe. Instead, an increase of *P* to 81 GPa resulted in the formation of two non-molecular allotropes, one of which was predicted, *oF*28 (space group *Fmm*2, #42), the other one previously unknown, *oC*44 (space group *Cmca*, #64) (Fig. 3.7-1). At 96 GPa three new non-molecular phases, *oC*20, *oF*36, and *oF*44 (Fig. 3.7-1), and one previously reported non-molecular phase, *oI*2, were found.

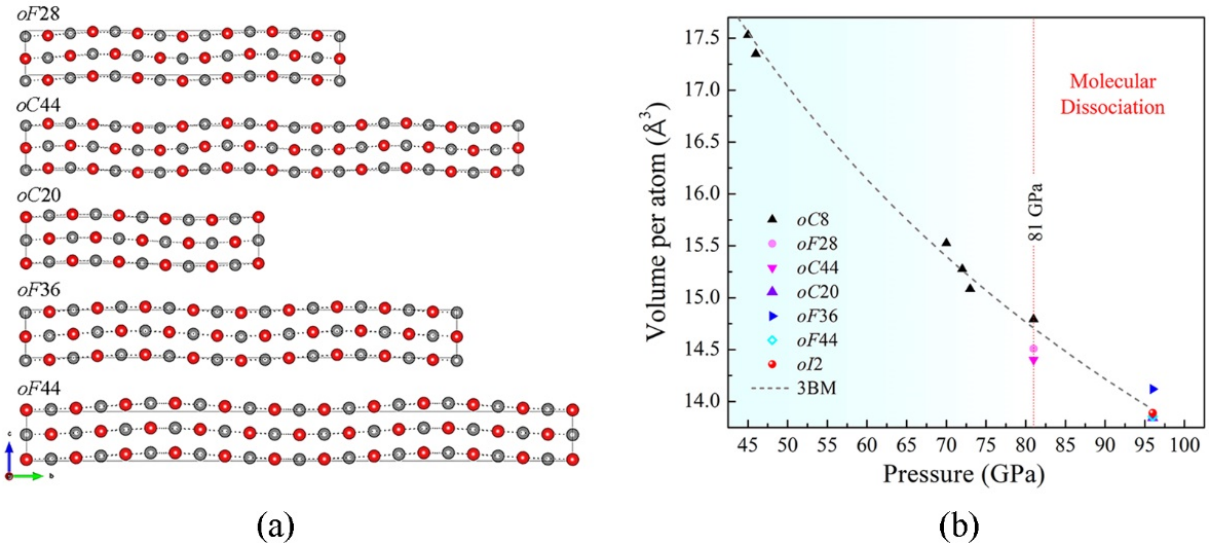

Fig. 3.7-1: (a) The structures of the novel non-molecular bromine allotropes synthesised in this work, *oF*28, *oC*44, *oC*20, *oF*36, and *oF*44. The unit cells are viewed along the *a*-direction. Bromine atoms in different planes are shown by different colours (red and grey), with planes separated by ½ *a*. Dotted lines highlight modulation waves. (b) Pressure dependence of volume per atom experimentally determined for all bromine allotropes synthesised in this work. Dashed black line represents the fit of the experimental data of *oC*8 using the third-order Birch-Murnaghan equation of state (3BM). The vertical line indicates the transition pressure between molecular and non-molecular allotropes.

b. *High-pressure polymorph of pyrene (W. Zhou and Y. Yin/Bayreuth, A. Aslandukov, L.S. Dubrovinsky, N.A. Dubrovinskaia/Bayreuth and M. Hanfland/Grenoble)*

Polycyclic aromatic hydrocarbons have long attracted interest as potential materials for various optical, optoelectronic, and electronic applications. In addition to application-oriented research, much work has been performed to understand fundamental processes associated with their structure-property relationships. For example, the electronic and excitonic processes in aromatic crystals have been strongly linked to both the number of aromatic rings in the molecular structure and the arrangement of molecules in the crystal. External pressure (*P*) is an effective way to affect packing of molecular units, and single-crystal X-ray diffraction (SCXRD) is the best method to study crystal structure.

In order to analyse the crystal structure of pyrene ($C_{16}H_{10}$) at high *P*, we loaded single crystals of pyrene into a BX90-type diamond anvil cell, with a culet size of 250 µm and using a rhenium gasket with a hole of ~ 120 µm in diameter. The samples were characterised using Raman spectroscopy in house and synchrotron SCXRD at the European Synchrotron Radiation Facility. SCXRD analysis shows that at 2.5 GPa we synthesised a new monoclinic phase that we term pyrene-IV (space group #14, $P2_1/c$, a = 7.6733(13) Å, b = 6.9186(3) Å, c = 16.4075(9) Å, β = 100.776(9)°), as three other pyrene polymorphs have been previously known. The structure of pyrene-IV was solved and refined to R1 = 10.9 % and closely reproduced by *ab initio*

calculations, which confirmed its dynamical stability. In the crystal structure of pyrene-IV, the molecules are arranged in a sandwich pattern (Fig. 3.7-2). Contrary to pyrene structure known at ambient conditions, in which molecules of four fused benzene rings are flat, in pyrene-IV four-ring molecules are curved (Fig. 3.7-2).

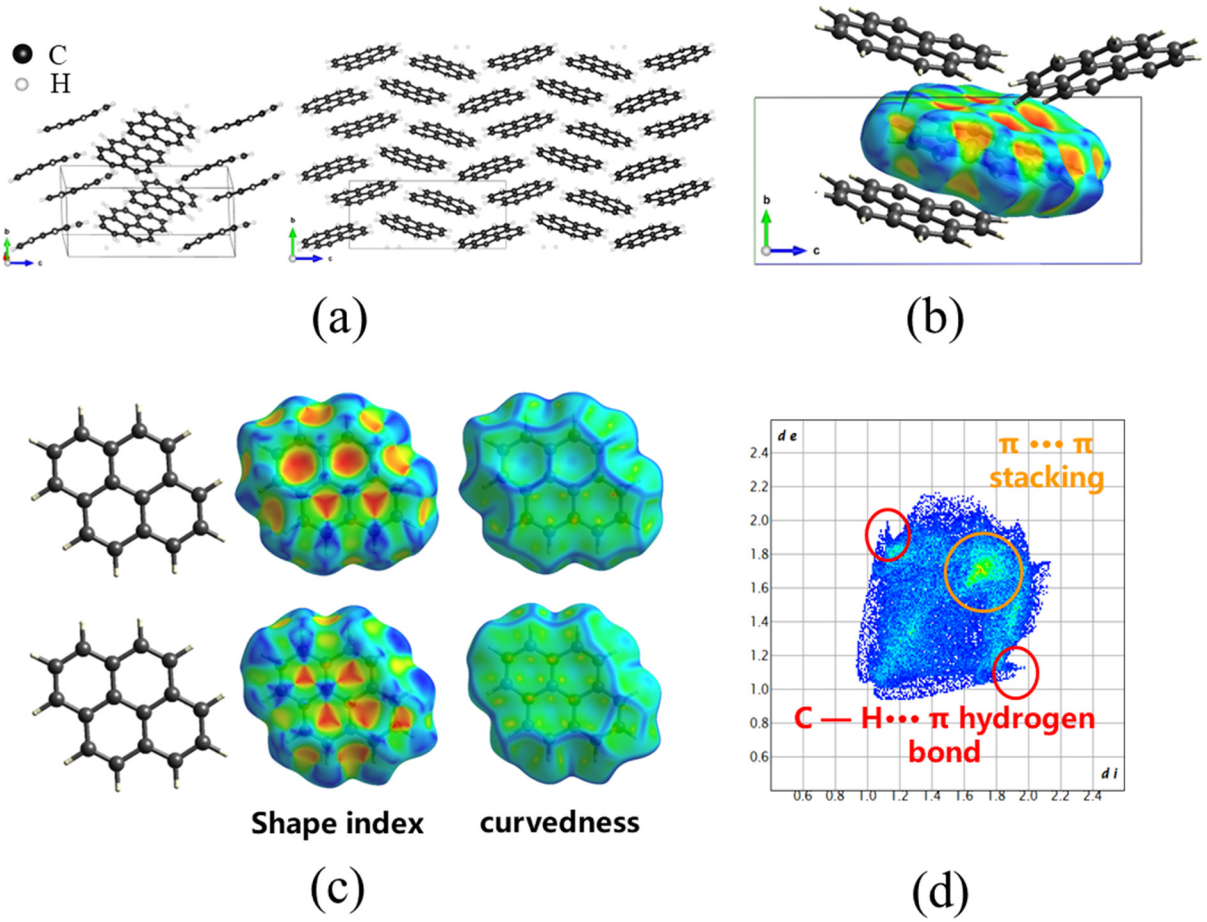

Fig. 3.7-2: Crystal structure of pyrene-IV at 2.5 GPa and the results of exploration of intermolecular interactions. (a) Ball-and-stick model of the structure of pyrene-IV; C and H atoms are shown in black and white, respectively. (b) Hirshfeld surface for one molecule of pyrene-IV (viewed along the *a*-direction), mapped with shape index. (c) Front and back views of the Hirshfeld surface mapped with shape index and curvedness. (d) Fingerprint plot for the single molecule in pyrene-IV; features characteristic of key intermolecular contacts are circled in red (C — H··· π hydrogen bonds) and orange (π ··· π stacking).

For an exploration of intermolecular interactions in crystals one can use Hirshfeld surfaces and fingerprint plots. The Hirshfeld surface envelops the molecule and defines the space where the promolecule electron density exceeds that from all neighboring molecules. The Hirshfeld surface itself is defined by the molecule and the proximity of its nearest neighbors, and hence encodes information about intermolecular interactions. The fingerprint plot represents two

different but useful distance measures in 2D: The distances from the internal or external atoms (d_i or d_e) to the Hirshfeld surface. Thus, the fingerprint plots are highly sensitive to the immediate environment of the molecule. They are unique for a given molecule in a particular polymorphic form. We used the Crystal Explorer program to produce the Hirshfeld surface for the single molecule in pyrene-IV, mapped with shaped index and curvature, and the fingerprint plot (Fig. 3.7-2). Front and back views of the Hirshfeld surface show that two sides of the molecule are involved in quite a different contact with neighbouring molecules. The analysis of the fingerprint plot reveals the features characteristic of key intermolecular contacts (Fig. 3.7-2). A pair of spikes at values of (d_i, d_e) ~ 1.9, 1.1 Å and *vice versa* (red circles) indicates the C — H$\cdots$ π hydrogen bonds. The green area in Fig. 3.7-2 (orange circle) is due to the π $\cdots$ π stacking with a distance of ~ 3.4 Å.

c. *Novel dysprosium carbides synthesised at high pressures (F.Ia. Akbar, A. Aslandukova, A. Aslandukov, Y. Yin and N.A. Dubrovinskaia/Bayreuth, L.S. Dubrovinsky, T. Fedotenko/ Hamburg and D. Laniel/Edinburgh)*

Carbides are important compounds in science and technology due to their useful and often unusual properties. Chemical composition, pressure (*P*), and temperature are major factors affecting the structure and properties of materials with different types of chemical bonding and crystal chemistry.

In this work, the dysprosium carbides, Dy_2C_3, Dy_4C_3, and Dy_3C_2 were synthesised by laser heating of metallic Dy in diamond anvil cells (DACs). We used the BX90 type DAC equipped with Boehler-Almax type anvils and a rhenium gasket. Flakes of pure Dy were loaded into the *P* chamber along with dried NaCl which served as a thermal insulator. The Dy samples were pressurised to 19, 55, and 58 GPa and heated up to 2500 K using NIR laser (1070 nm wavelength). The DACs with the samples were transferred to the Extreme Conditions Beamline (PETRA III at the German Electron Synchrotron) and ID11 beamline (ESRF) for *in situ* single-crystal X-ray diffraction.

Dy_4C_3 (space group *I-43d*) was synthesised at 19, 55, and 58 GPa (Fig. 3.7-3). This compound has not been known previously. Its structure belongs to the anti-Th_3P_4 structure type, which has been described for scandium carbide, but not observed in lanthanides carbides. It consists of single carbon and dysprosium atoms forming dysprosium (III) methanide, $Dy^{3+}{}_4C^{4-}{}_3$. According to *ab initio* simulations in the harmonic approximation at 0 K, Dy_4C_3 is dynamically stable even at ambient *P*.

The cubic Dy_2C_3 sesquicarbide was synthesised in this work at 19 GPa (lattice parameter *a*=7.9208(5) Å), previously described at ambient conditions with *a*=8.198(2) Å. This compound is an ethylide and contains C=C groups (Fig. 3.7-3). Its structure has the same space

group (*I-43d*) as that of Dy_4C_3, and their structures are closely related: Dy_2C_3 can be derived from Dy_4C_3, as the positions of the centres of dumbbells [C_2] in Dy_2C_3 coincide with the positions of single carbon atoms in Dy_4C_3, and the coordinates of Dy atoms are the same.

Dy_3C_2 (space group *P4/mbm*) was discovered at 55 GPa (Fig. 3.7-3). This carbide is isostructural to the predicted Ca_3C_2 calcium carbide. Dy_3C_2 is an ethanide, containing C-C dumbbells with a C-C distance of 1.51(3) Å, slightly shorter than the C-C distance in ethane.

Ab initio simulations of the convex hull (Fig. 3.7-3) suggest that at 60 GPa the phases we observed in this work (Dy_2C_3, Dy_3C_2, and Dy_4C_3) are thermodynamically stable.

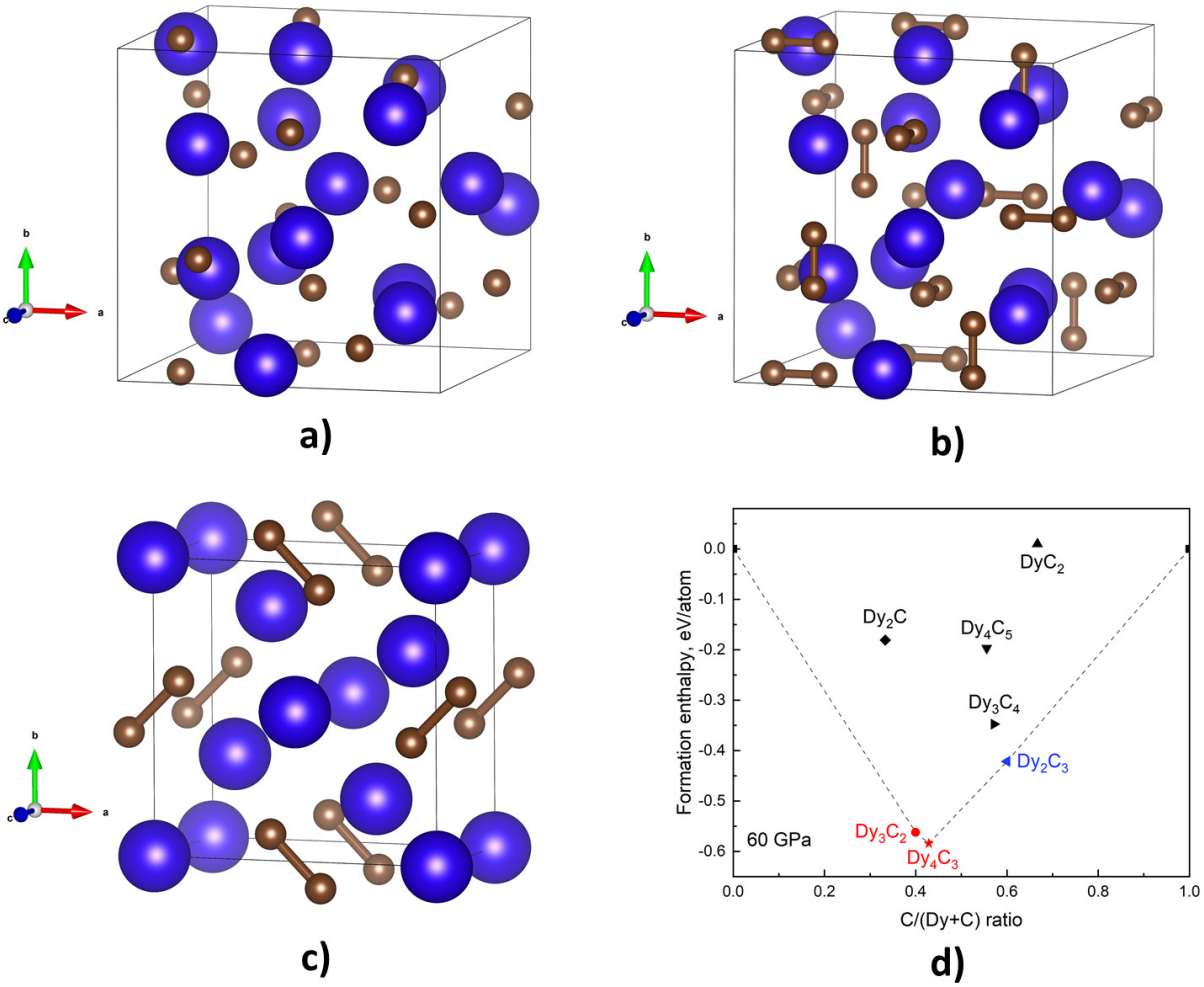

Fig. 3.7-3: Structures of dysprosium carbides synthesised in a laser-heated diamond anvil cell: a) Dy_4C_3 (19 GPa, 55 GPa, 58 GPa), b) Dy_2C_3 (19 GPa), c) Dy_3C_2 (55 GPa). The blue and brown spheres represent dysprosium and carbon, respectively. d) Calculated convex hull (dashed lines) for the Dy-C binary system; carbides previously reported are given in black, carbides synthesised in this work are given in red (previously unknown) and in blue (previously known).

d. *Anionic N_{18} macrocycles and polynitrogen double helix in novel yttrium nitrides YN_6 and Y_2N_{11} at 100 GPa (A. Aslandukov, A. Aslandukova, S. Khandarkhaeva, L.S. Dubrovinsky, N.A. Dubrovinskaia/Bayreuth, F. Trybel and I. Abrikosov/Linköping, D. Laniel/Edinburgh, T. Fedotenko/Hamburg, G. Aprilis, C. Giacobbe/Grenoble and E.L. Bright/Grenoble)*

The chemistry of nitrogen has long been thought to be very limited due to the extreme stability of the triple-bonded N_2 molecule. As a result, in inorganic solid-state compounds at ambient pressure (*P*), nitrogen is typically present in the form of a nitride anion N^{3-} and does not form catenated polyanions (with an exception of azides). However, over the past 20 years, it has been shown that nitrogen chemistry significantly changes at high *P*: Charged nitrogen N_2^{x-} dimers, tetranitrogen N_4^{4-} units, pentazolate N_5^- rings, hexazine N_6 rings, and different polynitrogen chains have been synthesised. Such a variety of nitrogen species can suggest that the diversity of nitrogen chemistry at high *P* may be close to the very rich carbon chemistry at ambient *P*. In addition to the discoveries of unique nitrogen entities that push the boundaries of fundamental nitrogen chemistry, nitrides synthesised under high *P* often possess key properties for functional applications. For example, ReN_2, recoverable to ambient conditions, has an extremely high hardness; a single layer of BeN_4 is a 2D material with unique electronic properties; a variety of nitrides with high nitrogen content are promising for applications as high energy density materials.

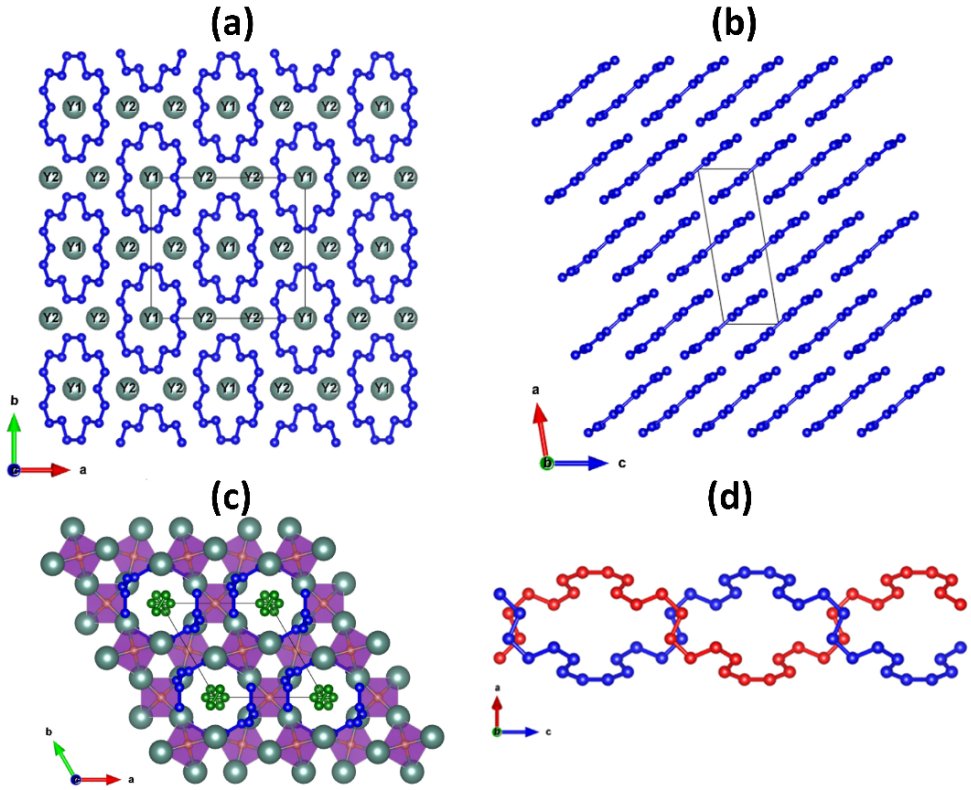

Fig. 3.7-4: (a) View of the crystal structure of YN_6 along the *c*-axis and (b) along the *b*-axis; yttrium atoms are omitted; (c) view of the crystal structure of Y_2N_{11} along the *c*-axis; (d) double helix formed by two polynitrogen chains running along the *c*-direction around the 6_2 screw-axis. All Y atoms are greenish, all other colors represent N atoms.

In this study, two novel yttrium nitrides, YN_6 and Y_2N_{11}, were synthesised by direct reaction between yttrium and nitrogen at ~100 GPa and ~3000 K in a laser-heated diamond anvil cell. High-*P* synchrotron single-crystal X-ray diffraction revealed that the crystal structures of YN_6 (space group *C*2/*m*) and Y_2N_{11} (space group $P6_222$) feature a unique organisation of nitrogen atoms—a previously unknown anionic N_{18} macrocycle and a polynitrogen double helix, respectively (Fig. 3.7-4). Density functional theory calculations confirm the dynamical stability of the YN_6 and Y_2N_{11} compounds and reveal an anion-driven metallicity, explaining the unusual bond orders in the polynitrogen units. The discovery of such compounds encourages further exploration of the remarkable inorganic chemistry of polynitrides. Moreover, the ability of nitrogen to form such structural units shows that we may be at the verge of opening a new branch of chemistry: nitrogen organic chemistry at ultrahigh *P*.

e. *Y-H system under high-pressure high-temperature conditions (A. Aslandukova, A. Aslandukov, Y. Yin/Bayreuth, F.Ia. Akbar, L.S. Dubrovinsky, N.A. Dubrovinskaia/Bayreuth, D. Laniel/Edinburgh, T. Fedotenko/Hamburg, K. Glazyrin/Hamburg and M. Hanfland/ Grenoble)*

Despite the optimistic reports about close-to-room temperature superconductivity in high-pressure (*P*) yttrium hydrides, many inconsistencies and problems in the published results exist, including unknown or poorly characterised phases. So far, all phases of yttrium hydrides under high *P* were studied only by the combination of powder X-ray diffraction (XRD) analysis and theoretical structural search approach. Therefore, for better characterising the Y-H system at high *P*, the systematic study of its crystal chemistry with the help of single-crystal (SC) XRD is mandatory.

In this work we studied the Y-H system by means of XRD at *P* up to 170 GPa and temperatures up to 3500 K, supported by density functional theory (DFT) calculations. The hydrides were obtained in diamond anvil cells via the laser heating of *hcp* Y (as starting material) with two sorts of hydrogen-rich precursors - ammonia borane and paraffine oil. As a result, besides three known (YH_3 with $Fm\bar{3}m$ and *I*4/*mmm* symmetry, YH_4 with *I*4/*mmm* symmetry), five novel yttrium hydrides were synthesised: Y_3H_{11}, Y_2H_9, Y_4H_{23}, $YH_{6-\delta}$, Y_4H_{25} (Fig. 3.7-5). The atomic positions of Y atoms were determined from synchrotron SCXRD data; as the positions of the H atoms cannot be constrained by XRD data, hydrogen content was estimated based on the dependence of volume per atom on the hydride stoichiometry and DFT calculations. Moreover, regardless of the hydrogen source used, three new yttrium compounds were obtained along with hydrides, YC_2, Y_3N_{10}, and YN_3, underlining the chemical complexity of reaction products.

Thus, our results demonstrate that the Y-H system at high *P* shows a richer chemistry than expected, and previous experimental and theoretical works missed important details. New findings are important for the interpretation (and re-interpretation) of experiments aiming to detect superconductivity in Y-H compounds.

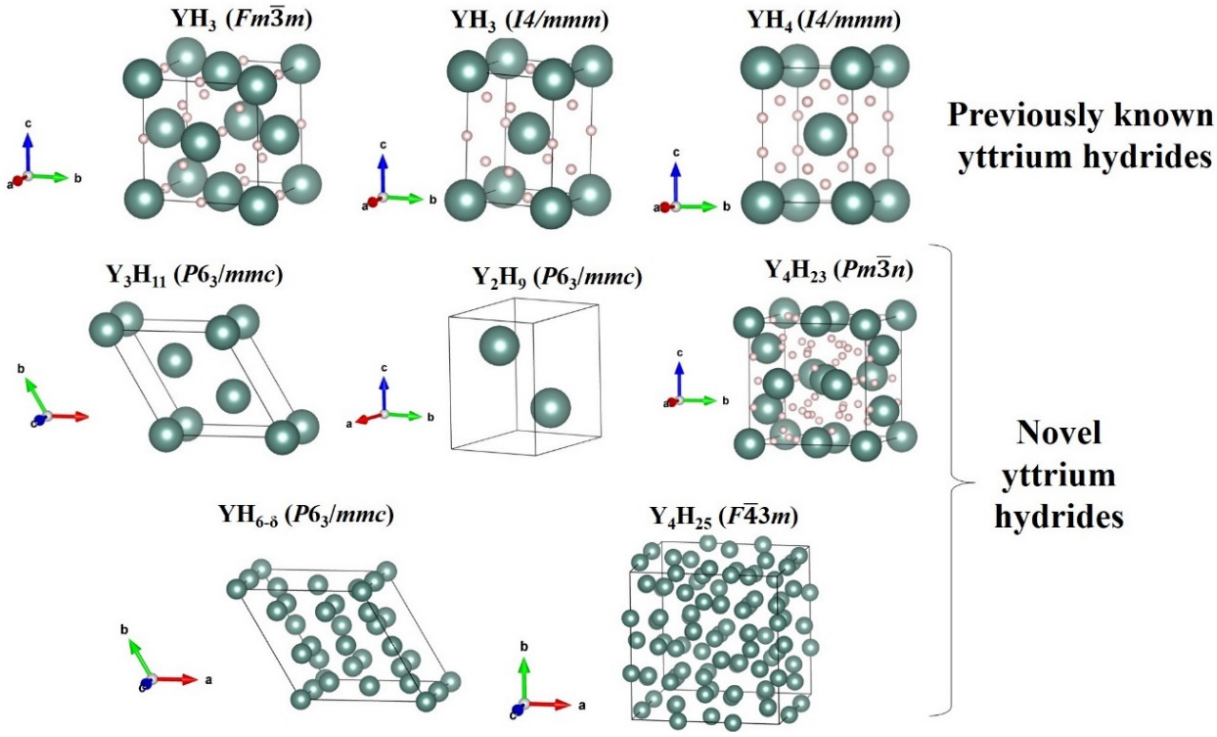

Fig. 3.7-5: Yttrium hydrides synthesised in this work. Yttrium and hydrogen atoms are shown in green and light pink, respectively. For Y_3H_{11}, Y_2H_9, $YH_{6-\delta}$, and Y_4H_{25} only a metal framework is shown since the positions of hydrogen atoms in these structures were not determined.

f. *High-pressure synthesis of seven lanthanum hydrides with a significant variability of hydrogen content (D. Laniel/Edinburgh, F. Trybel/Linköping, B. Winkler/Frankfurt a. M., F. Knoop/Linköping, T. Fedotenko/Hamburg, S. Khandarkhaeva, A. Aslandukova, T. Meier/ Beijing, S. Chariton/Chicago, K. Glazyrin/Hamburg, V. Milman/Cambridge, V.B. Prakapenka/ Chicago, I. Abrikosov/Linköping, L.S. Dubrovinsky and N.A. Dubrovinskaia/Bayreuth)*

Of fundamental significance and with tremendous technological potential, achieving superconductivity has been a long-standing goal. Since 2015, high-pressure (P) sciences are at the leading edge of the synthesis of high superconducting critical temperature (T_c) materials, namely with a breakthrough T_c of 260 K reported in the La-H system at 160 GPa. Only the LaH_3 and LaH_{10} compounds have been conclusively observed from experimental measurements, the latter assumed to yield the high T_c value. Yet, inconsistencies in resistivity measurements as well as unexplained diffraction lines suggest other phases to be present along with these compounds. These undiscovered lanthanum hydrides likely play an active role in the interpretation of resistivity and magnetic susceptibility employed to assess superconductivity, and experimentally verifying if these solids can be formed is therefore of critical importance.

In this study, we employed synchrotron single-crystal X-ray diffraction of polycrystalline samples accompanied by density functional theory (DFT) calculations to investigate the

lanthanum-hydrogen system between 50 and 176 GPa. We found the La-H system to feature a remarkably rich compositional and structural diversity, with seven synthesised lanthanum hydrides: the previously known LaH_3 and $LaH_{10+\delta}$, but also the hitherto unknown $LaH_{\sim 4}$, $LaH_{4+\delta}$, La_4H_{23}, $LaH_{6+\delta}$, $LaH_{9+\delta}$ solids (Fig. 3.7-6) Except for $LaH_{\sim 4}$, all these compounds have La arrangements identical to those previously known in other rare earth-H systems, suggesting crystal-chemical regularities common for various rare earth-H systems. Moreover, we demonstrate that these La-H compounds exhibit a variability of hydrogen content for a given arrangement of La atoms, underpinning difficulties of DFT calculations to accurately determine the content and the position of the H atoms in these solids.

This established variability in hydrogen content and the newly discovered La-H compounds, will undoubtedly provide the impetus for many new investigations of the La-H system, ultimately leading to an imprived understanding of superconductivity in high-*P* hydrides.

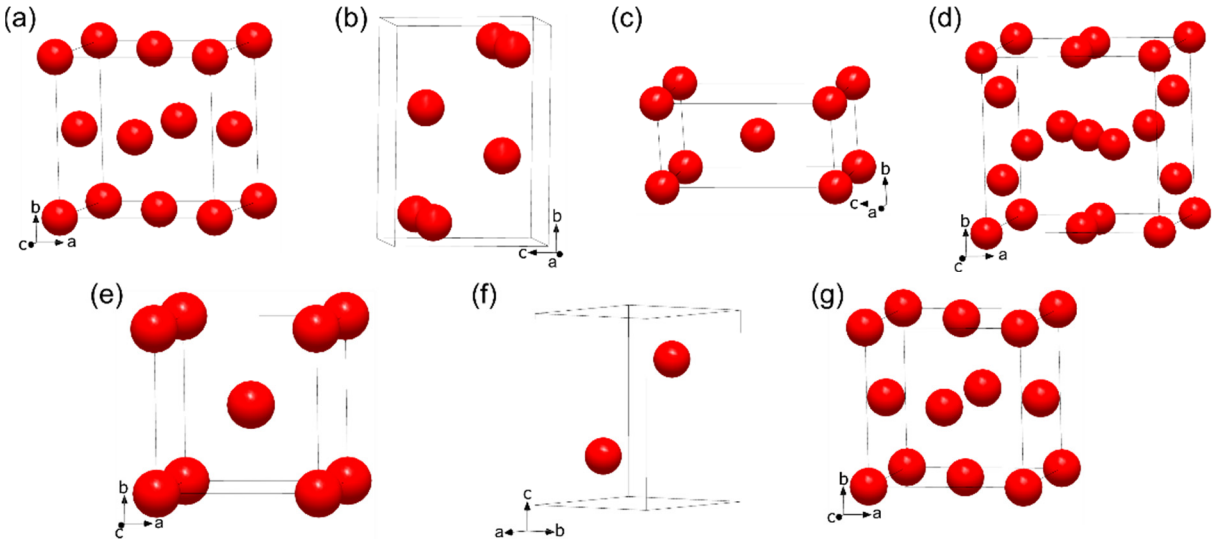

Fig. 3.7-6: Arrangement of lanthanum atoms in the lanthanum hydrides synthesised in this work. (a) LaH_3; (b) $LaH_{\sim 4}$; (c) $LaH_{4+\delta}$; (d) La_4H_{23}; (e) $LaH_{6+\delta}$; (f) $LaH_{9+\delta}$; (g) $LaH_{10+\delta}$.

g. *Synthesis, crystal structure, and properties of stoichiometric hard tungsten tetraboride, WB_4 (E. Bykova, S.V. Ovsyannikov, Y. Yin and N.A. Dubrovinskaia/Bayreuth, L.S. Dubrovinsky, M. Bykov/Köln, T. Fedotenko/Hamburg; S. Gabel, H. Holz and B. Merle/Nürnberg; S. Chariton and V.B. Prakapenka/Chicago and A.F. Goncharov/Washington D.C.)*

Tungsten tetraboride has been known as a non-stoichiometric compound with variable composition (*e.g.*, WB_{4-x}, WB_{4+x}). Its mechanical properties could exceed those of hard tungsten carbide, which is widely used in technology and science. However, the existence of stoichiometric WB_4 has not been proven yet, and its structure and crystal chemistry remain

debated to date. Here we report the synthesis of single crystals of stoichiometric WB_4 at high-pressure (P) high-temperature conditions (Fig. 3.7-7). The crystal structure of WB_4 was determined using synchrotron single-crystal X-ray diffraction, and *in situ* high-P compressibility measurements yield a bulk modulus of 238.6(2) GPa for WB_4, with $B' = 5.6(0)$. Measurements of mechanical properties on bulk polycrystalline samples with sub-millimeter size at ambient conditions yield a hardness of ~ 36 GPa (Fig. 3.7-7), confirming that WB_4 is a superhard material.

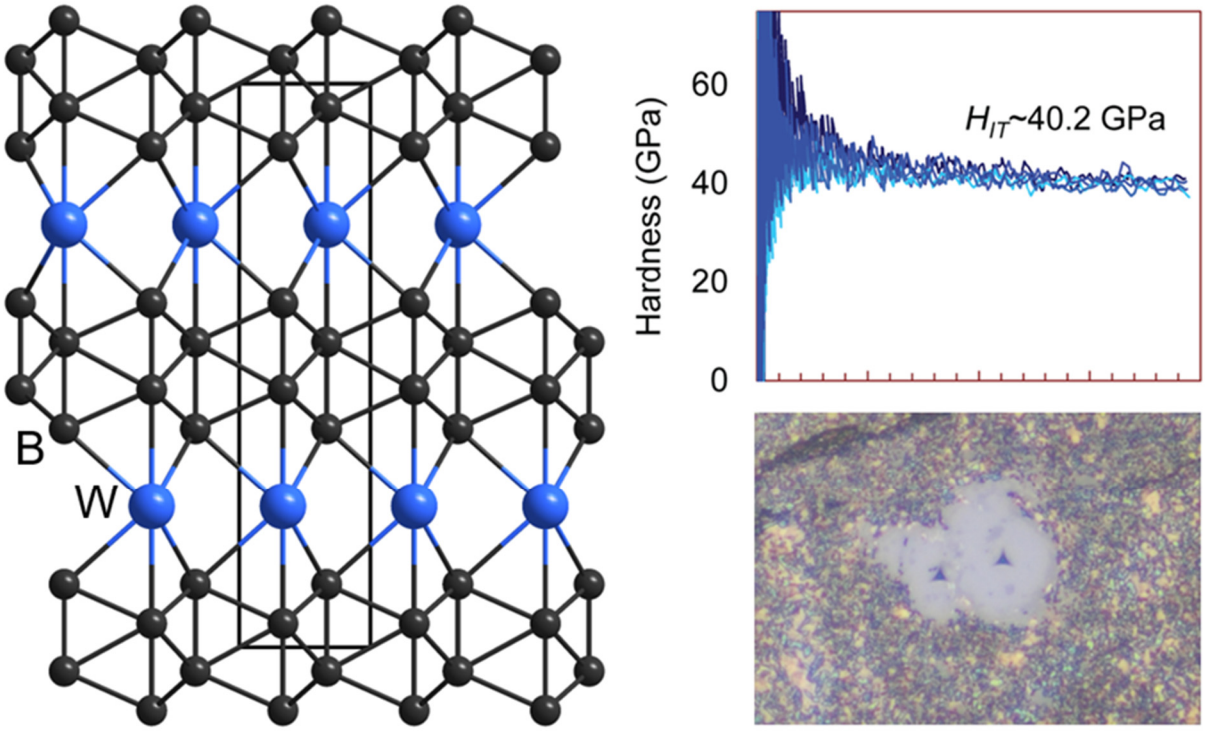

Fig. 3.7-7: Crystal structure of WB_4 synthesised in the current work; blue spheres are tungsten atoms, black spheres are boron atoms (left panel). The nanoindentation hardness, H_{IT} of a single crystal of WB_4 at 295 K (right panel, top) and optical micrographs of the sample after nanoindentation (right panel, bottom).

h. *Plastic deformation of a layered chalcogenide (S.V. Ovsyannikov and N. Miyajima)*

At ambient conditions, SnSe crystallises in a layered structure with the *Pnma* symmetry (Fig. 3.7-8), and it has an indirect band gap of about E_g=0.8-1 eV (Fig. 3.7-8). Recently, the excellent thermoelectric properties of SnSe single crystals were discovered at high temperature (T) above 800 K. Further studies experimentally found that promising thermoelectric properties of SnSe can be reached even at room T if it is appropriately doped. Generally, a sizable narrowing of the band gap of SnSe could optimise its electronic transport to make it more efficient for room-T energy conversion and other technological applications.

The SnSe single crystals were subjected to non-hydrostatic compression up to 9 GPa in a solid pressure-transmitting medium. Both pristine crystals and recovered samples were examined by structural, optical, and microstructural techniques at ambient conditions. X-ray diffraction (XRD) studies showed that the recovered samples have the same *Pnma* structure and largely conserve a crystallographic orientation of the pristine single crystals (Fig. 3.7-8). Thus, the recovered SnSe samples were neither single-crystalline nor polycrystalline. We analysed their XRD patterns using a full-profile Rietveld refinement (Fig. 3.7-8) and found unit-cell parameters very close to initial values. A near-infrared absorption spectroscopy examination showed that the recovered samples have an indirect band gap of about E_g=0.50 eV, *i.e.*, significantly smaller than in the pristine crystal (inset in Fig. 3.7-8), although traces of the original absorption edge at 0.8 eV were still visible in the spectra of the recovered samples (inset in Fig. 3.7-8).

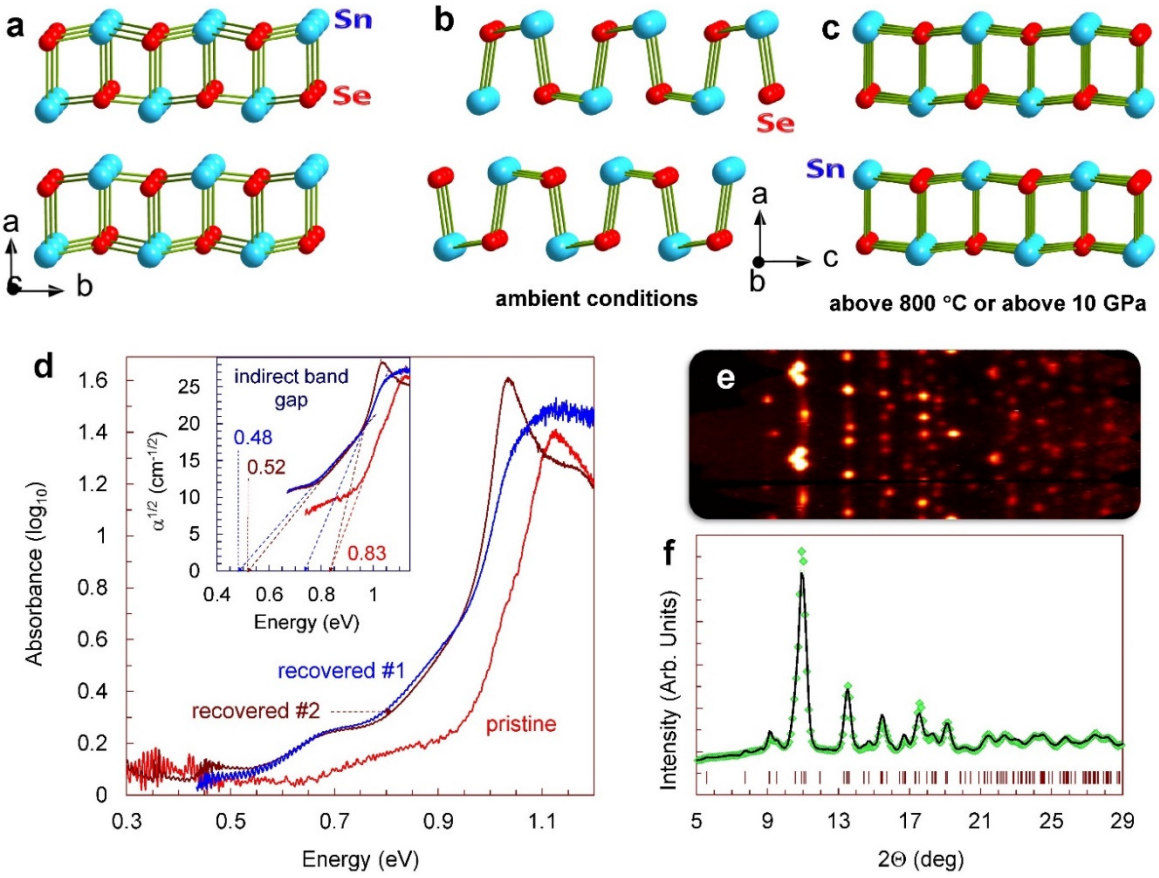

Fig. 3.7-8: Structural and optical properties of SnSe crystals at 295 K. (*a-c*) Layered crystal structure of SnSe in different crystallographic projections. A projection along the layers, shown in (*a*), is the same for the ambient-pressure (*P*) *Pnma*, the high-temperature *Cmcm*, and the high-pressure *Bbmm* structures of SnSe; perpendicular projections differ (*b, c*). (*d*) Near-infrared absorption spectra of the pristine SnSe crystal and two samples recovered after high-*P* experiments. The inset shows the determination of indirect band gaps in the samples. (*e*) Azimuth and (*f*) 2D X-ray diffraction patterns of one of the high-*P* samples. A Rietveld refinement of this pattern confirmed that this sample has the same *Pnma* structure as in the pristine crystal (e). The symbols are experimental data, the solid line is a calculated profile, and the ticks are anticipated reflections for *Pnma* symmetry.

To understand the band-structure reconstruction, we investigated the microstructure of the recovered samples both by visual examinations with the optical microscope (polarised light) of their well-polished surfaces and by transmission electron microscopy (TEM) of their thin sections (Fig. 3.7-9). The surface morphology of the samples was highly unusual: It exhibited numerous wavy stripes of irregular shapes, indicating a smooth but significant alteration in the crystallographic orientation throughout the sample. Apparently, these crystallographic variations arise due to severe plastic deformation inside the layers of the crystal (*b*-*c* plane in Fig. 3.7-8). Using a focused ion beam (FIB), we cut this sample across the layers and investigated its section by TEM. This examination revealed the formation of deformation bands at the submicron level. Thus, one can conclude that the SnSe crystals were predominantly deformed inside the layers, while they retained their stacking with some displacements along the layers. In high-resolution TEM, we observed the formation of numerous deformation lamellae or bands and lattice fringes along the *a*-direction (Fig. 3.7-9).

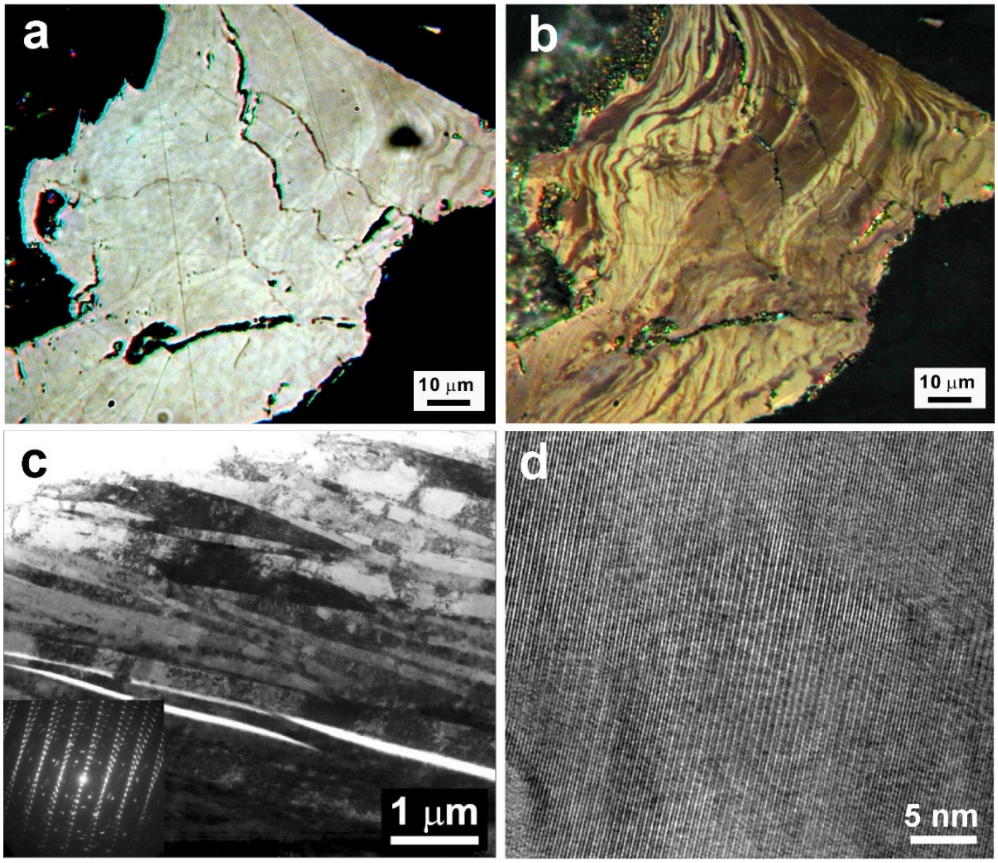

Fig. 3.7-9: Microstructural characterisation of the SnSe samples at 295 K. (*a, b*) Optical images of the same well-polished SnSe sample recovered from a high-pressure experiment. They were obtained using a reflected polarised light microscope with a single nicol/polariser (*a*) and with crossed nicols (*b*). Both images in different manners show smooth alterations in the crystallographic orientation throughout the sample. These crystallographic variations arise from severe plastic deformation inside the layers of the crystal (*b*-*c* plane in Fig. 3.7-8). (*c*) Bright-field TEM image of the same recovered SnSe sample cut with a FIB across the layers (along the *a*-axis). (*d*) Characteristic HRTEM image of the same recovered SnSe sample. It shows the formation of numerous deformation lamellae and lattice fringes of the (h00) plane.

The TEM findings indicate that under moderately high pressure, the SnSe crystals undergo a crossover to a more ductile state, facilitating their plastic deformation without cracking. This fact suggests that "viscous" forces dominated inside the layers of SnSe. We presume that the crossover in mechanical properties becomes possible due to a drastic alteration in the nature of the chemical bonding, from prevalently covalent to metavalent. A metavalent type of chemical bond was recently singled out as an intermediate between a covalent bond (localised electrons) and metallic one (delocalised electrons). Considering the facts that metavalent bonds are strongly anharmonic, and that it is "intermediate" between a "brittle" covalent bond and a "plastic" metallic bond, one can expect a tendency to ductility enhancement when a metavalent type of bond becomes predominant. Recall that "brittle-plastic" transitions in solids are not so rare, and chalcogenides are particularly prone to them.

3.8 Methodological developments

Technical and methodological developments are an intrinsic part of experimentation at high pressures and temperatures. Since the physical environments inside the Earth and other planets exceed by far the technically accessible conditions, pushing the limits of experimentally feasible conditions as well as *in situ* measurements at these conditions remains a constant challenge. For these reasons, BGI scientists have put effort into establishing new experimental approaches, particularly at high pressures and high temperatures.

This year, we have three contributions in this field. The first contribution concerns stress measurements during deformation experiments in an in-house multianvil press. In standard experimental setups, sample stresses can only be measured using *in situ* X-ray diffraction with synchrotron radiation. However, since synchrotron beam time is limited, a new method is needed to measure stresses under laboratory conditions. Dolinschi *et al.* have made it possible to measure stresses employing piezoelectric crystals, which are integrated into their experimental setup. In this way, they successfully measured the applied stress at high temperatures and pressures in a multianvil press. The second contribution is devoted to the measurement of sample length in a multianvil press at high pressure and temperature. Neri *et al.* have developed a method to determine the sample pressure and length by simultaneously measuring P- and S-wave travel times, making it possible to determine these two parameters without the use of synchrotron radiation. Lastly, Dominijanni *et al.* have evaluated the feasibility of the Ir-Fe oxygen fugacity sensor to determine the oxygen fugacity in high-pressure experiments using a multianvil press and a diamond anvil cell. This sensor is well suited for measuring oxygen fugacity at high temperatures, but is not well calibrated for high-pressure conditions. By updating the thermodynamic model for this sensor with the pressure effects, an improved measurement of oxygen fugacity can be demonstrated for multianvil and especially laser-heated diamond-anvil-cell experiments, making it particularly valuable for experiments at very high pressures.

a. *Development of a novel technique to measure deformation stress* in situ *in large-volume presses utilizing the direct piezoelectric effect (J. Dolinschi, A. Néri, L. Man and D.J. Frost)*

Methods to experimentally achieve high pressures and temperatures in the Earth's interior have been developed extensively for decades. Various techniques and methods have experimentally simulated the Earth from the surface to the core. Progress in creating more accurate experimental conditions continues, including recent advances in redox control. However, the Earth's interior is not hydrostatic. The Earth is a dynamic planet, currently the only one known to have mantle convection and plate tectonics. These processes cause stresses and strains in the interior, adding a complicated extra layer over an already complex interior. It is known that stresses can shift the stability fields of constituting minerals in the temperature and pressure space, change the fractions of stable phases, and prevent phase

transitions. However, little work has been done to understand how stresses affect the Earth's interior. Although stresses can be measured *ex situ* by methods using a pressure marker, this method is feasible only when synchrotron X-rays are available. Therefore, the BGI is developing a novel method to measure stresses *in situ* without synchrotron X-rays. Although work on this method has been ongoing, its assembly has already been completed, as explained below. Data on Earth's materials during deformation are being actively collected, and the stresses measured using this method are being compared with those estimated using simultaneous X-ray diffraction at a synchrotron beamline.

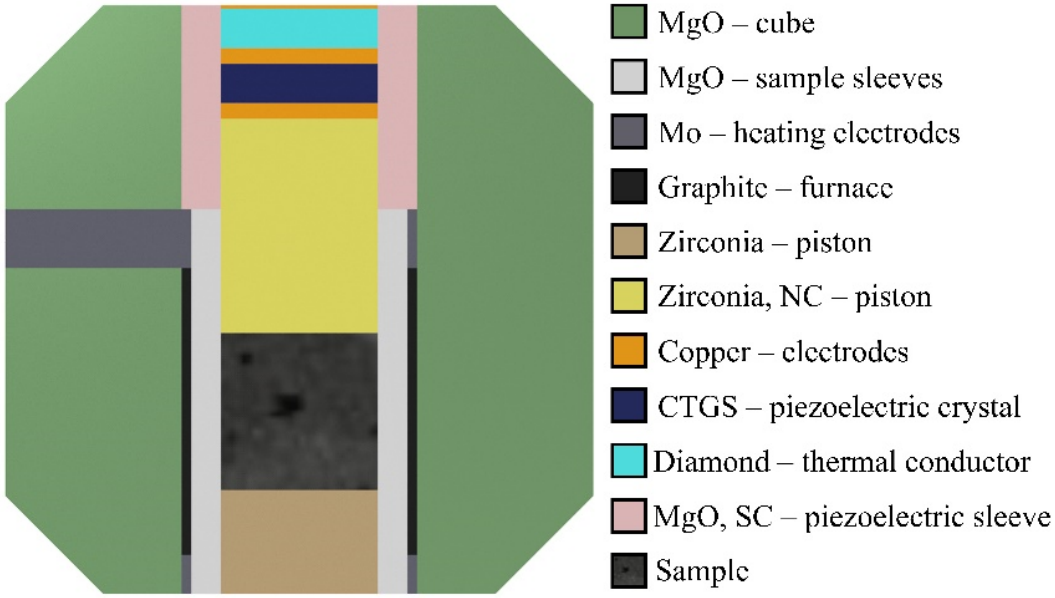

Fig. 3.8-1: A schematic drawing of the assembly design for deformations up to 1400 °C and up to 5 GPa. 'Zirconia, NC' is a non-crushable form of zirconia with low porosity. 'MgO, SC' is a single crystal sleeve around the piezoelectric crystal.

The finalized design uses a piezoelectric crystal placed inside the deformation column made of low-porosity zirconia (Fig. 3.8-1). Electrodes on the two opposing faces are connected to it. When the crystal experiences stresses, a small voltage is generated. This voltage is picked up by the electrodes and measured using a charge integrator. The amount of charge generated is proportional to the stress experienced by the crystal, with a factor defined by the piezoelectric coefficient. This year, most of the problems with the previous design have been solved, and the assembly is ready to obtain real data on Earth's materials. Currently, the most serious problem is the drop in electrical resistance across the crystal at high pressures, especially at high temperatures. This low resistance almost instantaneously leaks charges generated by stresses, leading to inaccurate stress measurements. To solve this problem, the following three improvements have been made. First, a quartz crystal of piezometer in the previous design has been replaced by a CTGS ($Ca_3TaGa_3Si_2O_{14}$) crystal. CTGS has an order of magnitude higher resistance and a twice higher piezoelectric coefficient than quartz. Second, a diamond disk has been placed between the carbide anvil

and the piezometer sandwiched by copper foils, helping heat exhaust from the crystal to the anvil. This heat exhaust keeps the crystal temperature one-third of the sample temperature during heating, which increases the piezometer resistance. Third, since polycrystalline MgO around the piezometer may leak charges due to grain-boundary conduction, the polycrystalline MgO sleeve has been replaced by a single crystal MgO sleeve. These improvements allowed us to collect high-temperature deformation data on single crystal MgO (Fig. 3.8-2). The compressional and tensile deformations at high temperatures indicate decreases in the strength of MgO. For example, the strength was less than half at 1300 °C than at 25 °C after 8 % strain.

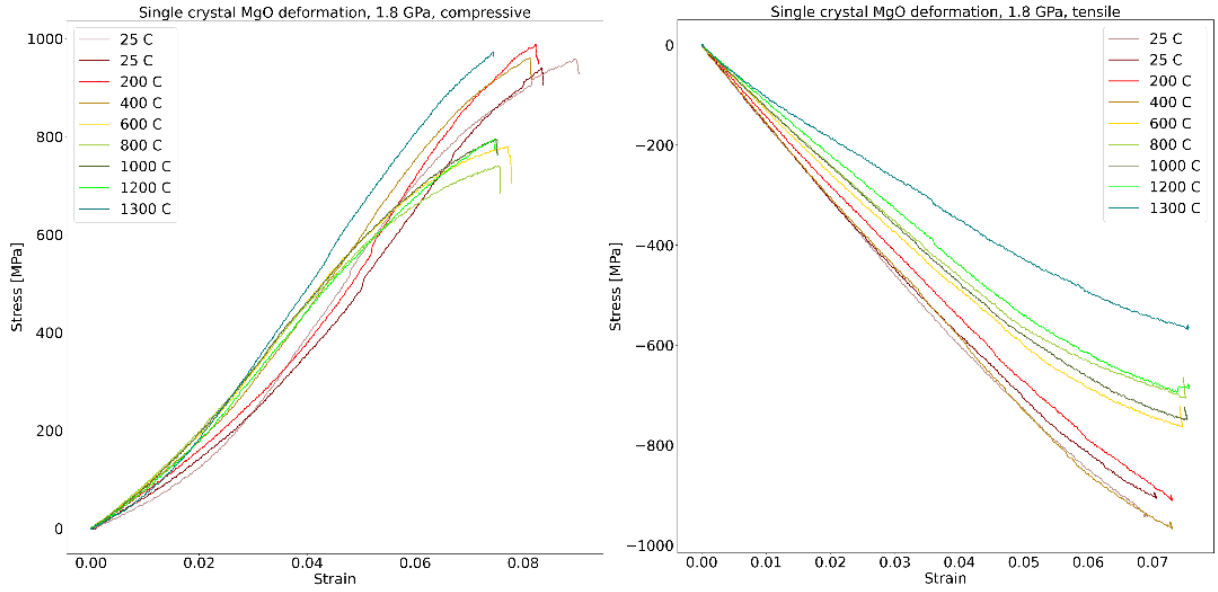

Fig. 3.8-2: Stress-strain relations in a deformation experiment at a pressure of 1.8 GPa, temperatures up to 1300 °C, and a strain rate of 4.0×10^{-5} s^{-1} for 10 minutes. The left and right diagrams are from compressive and tensile deformations, respectively. As was expected, the stress on the single crystal MgO lowers with increasing temperature.

b. *Development of internal pressure standards using ultrasonic interferometry (A. Néri, L. Man, T. Boffa Ballaran and D.J. Frost, in collaboration with J. Chantel/Lille and R. Farla/Hamburg)*

The laboratory wave-velocity measurement is a powerful tool for determining equations of state (EoSs) of mantle minerals and better understanding the complex structure of the Earth's mantle. Ultrasonic interferometry is commonly used to measure wave velocities in multianvil presses. In this type of experiments, a piezoelectric crystal is attached to the back of an anvil and simultaneously sends compressional (P-) and shear (S-) waves traveling from the anvil to the sample through a buffer rod. The elastic waves are reflected on the surfaces of the sample, producing echoes returning to the piezoelectric crystal. The time difference between two successive echoes gives the two-way travel time of the waves in the sample.

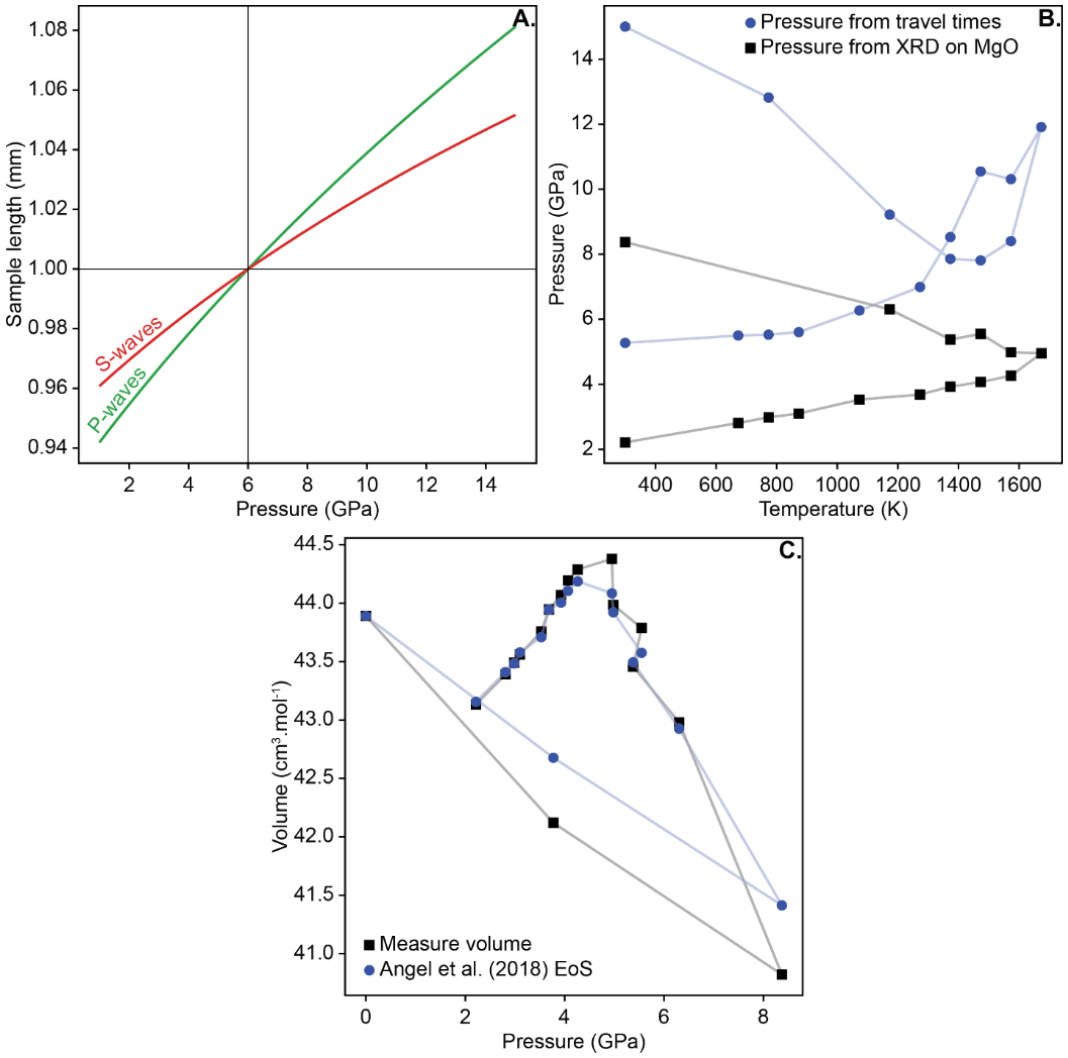

Fig. 3.8-3: (A) The predicted relation between the sample length and pressure for given P- and S-wave travel times at ambient temperature. The intersection of these curves indicates the actual pressure and sample length. (B) Comparison between pressures determined from the unit cell volume of MgO and from the travel time cross-calibration method on olivine, as a function of temperature. (C) Comparison between the measured and predicted olivine unit cell volume using literature data. The excellent agreement between our data and the values predicted using the bulk modulus and its pressure and temperature derivatives in literature implies that the shear modulus and its derivatives may be responsible for the discrepancy shown in (B).

Accurate pressure determination is necessary to analyze the collected data and to extrapolate them to higher pressures. Therefore, ultrasonic interferometry is combined with synchrotron radiation to determine pressure and sample length by X-ray diffraction (XRD) and radiography, respectively. To allow equivalent acoustic measurements in an in-house facility, it is crucial to determine sample pressure and length without X-rays. Previous attempts used P- and S-wave travel times through the buffer rod to measure pressure. However, the parametrization obtained in a calibration experiment can only be applied to experiments with identical assemblies. To overcome this limitation, we have developed a

novel method to determine sample pressure and length by simultaneously measuring P- and S-wave travel times. As shown in Figure 3.8-3A, combining the travel times, sample temperature, and EoS of the material predict the relations between the sample length and pressure for P- and S-waves individually. This method is similar to the XRD cross-calibration for simultaneous pressure and temperature determination. Note that this method does not require any assumption on the deformation of the sample, *i.e.*, elastic, plastic or viscous.

To check the validity of this method, we simultaneously collected XRD patterns and P- and S-wave travel times of an olivine single-crystal in beamline P61B at DESY. Figure 3.8-3B compares pressures determined using the conventional XRD using reference MgO and the new travel-time method. They show an extremely poor agreement, especially at high temperatures. To clarify the reasons for the disagreement, we compared the measured unit cell volume of olivine with the existing olivine EoS (Fig. 3.8-3C), showing a very good agreement. Thus, the literature data on the olivine's bulk modulus, its pressure and temperature derivatives are consistent with our measurement. On the other hand, the shear modulus and its pressure and temperature derivatives in literature seem problematic. To verify this idea, we will obtain the shear modulus and its derivatives of olivine from our data and compare them with the literature data.

c. *Calibration of the Fe-Ir redox sensor at high pressure and application to oxygen fugacity in laser-heated diamond anvil cell experiments (S. Dominijanni, C.A. McCammon, D.J. Frost, L.S. Dubrovinsky, N. Miyajima, T. Boffa Ballaran, E. Koemets/Oxford, G. Aprilis/Grenoble, S. Chariton/Chicago, Z. Liu/Changchun, V. Cerantola/Milano and A. Chumakov/Grenoble)*

Since the 1990s, redox sensors have been widely used to estimate oxygen fugacity fO_2 in high-pressure/-temperature experiments to simulate the Earth and terrestrial planetary interiors. The fO_2 sensors are based on the equilibrium of an alloy of a transition metal and noble metal with the oxide of the transition metal. The fractions of the transition metal in the alloy and oxide indicate the deviation of fO_2 from that buffered by the pure transition metal and its oxide. Typical examples are a combination of alloys of Fe with a noble metal such as Ir, Pd, and Pt with wustite, which measures the deviation of fO_2 from the iron-wustite buffer. Since many alloys of a transition metal and noble metal are not ideal mixtures, the activity-composition relations have to be known for this purpose. Theoretically, many noble metals might be used as a redox sensor if their activity-composition relations are well known. Among various candidates, Ir may be the most suitable because an *fcc*-structured phase is stable in the Fe-Ir system over a broad temperature range, and its activity-composition relations and volume of mixing are well known at zero pressure. However, the pressure dependencies of these thermodynamic parameters are still unknown. To obtain the pressure dependencies, we have updated the thermodynamic model for the Fe-Ir redox sensor by including the pressure effect to determine the oxygen fugacity more accurately at high

pressures. Oxygen fugacity has rarely been measured or controlled in diamond anvil cells, preventing investigation of the stability and phase equilibria of ultrahigh-pressure phases. For example, previous studies conducted at potentially different oxygen fugacity conditions provided contradictory results about whether Fe- or Ca-based Tetracarbonates break down under lower-mantle conditions. We, therefore, applied the updated Fe-Ir redox sensor to determine oxygen fugacity in the laser-heated diamond anvil cell (LHDAC) and performed complementary multianvil experiments using the same starting mixture at similar experimental conditions for comparison.

LHDAC experiments with *in situ* XRD were performed on a mixture of ferropericlase and Ir metal as a starting material at pressures up to 61 GPa and temperatures up to 2000 K at the European Synchrotron Radiation Facility. We measured compositions of Fe-Ir alloys formed by laser-heating to track the fO_2 conditions. We also conducted high-resolution synchrotron Mössbauer spectroscopy (SMS), powder X-ray diffraction (XRD), X-ray absorption near-edge structure spectroscopy (XANES), electron energy loss spectroscopy (EELS), and chemical analyses. Multianvil experiments were performed on the same starting material as the DAC experiments at 26 GPa and 2000K using a 1200-ton Kawai-type press at BGI.

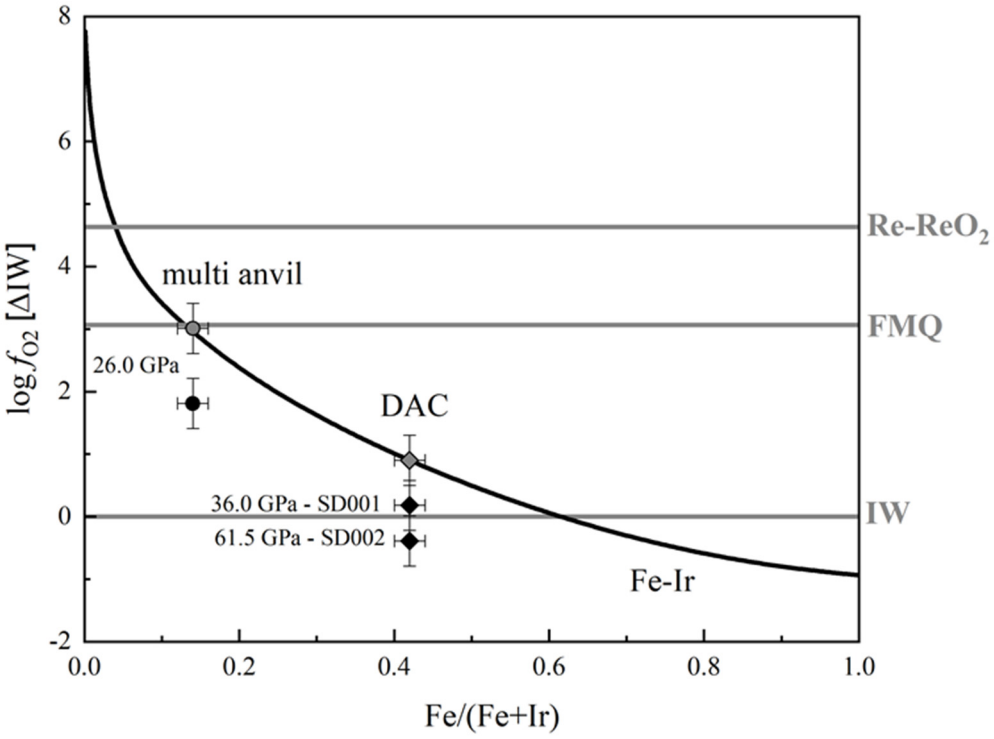

Fig. 3.8-4: Oxygen fugacity determined using the existing redox sensor thermodynamic model (grey symbols) compared to log fO_2 obtained using the model updated to include the effect of pressure (black symbols) for multianvil (circles) and DAC (diamonds) experiments. Grey horizontal lines show log fO_2 buffered by pure phases, *i.e.*, Re-ReO_2, FMQ, and IW, at zero pressure. The solid black curve represents log fO_2 normalized to IW as a function of the Fe/(Fe+Ir) ratio in the entire compositional range at zero 1 atm.

LHDAC experiments with *in situ* XRD were performed on a mixture of ferropericlase and Ir metal as a starting material at pressures up to 61 GPa and temperatures up to 2000 K at the European Synchrotron Radiation Facility. We measured compositions of Fe-Ir alloys formed by laser-heating to track the fO_2 conditions. We also conducted high-resolution synchrotron Mössbauer spectroscopy (SMS), powder X-ray diffraction (XRD), X-ray absorption near-edge structure spectroscopy (XANES), electron energy loss spectroscopy (EELS), and chemical analyses. Multianvil experiments were performed on the same starting material as the DAC experiments at 26 GPa and 2000 K using a 1200-ton Kawai-type press at BGI.

EELS, XANES, and SMS spectroscopies showed negligible ferric iron in ferropericlase, leading to reducing conditions in DAC. We estimated fO_2 in the DAC at pressures of 36 and 61 GPa based on the measured compositions of the Fe-Ir alloys. Correcting the fO_2 using the compressibility of Fe-Ir and ferropericlase in literature lowered fO_2 by 1 log unit. It was found that the fO_2 in the DAC is at the iron-wustite buffer, whereas that in the multianvil press is by 2 log units higher (Fig. 3.8-4).

4. Publications, Conference Presentations, Seminars

4.1 Publications (published)

Supplement to **2021** (papers published at the end of 2021):

BLANCHARD, I.; RUBIE, D.C.; JENNINGS, E.S.; FRANCHI, I.A.; ZHAO, X.; PETITGIRARD, S.; MIYAJIMA, N.; JACOBSON, S.A.; MORBIDELLI, A. (2021): The metal–silicate partitioning of carbon during Earth's accretion and its distribution in the early solar system. Earth Planet. Sci. Lett. 580, 117374, https://doi.org/10.1016/j.epsl.2022.117374

2022

Refereed international journals

ABEYKOON, S.; AUDÉTAT, A. (2022): The single-crystal diamond trap (SCDT): a new method to determine the composition of high-P-T fluids. Contrib. Mineral. Petrol. 177, 24, https://doi.org/10.1007/s00410-021-01882-6

ARATÓ, R.; AUDÉTAT, A. (2022): Titanomagnetite – silicate melt oxybarometry. – In: Magma redox geochemistry (Eds. Moretti, R.; Neuville, D.R.): Geophysical Monograph Series 266, 369-380, https://doi.org/10.1002/9781119473206.ch18

ARZILLI, F.; POLACCI, M.; LA SPINA, G.; LE GALL, N.; LLEWELLIN, E.W.; BROOKER, R.A.; TORRES-OROZCO, R.; DI GENOVA, D.; NEAVE, D.A.; HARTLEY, M.E.; MADER, H.M.; GIORDANO, D.; ATWOOD, R.; LEE, P.D.; HEIDELBACH, F.; BURTON, M.R. (2022): Dendritic crystallization in hydrous basaltic magmas controls magma mobility within the Earth's crust. Nat. Commun. 31, 3354, https://doi.org/10.1038/s41467-022-30890-8

ASLANDUKOV, A.; ASLANDUKOV, M.; DUBROVINSKAIA, N.; DUBROVINSKY, L. (2022): Domain Auto Finder (DAFi) program: the analysis of single-crystal X-ray diffraction data from polycrystalline samples. J. Appl. Cryst. 55 (5), 1383-1391, https://doi.org/10.1107/S1600576722008081

ASLANDUKOV, A.; TRYBEL, F.; ASLANDUKOVA, A.; LANIEL, D.; FEDOTENKO, T.; KHANDARKHAEVA, S.; APRILIS, G.; GIACOBBE, C.; BRIGHT, E.L.; ABRIKOSOV, I.A.; DUBROVINSKY, L.; DUBROVINSKAIA, N. (2022): Anionic N_{18} macrocycles and a polynitrogen double helix in novel yttrium polynitrides YN_6 and Y_2N_{11} at 100 GPa. Angew. Chem. Int. Ed. 61 (34), e202207469, https://doi.org/10.1002/anie.202207469

BAROSCH, J.; and the Hayabusa2 Initial Analysis Chemistry Team (63 members including BOUVIER, A.) (2022): Presolar stardust in asteroid Ryugu. The Astrophys. J. Lett. 935, L3, https://doi.org/10.3847/2041-8213/ac83bd

BINCK, J.; LANIEL, D.; BAYARJARGAL, L.; KHANDARKHAEVA, S.; FEDOTENKO, T.; ASLANDUKOV, A.; GLAZYRIN, K.; MILMAN, V.; CHARITON, S.; PRAKAPENKA, V.B.; DUBROVINSKAIA, N.; DUBROVINSKY, L.; WINKLER, B. (2022): Synthesis of calcium orthocarbonate, Ca_2CO_4-Pnma at PT conditions of Earth's transition zone and lower mantle. Am. Mineral. 107 (3), 336-342, https://doi.org/10.2138/am-2021-7872

BLANCHARD, I.; PETITGIRARD, S.; LAURENZ, V.; MIYAJIMA, N.; WILKE, M.; RUBIE, D.C.; LOBANOV, S.S.; HENNET, L.; MORGENROTH, W.; TUCOULOU, R.; BONINO, V.; ZHAO, X.C.; FRANCHI, I. (2022): Chemical analysis of trace elements at the nanoscale in samples recovered from laser-heated diamond anvil cell experiments. Phys. Chem. Minerals 49 (6), https://doi.org/10.1007/s00269-022-01193-7

BONDAR, D.; ZANDONÀ, A.; WITHERS, A.C.; FEI, H.; GENOVA, D.D.; MIYAJIMA, N.; KATSURA, T. (2022): Rapid-quenching of high-pressure depolymerized hydrous silicate (peridotitic) glasses. J. Non Cryst. Solids 578, 121347, https://doi.org/10.1016/j.jnoncrysol.2021.121347

BRITVIN, S.N.; VLASENKO, N.S.; ASLANDUKOV, A.; ASLANDUKOVA, A.; DUBROVINSKY, L.; GORELOVA, L.; KRZHIZHANOVSKAYA, M.G.; VERESHCHAGIN, O.S.; BOCHAROV, V.N.; SHELUKHINA, Y.S.; LOZHKIN, M.S.; ZAITSEV, A.N.; NESTOLA, F. (2022): Natural cubic perovskite, $Ca(Ti,Si,Cr)O_{3-\delta}$, a versatile potential host for rock-forming and less-common elements up to Earth's mantle pressure. Am. Mineral. 107 (10), 1936-1945, https://doi.org/10.2138/am-2022-8186

BYKOVA, E.; JOHANSSON, E.; BYKOV, M.; CHARITON, S.; FEI, H.; OVSYANNIKOV, S.V.; ASLANDUKOVA, A.; GABEL, S.; HOLZ, H.; MERLE, B.; ALLING, B.; ABRIKOSOV, I.A.; SMITH, J.S.; PRAKAPENKA, V.B.; KATSURA, T.; DUBROVINSKAIA, N.; GONCHAROV, A.F.; DUBROVINSKY, L. (2022): Novel class of rhenium borides based on hexagonal boron networks interconnected by short B 2 dumbbells. Chem. Mater. 34 (18), 8138-8152, https://doi.org/10.1021/acs.chemmater.2c00520

BYKOVA, E.; OVSYANNIKOV, S.V.; BYKOV, M.; YIN, Y.; FEDOTENKO, T.; HOLZ, H.; GABEL, S.; MERLE, B.; CHARITON, S.; PRAKAPENKA, V.B.; DUBROVINSKAIA, N.; GONCHAROV, A.F.; DUBROVINSKY, L. (2022): Synthesis, crystal structure, and properties of stoichiometric hard tungsten tetraboride, WB_4. J. Mater. Chem. A 2022, 10 (37), 20111-20120, https://doi.org/10.1039/D2TA02268K

CHAKRABORTI, A.; JAY, A.; HARDOUIN DUPARC, O.; SJAKSTE, J.; BÉNEUT, K.; VAST, N.; LE GODEC, Y. (2022): Boron carbide under torsional deformation: Evidence of the formation of chain vacancies in the plastic regime. Acta Materialia 226, 117553, https://doi.org/10.1016/j.actamat.2021.117553

CHANG, J.; AUDÉTAT, A. (2022): Post-subduction porphyry Cu magmas in the Sanjiang region of southwestern China formed by fractionation of lithospheric mantle-derived mafic magmas. Geology 51 (1), 64-68, https://doi.org/10.1130/G50502.1

CHANYSHEV, A.; ISHII, T.; BONDAR, D.; BHAT, S.; KIM, E.J.; FARLA, R.; NISHIDA, K.; LIU, Z.; WANG, L.; NAKAJIMA, A.; YAN, B.; TANG, H.; CHEN, Z.; HIGO, Y.; TANGE, Y.; KATSURA, T. (2022): Depressed 660-km discontinuity caused by akimotoite-bridgmanite transition. Nature 601(7891), 69-73, https://doi.org/10.1038/s41586-021-04157-z

CHEN, S.; SUN, P.; NIU, Y.; GUO, P.; ELLIOTT, T.; HIN, R.C. (2022): Molybdenum isotope systematics of lavas from the East Pacific Rise: Constraints on the source of enriched mid-ocean-ridge basalt. Earth Planet. Sci. Lett. 578, 117283, https://doi.org/10.1016/j.epsl.2021.117283

DOMINIJANNI, S.; MCCAMMON, C.A.; OHTANI, E.; IKUTA, D.; SAKAMAKI, T.; ISHII, T.; CRINITI, G.; DUBROVINSKY, L.; KHANDARKHAEVA, S.; FEDOTENKO, T.; GLAZYRIN, K.; UCHIYAMA, H.; FUKUI, H.; BARON, A.Q.R. (2022): Sound velocity measurements of B2-Fe-Ni-Si alloy under high pressure by inelastic X-ray scattering: Implications for the composition of Earth's core. Geophys. Res. Lett. 49 (15), https://doi.org/10.1029/2021GL096405

DRUZHBIN, D.; FEI, H.; HAO, J.; ZHANG, C.; LIN, Y.; DOHMEN, R.; KATSURA, T. (2022): Water enhancement of Si self-diffusion in wadsleyite. J. Geophys. Res. Solid Earth 127 (3), e2021JB023440, https://doi.org/10.1029/2021JB023440

DUBROVINSKY, L.; KHANDARKHAEVA, S.; FEDOTENKO, T.; LANIEL, D.; BYKOV, M.; GIACOBBE, C.; BRIGHT, E.L.; SEDMAK, P.; CHARITON, S.; PRAKAPENKA, V.; PONOMAREVA, A.V.; SMIRNOVA, E.A.; BELOV, M.P.; TASNÁDI, F.; SHULUMBA, N.; TRYBEL, F.; ABRIKOSOV, I.A.; DUBROVINSKAIA, N. (2022): Materials synthesis at terapascal static pressures. Nature 605, 274-278, https://doi.org/10.1038/s41586-022-04550-2

EBERHARD, L.; THIELMANN, M.; EICHHEIMER, P.; NÉRI, A.; SUZUKI, A.; OHL, M.; FUJITA, W.; UESUGI, K.; NAKAMURA, M.; GOLABEK, G.J.; FROST, D.J. (2022): A new method for determining fluid flux at high pressures applied to the dehydration of subduction zone serpentinites. Geochem. Geophys. Geosyst. 23 (9), e2021GC010062, https://doi.org/10.1029/2021GC010062

EHLERS, A.M.; ZAFFIRO, G.; ANGEL, R.J.; BOFFA BALLARAN, T.; CARPENTER, M.A.; ALVARO, M.; ROSS, N.L. (2022): Thermoelastic properties of zircon: Implications for geothermobarometry. Am. Mineral. 107 (1), 74-81, https://doi.org/10.2138/am-2021-7731

FANG, J.; AUDÉTAT, A. (2022): The effects of pressure, fO_2, fS_2 and melt composition on the fluid–melt partitioning of Mo: Implications for the Mo-mineralization potential of upper crustal granitic magmas. Geochim. Cosmochim. Acta 336, 1-14, https://doi.org/10.1016/j.gca.2022.08.016

FANG, L.; FROSSARD, P.; BOYET, M.; BOUVIER, A.; BARRAT, J.-A.; CHAUSSIDON, M.; MOYNIER F. (2022): Half-life and initial Solar System abundance of ^{146}Sm determined from the oldest andesitic meteorite. PNAS 119 (12), e2120933119, https://doi.org/10.1073/pnas.2120933119

FARLA, R.; BHAT, S.; SONNTAG, S.; CHANYSHEV, A.; MA, S.; ISHII, T.; LIU, Z.; NÉRI, A.; NISHIYAMA, N.; ABREU FARIA, G.; WROBLEWSKI, T.; SCHULTE-SCHREPPING, H.; DRUBE, W.; SEECK, O.; KATSURA, T. (2022): Extreme conditions research using the large-volume press at the P61B endstation, PETRA III. J. Synchrotron Rad. 29, 409-423, https://doi.org/10.1107/S1600577522001047

FEI, H.; KATSURA, T. (2022): The effect of oxygen fugacity on ionic conductivity in olivine. Geosci. Front. 13 (1), 101270, https://doi.org/10.1016/j.gsf.2021.101270

FEI, H.; ZHANG, B.; LIU, J.; YOSHINO, T. (2022): Editorial: water in the Earth's interior. Front. Earth Sci. 10, 1030793, https://doi.org/10.3389/feart.2022.1030793

FROSSARD, P.; ISRAEL, C.; BOUVIER, A.; BOYET, M. (2022): Earth's composition was modified by collisional erosion. Science 377 (6614), 1529-1532, https://doi.org/10.1126/science.abq7351

GAVRYUSHKIN, P.N.; MARTIROSYAN, N.S.; RASHCHENKO, S.V.; SAGATOVA, D.N.; SAGATOV, N.E.; SEMERIKOVA, A.I.; FEDOTENKO, T.M.; LITASOV, K.D. (2022): First experimental synthesis of Mg orthocarbonate by the $MgCO_3 + MgO = Mg_2CO_4$ reaction at pressures of the Earth's lower mantle. JETP Lett. 116, 477-484, https://doi.org/10.1134/S0021364022601798

GILLMANN, C.; WAY, M.J.; AVICE, G.; BREUER, D.; GOLABEK, G.J.; HÖNING, D.; KRISSANSEN-TOTTON, J.; LAMMER, H.; O'ROURKE, J.G.; PERSSON, M.; PLESA, A.-C.; SALVADOR, A.; SCHERF, M.; ZOLOTOV, M.Y. (2022): The long-term evolution of the atmosphere of Venus: Processes and feedback mechanisms. Space Sci. Rev. 218, 56, https://doi.org/10.1007/s11214-022-00924-0

GORELOVA, L.; VERESHCHAGIN, O.; ASLANDUKOV, A.; ASLANDUKOVA, A.; SPIRIDONOVA, D.; KRZHIZHANOVSKAYA, M.; KASATKIN, A.; DUBROVINSKY, L. (2022): Hydroxylherderite ($Ca_2Be_2P_2O_8(OH)_2$) stability under extreme conditions (up to 750 °C/100 GPa). J. Am. Ceram. Soc., 1-13, https://doi.org/10.1111/jace.18923

GÜLCHER, A.J.P.; GOLABEK, G.J.; THIELMANN, M.; BALLMER, M.D.; TACKLEY, P.J. (2022): Narrow, fast, and "cool" mantle plumes caused by strain-weakening rheology in Earth's lower mantle. Geochem. Geophys. Geosyst. 23 (10), e2021GC010314, https://doi.org/10.1029/2021GC010314

HIN, R.C.; HIBBERT, K.E.J.; CHEN, S.; WILLBOLD, M.; ANDERSEN, M.B.; KISEEVA, E.S.; WOOD, B.J.; NIU, Y.; SIMS, K.W.W.; ELLIOTT, T. (2022): The influence of crustal recycling on the molybdenum isotope composition of the Earth's mantle. Earth Planet. Sci. Lett. 595, 117760, https://doi.org/10.1016/j.epsl.2022.117760

HOPP, T.; and the Hayabusa2 Initial Analysis Chemistry Team (63 members including BOUVIER, A.) (2022): Ryugu's nucleosynthetic heritage from the outskirts of the Solar System. Sci. Adv. 8 (46), eadd8141, https://doi.org/10.1126/sciadv.add8141

HSIEH, W.-P.; MARZOTTO, E.; TSAO, Y.-C.; OKUCHI, T.; LIN, J.-F. (2022): High thermal conductivity of stishovite promotes rapid warming of a sinking slab in Earth's mantle. Earth Planet. Sci. Lett. 584, 117477, https://doi.org/10.1016/j.epsl.2022.117477

HSIEH, W.-P.; MARZOTTO, E.; ISHII, T.; DUBROVINSKY, L.; ASLANDUKOVA, A.A.; CRINITI, G.; TSAO, Y.-C.; LIN, C.-H.; TSUCHIYA, J.; E. OHTANI (2022): Low thermal conductivity of hydrous phase D leads to a self-preservation effect within a subducting slab. JGR Solid Earth 127 (6), e2022JB024556, https://doi.org/10.1029/2022JB024556

HUANG, D.; MURAKAMI, M.; BRODHOLT, J.; MCCAMMON, C.; PETITGIRARD, S. (2022): Structural evolution in a pyrolitic magma ocean under mantle conditions. Earth Planet. Sci. Lett. 584, 117473, https://doi.org/10.1016/j.epsl.2022.117473

ISHII, T.; CHANYSHEV, A.; KATSURA, T. (2022): A new approach determining a phase transition boundary strictly following a definition of phase equilibrium: an example of the post-spinel transition in Mg_2SiO_4 system. Minerals 12 (7), 820, https://doi.org/10.3390/min12070820

ISHII, T.; CRINITI, G.; OHTANI, E.; PUREVJAV, N.; FEI, H.; KATSURA, T.; MAO, H.K. (2022): Superhydrous aluminous silica phases as major water hosts in high-temperature lower mantle. PNAS 119 (44) e2211243119, https://doi.org/10.1073/pnas.2211243119

ISHII, T.; OHTANI, E.; SHATSKIY, A. (2022): Aluminum and hydrogen partitioning between bridgmanite and high-pressure hydrous phases: Implications for water storage in the lower mantle. Earth Planet. Sci. Lett. 583, 117441, https://doi.org/10.1016/j.epsl.2022.117441

ISHII, T.; MIYAJIMA, N.; CRINITI, G.; HU, Q.; GLAZYRIN, K.; KATSURA, T. (2022): High pressure-temperature phase relations of basaltic crust up to mid-mantle conditions. Earth Planet. Sci. Lett. 584, 117472, https://doi.org/10.1016/j.epsl.2022.117472

KATSURA, T. (2022): A revised adiabatic temperature profile for the mantle. JGR Solid Earth 127 (2), e2021JB023562, https://doi.org/10.1029/2021JB023562

KEPPLER, H.; CIALDELLA, L.; COUFFIGNAL, F.; WIEDENBECK, M. (2022): The solubility of N_2 in silicate melts and nitrogen partitioning between upper mantle minerals and basalt. Contrib. Mineral. Petrol. 177, 83, https://doi.org/10.1007/s00410-022-01948-z

KISEEVA, E.S.; KOROLEV, N.; KOEMETS, I.; ZEDGENIZOV, D.A.; UNITT, R.; MCCAMMON, C.; ASLANDUKOVA, A.; KHANDARKHAEVA, S.; FEDOTENKO, T.; GLAZYRIN, K.; BESSAS, D.; APRILIS, G.; CHUMAKOV, A.I.; KAGI, H.; DUBROVINSKY, L. (2022): Subduction-related oxidation of the sublithospheric mantle evidenced by ferropericlase and magnesiowüstite diamond inclusions. Nat. Commun. 13, 7517, https://doi.org/10.1038/s41467-022-35110-x

KHANDARKHAEVA, S.; FEDOTENKO, T.; CHARITON, S.; BYKOVA, E.; OVSYANNIKOV, S.V.; GLAZYRIN, K.; LIERMANN, H.-P.; PRAKAPENKA, V.; DUBROVINSKAIA, N.; DUBROVINSKY, L. (2022): Structural diversity of magnetite and products of its decomposition at extreme conditions. Inorg. Chem. 61, 1091-1101, https://doi.org/10.1021/acs.inorgchem.1c03258

KOEMETS, I.; ISHII, T.; DUBROVINSKY, L.; HANFLAND, M. (2022): Equations of state of α-SiC (6H) and β'-$Mg_2Si_{1.1}$ from single-crystal X-ray diffraction data and novel high-pressure magnesium silicide Mg_2Si_7. Phys. Chem. Minerals 49, 12, https://doi.org/10.1007/s00269-022-01189-3

LAFONTAINE, D.; BOUVIER, A.; HILL, M.L. (2022): Garnet geochemistry and Lu-Hf geochronology of a gold-bearing sillimanite-garnet-biotite gneiss at the Borden Lake Belt. Geosciences 12 (5), 218, https://doi.org/10.3390/geosciences12050218

LANGHAMMER, D.; DI GENOVA, D.; STEINLE NEUMANN, G. (2022): Modelling viscosity of volcanic melts with artificial neural networks. Geochem. Geophys. Geosyst. 23 (12), e2022GC010673, https://doi.org/10.1029/2022GC010673

LANIEL, D.; FEDOTENKO, T.; WINKLER, B.; ASLANDUKOVA, A.; ASLANDUKOV, A.; APRILIS, G.; CHARITON, S.; MILMAN, V.; PRAKAPENKA, V.; DUBROVINSKY, L.; DUBROVINSKAIA, N. (2022): A reentrant phase transition and a novel polymorph revealed in high-pressure investigations of CF_4 up to 46.5 GPa. J. Chem. Phys. 156 (4), 044503, https://doi.org/10.1063/5.0079402

LANIEL, D.; TRYBEL, F.; NÉRI, A.; YIN, Y.; ASLANDUKOV, A.; FEDOTENKO, T.; KHANDARKHAEVA, S.; TASNÁDI, F.; CHARITON, S.; GIACOBBE, C.; BRIGHT, E.L.; HANFLAND, M.; PRAKAPENKA, V.; SCHNICK, W.; ABRIKOSOV, I.A.; DUBROVINSKY, L.; DUBROVINSKAIA, N. (2022): Revealing phosphorus nitrides up to the megabar regime: Synthesis of α′-P_3N_5, δ-P_3N_5 and PN_2. Chemistry – A European Journal 28 (62), e202201998, https://doi.org/10.1002/chem.202201998

LANIEL, D.; WINKLER, B.; FEDOTENKO, T.; ASLANDUKOVA, A.; ASLANDUKOV, A.; VOGEL, S.; MEIER, T.; BYKOV, M.; CHARITON, S.; GLAZYRIN, K.; MILMAN, V.; PRAKAPENKA, V.; SCHNICK, W.; DUBROVINSKY, L.; DUBROVINSKAIA, N. (2022): High-pressure $Na_3(N_2)_4$, $Ca_3(N_2)_4$, $Sr_3(N_2)_4$, and $Ba(N_2)_3$ featuring nitrogen dimers with noninteger charges and anion-driven metallicity. Phys. Rev. Materials 6, 023402, https://doi.org/10.1103/PhysRevMaterials.6.023402

LANIEL, D.; TRYBEL, F.; WINKLER, B.; KNOOP, F.; FEDOTENKO, T.; KHANDARKHAEVA, S.; ASLANDUKOVA, A.; MEIER, T.; CHARITON, S.; GLAZYRIN, K.; MILMAN, V.; PRAKAPENKA, V.; ABRIKOSOV, I.A.; DUBROVINSKY, L.; DUBROVINSKAIA, N. (2022): High-pressure synthesis of seven lanthanum hydrides with a significant variability of hydrogen content. Nat. Commun. 13, 6987, https://doi.org/10.1038/s41467-022-34755-y

LAYEK, S.; GREENBERG, E.; CHARITON, S.; BYKOV, M.; BYKOVA, E.; TROTS, D.M.; KURNOSOV, A.V.; CHUVASHOVA, I.; OVSYANNIKOV, S.V.; LEONOV, I.; ROZENBERG, G.K. (2022): Verwey-type charge ordering and site-selective Mott transition in Fe_4O_5 under pressure. J. Am. Chem. Soc. 144, 10259-10269, https://doi.org/10.1021/jacs.2c00895

LIU, X-N.; HIN, R.C.; COATH, C.D.; VAN SOEST, M.; MELEKHOVA, E.; ELLIOTT, T. (2022): Equilibrium olivine-melt Mg isotopic fractionation explains high δ^{26}Mg in arc lavas. Geochem. Persp. Lett. 22, 42-47, https://doi.org/10.7185/geochemlet.2226

MA, N.; NEUMANN, W.; NÉRI, A.; SCHWARZ, W.H.; LUDWIG, T.; TRIELOFF, M.; KLAHR, H.; BOUVIER, A. (2022): Early formation of primitive achondrites in an outer region of the protoplanetary disc, 2022. Geochem. Persp. Lett. 23, 33-37, https://doi.org/10.7185/geochemlet.2234

MAH, J.; BRASSER, R.; BOUVIER, A.; MOJZSIS, S.J. (2022): Effects of pebble accretion on the growth and composition of planetesimals in the inner solar system. Monthly Notices Royal Astron. Soc. 511 (1), 158-175, https://doi.org/10.1093/mnras/stab3766

MAH, J.; BRASSER, R.; WOO, J.; BOUVIER, A.; MOJZSIS, S.J. (2022): Evidence for an incipient isotopic gradient in the inner region of the solar protoplanetary disc. Astron. Astrophys. 660, A36, https://doi.org/10.1051/0004-6361/202142926

MAITANI, S.; SINMYO, R.; ISHII, T.; KAWAGUCHI, S.I.; HIRAO, N. (2022): The electrical conductivity of Fe_4O_5, Fe_5O_6, and Fe_7O_9 up to 60 GPa. Phys. Chem. Minerals 49, 11, https://doi.org/10.1007/s00269-022-01188-4

MARTIROSYAN, N.S.; SHATSKIY, A.; LITASOV, K.D.; SHARYGIN, I.S.; YOSHINO, T. (2022): Interaction of carbonates with peridotite containing iron metal: Implications for carbon speciation in the upper mantle. Lithos 428-429, 106817, https://doi.org/10.1016/j.lithos.2022.106817

MEIER, T.; TRYBEL, F.; KHANDARKHAEVA, S.; LANIEL, D.; ISHII, T.; ASLANDUKOVA, A.; DUBROVINSKAIA, N.; DUBROVINSKY, L. (2022): Structural independence of hydrogen-bond symmetrisation dynamics at extreme pressure conditions. Nat. Commun. 13, 3042, https://doi.org/10.1038/s41467-022-30662-4

MORBIDELLI, A.; BAILLIÉ, K.; BATYGIN, K.; CHARNOZ, S.; GUILLOT, T.; RUBIE, D.C.; KLEINE, T. (2022): Contemporary formation of early solar system planetesimals at two distinct radial locations. Nat. Astron. 6, 72-79, https://doi.org/10.1038/s41550-021-01517-7

MOROZOVA, N.V.; KOROBEYNIKOV, I.V.; MIYAJIMA, N.; OVSYANNIKOV, S.V. (2022): Giant room-temperature power factor in p-type thermoelectric SnSe under high pressure. Advanced Science, 9 (20), https://doi.org/10.1002/advs.202103720

MOSENFELDER, J.L.; VON DER HANDT, A.; WITHERS, A.C.; BUREAU, H.; RAEPSAET, C.; ROSSMAN, G.R. (2022): Coupled hydrogen and fluorine incorporation in garnet: New constraints from FTIR, ERDA, SIMS, and EPMA. Am. Mineral. 107, 587-602, https://doi.org/10.2138/am-2021-7880

MOYNIER, F.; and the Hayabusa2 Initial Analysis Chemistry Team (63 members including BOUVIER, A.) (2022): The solar system calcium isotopic composition inferred from Ryugu samples. Geochem. Persp. Lett. 24, 1-6, https://doi.org/10.7185/geochemlet.2238

MURAKAMI, M.; GONCHAROV, A.F.; MIYAJIMA, N.; YAMAZAKI, D.; HOLTGREWE, N. (2022): Radiative thermal conductivity of single-crystal bridgmanite at the core-mantle boundary with implications for thermal evolution of the Earth. Earth Planet. Sci. Lett. 578, 117329, https://doi.org/10.1016/j.epsl.2021.117329

PAKHOMOVA, A.; COLLINGS, I.E.; JOURNAUX, B.; PETITGIRARD, S.; BOFFA BALLARAN, T.; HUANG, D.Y.; OTT, J.; KURNOSOV, A.; HANFLAND, M.; GARBARINO, G.; COMBONI, D. (2022): Host-guest hydrogen bonding in high-pressure acetone clathrate hydrates: *In situ* single-crystal X-ray diffraction study. J. Phys. Chem. Lett. 13 (7), 1833-1838, https://doi.org/10.1021/acs.jpclett.1c03911

POSNER, E.; STEINLE-NEUMANN, G. (2022): Compositional effects in the liquid Fe–Ni–C system at high pressure. Phys. Chem. Minerals 49, 43, https://doi.org/10.1007/s00269-022-01219-0

REYNARD, B.; FELLAH, C.; MCCAMMON, C. (2022): Iron oxidation state in serpentines and magnesian chlorites of subduction-related rocks. Eur. J. Mineral. 34, 645-656, https://doi.org/10.5194/ejm-34-645-2022

ROJAS-AGRAMONTE, Y.; KAUS, B.J.P.; PICCOLO, A.; WILLIAMS, I.S.; GERDES, A.; WONG, J.; XIE, H.X.; BUHRE, S.; TOULKERIDIS, T.; MONTERO, P.; GARCIA-CASCO, A. (2022): Zircon dates long-lived plume dynamics in oceanic islands. Geochem. Geophys. Geosyst. 23, e2022GC010485, https://doi.org/10.1029/2022GC010485

SATTA, N.; MORALES, L.F.G.; CRINITI, G.; KURNOSOV, A.; BOFFA BALLARAN; T.; SPEZIALE, S.; MARQUARDT; K.; CAPITANI, G.C.; MARQUARDT, H. (2022): Single-crystal elasticity of antigorite at high pressures and seismic detection of serpentinized slabs. Geophys. Res. Lett. 49 (16), e2022GL099411, https://doi.org/10.1029/2022GL099411

SCARANI, A.; ZANDONÀ, A.; DI FIORE, F.; VALDIVIA, P.; MIYAJIMA, N.; BORNHÖFT, H.; VONA, A.; DEUBENER, J.; ROMANO, C.; DI GENOVA, D. (2022): A chemical threshold controls nanocrystallization and degassing behaviour in basalt magmas. Commun. Earth Environ. 3, 284, https://doi.org/10.1038/s43247-022-00615-2

SZLACHTA, V.; VLASOV, K.; KEPPLER, H. (2022): On the stability of acetate in subduction zone fluids. Geochem. Persp. Lett. 21, 28-31, https://doi.org/10.7185/geochemlet.2213

VLASOV, K.; KEPPLER, H. (2022): Electrical conductivity of KCl-H_2O fluids in the crust and lithospheric mantle. JGR Solid Earth 127, e2022JB024080, https://doi.org/10.1029/2022JB024080

WANG, L.; CHANYSHEV, A.; MIYAJIMA, N.; KAWAZOE, T.; BLAHA, S.; CHANG, J.; KATSURA, T. (2022): Small effects of water incorporation on dislocation mobility in olivine: negligible creep enhancement and water-induced fabric transition in the oceanic asthenosphere. Earth Planet. Sci. Lett. 579, 117360, https://doi.org/10.1016/j.epsl.2021.117360

WALTE, N.P.; GOLABEK, G.J. (2022): Olivine aggregates reveal a complex collisional history of the Main Group Pallasite Parent Body. Meteorit. Planet. Sci. 57 (5), 1098-1115, https://doi.org/10.1111/maps.13810

WU, S.; AUDÉTAT, A.; JOCHUM, K.P.; WANG, H.; CHEN, J.; STOLL, B.; ZHANG, C.; BAO, Z.; YANG, S.; LI, C.; WANG, X.; XU, C.; XU, L.; HUANG, C.; XIE, L.; YANG, Y.; YANG, J. (2022): Three natural andesitic to rhyolitic glasses (OJY-1, OH-1, OA-1) as reference materials for *in situ* microanalysis. Geostand. Geoanal. Res. 46 (4), 673-700, https://doi.org/10.1111/ggr.12449

YIN, Y.; AKBAR, F.I.; BYKOVA, E.; ASLANDUKOVA, A.; LANIEL, D.; ASLANDUKOV, A.; BYKOV, M.; HANFLAND, M.; GARBARINO, G.; JIA, Z.; DUBROVINSKY, L.; DUBROVINSKAIA, N. (2022): Synthesis of rare-earth metal compounds through enhanced reactivity of alkali halides at high pressures. Commun. Chem. 5, 122, https://doi.org/10.1038/s42004-022-00736-x

YOKOYAMA, T.; and the Hayabusa2 Initial Analysis Chemistry Team (63 members including BOUVIER, A.) (2022): Samples returned from the asteroid Ryugu are similar to Ivuna-type carbonaceous meteorites. Science 379, eabn7850, https://doi.org/10.1126/science.abn7850

YUAN, H.; MAN, L.; KIM, D.Y.; POPOV, D.; MENG, Y.; GREENBERG, E.; PRAKAPENKA, V.; ZHANG, L. (2022): HP-PdF_2-type $FeCl_2$ as a potential Cl-carrier in the deep Earth. Am. Mineral. 107 (2), 313-317, https://doi.org/10.2138/am-2022-8283

YUAN, L.; STEINLE-NEUMANN, G. (2022): Possible control of Earth's boron budget by metallic iron. Geophys. Res. Lett. 49, e2021GL096923, https://doi.org/10.1029/2021GL096923

ZHANG, B.; FEI, H.; GE, J.; ZENG, L.; XIA, Q. (2022): Crustal melting in orogenic belts revealed by eclogite thermal properties. Nat. Commun. 13, 4673, https://doi.org/10.1038/s41467-022-32484-w

ZHANG, J.; CHANG, J; WANG, R.; AUDÉTAT, A. (2022): Can post-subduction porphyry Cu magmas form by partial melting of typical lower crustal amphibole-rich cumulates? Petrographic and experimental constraints from samples of the Kohistan and Gangdese arc roots. J. Petrol. 63 (11), egac101, https://doi.org/10.1093/petrology/egac101

4.2 Publications (submitted, in press)

ABEYKOON, S.; LAURENZ, V.; FROST, D.J.; MIYAJIMA, N.; MCCAMMON, C.: An experimental investigation of factors controlling the oxygen content of sulphide melts in the Earth's upper mantle. Contrib. Mineral. Petrol. (in press), https://doi.org/10.1007/s00410-023-01992-3

ASLANDUKOVA, A.; ASLANDUKOV, A.; LANIEL, D.; KHANDARKHAEVA, S.; STEINLE-NEUMANN, G.; FEDOTENKO, T.; OVSYANNIKOV, S.V.; YIN, Y.; IASMIN AKBAR, F.; GLAZYRIN, K.; HANFLAND, M.; DUBROVINSKY, L.; DUBROVINSKAIA, N.: High-pressure *hP*3 yttrium allotrope with $CaHg_2$-type structure as a prototype of the *hP*3 rare-earth hydride series. Phys. Rev. B (in press), https://doi.org/10.1103/PhysRevB.107.014103

AUDÉTAT, A.; SCHMITT, A.; NJUL, R.; HARRIS, M.; BORISOVA, A.; LU, Y.: New constraints on Ti diffusion in quartz and the priming of silicic volcanic eruptions. Nat. Commun. (submitted)

AUDÉTAT, A.: A plea for more skepticism towards fluid inclusions: part II. Homogenization via halite dissolution in brine inclusions from magmatic-hydrothermal systems is commonly the result of postentrapment modifications. Econ. Geol. (in press), https://doi.org/10.5382/econgeo.4974

ABEYKOON, S.; AUDÉTAT, A.: The single-crystal diamond trap (SCDT): a new method to determine the composition of high-P-T fluids. Contrib. Mineral. Petrol. (in press), https://doi.org/10.1007/s00410-021-01882-6

BALLANTYNE, H.A.; JUTZI, M.; GOLABEK, G.J.; MISHRA, L.; CHENG, K.W.; ROZEL, A.; TACKLEY, P.J.: Investigating the feasibility of an impact-induced Martian dichotomy. Icarus (in press), https://doi.org/10.1016/j.icarus.2022.115395

BONDAR, D.; WITHERS, A.C.; WHITTINGTON, A.; FEI, H.; KATSURA, T.: Dissolution mechanisms of water in depolymerized silicate (peridotitic) glasses based on infrared spectroscopy. Geochim. Cosmochim. Acta (in press), https://doi.org/10.1016/j.gca.2022.11.029

BUCHEN, J.; PARDO, O.; DOBROSAVLJEVIC, V.V.; STURHAHN, W.; ISHII, T.; CHARITON, S.; GREENBERG, E.; TOELLNER, T.S.; JACKSON, J.M.: Ferric iron controls water activity in Earth's lower mantle. Nature (submitted)

CHAKRABORTI, A.; CHO, Y.; SJAKSTE, J.; BAPTISTE, B.; HENRY, L.; GUIGNOT, N.; LE GODEC, Y.; VAST, N.: When carbon impurities trigger the synthesis of alpha boron at high pressure and high temperature. Acta Materialia (in press), https://doi.org/10.1016/j.actamat.2023.118820

CHANYSHEV, A.; FEI, H.; BONDAR, D.; WANG, B.; LIU, Z.; ISHII, T.; FARLA, R.; MCCAMMON, C.; KATSURA, T.: Ferric iron substitution mechanism in bridgmanite under SiO_2-saturated conditions at 27 GPa. ACS Earth and Space Chemistry (in press), https://doi.org/10.1021/acsearthspacechem.2c00326

CRINITI, G.; ISHII, T.; KURNOSOV, A.; GLAZYRIN, K.; HUSBAND, R.J.; BOFFA BALLARAN, T.: Structure and compressibility of Fe-bearing Al-phase D. Am. Mineral. (in press)

CRINITI, G.; ISHII, T.; KURNOSOV, A.; GLAZYRIN, K.; BOFFA BALLARAN, T.: High-pressure phase transition and equation of state of hydrous Al-bearing silica. Am. Mineral. (in press)

DI GENOVA, D.; BONDAR, D.; ZANDONÁ, A.; VALDIVIA, P.; AL-MUKADAM, R.; FEI, H.; WITHERS, A.C.; BOFFA BALLARAN, T.; KURNOSOV, A.; MCCAMMON, C.; DEUBENER, J.; KATSURA, T.: Viscosity of anhydrous and hydrous peridotite melts. Chem. Geol. (in press), https://doi.org/10.1016/j.chemgeo.2023.121440

FACCINCANI, L.; CRINITI, G.; KURNOSOV, A.; BOFFA BALLARAN, T.; WITHERS, A.C.; MAZZUCCHELLI, M.; NESTOLA, F.; COLTORTI, M.: Sound velocities and single-crystal elasticity of hydrous Fo90 olivine to 12 GPa. Phys. Earth Planet. Inter. (in press), https://doi.org/10.1016/j.pepi.2023.107011

GATTACCECA, J.; MCCUBBIN, F.; GROSSMAN, J.; BOUVIER, A.; CHABOT, N.L.; D'ORAZIO, M.; GOODRICH, C.; GRESHAKE, A.; GROSS, J.; KOMATSU, M.; MIAO, B.; SCHRADER, D.: The Meteoritical Bulletin, No. 110. Meteorit. Planet. Sci. (in press), https://doi.org/10.1111/maps.13918

HOUDE, V.; FLEMMING, R.L.; BOUVIER, A.; TERSKIKH, V.: Cation ordering in spinel from calcium-aluminium-rich inclusions in carbonaceous chondrites NWA 2364 and NWA 6991 to quantify temperature in the Early Solar System. Can. Mineral. (submitted)

HUANG, Y.; NAKATANI, T.; SAWA, S.; NAKAMURA, M.; MCCAMMON, C.: The effect of faceting on olivine wetting properties. Am. Mineral. (submitted)

ISHII, T.; CRINITI, G.; WANG, X.; GLAZYRIN, K.; BOFFA BALLARAN, T.: Synthesis and structure analysis of $CaFe_2O_4$-type single crystals in the $NaAlSiO_4$-$MgAl_2O_4$-Fe_3O_4 system. Am. Mineral. (in press), https://doi.org/10.2138/am-2022-8748

ISHII, T.; MCCAMMON, C.; KATSURA, T.: Iron and aluminum substitution mechanism in perovskite phase in the system $MgSiO_3$-$FeAlO_3$-MgO. Am. Mineral. (in press), https://doi.org/10.2138/am-2022-8457

KAWASAKI, N.; and the Hayabusa2 Initial Analysis Chemistry Team (63 members including BOUVIER, A.): Bimodal distribution of oxygen isotopic compositions in Ryugu and Ivuna anhydrous primary minerals. Sci. Adv. (submitted)

KISLYAKOVA, K.G.; NOACK, L.; SANCHIS, E.; FOSSATI, L.; VALYAVIN, G.G.; GOLABEK, G.J.; GÜDEL, M.: Induction heating of planetary interiors in white dwarf systems. Astron. Astrophys. (submitted)

LANIEL, D.; TRYBEL, F.; ASLANDUKOV, A.; KHANDARKHAEVA, S.; FEDOTENKO, T.; YIN, Y.; TASNÁDI, F.; PONOMAREVA, A.V.; WECK, G.; AKBAR, F.I.; WINKLER, B.; NÉRI, A.; CHARITON, S.; GIACOBBE, C.; WRIGHT, J.; GARBARINO, G.; WEHINGER, B.; PAKHOMOVA, A.; MEZOUAR, M.; PRAKAPENKA, V.; MILMAN, V.; SCHNICK, W.; ABRIKOSOV, I.A.; DUBROVINSKY, L.; DUBROVINSKAIA, N.: Synthesis of ultra-incompressible carbon nitrides featuring three-dimensional frameworks of CN_4 tetrahedra recoverable at ambient conditions. Nature (in press), https://doi.org/10.48550/arXiv.2209.01968

LANIEL, D.; TRYBEL, F.; YIN, Y.; FEDOTENKO, T.; KHANDARKHAEVA, S.; ASLANDUKOV, A.; ABRIKOSOV, A.I.; MASOOD, T.B.; GIACOBBE, C.; BRIGHT, E.L.; GLAZYRIN, K.; HANFLAND, M.; HOTZ, I.; ABRIKOSOV, I.A.; DUBROVINSKY, N.; DUBROVINSKAIA, N.: Aromatic hexazine $[N_6]^{4-}$ anion revealed in the complex structure of the high-pressure potassium nitride K_9N_{56}. Nat. Chem. (in press), https://doi.org/10.48550/arXiv.2112.09857

LIN, Y.; ISHII, T.; VAN WESTRENEN, W.; KATSURA, T.; MAO, H.K.: Extreme temperatures at the bottom of a reduced terrestrial magma ocean. Science (submitted)

LIU, D.; PUREVJAV, N.; FEI, H.; WITHERS, T.; YE, Y.; KATSURA, T.: Contribution of majorite to H_2O storage capacity in the transition zone and topmost lower mantle. JGR Solid Earth (submitted)

MARTIROSYAN, N.S.; EFTHIMIOPOULOS, I.; JAHN, S.; LOBANOV, S.S.; WIRTH, R.; REICHMANN, H.-J.; KOCH-MÜLLER, M.: High-pressure polymorphs of the ferroan dolomite: Possible host structures for carbon in the lower mantle. Am. Mineral. (submitted)

MELAI, C.; BOFFA BALLARAN, T.; UENVER-THIELE, L.; KURNOSOV, A.; CHUMAKOV, A.I.; BESSAS, D.; FROST, D.J.: Compressibilities along the magnetite-magnesioferrite solid solution. Phys. Chem. Minerals (in press), https://doi.org/10.1007/s00269-022-01217-2

MIYAJIMA, N.; BUCHEN, J.; KAWAZOE, T.: Twinning in hydrous wadsleyite: symmetry relations, origin, and consequences. Am. Mineral. (submitted)

MONNEREAU, M.; GUIGNARD, J.; NÉRI, A.; TOPLIS, M.J.; QUITTÉ, G.: Differentiation time scales of small rocky bodies. Icarus (in press), https://doi.org/10.1016/j.icarus.2022.115294

NATHAN, G.; RUBIE, D.C.; JACOBSON, S.A.: Constraining the origin of Mars with simulations of multi-stage core formation. Icarus (submitted)

NESTOLA, F.; REGIER, M.E.; LUTH, R.W.; PEARSON, D.G.; STACHEL, T.; MCCAMMON, C.; WENZ, M.D.; JACOBSEN, S.D.; ANZOLINI, C.; BINDI, L.; HARRIS, J.W.: Extreme redox gradients documented by a superdeep diamond and its implications for deep mantle hydration and metal saturation. Nature (in press)

NEUMANN, W.; MA, N.; BOUVIER, A.; TRIELOFF, M.: Temporally distributed parent body accretion in the high-^{54}Cr solar system region. Nat. Commun. (submitted)

ORIOLO, S.; SCHULZ, B.; HUECK, M.; OYHANTÇABAL, P.; HEIDELBACH, F.; SOSA, G.; VAN DEN KERKHOF, A.; WEMMER, K.; FOSSEN, H.; DRUGUET, E.; WALTER, CAVALCANTE, C.; J.; SIEGESMUND, S.: The petrologic and petrochronologic record of progressive vs polyphase deformation: Opening the analytical toolbox. Earth Sci. Rev. (in press), https://doi.org/10.1016/j.earscirev.2022.104235

OVSYANNIKOV, S.V.; KARKIN, A.E.; KOROBEYNIKOV, I.V.; MOROZOVA, N.V.; BYKOV, M.; BYKOVA, E.; WILHELM, F.; ROGALEV, A.; DUBROVINSKY, L.: Electronic properties of single-crystalline Fe_4O_5. Inorg. Chem. (submitted)

PAQUET, M.; and the Hayabusa2 Initial Analysis Chemistry Team (63 members including BOUVIER, A.): Copper and zinc isotopic fingerprints of the contribution of Ryugu to Earth's Volatile Inventory. Nat. Astron. (in press)

PAUL, J.; CONRAD, C.P.; BECKER, T.W.; GHOSH, A.: Convective self-compression of cratons and the stabilization of old lithosphere. Geophys. Res. Lett. (in press), https://doi.org/10.1029/2022GL101842

PUREVJAV, N.; TOMIOKA, N.; YAMASHITA, S.; SHINODA, K.; KOBAYASHI, S.; SHIMIZU, K.; ITO, M.; FU, S.; GU, J.; HOFFMANN, C.; LIN, J.-F.; OKUCHI, T.: Hydrogen incorporation mechanism in aluminous-ferrous bridgmanite. Am. Mineral. (submitted)

PUTAK JURICEK, M.; KEPPLER, H.: Amphibole stability, water storage in the mantle, and the nature of the lithosphere-asthenosphere boundary. Earth Planet. Sci. Lett. (in press), https://doi.org/10.1016/j.epsl.2023.118082

REGER, P.M.; RÖBBERT, Y.; NEUMANN, W.; GANNOUN, A.; REGELOUS, M.; SCHWARZ, W.H.; LUDWIG, T.; TRIELOFF, M.; WEYER, S.; BOUVIER, A.: Al-Mg and U-Pb chronological records of Erg Chech 002 ungrouped achondrite meteorite. Geochim. Cosmochim. Acta (in press), https://doi.org/10.1016/j.gca.2022.12.025

REYNARD, B.; FELLAH, C.; MCCAMMON, C.: Iron oxidation state in serpentines and magnesian chlorites of subduction-related rocks. Eur. J. Mineral. (in press), https://doi.org/10.5194/ejm-34-645-2022

ROGOWITZ, A.; THIELMANN, M.; KRAUS, K.; GRASEMANN, B.; RENNER, J.: The Effect of the garnet content on deformation mechanisms and weakening of eclogite: Insights from deformation experiments and numerical simulations. Geochem. Geophys. Geosyst. (in press), https://doi.org/10.1029/2022GC010743

SIERSCH, N.C.; CRINITI, G.; KURNOSOV, A.; GLAZYRIN, K.; ANTONANGELI D.: Thermal equation of state of Fe_3O_4 magnetite up to 16 GPa and 1100 K. Am. Mineral. (in press)

TANG, H.; and the Hayabusa2 Initial Analysis Chemistry Team (63 members including BOUVIER, A.): The oxygen isotopic composition of samples returned from asteroid Ryugu with implications for the aqueous alteration of planetesimals. Sci. Adv. (submitted)

TIRABOSCHI, C.; MCCAMMON, C.; ROHRBACH, A.; KLEMME, S.; BERNDT, J.; SANCHEZ-VALLE, C.: Preferential mobilization of oxidized iron by slab-derived hydrous silicate melts. Geochem. Persp. Lett. (in press), https://doi.org/10.7185/geochemlet.2304

VASIUKOV, D.M.; KHANAL, G.; KUPENKO, I.; APRILIS, G.; OVSYANNIKOV, S.V.; CHARITON, S.; CERANTOLA, V.; POTAPKIN, V.; CHUMAKOV, A.I.; DUBROVINSKY, L.; HAULE, K.; BLACKBURN, E.: Symmetry protected 1D chains in mixed-valence iron oxides. Nat. Commun. (in press), https://doi.org/10.48550/arXiv.2207.14111

WANG, F.; THOMPSON, E.C.; ZHANG, D.; XU, J.; ALP, E.E.; JACOBSEN, S.D.: Hydrous wadsleyite crystal structure up to 32 GPa. Am. Mineral. (in press), https://doi.org/10.2138/am-2022-8380

WANG, L.; LIU, Z.; KOIZUMI, S.; BOFFA BALLARAN, T.; KATSURA, T.: Aluminum components in bridgmanite coexisting with corundum and CF-phase with temperature. JGR Solid Earth (in press), https://doi.org/10.1029/2022JB025739

WOODLAND, A.B.; UENVER-THIELE, L.; BOFFA BALLARAN, T.; MIYAJIMA, N.; ROSBACH, K.; ISHII, T.: Stability of Fe_5O_6 and its relation to other Fe-Mg-oxides at high pressures and temperatures. Am. Mineral. (in press), https://doi.org/10.2138/am-2022-8370

WU, J.; LI, H.; MATHUR, R.; BOUVIER, A.; POWELL, W.; YONEZU, K.; ZHU, D.: Compositional variation and Sn isotope fractionation of cassiterite during magmatic-hydrothermal process. Geochim. Cosmochim. Acta (submitted)

ZHANG, B.; LIN, Y.; HAO, J.; SCHRADER, D.L.; WADHWA, M.; KOROTEV, R.L.; HARTMANN, W.K.; BOUVIER, A.: SIMS U-Pb dating of micro-zircons in the lunar meteorites Dhofar 1528 and Dhofar 1627. Moderate revisions, Meteorit. Planet. Sci. (submitted)

ZHANG, D.; AUDÉTAT, A.: A plea for more skepticism towards fluid inclusions: part (I). Postentrapment changes in fluid density and fluid salinity are very common. Econ. Geol. (in press), https://doi.org/10.5382/econgeo.4966

4.3 Presentations at scientific institutions and at congresses

ASLANDUKOV, A.; ASLANDUKOV, M.; DUBROVINSKAIA, N.; DUBROVINSKY, L.: 07.-09.02.2022, ESRF user meeting 2022, Grenoble, France: "Domain Auto Finder (DAFi) program: the analysis of single-crystal X-ray diffraction data from polycrystalline samples"

ASLANDUKOV, A.; ASLANDUKOV, M.; DUBROVINSKAIA, N.; DUBROVINSKY, L.: 25.-26.06.2022, 1st IUCr Diffraction Microstructure Imaging Workshop, Washington D.C., USA: "Domain Auto Finder (DAFi) program: the analysis of single-crystal X-ray diffraction data from polycrystalline samples"

ASLANDUKOV, A.; ASLANDUKOV, M.; DUBROVINSKAIA, N.; DUBROVINSKY, L.: 06.-10.12.2022, IUCr High-pressure Workshop 'Advanced High-Pressure Crystallography', Chicago, USA: "Domain Auto Finder (DAFi) program: the analysis of single-crystal X-ray diffraction data from polycrystalline samples"

AUDÉTAT, A.: 24.06.2022, GeoTag 2022, Aachen, Germany: "Magmatic-hydrothermal fluids"

BONDAR, D.; WITHERS, A.; FEI, H.; DI GENOVA, D.; ZANDONÀ, A.; MIYAJIMA, N.; KATSURA, T.: 12.-16.12.2022, AGU Fall Meeting 2022, Chicago, USA: "Speciation and effect of water on hydrous peridotitic glasses quenched by a novel rapid-quench multianvil technique"

BOUVIER, A. 06.07.2022, Goethe-Universität Frankfurt/M., Colloquium Series, Institut für Geowissenschaften, Frankfurt/M., Germany (*invited*): "Making Earth: A recipe from meteorites?"

BOUVIER, A.: 11.-15.09.2022, GeoMinKöln 2022, Köln, Germany (*keynote*): "Building Earth"

BOUVIER, A.: 07.-13.11.2022, Forming and Exploring Habitable Worlds, Edinburgh, U.K. (*keynote*): "Making Earth"

BOUVIER, A.: 14.-18.11.2022, Earth's History, Dynamics and Planetary Habitability, University of Oslo, Norway (*keynote*): "Making Earth"

BYKOVA, E.: 25.-26.06.2022, Diffraction Microstructure Imaging Workshop, Washington DC, USA (*virtual*): "Applying methods of high-pressure crystallography in studies of earth-related and technology-relevant materials"

BYKOVA E.: 23.-27.08.2022, 33rd European Crystallography Meeting, Versailles, France: "Chemical versatility of iron oxides at extreme pressures and temperatures"

BYKOVA, E.: 28.-30.09.2022, 10th Joint Workshop on High Pressure, Planetary and Plasma Physics (HP4), Brussels, Belgium: "Chemical versatility of iron oxides at extreme pressures and temperatures"

CHAKRABORTI, A.; JAY, A.; HARDOUIN DUPARC, O.; SJAKSTE, J.; PARISIADIS, P.; GARBARINO, G.; BÉNEUT, K.; VAST, N.; LE GODEC, Y.: 17.-22.07.2022, Research at High Pressure Gordon Research Conference, Holderness, USA: "Superhard boron carbide: New insights into dynamic anomalous failure and how to reinforce it"

CHAKRABORTI, A.; JAY, A.; HARDOUIN DUPARC, O.; SJAKSTE, J.; PARISIADIS, P.; GARBARINO, G.; BÉNEUT, K.; VAST, N.; LE GODEC, Y.: 05.-09.09.2022, 21st International Symposium on Boron, Borides and related materials (ISBB2022), Paris, France: " Superhard boron carbide: New insights into dynamic anomalous failure and how to reinforce it"

CHANG, J.; AUDÉTAT; A.: 22.-27.05.2022, Geochemistry of Mineral Deposits Gordon Research Conference, Barcelona, Spain: "Post-subduction porphyry Cu magmas formed by fractionation of lithospheric mantle-derived mafic magmas"

CHANG, J.; AUDÉTAT; A.: 05.-09.09.2022, International School on Understanding Oxygen Fugacity in Geoscience, Trieste, Italy: "Experimental crystallization of potassic mafic magmas at 1.0 GPa: Implications for the origin and volatile contents of post-subduction porphyry Cu magmas"

CHANG, J.; AUDÉTAT; A.: 11.-15.09.2022, GeoMinKöln 2022, Köln, Germany: "On the genesis of post-subduction porphyry copper magmas"

CHANYSHEV, A.; ISHII, T.; BONDAR, D.; BHAT, S.; KIM, E.J.; FARLA, R.; NISHIDA, K.; LIU, Z.; WANG, L.; NAKAJIMA, A.; YAN, B.; TANG, H.; CHEN, Z.; HIGO, Y.; TANGE, Y.; KATSURA, T.: 23.-27.05.2022, EGU General Assembly 2022, Wien, Austria & online: "Depressed 660-km seismic discontinuity beneath cold subduction zones caused by akimotoite-bridgmanite phase transition", EGU22-5045

COMODI, P.; ZUCCHINI, A.; MCCAMMON, C.; FASTELLI, M.; BOFFA-BALLARAN, T.: 18.-22.07.2022, 23rd General Meeting of the International Mineralogical Association (IMA 2022), Lyon, France: "Cation disorder in thermally treated ankerites"

CRINITI, G.; KURNOSOV, A.; GLAZYRIN, K.; HUSBAND, R.J.; LIU, Z.; BOFFA BALLARAN, T.; FROST, D.J.: 24.01.2022, Satellite workshop of the DESY Photon Science Users' Meeting 2022 on Status and research high-lights of the ECB (P02.2) at PETRA III (*invited*): "Effect of $AlAlO_3$ and $MgAlO_{2.5}$ incorporation on the equation of state of $MgSiO_3$ bridgmanite"

CRINITI, G.; KURNOSOV, A.; GLAZYRIN, K.; HUSBAND, R.; LIU, Z.; BOFFA BALLARAN, T.; FROST, D.J.: 23.-27.08.2022, 33rd European Crystallography Meeting, Versailles, France: "Crystal structure and equation of state of Al-bearing bridgmanite at high pressure and high temperature"

CRINITI, G.; ISHII, T., KURNOSOV, A.; GLAZYRIN, K.; BOFFA BALLARAN, T.: 18.-22.07.2022, 23rd General Meeting of the International Mineralogical Association (IMA 2022), Lyon, France: "High-pressure phase transition and equation of state of hydrous Al-bearing silica"

CRINITI, G.; KURNOSOV, A.; BOFFA BALLARAN, T.; FROST, D.J.: 18.-22.07.2022, 23rd General Meeting of the International Mineralogical Association (IMA 2022), Lyon, France (*invited*): "Single-crystal elasticity of $MgSiO_3$ bridgmanite to mid-lower mantle pressure"

CZEKAY, L.; MIYAJIMA, N.; MCCAMMON, C.; FROST, D.: 11.-15.09.2022, GeoMinKöln 2022, Köln, Germany: "Al, Si interdiffusion in Al-bearing bridgmanite under lower mantle conditions: Analytical TEM study"

CZEKAY, L.; MIYAJIMA, N.; MCCAMMON, C.; FROST, D.: 11.-15.09.2022, GeoMinKöln 2022, Köln, Germany: "Earth's lower mantle may be harder than expected: Al, Si diffusion in bridgmanite"

DOLINSCHI, J.; NERI, A.; MAN, L.; FROST, D.J.: 25.01.2022, DESY Photon Science Users' Meeting 2022, Satellite Workshop '*In situ* studies at extreme conditions using the LVP at P61B', virtual: "Novel method of measuring *in situ* stress of deformation experiments using piezoelectric effect"

DOLINSCHI, J.; NERI, A.; MAN, L.; FROST, D.J.: 18.-22.07.2022, 23rd General Meeting of the International Mineralogical Association (IMA 2022), Lyon, France: "*In situ* stress measurement in a large anvil press utilizing a piezoelectric crystal"

DUBROVINSKY, L.: 07.-09.06.2022, The 5th International Conference on Matter and Radiation at Extremes (ICMRE), virtual: "High-pressure chemical crystallography: From mineral physics to material sciences"

DUBROVINSKY, L.: 06.-10.12.2022, IUCr High-pressure Workshop 'Advanced High-Pressure Crystallography', Chicago, USA: "High-pressure chemical crystallography and it application in mineral physics"

FACCINCANI, L.; CRINITI, G.; KURNOSOV, A.; BOFFA BALLARAN, T.; WITHERS, A.C.; MAZZUCCHELLI, M.; NESTOLA, F.: 19.-21.09.2022, SGI-SIMP Congress, Turin, Italy: "Sound velocities and single-crystal elasticity of hydrous Fo90 olivine to 12 GPa"

FACCINCANI, L.; CRINITI, G.; KURNOSOV, A.; BOFFA BALLARAN, T.; WITHERS, A.C.; MAZZUCCHELLI, M.; NESTOLA, F.; COLTORTI, M.: 12.-15.09.2022, 4th Earth Mantle Workshop (EMAW), Toulouse, France: "Effect of OH^- incorporation on the elastic properties and sound wave velocities of Fo90 olivine"

FANG, L.; FROSSARD, P.; BOYET, M.; BOUVIER, A.; BARRAT, J.-A.; CHAUSSIDON, M.; MOYNIER, F.: 14-19.08.2022, 85th Annual Meeting of Meteoritical Society, Glasgow, U.K.: "Half-life and initial Solar System abundance of ^{146}Sm determined from the oldest andesitic meteorite"

FEI, H.: 10.-15.07.2022, Goldschmidt 2022, Honolulu, USA (*invited*): "Water content in hydrous silicate melt at the topmost lower mantle conditions"

FEI, H.: 18.-19.07.2022, International conference on 'Physics under Synergetic Extreme Conditions', Jilin University, Jilin, P.R. China: "Bridgmanite grain size variation accounts for the mid-mantle viscosity jump"

FROST, D.; MELAI, C.; MCCAMMON, C.; BOFFA BALLARAN, T.; MIYAJIMA, N.; HUANG, R.: 10.-15.07.2022, Goldschmidt 2022, Honolulu, USA: "The ferric iron contents of lower mantle minerals and their use in the determination of deep diamond formation conditions"

FROST, D.; MELAI, C.; CRINITI, G.; HUANG, R.; KURNOSOV, A.; BOFFA BALLARAN, T.; MCCAMMON, C.: 17.06.2022, Oxford University, Department of Earth Sciences, Oxford, U.K.: "The composition of the lower mantle and processes leading to deep mantle diamond formation"

FROST, D.: 05.-09.09.2022, International School on Understanding Oxygen Fugacity in Geoscience, Trieste, Italy: "Oxidation state of the Earth from the core to the mantle transition zone"

FUKUSHIMA, R.; TSUJIMORI, T.; MIYAJIMA, N.: 22.-27.05.2022 Japan Geoscience Union Meeting 2022, Chiba, Japan: "Toward an understanding of fluid-induced growth of oscillatory-zoned garnets in Group-C eclogites: Temporal constraints from nanoscale cation-diffusion modeling"

FUKUSHIMA, R.; TSUJIMORI, T.; MIYAJIMA, N.: 10.-13.07.2022, 14th International Eclogite Conference (IEC-14), Lyon, France: “Cryptic chemical heterogeneity in omphacite: FIB-STEM analysis of antiphase domains in garnet-hosted omphacite from Syros, Greece"

FUKUSHIMA, R.; TSUJIMORI, T.; MIYAJIMA, N.: 18.-22.07.2022, 23rd General Meeting of the International Mineralogical Association (IMA 2022), Lyon, France: "Constraints from garnet-hosted omphacite: FIB-STEM analysis of compositional heterogeneity"

GOLABEK, G.J.; GILLMANN, C.; RAYMOND, S.; SCHÖNBÄCHLER, M.; TACKLEY, P.J.; DEHANT, V.; DEBAILLE, V.: 17.11.2022, University of Groningen, The Netherlands: "Clues on late accretion from Venus' coupled atmosphere and internal evolution"

GOLABEK, G.J.; LICHTENBERG, T.; TACKLEY, P.J.: 30.08.-02.09.2022, Ada Lovelace Workshop on Mantle and Lithosphere Dynamics, Hévíz, Hungary: "Magma oceanography of the dense, ultrashort-period sub-Earth GJ 367b"

GOLABEK, G.J.; WALTE, N.P.; SOLFERINO, G.F.D.; NIMMO, F.; SCHMIDT, M.W.: 22.06.2022, Museum für Naturkunde Berlin, Germany:"Impact origin of pallasite meteorites"

GOLABEK, G.J.; LICHTENBERG, T.; GERYA, T.V.; MEYER, M.R.; BURN, R.; ALIBERT, Y.; MORDASINI, C.: 20.05.2022, ETH Zurich, Switzerland: "Desiccation in the early solar system and beyond"

GOLABEK, G.J.; GILLMANN, C.; RAYMOND, S.; SCHÖNBÄCHLER, M.; TACKLEY, P.J.; DEHANT, V.; DEBAILLE, V.: 17.01.2022, FU Berlin, Germany: "Clues on late accretion from Venus' coupled atmosphere and internal evolution"

HIN, R.C.: 11.-15.09.2022, GeoMinKöln 2022, Köln, Germany (*keynote*): "Isotopic fractionation during planetary-scale processes"

ISHII, T.; CRINITI, G.; OHTANI, E.; PUREVJAV, N.; FEI, H.; KATSURA, T.; MAO, H.-K.: 22.-27.05.2022 Japan Geoscience Union Meeting 2022, Chiba, Japan: "Water solubility of aluminous post-stishovite at top lower mantle conditions: Implications for water cycle in the deep mantle", SIT20-01

ISHII, T.; CRINITI, G.; MIYAJIMA, N.; KURNOSOV, A.; SIERSCH, N.; GLAZYRIN, K.; BOFFA BALLARAN, T.: 22.-27.05.2022 Japan Geoscience Union Meeting 2022, Chiba, Japan: "Crystal chemistry and compressibility of Fe^{2+}- and oxygen vacancy-rich aluminous bridgmanite: Implications for lower mantle structure and dynamics", SMP26-01

ISHII, T.; CHANYSHEV, A.; BONDAR, D.; BHAT, S.; KIM, E.J.; FARLA, R.; NISHIDA, K.; LIU, Z.; WANG, L.; NAKAJIMA, A.; YAN, B.; TANG, H.; CHEN, Z.; HIGO, Y.; TANGE, Y.; KATSURA, T.: 15.-19.07.2022, The 1st International Conference on Physics under Synergetic Extreme Conditions and SECUF-2022, Beijing and Changchun, P.R. China: "A new approach determining a phase transition boundary strictly based on a defintion of phase equilibrium by means of *in situ* multianvil technique"

ISHII, T.; CHANYSHEV, A. KATSURA, T.: 12.-16.12.2022, AGU Fall Meeting 2022, Chicago, USA: "A new approach determining an accurate and precise phase transition boundary strictly based on a definition of phase equilibrium by means of *in situ* multianvil technique"

KATSURA, T.: 25.01.2022, DESY Photon Science Users' Meeting 2022, Satellite Workshop '*In situ* studies at extreme conditions using the LVP at P61B', virtual: "Recent progress and future plan of multianvil *in situ* X-ray diffraction experiments at P61B by the BGI UltraLVP group"

KATSURA, T.: 20.-24.03.2022, ACS Spring 2022, virtual & San Diego, USA: "Accurate determination of the akimotoite-bridgmanite transition and dissociation of ringwoodite to bridgmanite plus periclase and a new interpretation for the depression of the 660-km discontinuity under cold subduction zones"

KATSURA, T.: 01.06.2022, University of Lille, TimeMan Seminar, Lille, France: "Accurate determination of the akimotoite-bridgmanite transition and dissociation of ringwoodite to bridgmanite plus periclase and a new interpretation for the depression of the 660-km discontinuity under cold subduction zones"

KATSURA, T.: 11.07.2022, Zhejiang University, Graduate School of Geoscience 2022 Summer Semester Online Lecture by Leading Overseas Scholars, Hangzhou, P.R. China: "Overview of the structure and dynamics of the Earth's lower mantle"

KATSURA, T.: 15.-19.07.2022, The 1st International Conference on Physics under Synergetic Extreme Conditions and SECUF-2022, Beijing and Changchun, P.R. China: "Recent development of Kawai-type multianvil technology by the UltraLVP group at the University of Bayreuth"

KATSURA, T.: 22.07.2022, The University of Tokyo, Geochemical Research Center, Tokyo, Japan: "A rapid quench technique for multianvil experiments and its applications"

KATSURA, T.: 26.07.2022, The University of Tokyo, Department of Earth and Planetary Science, Tokyo, Japan: "Accurate determination of the akimotoite-bridgmanite transition and dissociation of ringwoodite to bridgmanite plus periclase and a new interpretation for the depression of the 660-km discontinuity under cold subduction zones"

KATSURA, T.: 03.08.2022, Graduate School of Science, Osaka University, Toyonaka, Japan: "Accurate determination of the akimotoite-bridgmanite transition and dissociation of ringwoodite to bridgmanite plus periclase and a new interpretation for the depression of the 660-km discontinuity under cold subduction zones"

KATSURA, T.: 21.09.2022, Center for High Pressure Science and Technology Advanced Research (HPSTAR), Shanghai, P.R. China: "Accurate determination of the akimotoite-bridgmanite transition and dissociation of ringwoodite: a new interpretation for the depression of the 660-km discontinuity"

KATSURA, T.: 28.09.2022, Center for High Pressure Science and Technology Advanced Research (HPSTAR), Beijing, P.R. China: "Determination of the H_2O-content dependence on the dislocation mobility in olivine by means of the dislocation recovery technique"

KATSURA, T.: 30.09.2022, Center for High Pressure Science and Technology Advanced Research (HPSTAR), Beijing, P.R. China: "Some recent developments of multianvil technology"

KATSURA, T.; WANG, L.; CHANYSHEV, A.; MIYAJIMA, N.; KAWAZOE, T.; BLAHA, S.: 06.-10.12.2022, IUCr High-pressure Workshop 'Advanced High-Pressure Crystallography', Chicago, USA: "Determination of the H_2O-content dependence on the dislocation mobility in olivine by means of the dislocation recovery technique"

KATSURA, T.; FEI, H.; ISHII, T.; LIU, Z.; BONDAR, D.; ZAREI, A.; NISHIDA, K.; CHANYSHEV, A.; LI, Y.; WITHERS, A.; MIYAJIMA, N.; MYHILL, R.; BHAT, S.; FARLA, R.; TANGE, Y.; HIGO, Y.: 12.-16.12.2022, AGU Fall Meeting 2022, Chicago, USA: "Recent developments of large-volume multianvil technologies for advanced high-pressure/-temperature research"

KATSURA, T.; WANG, L.; CHANYSHEV, A.; MIYAJIMA, N.; KAWAZOE, T. BLAHA, S.: 12.-16.12.2022, AGU Fall Meeting 2022, Chicago, USA: "Enhancement of olivine dislocation mobility by H_2o incorporation determined by the dislocation recovery technique: negligible hydrous weakening and H_2o-induced fabric transition in the asthenosphere"

KATSURA, T.: 13.-15.12. 2022, The 63rd High Pressure Conference of Japan, Ibaraki, Japan: "Development of experimental technologies of multianvil high-pressure apparatus and its application to geophysics"

KEPPLER, H.: 28.-31.03.2022, Dynamics of Ore Metal Enrichment, SPP 2238 General Assembly, Goslar, Germany: "Cassiterite solubility, tin partitioning, and the origin of porphyry tin deposits"

KEPPLER, H.: 04.-06.07.2022, Magma and Fluids Workshop, Orleans, France: "Magma degassing and crystallization as seen in a moissanite cell"

KUBIK, E.; SOSSI, P.; NERI, A.; BOUVIER, A.: 10.-15.07.2022, Goldschmidt 2022, Honolulu, USA: "Iron isotopic fractionation between core and mantle in large terrestrial planets"

KUBIK, E.; SOSSI, P.; NERI, A.; BOUVIER, A.: 18.-22.07.2022, 23rd General Meeting of the International Mineralogical Association (IMA 2022), Lyon, France: "Iron isotopic fractionation between core and mantle in large terrestrial planets"

KURNOSOV, A.; CRINITI, G.; BOFFA BALLARAN, T.; WITHERS, A.C.; FROST, D.J.; MARQUARDT, H.: 18.-22.07.2022, 23rd General Meeting of the International Mineralogical Association (IMA 2022), Lyon, France: "High-pressure/high-temperature Brillouin scattering measurements of pyrope single crystal"

LI, X.; BYKOVA, E.; APRILIS, G.; VASIUKOV, D.; CHARITON, S.; CERANTOLA, V.; BYKOV, M.; PAKHOMOVA, A.; AKBAR, F.; MUKHINA, E.; COMBONI, D.; MCCAMMON, C.; CHUMAKOV, A.; SANCHEZ-VALLE, C.; DUBROVINSKY, L.; KUPENKO, I.: 11.-15.09.2022, GeoMinKöln 2022, Köln, Germany: "Complex electronic, magnetic, and structural transformations in FeO"

LIBON, L.; SPIEKERMANN, G.; SIEBER, M.; KAA, J.; DOMINIJANNI, S.; ELBERS, M.; BLANCHARD, I.; ALBERS, C.; BIERDERMANN, N.; MORGENROTH, W.; APPEL, K.; MCCAMMON, C.; SCHREIBER, A.; RODDATIS, V.; GLAZYRIN, K.; HUSBAND, R.; HENNET, L.; WILKE, M.: 23.-27.05.2022, EGU General Assembly 2022, Wien, Austria & online: "Subducted carbon in the Earth's lower mantle: The fate of magnesite", EGU22-9318

LIBON, L.; SPIEKERMANN, G.; SIEBER, M.; KAA, J.; DOMINIJANNI, S.; ELBERS, M.; BLANCHARD, I.; ALBERS, C.; BIERDERMANN, N.; MORGENROTH, W.; APPEL, K.; MCCAMMON, C.; SCHREIBER, A.; RODDATIS, V.; GLAZYRIN, K.; HUSBAND, R.; HENNET, L.; WILKE, M.: 18.-22.07.2022, 23rd General Meeting of the International Mineralogical Association (IMA 2022), Lyon, France: "The fate of subducted magnesite in the Earth's lower mantle"

MARRAS, G.; MIKHAILENKO, D.; DOMINIJANNI, S.; LOGVINOVA, A.; MCCAMMON, C.A.; STAGNO, V.: 18.-22.07.2022, 23rd General Meeting of the International Mineralogical Association (IMA 2022), Lyon, France: "Iron oxidation state in garnet and clinopyroxene inclusions in E-type diamonds from Udachnaya"

MARRAS, G.; MIKHAILENKO, D.; DOMINIJANNI, S.; LOGVINOVA, A.; MCCAMMON, C.; STAGNO, V.: 05.-09.09.2022, International School on Understanding Oxygen Fugacity in Geoscience, Trieste, Italy: "Investigation of Fe oxidation state in mineral inclusions in Siberian E-type diamonds: implications for the redox state of Archean oceanic crust and diamond formation"

MCCAMMON, C.: 23.-27.05.2022, EGU General Assembly 2022, Wien, Austria & online: "Towards an academic evaluation system that celebrates diversity of talent"

MCCAMMON, C.: 07.-08.07.2022, Final meeting of DFG FOR2125/2, Wehrheim, Germany: "Oxygen fugacity in the diamond anvil cell and implications for carbonate stability in the mantle"

MCCAMMON, C.: 05.-09.09.2022, International School on Understanding Oxygen Fugacity in Geoscience, Trieste, Italy: "The oxidation state of Fe through Mössbauer spectroscopy"

MCCAMMON, C.; CERANTOLA, V.: 05.-09.09.2022, International School on Understanding Oxygen Fugacity in Geoscience, Trieste, Italy: "Data processing in Mössbauer spectroscopy"

MCCAMMON, C.: 12.-15.09.2022, 4th Earth Mantle Workshop (EMAW), Toulouse, France: "Earth's volatile cycles - past, present and future"

MELAI, C.; FROST, D.J.; BOFFA BALLARAN, T. MARQUARDT, K.; MCCAMMON, C.: 05.-09.09.2022, International School on Understanding Oxygen Fugacity in Geoscience, Trieste, Italy: "The oxygen fugacity of sublithospheric diamond formation and the conditions encountered during their ascent to the surface"

MIYAJIMA, N.; CALVO, L.M.; BOFFA BALLARAN, T.; RUSTIONI, G.: 11.-15.09.2022, GeoMinKöln 2022, Köln, Germany: "Diffraction intensities of ordered omphacite, measured from precession electron diffraction"

NÉRI, A.; MAN, L.; BOFFA BALLARAN, T.; FROST, D.J.; CHANTEL, J.; FARLA, R.: 25.01.2022, 25.01.2022, DESY Photon Science Users' Meeting 2022, Satellite Workshop '*In situ* studies at extreme conditions using the LVP at P61B', virtual: "Setting up ultrasonic interferometry on P61B – Preliminary results on olivine-sulfide melt aggregates"

NÉRI, A.; GUIGNARD, J.; MONNEREAU, M.; TOPLIS, M.; QUITTÉ, G.: 28.02.2022, Université de Lille, Unité Matériaux et Transformation – UMET, Lille, France: "Metal-silicate differentiation of primitive achondrites: a multidisciplinary approach"

NÉRI, A.; GUIGNARD, J.; MONNEREAU, M.; TOPLIS, M.; QUITTÉ, G.: 28.02.2022, Centre de Recherche Pétrographiques et Géochimiques – CRPG, Nancy, France: "Metal-silicate differentiation of primitive achondrites: a multidisciplinary approach"

NÉRI, A.; MAN, L.; BOFFA BALLARAN, T.; FROST, D.J.; CHANTEL, J.; FARLA, R.: 01.03.2022, Université de Lille, Unité Matériaux et Transformation – UMET, Lille, France: "Setting up ultrasonic interferometry at BGI and DESY – Preliminary results on olivine-sulfide melt aggregates"

NÉRI, A.; MAN, L.; BOFFA BALLARAN, T.; FROST, D.; CHANTEL, J.; FARLA, R.: 13.-17.06.2022, 13^{e} Forum des technologies Hautes Pressions, Blériot-Plage (Pas-de-Calais), France: "Ultrasonic interferometry at BGI and on the beamline P61B (DESY): Development of internal pressure standards for in-house elastic wave velocity measurements"

NÉRI, A.; CHANYSHEV, A.; FARLA, R.; BHAT, S.; SONNTAG, S.; MA, S.; SPEKTOR, K.: 13.-17.06.2022, 13^{e} Forum des technologies Hautes Pressions, Blériot-Plage (Pas-de-Calais), France: "Extreme conditions in the large-volume press at the beamline P61B (DESY)

NÉRI, A.; MAN, L.; BOFFA BALLARAN, T.; FROST, D.J.; CHANTEL, J.; FARLA, R.: 18.-22.07.2022, 23rd General Meeting of the International Mineralogical Association (IMA 2022), Lyon, France: "Development of internal pressure standards for in-house elastic wave velocity measurements"

NEUMANN, W.; TRIELOFF, M.; MA, N.; BOUVIER, A.: 10.-15.07.2022, Goldschmidt 2022, Honolulu, USA: "The origin of Ryugu in the context of modeling and chronology based CC parent body accretion timing"

NEUMANN, W.; TRIELOFF, M.; MA, N.; BOUVIER, A.: 18-23.09.2022, Europlanet Science Congress 2022, Granada, Spain: "Temporally distributed accretion of chondritic and differentiated meteorite parent bodies in the C reservoir of the early solar system"

PAUL, J.; GOLABEK, G.; ROZEL, A.; TACKLEY, P.; KATSURA, T.; FEI, H.: 12.-16.12.2022, AGU Fall Meeting 2022, Chicago, USA: "Modeling Earth's mantle evolution using olivine and bridgmanite grain growth parameters"

PAUL, J.; CONRAD, C.P.; BECKER, T.; GHOSH, A.: 12.-16.12.2022, AGU Fall Meeting 2022, Chicago, USA: "Self-induced craton compression: Potential implications for craton stability"

PAUL, J.; GOLABEK, G.; ROZEL, A.; TACKLEY, P.; KATSURA, T.; FEI, H.: 30.08.-02.09.2022, Ada Lovelace Workshop on Mantle and Lithosphere Dynamics, Hévíz, Hungary: "Effect of heterogeneous grain-growth in Earth's mantle"

PAUSCH, T.; VAZHAKUTTIYAKAM, J.; WITHERS, A.C.; LUDWIG, T.; JOACHIM-MROSKO, B.; KONZETT, J.: 10.-15.07.2022, Goldschmidt 2022, Honolulu, USA: "Ca-phosphates in the deep Earth: Phase stability and volatile incorporation of tuite, γ-$Ca_3(PO_4)_2$"

PAUSCH, T.; VAZHAKUTTIYAKAM, J.; WITHERS, A.C.; LUDWIG, T.; JOACHIM-MROSKO, B.; KONZETT, J.: 11.-15.09.2022, GeoMinKöln 2022, Köln, Germany: "The stability of Tuite [γ-$Ca_3(PO_4)_2$] in peridotitic bulk systems and its significance for volatile and trace element transport into the deep Earth"

PICCOLO, A.; THIELMANN, M.: 23.-27.05.2022, EGU General Assembly 2022, Wien, Austria & online: "Controls on slab detachment and subsequent topography evolution", EGU22-7483

PICCOLO, A.; THIELMANN, M.: 12.10.-14.10.2022, 6th Annual AlpArray Scientific Meeting, Prague, Czech Republik: "The upper mantle controls on the slab detachment process and its surface expressions"

PÖPPELBAUM, M.; NÉRI, A.; FROST, D.J.: 21.-22.10.2022, Joint Meeting of the DMG Sections Geochemistry, Petrology & Petrophysics, Mainz, Germany: "The diffusivity of water in mantle minerals under subduction zone conditions"

POHLNER, J.E.; EL KORH, A.; CHIARADIA, M.; MCCAMMON, C.; RUBATTO, D.; KLEMD, R.; GROBÉTY, B.: 11.-15.09.2022, GeoMinKöln 2022, Köln, Germany: "Iron and oxygen isotope fractionation between eclogite minerals of the Münchberg Massif (Germany)"

PUREVJAV, N.; TOMIOKA, N.; YAMASHITA, S.; SHINODA, K.; KOBAYASHI, S.; SHIMIZU, K.; ITO, M.; FU, S.; GU, J.; HOFFMANN, C.; LIN, J.-F.; OKUCHI, T.: 17.-19.09.2022, The 2022 Annual Meeting of Japan Association of Mineralogical Sciences (JAMS), Niigata, Japan & online: "Superhydrous aluminous silica phases as major water hosts in high-temperature lower mantle"

STEWART, A.G.; HARTLEY, M.E.; JONES, R.H.; MCCAMMON, C.A.; NEAVE, D.N.: 05.-09.09.2022, International School on Understanding Oxygen Fugacity in Geoscience, Trieste, Italy: "Clinopyroxene Fe-oxybarometry in magmatic systems"

THIELMANN, M.; DURETZ, T.: 28.01.2022, Njord Seminar, University of Oslo, Norway: "Ductile deep earthquakes – a numerical perspective"

THIELMANN, M.; SCHMALHOLZ, S.: 07.-13.03.2022, 19th Symposium on 'Tectonics, Structural Geology and Crystalline Geology' (TSK 19), Halle/Saale, Germany: "Contributions of grain damage, thermal weakening and necking to slab detachment"

THIELMANN, M.; DURETZ, T.: 23.-27.05.2022, EGU General Assembly 2022, Wien, Austria & online: "Crushed and fried: Ductile rupture at depth due to grain size reduction and shear heating", EGU22-11762

THIELMANN, M.; DURETZ, T.: 22.11.2022, ENS Paris, Seminaire du Laboratoire de Géologie, Paris, France: "Ductile deep earthquakes – a numerical perspective"

UENVER-THIELE, L.; WOODLAND, A.; MIYAJIMA, N.; BOFFA BALLARAN, T.: 18.-22.07.2022, 23rd General Meeting of the International Mineralogical Association (IMA 2022), Lyon, France: "High-P phase relations of Al-bearing Fe_3O_4: Implications for natural occurrence in diamond"

VALDIVIA, P.; BOFFA BALLARAN, T.; KURNOSOV, A.; ZANDONA, A.; DEUBENER, J.; DI GENOVA, D.: 29.09.-01.10.2022, 5a Conferenza A. Rittmann 2022, Catania, Italy: "Viscosity of Stromboli magmas: are melts less viscous than we thought?"

VAZHAKUTTIYAKAM, J.; PAUSCH, T.; WITHERS, A.C.; JOACHIM-MROSKO, B.; KONZETT, J.: 11.-15.09.2022, GeoMinKöln 2022, Köln, Germany: "Experimental investigation of tuite stability in peridotite bulk and its role in the Earth's phosphorus cycle"

WANG, F.; FEI, H.; WANG, L.; MCCAMMON, C.; FROST, D.; KATSURA, T.: 12.-16.12.2022, AGU Fall Meeting 2022, Chicago, USA: "$Fe^{3+}/\sum Fe$ in bridgmanite decreases with increasing temperature at upper lower mantle conditions"

WOODLAND, A.; UENVER-THIELE, L.; BOFFA BALLARAN, T.; MIYAJIMA, N.; ROSBACH, K.; ISHII, T.: 18.-22.07.2022, 23rd General Meeting of the International Mineralogical Association (IMA 2022), Lyon, France: "The stability of Fe_5O_6 and $(Mg,Fe)_3Fe_2O_6$ solid solutions at high pressure and temperature"

YURIMOTO, H.; and the Hayabusa2 Initial Analysis Chemistry Team (63 members including BOUVIER, A.): 07.-11.03.2022, 53rd Lunar and Planetary Science Conference, Houston, USA: "Chemical and isotopic characterization of asteroid Ryugu"

ZHANG, B.; GREER, J.; ISHEIM, D.; SEIDMA, D.N.; BOUVIER, A.; HECK, P.R.: 26-28.10.2022, Apollo 17 (ANGSA) Workshop, Houston, USA: "Atom probe tomography of a 4.45 Ga zircon supporting early cystallization of the lunar magma ocean"

4.4 Lectures and seminars at Bayerisches Geoinstitut

ALKHIMENKOV, Yury, University of Lausanne, Istitute of Earth Sciences, Lausanne, Switzerland (online): "Resolving coupled physical processes in porous rocks", 24.01.2022

BONDAR, Dmitry: Bayerisches Geoinstitut, Bayreuth, Germany: "Speciation of water and molar absorptivities of near-infrared OH- and H_2O bands in hydrous peridotitic glasses", 09.06.2022

BOULLIUNG, Julien, Oxford University, Department of Earth Sciences, Oxford, U.K.: "Sulphur behaviour in silicate melts: An experimental study", 01.12.2022

BUIAN, Andrea, Università degli Studi di Firenze, Italy: "Characterization of the mantle beneath the Ngaoundéré Plateau (Cameroon Volcanic Line) using geochemistry and petrology on ultramafic xenoliths and host lavas", 12.10.2022

DE WINTER, Bram, Vrije Universiteit Amsterdam, The Netherlands: "Crystallisation of garnet in an aluminium-rich lunar mantle", 07.07.2022

CHANG, Jia, Bayerisches Geoinstitut, Bayreuth, Germany: "Controls on the porphyry Cu-Au mineralizing potential of magmas in post-subduction settings", 17.11.2022

CHANYSHEV, Artem, Bayerisches Geoinstitut, Bayreuth, Germany (online): "Akimotoite-bridgmanite phase transition explains depressed 660-km seismic discontinuity beneath subduction zones", 05.05.2022

DAVAILLE, Anne, Université Paris-Saclay, Laboratoire FAST, Orsay, France: "Convection in complex fluids: from the lab to Venus", 27.10.2022

DE MONTSERRAT NAVARRO, Albert, Università degli Studi di Padua, Dipartimento di Geoscienze, Italy (online): "Extrinsic viscous anisotropy: from micro to macro scale", 13.01.2022

FERRAND, Thomas, Freie Universität Berlin, Arbeitsbereich Mineralogie-Petrologie, Berlin, Germany: "Understanding the seismic rupture: a transdisciplinary journey", 10.11.2022

GLÄSER, Leon, Friedrich-Alexander-Universität Erlangen-Nürnberg, Germany: "The high-K calc-alkaline to shoshonitic volcanism of Limnos, Greece: Implications for the geodynamic evolution of the northern Aegean", 11.07.2022

HIRSCHMANN, Marc, University of Minnesota, Department of Earth and Environmental Sciences, Minneapolis, USA: "Earth's redox dynamics, from the magma ocean to the present", 15.12.2022

IOANNIDI, Paraskevi Io, Iowa State University, Ames, USA (online): "Deformation and rheology of heterogeneous rocks: from field observations to numerical models", 26.01.2022

KNAFELC, Joseph, Queensland University of Technology, School of Earth and Atmospheric Sciences, Brisbane, Australia (online): "Petrology of the Havre 2012 rhyolite pumice raft: Reassessing evidence for deep sea explosive eruptions", 31.03.2022

KOCH, Lennart, Georg-August-Universität Göttingen, Abteilung Mineralogie, Göttingen, Germany: "CO_2 diffusion in a leucititic melt from the Colli Albani Volcanic District, Italy", 06.10.2022

KOLZENBURG, Stephan, University at Buffalo, Department of Geology, Buffalo, USA (online): "How low can you flow? Stopping criteria for lava flows at conditions relevant to nature", 03.02.2022

LANGHAMMER, Dominic, Bayerisches Geoinstitut, Bayreuth, Germany: "Data driven modelling of magma viscosity", 28.04.2022

LE BRETON, Eline, Freie Universität Berlin, Institut für Geologische Wissenschaften, Germany (online): "From rifting to subduction and exhumation: the life cycle of the Alpine Ocean", 10.02.2022

MALTESE, Alessandro, Institut de Physique du Globe de Paris, France: "Earth's early differentiation history – a geochemical perspective from the Indian subcontinent", 19.05.2022

MIYAJIMA, Nobuyoshi, Bayerisches Geoinstitut, Bayreuth, Germany: "Dauphiné twin in a naturally deformed quartz: Characterization by electron channelling contrast imaging in SEM and large-angle convergent-beam diffraction in TEM", 21.07.2022

MUTO, Jun, Tohoku University, Division of Geosphere Evolution, Sendai, Japan (online): "Experimental investigation of rock pulverization under high strain rate", 27.06.2022

NÉRI, Adrien, Bayerisches Geoinstitut, Bayreuth, Germany (online): "Setting up ultrasonic interferometry at BGI and DESY – preliminary results on olivine – sulfide melt aggregates", 20.01.2022

PIANI, Laurette, Université de Lorraine, Nancy, France (online): "H distribution of water in the inner Solar System and interest for the origin of water on Earth", 27.01.2022

PUTAK JURICEK, Marija, Bayerisches Geoinstitut, Bayreuth, Germany (online): "Water in the Earth's mantle: Metasomatism and melting", 17.03.2022

SCHMÄDICKE, Esther, Friedrich-Alexander-Universität Erlangen-Nürnberg, Germany (online): "Is OH in opx of abyssal peridotite a proxy for water in the suboceanic mantle?", 28.07.2022

SCHMIDT, Julia, Freie Universität Berlin, Planetare Geodynamik, Berlin, Germany: "Small elements with large influence – Modelling the redistribution of trace elements and its effect on the thermal evolution of rocky planets", 24.11.2022

SOSSI, Paolo, ETH Zurich, Institute of Geochemistry and Petrology, Zurich Switzerland: "Stochastic accretion of the Earth", 23.06.2022

SPANG, Arne, Johannes-Gutenberg University Mainz, Germany (online): "Geomechanical modeling of magmatic systems", 27.01.2022

STEPHANT, Alice, National Institute of Astrophysics, Rome, Italy (online): "Protosolar hydrogen source for water in the Moon and the Early Earth", 16.05.2022

TAJCMANOVA, Lucie, Universität Heidelberg, Institut für Geowissenschaften, Heidelberg, Germany: "Quantification of micro-scale processes in mineral systems under stress", 30.06.2022

VLASOV, Kirill, Bayerisches Geoinstitut, Bayreuth, Germany: "Hydrous fluids in the mantle", 13.06.2022

VULPIUS, Sara, Freie Universität Berlin, Institut für Geologische Wissenschaften, Berlin, Germany: "Contribution of volatiles from mafic intrusions to the atmosphere", 20.06.2022

4.5 Conference organization

January & February 2022, Intensive Lecture Series "Mineral Physics I" Student Exchange Promotion Program for Graduate Schools of Science of the 10 National Universities (STEP10) of Japan, virtual (T. KATSURA)

23.-27.05.2022, European Geosciences Union General Assembly 2022, Vienna, Austria: 'Solving geoscience problems using mineralogy' (J. INGRIN, C. MCCAMMON, J. MAJZLAN, E. ZHITOVA)

16.-24.07.2022, COSPAR 2022, 44th Scientific Assembly, Athens, Greece, Member of the Scientific Organizing Committee for session B4.4 'Mars Sample Return' (A. BOUVIER)

18.-22.07.2022, 23rd General Meeting of the International Mineralogical Association (IMA 2022), Lyon, France: 'Mineralogy at extreme conditions' (C. MCCAMMON, H.-P. SCHERTL, S. ANGIBOUST, M. GREGOIRE, C. BONADIMAN, M. MATUSIAK-MALEK, I. BAZIOTIS, L. FERRIERE, G. LIBOUREL, A. WOODLAND, J. VAN DRIEL, H. LUO, L. VOČADLO, P. COMODI, B. REYNARD, M. PAMATO)

14.-19.08.2022, 85th Annual Meeting of Meteoritical Society, Glasgow, U.K., Member of the Scientific Program Committee (A. BOUVIER)

23.-27.08.2022, 33rd European Crystallography Meeting, Versailles, France: Microsymposium MS27 'Minerals and Materials under extreme Conditions' (T. BOFFA BALLARAN)

05.-09.09.2022, International School 'Understanding Oxygen Fugacity in Geoscience', Trieste, Italy (L. ZIBERNA, G. YAXLEY, V. STAGNO, E. GREEN, V. CERANTOLA, C. MCCAMMON, S. SCHORN)

15.-16.09.2022, 3rd Workshop on Giant Collisions and their Effects on the Thermochemical Evolution of Planets, Berlin, Germany (G. GOLABEK)

28.-30.09.2022, Science Community Workshop on the Proposed First Sample Depot for the Mars Sample Return Campaign, online, Member of the Scientific Program Committee (A. BOUVIER)

21.-22.10.2022, Joint Meeting of the Deutsche Mineralogische Gesellschaft Geochemistry and Petrology/Petrophysics sections, Mainz, Germany, Co-Chair of the Organising and Program Committee (A. BOUVIER)

12.-16.12.2022, AGU Fall Meeting 2022, Chicago, USA: Session MR45A 'Advanced Experimental, Computational and Analytical Approaches in Exploring Deep Planetary Interiors III Oral' (K. TSUNO, S. GRÉAUX, J. DOLINSCHI)

5. Visiting Scientists

5.1 Visiting scientists funded by the Bayerisches Geoinstitut

BOULLIUNG, Julien, Oxford University, Department of Earth Sciences, Oxford, U.K.: 30.11.-02.12.2022

BUCHEN, Johannes, Oxford University, Department of Earth Sciences, Oxford, U.K.: 13.-17.12.2022

BUIAN, Andrea, Università degli Studi di Firenze, Italy: 10.-14.10.2022

DAVAILLE, Anne, Université Paris-Saclay, Laboratoire FAST, Orsay, France: 26.-29.10.2022

DE WINTER, Bram, Vrije Universiteit Amsterdam, The Netherlands: 06.-09.07.2022

DI GENOVA, Danilo, Istituto Nazionale di Geofisica e Vulcanologia, Rome, Italy: 08.-19.06.2022

GLÄSER, Leon, Friedrich-Alexander-Universität Erlangen-Nürnberg, Germany: 10.-11.07.2022

KOCH, Lennart, Georg-August-Universität Göttingen, Abteilung Mineralogie, Göttingen, Germany: 06.-07.10.2022

MÄRZ, Amelie, A.B. von Stettensches Institut, Augsburg, Germany: 01.-04.08.2022

MALTESE, Alessandro, Institut de Physique du Globe de Paris, France: 18.-20.05.2022

MARRAS, Giulia, Sapienza Università di Roma, Dipartimento di Scienze della Terra, Rome, Italy: 09.05.-23.09.2022

SCHMIDT, Julia, Freie Universität Berlin, Planetare Geodynamik, Berlin, Germany: 23.-25.11.2022

SOSSI, Paolo, ETH Zurich, Institute of Geochemistry and Petrology, Zurich, Switzerland: 22.-24.06.2022

TAJCMANOVA, Lucie, Universität Heidelberg, Institut für Geowissenschaften, Heidelberg, Germany: 30.06.-01.07.2022

VULPIUS, Sara, Freie Universität Berlin, Institut für Geologische Wissenschaften, Berlin, Germany: 20.-24.06.2022

5.2 Visiting scientists supported by other externally funded BGI projects

BLANCHARD, Ingrid, Universität Potsdam, Institut für Geowissenschaften, Potsdam, Germany: 07.-11.06.2022 (DFG[*B])

FEDOTENKO**,** Timofey, Deutsches Elektronen-Synchrotron DESY, PETRA III, Hamburg, Germany: 17.-21.03.2022 (DFG[*B])

PETITGIRARD, Sylvain, ETH Zurich, Institute of Geochemistry and Petrology, Zurich Switzerland: 06.-09.06.2022 (DFG[*B])

WALTE, Nico, TU München, Forschungs-Neutronenquelle Heinz Maier-Leibnitz (FRM II), Garching, Germany: 07.-08.06.2022 (BMBF[*A])

[*A] BMBF: Bundesministerium für Bildung und Forschung

[*B] DFG: Deutsche Forschungsgemeinschaft

5.3 Visitors (externally funded)

BARATELLI, Lisa, Università degli Studi di Milano, Dipartimento di Scienze della Terra 'Ardito Desio', Milano, Italy: 07.-11.03.2022

BRUNNER, Tanja, Universität Würzburg, Germany: 17.11.2022

BYKOV, Maxim, Universität zu Köln, Institut für Anorganische Chemie, Köln, Germany: 01.-03.09.2022, 22.-26.10.2022

BYKOVA, Elena, Universität zu Köln, Institut für Anorganische Chemie, Köln, Germany: 22.-26.10.2022

CAMPOMENOSI, Nicola, Universität Hamburg, Mineralogisch-Petrographisches Institut, Hamburg, Germany: 07.-11.03.2022

ENDER, Christopher, Max Planck Institute for Polymer Research, Mainz, Germany: 18.-20.07.2022

FACCINCANI, Luca, Università degli Studi di Ferrara, Dipartimento di Fisica e Scienze della Terra, Ferrara, Italy: 10.-31.01.2022

FEDOTENKO, Timofey, Deutsches Elektronen-Synchrotron DESY, Hamburg, Germany: 22.-26.06.2022

FORERO FUENTES, Valentina, Universitdad de los Andes, Bogotá, Colombia: 13.06.-25.07.2022

FRULLA, Francesca, Politecnico di Milano, Department of Physics, Milano, Italy: 05.-09.12.2022

FUKUSHIMA, Ryo, Tohoku University, Center for Northeast Asian Studies, Sendai, Japan: 20.06.-02.07.2022

GHOSH, Sujoy, Indian Institute of Technology, Department of Geology & Geophysics, Kharagpur, India: 15.06.-13.07.2022

GONCHAROV, Alexander, Universität zu Köln, Institut für Anorganische Chemie, Köln, Germany: 01.-03.09.2022

HECKEL, Catharina, Johann Wolfgang Goethe-Universität, Institut für Geowissenschaften, Frankfurt/M, Germany: 02.-06.05.2022, 05.-09.09.2022

KOEMETS, Egor: University of Oxford, Department of Earth Sciences, Oxford, U.K.: 19.-25.02.2022, 21.-29.06.2022, 26.10.-01.11.2022

KOEMETS, Iuliia: University of Oxford, Department of Earth Sciences, Oxford, U.K.: 26.10.-01.11.2022

KULKA, Britany, University of Oxford, Department of Earth Sciences, Oxford, U.K.: 01.-08.01.2022, 05.-09.04.2022, 31.07.-16.08.2022

LI, Xiang, Universität Münster, Institut für Mineralogie, Münster, Germany: 17.-23.09.2022

LÖSCHMANN, Jessica, TU Clausthal, Institut für Nichtmetallische Werkstoffe, Clausthal Germany: 28.11.-09.12.2022

MARTYNOVA, Natalia, Universität zu Köln, Institut für Anorganische Chemie, Köln, Germany: 01.-03.09.2022

MASIN, Max, Stone Gallery, Baarn, Netherlands: 16.02.2022

MASIN, Roy, Stone Gallery, Baarn, Netherlands: 16.02.2022

OHASHI, Tomonori, Tohoku University, Department of Earth Science, Sendai, Japan: 05.-30.09.2022

PAUSCH, Tristan, Universität Innsbruck, Institut für Mineralogie und Petrographie, Austria: 04.-18.04.2022

RAGAZZOLA, Federica, Stazione Zoologica Anton Dohrn, Naples, Italy: 10.-28.01.2022

RASHCHENKO, Sergey, Novosibirsk State University, Sobolev Institute of Geology and Mineralogy, Novosibirsk, Russia: 04.-11.11.2022

RÖSCHE, Costanze, Universität Hamburg, Mineralogisch-Petrographisches Institut, Germany: 21.03.-08.04.2022

ROMANENKO, Alexandr, Novosibirsk State University, Sobolev Institute of Geology and Mineralogy, Novosibirsk, Russia: 04.-11.11.2022

ŠARIĆ, Lovro, LMU München, Department of Earth and Environmental Sciences, München, Germany: 26.06.-09.10.2022

SATTA, Niccolò, University of Oxford, Department of Earth Sciences, Oxford, U.K.: 09.-11.02.2022, 21.-24.06.2022

SCHUMANN, Katrin, Johann Wolfgang Goethe-Universität, Institut für Geowissenschaften, Frankfurt/M., Germany: 01.-06.11.2022

SPOHN, Matthias, Universität Ulm, Institut für Quantenoptik, Ulm, Germany: 13.-15.09.2022

TIMONER Bosch, Cristian, Universidad Compluetense Madrid, Spain: 06.09.2022

TRUBOWITZ, Charlotte, ETH Zurich, Institute of Geochemistry and Petrology, Zurich Switzerland: 03.-09.07.2022

UENVER-THIELE, Laura, Johann Wolfgang Goethe-Universität, Institut für Geowissenschaften, Frankfurt/M., Germany: 30.06.-03.07.2022, 01.-06.11.2022

WOODLAND, Alan, Johann Wolfgang Goethe-Universität, Institut für Geowissenschaften, Frankfurt/M., Germany: 22.-26.08.2022

6. Additional scientific activities

6.1 Habilitation/Theses

Habilitation

THIELMANN, Marcel: Seismische Wellen und die Physik von Erdbeben.

Ph.D. theses

ABEYKOON, Sumith: Experimental constraints on the compositions of sulphides and aqueous fluids in the Earth's interior.

BONDAR, Dmitry: Speciation of water and molar absorptivities of near-infrared OH^- and H_2O bands in hydrous peridotitic glasses quenched by a novel rapid-quench multi-anvil technique.

DOMINIJANNI, Serena: Physicochemical properties of Fe-bearing minerals and metal alloys at deep Earth conditions.

IMMOOR, Julia: Experimental deformation of mantle minerals at simultaneous high-pressure and high-temperature.

PUTAK JURIČEK, Marija: Water in Earth's mantle: Metasomatism and melting.

VLASOV, Kirill: Hydrous fluids in the mantle.

M.Sc. theses

CALVO, Lucas: Volatile and trace element partitioning during arc magma fractionation in the lower crust.

PÖPPELBAUM, Melanie: The speciation of sulphur in fluids released from sulphide-bearing serpentinite.

RIZALDI, Putra: Melt chemistry control on crystal and bubble formation in basalts.

ROGMANN, Elena-Marie: Elastic behaviour of (Na,Mg,Fe) (Al,Si,Fe)O_4 calcium-ferrite type phase at high pressure.

WANG, Xiaoyu: The viscosity of Fe and Fe-alloys at conditions of Earth's core.

ZHAO, Ran: The origin and impact history of LL6 ordinary chondrite melt breccia NWA 12520.

6.2 Honours and awards

CRINITI, Giacomo	2022 John C. Jamieson Student Paper Award of the Mineral and Rock Physics Section of the American Geophysical Union

CHAKRABORTI, Amrita	Best Poster Award, High Pressure Gordon Research Conference, 2022
KATSURA, Tomoo	Fellow of the Japan Geoscience Union Award of the Japan Society of High Pressure Science and Technology
KEPPLER, Hans	A.G. Werner Medal of the German Mineralogical Society
KUBIK, Edith	2022 Geophysics Prize (Ph.D. award) of the French National Committee for Geodesy and Geophysics (CNFGG)

6.3 Editorship of scientific journals

AUDÉTAT, Andreas	Associate Editor "Journal of Petrology" Associate Editor "Economic Geology
BOFFA BALLARAN, Tiziana	Associate Editor for European Journal of Mineralogy
BOUVIER, Audrey	Associate Editor "Geochimica et Cosmochimica Acta" Guest Editor "Progress in Earth and Planetary Sciences", Special Issue "Thermal, dynamical, and chemical processes in our early Solar System"
FEI, Hongzhan	Guest Associate Editor "Frontiers in Earth Science", Research Topic "Water in the Earth interior"
DUBROVINSKY, Leonid	Member, Editorial Board of the Journal of "High Pressure Research" Member, Advisory Board, Minerals
KEPPLER, Hans	Editorial Board "Contributions to Mineralogy and Petrology" Editorial Board "ACS Earth and Space Chemistry"
MCCAMMON, Catherine	Editor in Chief "Physics and Chemistry of Minerals"
MIYAJIMA, Nobuyoshi	Associate Editor "European Journal of Mineralogy"

6.4 Membership of scientific advisory bodies

BOUVIER, Audrey	Vice-Chair, Section Geochemistry, Deutsche Mineralogische Gesellschaft (DMG) Member, Mars Sample Return Campaign Group, NASA and ESA Chair, V. M. Goldschmidt Award Committee, Geochemical Society Member, Scientific committee of the ATTARIK Foundation
DUBROVINSKY, Leonid	Member, Review Panel of Canadian Light Source Chair Subcommission on Spectroscopy, Diffraction, and new Instrumentations in Mineral Physics of the International Mineralogical Association Member Review Panel of PETRA III Member Review Panel of Research Council of Lithuania
FROST, Dan	Member, Bavarian Academy of Sciences Member, German National Academy of Sciences (Leopoldina) Member of the Royal Society Scientific Advisory Committee of the GeoForschungsZentrum Potsdam Member, Royal Society Fellows Sectional Committee SC5 Member, Governing Council of the European Association of Geochemistry
KATSURA, Tomoo	Japan Association of Mineralogical Sciences Award Committee Vice Chair
KEPPLER, Hans	Member, German National Academy of Sciences (Leopoldina) Member, Bavarian Academy of Sciences Member, Advisory Board, Dachverband Geowissenschaften
MCCAMMON, Catherine	Chair, Governance Review Task Force, American Geophysical Union Member, Implementation Task Force, American Geophysical Union Member, Project Review Panel P01, PETRA III Member, Council, International Mineralogical Association Member, Fellows Committee, VGP section, American Geophysical Union

	Member, Award Committee of the International Board on the Applications of Mössbauer Spectroscopy Chair, Sub-committee "Earth's Deep Interior" of the Commission of the Physics of Minerals, International Mineralogical Association Member, International Scientific Committee, 23rd General Meeting of the International Mineralogical Association, 2022
WITHERS, Anthony	Member, Project Review Panel P02.2 and P61.B, PETRA III

7. Scientific and Technical Personnel

Name		Position	Duration in 2022	Funding source
ABEYKOON, Sumith	M.Sc.	Wiss. Mitarbeiter		Leibniz
AKBAR, Fariia Iasmin	M.Sc.	Wiss. Mitarbeiterin	from 01.06.	DFG
ANDREIEVA, Daria	B.Sc.	Student. Hilfskraft	from 03.05.	DFG
ASLANDUKOV, Andrii	M.Sc.	Wiss. Mitarbeiter		DFG
ASLANDUKOVA, Alena	M.Sc.	Wiss. Mitarbeiterin		DFG
AUDÉTAT, Andreas	Dr.	Akad. Oberrat		BGI
BAUER, Gerald	Dipl.-Ing. (FH)	Techn. Angestellter		BGI
BOFFA BALLARAN, Tiziana	Dr.	Akad. Oberrätin		BGI
BONDAR, Dmitry	M.Sc.	Wiss. Mitarbeiter	to 14.06.	DFG
	Dr.	Wiss. Mitarbeiter	from 15.08.	EU
BOUVIER, Audrey	Prof. Dr.	Professorin		BGI
BUCHERT, Petra		Fremdsprachen-Sekretärin		BGI
BUBMANN, Daniela		Techn. Angestellte		BGI
BYKOVA, Elena	Dr.	Wiss. Mitarbeiterin	to 31.03.	DFG
CALOGERO, Meredith	Dr.	Wiss. Mitarbeiterin	from 15.08.	EU
CALVO, Lucas	B.Sc.	Student. Hilfskraft	to 30.09.	DFG
CHAKRABORTI, Amrita	Dr.	Wiss. Mitarbeiterin		DFG
CHANG, Jia	Dr.	Wiss. Mitarbeiter		DFG
CHANYSHEV, Artem	Dr.	Wiss. Mitarbeiter	to 31.03.	DFG
			from 01.04.	EU
CRINITI, Giacomo	M.Sc.	Wiss. Mitarbeiter		Leibniz
CZEKAY, Laura	M.Sc.	Wiss. Mitarbeiterin		DFG
DINIUS, Anna		Verwaltungsangestellte		BGI
DOLINSCHI, Jonathan	M.Sc.	Wiss. Mitarbeiter		Leibniz
DUBROVINSKY, Leonid	Apl. Prof. Dr.	Akad. Direktor		BGI
FEI, Hongzhan	Dr.	Wiss. Mitarbeiter		BGI
FISCHER, Heinz		Mechaniker		BGI
FROST, Daniel	Prof. Dr.	Stellvertr. Leiter		BGI
GOLABEK, Gregor	Prof. Dr.	Professor		BGI
HAMADI, Muhammad	M.Sc.	Student. Hilfskraft	from 10.11.	EU
HEIDELBACH, Florian	Dr.	Wiss. Mitarbeiter		BGI
HIN, Remco	Dr.	Wiss. Mitarbeiter	to 15.03.	EU
		Akad. Rat (Zeit)	from 16.03.	BGI
HIRSCHMANN, MARC	Prof. Dr.	Forschungspreisträger	from 12.09.	AvH

HLEDE, Matej	B.Sc.	Student. Hilfskraft	01.10.-30.11.	BGI
			from 01.12.	DFG
HOWARD, Christopher	Dr.	Wiss. Mitarbeiter	to 30.09.	BMBF
KATSURA, Tomoo	Prof. Dr.	Professor		BGI
KEPPLER, Hans	Prof. Dr.	Leiter		BGI
KIM, Eun Jeong	Dr.	Stipendiatin		AvH
KRAUßE, Detlef	Dipl.-Inform. (FH)	Techn. Angestellter		BGI
KRIEGL, Holger		Haustechniker		BGI
KUBIK, Edith	Dr.	Wiss. Mitarbeiterin		BGI/VP
KURNOSOV, Alexander	Dr.	Wiss. Mitarbeiter		DFG
LANGHAMMER, Dominic	M.Sc.	Wiss. Mitarbeiter		DFG
LINHARDT, Sven		Elektrotechniker		BGI
LIU, Siqi		Stipendiat	to 31.03.	CSC
MAN, Lianjie	M.Sc.	Wiss. Mitarbeiter		Leibniz
MARTIROSYAN, Naira	Dr.	Wiss. Mitarbeiterin	from 01.03.	DFG
MATTHÄUS, Rebecka		Chem.-Techn. Assistentin		BGI
MCCAMMON, Catherine	Privatdozentin Dr.	Akad. Direktorin		BGI
MELAI, Caterina	M.Sc.	Wiss. Mitarbeiterin	to 14.10.	Leibniz
MIYAJIMA, Nobuyoshi	Dr.	Akad. Oberrat		BGI
NÉRI, Adrien	Dr.	Wiss. Mitarbeiter		Leibniz
NJUL, Raphael		Präparator		BGI
OVSYANNIKOV, Sergey	Dr.	Wiss. Mitarbeiter	to 26.11.	DFG
PAUL, Jyotirmoy	Dr.	Wiss. Mitarbeiter		EU
PICCOLO, Andrea	Dr.	Wiss. Mitarbeiter		DFG
PÖPPELBAUM, Melanie	B.Sc.	Student. Hilfskraft	to 30.09.	DFG
	M.Sc.	Wiss. Mitarbeiterin	from 01.10.	DFG
POSNER, Esther	Dr.	Wiss. Mitarbeiterin		DFG
POTZEL, Anke		Chem.-Techn. Assistentin		BGI
PUREVJAV, Narangoo	Dr.	Wiss. Mitarbeiterin		BGI/VP
RAMMING, Gerd		Elektroniker	to 28.02.	BGI
RAUSCH, Oliver		Mechaniker		BGI
ROGMANN, Elena	B.Sc.	Student. Hilfskraft	to 30.09.	DFG
ROTHER, David Alexander		Präparator		BGI
RUBIE, David C.	Prof. Dr.	Professor	to 31.10.	DFG
RUSTIONI, Greta	Dr.	Wiss. Mitarbeiterin		DFG
SCHARNAGEL, Janina		Sekretärin		BGI
SCHULZE, Hubert		Präparator	to 30.11.	EU
SIKDAR, Jinia	Dr.	Wiss. Mitarbeiterin	from 01.08.	EU

SPANG, Arne	Dr.	Wiss. Mitarbeiter	from 01.10.	DFG
STEINLE-NEUMANN, Gerd	Privatdozent Dr.	Akad. Oberrat		BGI
TANG, Hu	Dr.	Stipendiat		AvH
THIELMANN, Marcel	Dr.	Wiss. Mitarbeiter		DFG
TIMONER BOSCH, Cristian	B.Sc.	Student. Hilfskraft	from 01.10.	BGI
TRENZ, Ulrike		Biol.-Techn. Assistentin		BGI
ÜBELHACK, Stefan		Mechaniker		BGI
VALDIVIA MUNOZ, Pedro Antonio	M.Sc.	Wiss. Mitarbeiter		DFG
VLASOV, Kirill	M.Sc.	Wiss. Mitarbeiter	to 30.06.	DFG
WANG, Fei	Dr.	Wiss. Mitarbeiter		EU
WANG, Lin	Dr.	Wiss. Mitarbeiter		EU
WANG, Xiaoyu	B.Sc.	Student. Hilfskraft	to 30.04.	BGI
			01.05.-31.10.	DFG
WIESNER, Dorothea		Techn. Assistentin		BGI
WITHERS, Antony	Dr.	Wiss. Mitarbeiter		BGI
YUAN, Liang	Dr.	Stipendiat	to 31.01.	AvH
		Wiss. Mitarbeiter	from 01.02.	DFG
ZHANG, Jingbo	M.Sc.	Stipendiat	to 31.01.	CSC
ZHAO, Ran	B.Sc.	Student. Hilfskraft	to 30.09.	DFG
	M.Sc.	Stipendiat	from 01.10.	CSC

Abbreviations/explanations:

AvH	Alexander von Humboldt Foundation
BGI	Staff Position of Bayerisches Geoinstitut
BGI/VP	Visiting Scientists' Program of Bayerisches Geoinstitut
BMBF	Federal Ministry of Education and Research
Carnegie	Carnegie Institution of Washington
DAAD	German Academic Exchange Service
CSC	China Scholarship Council
DFG	German Science Foundation
EU	European Union
IRTG	International Research Training Group "Deep Earth Volatile Cycles"
Leibniz	Leibniz-Preis der Deutschen Forschungsgemeinschaft Prof. Frost
UBT	Universität Bayreuth

Index